KU LEUVEN

ARENBERG DOCTORAL SCHOOL
Faculty of Science

Asteroseismology of γ Doradus stars with the *Kepler* space mission

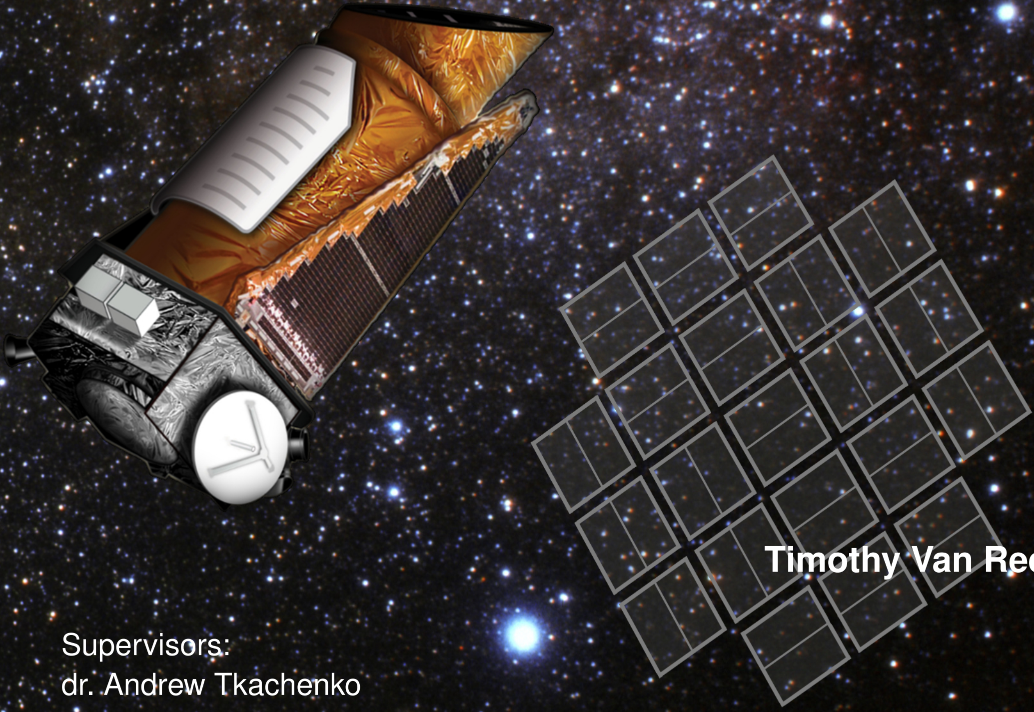

Timothy Van Reeth

Supervisors:
dr. Andrew Tkachenko
Prof. dr. Conny Aerts

March 2017

Asteroseismology of γ Doradus stars with the *Kepler* space mission

Timothy VAN REETH

Examination committee:
Prof. dr. Hans Van Winckel, chair
dr. Andrew Tkachenko, supervisor
Prof. dr. Conny Aerts, supervisor
dr. Peter Pápics
Prof. dr. Jon Sunqvist
Prof. dr. Tom Van Doorsselaere
Prof. dr. Jørgen Christensen-Dalsgaard
(Aarhus Universitet, Denmark)
Prof. dr. Stéphane Mathis
(CEA Paris-Saclay, France)
Prof. dr. Tamara Rogers
(Newcastle University, United Kingdom)

Dissertation presented in partial fulfilment of the requirements for the degree of Doctor of Science (PhD): Astronomy and Astrophysics

March 2017

Acknowledgements
The research presented in this PhD thesis was based on funding from the Research Foundation Flanders (FWO), Belgium, under grant agreement G.0B69.13.
We are very grateful to Bill Paxton, Richard Townsend, and their collaborators at the Universities of California at Santa Barbara and Wisconsin-Madison, for their great work on the stellar evolution code MESA and the stellar pulsation code GYRE and for offering these codes in open source to the community.

Cover image:
The *Kepler* space telescope in front of the "Summer Triangle": a triangle in the night sky composed of the three bright stars Altair (back cover), Deneb (right front cover), and Vega (lower front cover). The field-of-view of the original *Kepler* mission, shown in grey on the front cover, is located in this part of the sky. Original background image by ESA/Hubble (A. Fujii), artwork of the *Kepler* space telescope by NASA/*Kepler* mission. Image composition by Timothy Van Reeth.

Uitgegeven in eigen beheer, Timothy Van Reeth, Celestijnenlaan 200D box 2401, B-3001 Leuven (Belgium)

Preface

When the story of an adventure is told, it usually begins with *"once upon a time, in a country far away…"* or *"a long time ago, in a galaxy far away…"*. Otherwise, it has at least (with a non-zero probability) a big blue box or a majestic flying turtle in it.

This adventure, on the other hand, started not-so-far-away with a large pile of cardboard and a 2m-high inflatable rocket of Tintin. In hindsight, a PhD in astronomy really was the only logical outcome. However, it still took more than twenty years in total to get here, and the last four years in particular have been very interesting. Quite a few people have helped me along the way, and I would like to take this chance to thank everyone.

Conny and Andrew, thank you for all your help and patience over the past four years! I cannot begin to count the number of times I sent an e-mail late in the evening, only to still get a reply on the same day. Not to mention all the times when you pushed me ahead to meet a deadline, or when you were available for a discussion, often at a moment's notice. Needless to say, I wouldn't have made it to this point without you. Thank you!

I also have to thank Bill Paxton, Richard Townsend, and their collaborators at KITP and the University of Wisconsin-Madison, for their great work on the stellar evolution code MESA and the stellar pulsation code GYRE. Thank you for patiently answering the questions that *this lunatic* came up with, and for making your work freely available to the community. Without it, I would never have been able to make as much progress as I did, and would probably still be stuck coding the nitty-gritty details of stellar pulsation theory.

Bram, Cole, Dominic, Ehsan, Jonas, Konstanze, May, Paul, Peter P., Peter D. C., Pieter, Roy, Sanjay, Santiago, Steven, Valentina: thank you for introducing me to asteroseismology and keeping me there (along with Andrew and Conny). Thank you for brainstorming over all things asteroseismology (and eating all the cake), patiently answering my questions (and sharing cake) and looking for new questions to answer (and having more cake)!

Also a huge thanks to all the people who have been my office mates over the past few years! Bram, Enrico, Allard-Jan, Konstanze, Peter N., Valentina, Alejandra, Kaustubh, Jonas, Enya, Dominic: thanks for putting up with my quirky questions, encouraging me when things were a bit difficult, and helping me brainstorm when I struggled with some particular challenges. Thank you for making it a joy to come into the office every day!

Alejandra, Ana, Andrew, Bram, Cole, Ehsan Paul, Peter, Jonas, Jonathan, Joris, Kenneth, Marie, Michel, Mike, Peter, Pieter, Robin, Roy, Steven, Valentina: thanks for dragging me from behind my desk once in a while, and all the fun and interesting conversations, both inside and outside of the institute!

Thanks a lot to everyone else at IvS as well, both now and during the past few years! Thank you for making it so fun to be at IvS! Thanks to you all, it is one of very few places I know where you can hear people laughing so loud and often, and (in some cases) learn to recognise people's laughs faster than their names.

Mama, papa, Cathy, Bart, Veronique, Anne-Sophie, Nathan en Nora: dank je wel om er ook elke dag voor me te zijn! Bedankt dat jullie je altijd zo flexibel hebben opgesteld als er een reis nodig was, of een deadline eraan kwam, en bedankt dat jullie me ook af en toe achter mijn bureau vandaan hebben gehaald, en me het werk even lieten vergeten.

Dank je wel ook voor iedereen bij Akabe De Pioen en het Rode Kruis van Mol: Senne, Thomas, Hanne, Lien, Bart, Kris, Bruno, Jasper, Tom, Pieter, Marlies, Jolien, Wendy, Jan, Heidi, Lorenz, Yves, Birgit, Ilse, Raf, *et al.*: van harte bedankt voor de vele dagen aangename ontspanning, en jullie eindeloze geduld. Jullie zijn er zelfs in geslaagd om aan de verleiding te weerstaan me te knevelen als ik -weer maar eens- niet over sterrenkunde kon zwijgen!

There are a lot of people I haven't mentioned yet, but who have also been a huge support over the years, both before and during my PhD. You know who you are! Thank you for being there along the way and supporting me in all the ways you have.

Finally, one additional thank you to Conny and the rest of the senior staff: for making sure we have a great coffee machine in the kitchen, as well as a continuous supply of freshly roasted beans! ;-)

raises mug
Cheers!

Timothy,
Leuven, February 2017

Abstract

Gamma Doradus stars are intermediate-mass stars, i.e., a bit more massive than the Sun, burning hydrogen in their core and exhibiting gravity-mode and gravito-inertial mode pulsations. These pulsations experience the buoyancy as their main restoring force, and are most sensitive to the properties of the regions near the convective core in the deep stellar interior of stars. Thus, by analysing and theoretically modelling observed gravity-mode pulsations, the stellar structure in the deep interior of these stars can be constrained. In particular, theoretical studies in the literature have linked non-uniform pulsation period patterns of gravity modes to the chemical gradients, mixing processes and stellar rotation rate in the near-core regions of the pulsating stars. This is especially promising in the case of γ Doradus stars, which are located in the transition region between low-mass stars with a radiative core and a convective envelope, and higher-mass stars with a convective core and a radiative envelope.

Because the pulsations in γ Doradus stars typically have small amplitudes and periods on the order of a day, they are very challenging to study using only ground-based observations. Hence, thanks to the extensive high-precision white-light photometric observations of these stars with recent space missions such as *Kepler*, considerable progress is currently being made in the study of these stars.

We have developed a method to detect pulsation period patterns in the extensive high-precision white-light space-based photometric observations of γ Doradus stars. In the case of slowly rotating stars, we rely on échelle diagrams to detect pulsation period series, while for moderate to fast rotators we exploit the fact that visible patterns of different types of pulsations are often well-separated. Applications of the method on a synthetic data set, the *Kepler* data of KIC 11145123, a well-known γ Doradus star, as well as four other γ Doradus stars observed with the *Kepler* space telescope, constituted an important proof-of-concept study and justified using the method in a larger scale study. The analysis technique was found to fail for stars with either few visible pulsations in the light curve, or stars with a very large number of visible pulsations, i.e., stars which are likely moderate to fast rotators and have overlapping pulsation period series.

We then applied our method to a sample of 70 γ Doradus candidates, for which we collected both *Kepler* space photometry and ground-based high-resolution spectroscopic observations. We were able to confirm the γ Doradus type variability for 68 sample targets, and, despite the limitations of our method, detect pulsation period patterns for 50 of them. Thirteen targets were found to be part of multiple star systems, among which we have four single-lined binaries, four double-lined binaries, two triple systems and three systems with composite spectra but no detected radial velocity variations. Fundamental atmospheric parameters were determined for all single stars and single-lined binaries. In the subsequent sample characterisation study, we also found strong correlations between the morphology of the observed pulsation patterns and the projected rotational velocities of the stars, derived from the spectroscopic observations. These were in line with theoretical predictions in the literature.

We have exploited this strong correlation between the stellar pulsation properties and rotation, and developed a method to efficiently and reliably identify the pulsation mode geometry, and derive the stellar rotation rate in the deep stellar interior from the observed pulsation periods. This method was successfully applied to 40 of the 50 targets with detected pulsation period patterns. Our method also gave rise to the first detection of Rossby waves or r-modes in γ Doradus stars, i.e., a type of purely inertial pulsations which have the Coriolis force as their restoring force. We discovered such type of modes in ten of our targets. The presented method's main weakness is the (current) assumption that the analysed star is spherically symmetric and rigidly rotating. This limits its applicability, but our work is nevertheless a major step ahead compared to methods that were available prior to this thesis research.

The research presented in this dissertation forms a solid base for further detailed asteroseismic studies of individual γ Doradus stars, specifically with a focus on differential stellar rotation and the rotational mixing processes and angular momentum transport taking place during the core-hydrogen burning phase of intermediate-mass stars. Furthermore, the research methods developed in this work can also be applied to other types of gravity-mode pulsators, as was recently illustrated from applications to slowly pulsating B stars observed by the *Kepler* satellite. While the number of stars in our sample exhibiting special features like Rossby waves is limited, a dedicated sample composition and analysis of such stars would be very valuable, given that Rossby-wave asteroseismology has not yet been exploited.

Beknopte samenvatting

Gamma Doradus sterren zijn iets zwaarder en helderder dan onze eigen zon, en vertonen graviteitsgolven, waarvoor de stuwkracht van Archimedes optreedt als dominante herstelkracht. Graviteitsgolven worden het meeste beïnvloed door de sterstructuur van de radiatieve zones diep in de ster, in de buurt van de sterkern. Door deze pulsaties te bestuderen en theoretisch te modelleren, is het dus mogelijk om de eigenschappen van de sterstructuur binnenin de ster te bepalen. Recente theoretische studies in de literatuur voorspellen karakteristieke niet-uniforme patronen van pulsatieperiodes voor graviteitsgolven, waarbij de aanwezigheid van chemische stratificatie, mengprocessen en sterrotatie in de ster cruciaal zijn. Dergelijke studies zijn voor γ Doradus sterren veelbelovend, aangezien deze sterren zich in het fysisch interessante overgangsgebied tussen lage-massa sterren met een radiatieve kern en een convectieve enveloppe, en hoge-massa sterren met een convectieve kern, bevinden.

Tot enkele jaren geleden waren sterpulsaties in γ Doradus sterren moeilijk te bestuderen, omdat ze kleine amplitudes en pulsatieperiodes van de grootte-orde van een dag hebben, en er voor het merendeel enkel observaties met telescopen op het aardoppervlak beschikbaar waren. Dankzij de recente observaties met ruimtetelescopen zoals *Kepler* kwam hier verandering in, en momenteel wordt er in de studie van dergelijke sterren veel vooruitgang geboekt. Deze verhandeling levert hieraan een aanzienlijke en unieke bijdrage.

We hebben een methode ontwikkeld die toelaat om de karakteristieke niet-uniforme spectra van pulsatieperiodes, die voorspeld zijn in de literatuur, te detecteren in de precieze fotometrische observaties van γ Doradus sterren vanuit de ruimte. In het geval van traag-roterende sterren gebruiken we zogenaamde échelle diagrammen. Dit laat toe om overlappende series van pulsatieperiodes te detecteren. Voor middelmatig tot snel roterende sterren maken we gebruik van het feit dat verschillende zichtbare sterpulsatiepatronen vaak gescheiden zijn. We hebben onze detectiemethode gevalideerd door ze toe te passen op een artificiële dataset, en de *Kepler* lichtcurves van vijf γ Doradus sterren. Met

uitzondering van de analyse van twee γ Doradus sterren, waren alle toepassingen succesvol. Uit de twee mislukte toepassingen blijkt dat onze methode niet geschikt is voor sterren waarbij slechts een handvol pulsaties zichtbaar is, of waarbij er net bijzonder veel pulsaties geobserveerd worden, zodat verschillende reeksen van pulsatieperiodes moeilijk van mekaar onderscheiden kunnen worden.

Vervolgens hebben we onze methode toegepast op een steekproef van 70 γ Doradus kandidaatsterren, die samengesteld werd door Tkachenko et al. (2013a), en waarvoor wij zowel fotometrie van de *Kepler* ruimtetelescoop als hoge-resolutie spectroscopie van de HERMES spectrograaf verzamelden. 68 sterren uit de steekproef werden positief geïdentificeerd als γ Doradus ster, en voor 50 van hen werden (de theoretisch verwachte) sterpulsatiepatronen gedetecteerd, ondanks de beperkingen van onze methode. Dertien objecten bleken meervoudige sterren te zijn. Voor de enkelvoudige sterren en de enkelgelijnde dubbelsterren hebben we ook de waarden van de atmosferische parameters bepaald. Bij de daaropvolgende karakterisatiestudie van de steekproef vonden we ook een sterke correlatie tussen de morfologie van de sterpulsatiepatronen en de geprojecteerde rotatiesnelheid van de sterren. Dit is in overeenstemming met eerdere theoretische studies van γ Doradus sterren.

We hebben de sterke correlatie tussen de sterpulsaties en -rotatie uitgebuit, en een methode ontwikkeld om efficiënt de geometrie van de pulsaties te bepalen, en de rotatiefrequentie in het sterinwendige te meten. We hebben deze techniek succesvol toegepast op 40 van de 50 sterren waarvoor sterpulsatiepatronen gevonden werden. Dankzij ons onderzoek konden we ook in tien sterren voor het eerst Rossby golven ontdekken. Dit zijn zuivere inertiaalpulsaties in roterende sterren, waarbij de Corioliskracht als herstelkracht optreedt. De voornaamste zwakte van onze analysetechniek is de (huidige) aanname dat de bestudeerde ster sferisch symmetrisch is, en star roteert. Dit beperkt de toepasbaarheid, maar ons werk is een grote stap voorwaarts vergeleken met de kennis die er was vooraleer we ons doctoraatsonderzoek startten.

Ons onderzoek vormt een goede basis voor toekomstige gedetailleerde asteroseismische studies van individuele γ Doradus sterren. Hierbij is het wenselijk bijzondere aandacht te besteden aan differentiële rotatie, rotationele mengprocessen en transport van impulsmoment gedurende de hele fase van waterstofverbranding in sterren met middelgrote massa. Verder zijn toegewijde studies aan specifieke subklassen van γ Doradus sterren, zoals die met Rossby golven, veelbelovend omdat zulk type seismologische modellering nog nooit werd toegepast tot op heden; ons proefschrift levert nu voor het eerst sterren waarvoor dit mogelijk wordt. Tot slot kunnen de analysetechnieken die in dit onderzoek ontwikkeld werden, ook eenvoudig toegepast worden op andere types pulserende sterren die graviteitsgolven vertonen, zoals recent werd aangetoond voor traagpulserende B sterren in de literatuur.

Contents

Abstract iii

Contents vii

List of Figures xi

List of Tables xxv

1 Scientific framework 1

- 1.1 Stellar structure & evolution 2
  - 1.1.1 Stellar structure 2
  - 1.1.2 Stellar evolution of intermediate-mass stars 7
  - 1.1.3 The stellar evolution code MESA 11
- 1.2 Asteroseismology 12
  - 1.2.1 Stellar pulsations 13
  - 1.2.2 A zoo of pulsating stars 28
  - 1.2.3 The stellar pulsation code GYRE 32
- 1.3 Observations 33
  - 1.3.1 *Kepler* space photometry 34
  - 1.3.2 HERMES spectroscopy 35

1.4 Goal and outline of the thesis 36

2 The detection of gravity-mode period spacing patterns 39

2.1 Introduction 40

2.2 Methodology to identify period spacings 41

2.3 Applications 45

2.3.1 Simulations 45

2.3.2 A well-studied *Kepler* star: KIC 11145123 48

2.3.3 Four γ Dor stars in the *Kepler* field 53

2.4 Discussion and conclusions 58

3 A *Kepler* Guest Observer γ Dor sample selection and its characterisation 61

3.1 Introduction 62

3.2 Observations and data reduction 63

3.3 Spectroscopic analysis 64

3.3.1 Binarity 64

3.3.2 Fundamental parameters 67

3.4 Period spacing patterns in the *Kepler* photometry 68

3.5 Statistical analysis of the sample properties 76

3.6 Discussion and conclusions 84

4 Mode identification and interior rotation rate from ensemble modelling 87

4.1 Introduction 88

4.2 Grid of stellar models and pulsation frequencies 89

4.3 Method 89

4.4 Applications 92

4.4.1 Synthetic data 92

4.4.2 Slow and fast rotator 93
4.4.3 Sample study 98
4.5 Discussion and conclusions 108

5 Summary, ongoing research and future prospects 113
5.1 Summary 113
5.2 Towards asteroseismic modelling of individual stars 116
5.3 Future prospects from current data 123
5.4 Prospects from future space missions 126

A Additional material to Chapter 1 129
A.1 Example of a MESA inlist (v7385) 129
A.2 Example of a GYRE inlist (v4.3) 133

B Additional material to Chapter 2 137

C Additional material to Chapter 3 141
C.1 Detected period spacing patterns 153

D Additional material to Chapter 4 171

Bibliography 179

Curriculum Vitae 189

List of publications 191

List of Figures

1.1 Evolution tracks in the Hertzsprung-Russell diagram for stars with an initial mass M of $1.2\,\mathrm{M}_\odot$, $1.4\,\mathrm{M}_\odot$, $1.6\,\mathrm{M}_\odot$, $1.8\,\mathrm{M}_\odot$ and $2.0\,\mathrm{M}_\odot$. The full black lines are the evolution tracks for exponential overshooting with $f_{ov} = 0.0075$, while the dotted evolution tracks correspond to $f_{ov} = 0.030$. The dashed line indicates the ZAMS. The tracks were computed with MESA v7385 (for a description of the input physics, see Section 1.1.3), assuming initial hydrogen fraction $X = 0.71$, metallicity $Z = 0.014$, mixing-length parameter $\alpha_{\mathrm{MLT}} = 1.8$ and extra diffusive mixing $D_{\mathrm{mix}} = 1\,\mathrm{cm}^2\,\mathrm{s}^{-1}$. 9

1.2 The evolution of the convective core mass as a function of the central hydrogen mass fraction X_c (full red line), together with the luminosity which originates from the pp-chain hydrogen burning (full black line) and the CNO cycle (dashed black line). The models correspond to the evolution tracks in Figure 1.1 with the same mass ($1.2\,\mathrm{M}_\odot$,$1.4\,\mathrm{M}_\odot$, $1.6\,\mathrm{M}_\odot$ and $1.8\,\mathrm{M}_\odot$) and $f_{ov} = 0.0075$. 10

1.3 A snapshot of stellar pulsations with spherical degree $l = 3$ and different azimuthal orders m. They have $m = 0$ *(top row)*, $m = \pm 1$ *(*2^{nd} *row)*, $m = \pm 2$ *(*3^{rd} *row)*, $m = \pm 3$ *(bottom row)* respectively, at inclination angles of 30° *(left column)*, 60° *(middle column)* and 90° *(right column)*. The pulsations vary sinusoidally in time. At the chosen moment in the pulsation cycle, the blue and red sections are moving radially outwards and inwards, respectively. The surface nodal lines are shown in white. Figure courtesy of C. Aerts. 15

1.4 *Top panel:* The evolution of the parameter Π_0 for a $1.6\,\mathrm{M}_\odot$ stellar model on the main sequence, with input parameters $X = 0.71$, $Z = 0.014$, step core overshoot $\alpha_{\rm ov} = 0.3$ and diffusive mixing $D_{\rm mix} = 1\,\mathrm{cm}^2\,\mathrm{s}^{-1}$. *Bottom three panels:* The integrand used in Equation (1.10) for the computation of the parameter Π_0 at the selected stages of the stellar evolution indicated in the top panel. 18

1.5 *Left:* Part of a $1.6\,\mathrm{M}_\odot$ evolution track, with $X = 0.71$, $Z = 0.014$, step core overshoot $\alpha_{\rm ov} = 0.3$ and diffusive mixing $D_{\rm mix} = 1\,\mathrm{cm}^2\,\mathrm{s}^{-1}$. *Right:* Period spacing patterns computed for dipole modes of the marked models on the evolution track in the left plot. For each the hydrogen content of the core (X_c) is provided. 19

1.6 Period spacing patterns computed for dipole modes of a $1.6\,\mathrm{M}_\odot$ star with $X_c = 0.5$. *Left:* spacing patterns with and without extra diffusive mixing, with $D_{\rm mix} = 100\,\mathrm{cm}^2\,\mathrm{s}^{-1}$. *Right:* spacing patterns including the effect of extra diffusive mixing for a star rotating with $v_{\rm eq} = 73\,\mathrm{km\,s}^{-1}$, i.e., $f_{\rm rot} = 0.8\,\mathrm{d}^{-1}$, for the prograde (top) and retrograde (bottom) modes. We note the difference of the scales on the x- and y-axes. 20

1.7 Brunt-Väisälä frequency N (*top*) and the rotational kernel K_{nl} (*bottom*) for the lowest- and highest-order mode of the stellar model discussed in Section 4.4.1. The inset shows a zoom of K_{nl}. Both functions correlate with the sensitivity of the gravity-mode pulsations to the different regions inside the star. 24

1.8 The variation of the eigenvalue $\lambda_{k,m,s}$ as a function of the spin parameter s for various pulsations with $m = 1$. In this figure, the retrograde and prograde modes have $s < 0$ and $s > 0$, respectively. The classification parameter k indicates the type of pulsation mode (Lee & Saio 1997). If $k \geq 0$, the indicated pulsations have an equivalent in the non-rotating star, for which $l = k + |m|$. If $k \leq -2$, the pulsation is a Rossby wave, and the pulsations with $k = -1$ are retrograde Yanai modes. 25

1.9 *Top:* A snapshot of a $(l, m) = (1, 1)$ mode pulsation in a non-rotating star, at inclination angles of 30° *(left)*, 60° *(middle)* and 90° *(right)*. The assigned colour coding has the same meaning as in Figure 1.3. *Bottom:* A snapshot of the same pulsation mode, with $(l, m) = (1, 1)$ and at the same inclination angles, but in a star rotating at 50 % of its critical rotation rate. The spin parameter of the pulsation was taken to be $s = 6$, and the resulting equatorial constraint on the pulsation was computed using Equation (51) from Townsend (2003b). 26

1.10 An overview of different known classes of pulsating stars across the Hertzsprung-Russell diagram. The evolutionary tracks are taken from Schaller et al. (1992) and Driebe et al. (1998). Initial masses and evolutionary time scales are added in grey. The hatching corresponds to the dominant character of the pulsation modes, with forward and backward slanting representing p- and g-modes, respectively. The colour indicates the spectral type. The two vertical dashed lines mark the position of the classical instability strip, whereas the zero-age main sequence is represented by the light-grey dashed line. Figure courtesy of P. I. Pápics, adapted from a similar figure made by J. Christensen-Dalsgaard. 30

2.1 Part of the Fourier transform (grey) of a simulated light curve (described later on in Section 2.3.1). The full black vertical lines indicate the frequencies which were extracted using traditional prewhitening with $\mathrm{S/N} \geq 15$, while the red vertical lines indicate the remaining frequencies which were extracted with $\mathrm{S/N} \geq 4.0$. The thick black markers indicate the frequencies which were used as input. These were all extracted with our new definition based on the comparison criterion. 42

2.2 The Fourier transform (full black curve) of a simulated light curve. Using the presented comparison criterion, the frequency extraction is aborted when the amplitude of an extracted frequency (full red vertical lines) does not agree with the original Fourier transform within a specified margin (grey area). The accepted frequencies (for the specified margin) are marked with dashed lines. 43

2.3 Schematic summary of the methodology described in Section 2.2. While the values of α provided here work well for most γ Dor stars, they can of course be customised for individual stars. . . 46

2.4 The period spacings corresponding to several input frequencies in a simulated data set. The found spacings with $\alpha = 0.5$ are indicated by black squares, while spacings found for other values of α (from 0.4 to 0.1) are represented by grey squares. The original input period spacings are indicated by white dots. This is shown for both zonal (top) and prograde (bottom) dipole modes. 48

2.5 Fraction of extracted to input frequencies as a function of the number of prewhitened frequencies (full black line). The dashed grey line indicates the relative number of detected combination and noise frequencies as a function of the number of prewhitened frequencies when ignoring the comparison criterion. The upper axis provides the signal-to-noise ratio of the last extracted frequency. The shaded area indicates the number of accepted frequencies when adopting the comparison criterion with $\alpha = 0.5$, for which the number of extracted noise peaks remains modest, and the majority of the frequencies indicated by the dashed line are combination frequencies. 49

2.6 *Top left:* Period spacing patterns for simulated prograde (black dots) and retrograde (grey squares) dipole modes. The theoretical model used in this simulation is the same as the one used throughout Section 2.3.1, but with a much smaller rotation rate $f_{\rm rot}$ of $0.08\,{\rm d}^{-1}$. *Bottom left:* the period spacing pattern computed for the same pulsation periods, but assuming they are all part of the same series, i.e., have the same values for l and m. *Right:* the period échelle diagram for both simulated dipole mode series. 50

2.7 *Top:* A close-up of the Fourier transform of KIC 11145123 (black) and the accepted oscillation periods (dashed red), showing the detected period spacings. The thick black markers indicate the frequencies that were extracted for $\alpha = 0.5$. The amplitudes of some of the modes are ~3 mmag, but the Figure is zoomed in for clarity. *Bottom left:* A close-up of the échelle diagram showing the detected prograde (squares), retrograde (circles) and zonal (triangles) dipole modes. The frequencies that were extracted with $\alpha = 0.5$ are marked in black. *Bottom right:* The detected period spacings. For clarity, we shifted the spacings of the prograde and retrograde modes 150 s downwards and upwards, respectively. 51

2.8 Sections of the p-mode frequency spectrum of KIC 11145123 (black), with the detected frequencies marked by a dashed red line. Frequencies found for $\alpha = 0.5$ are marked with thick black markers, whereas the one found by Kurtz et al. (2014) but not by us is indicated by a dashed line. The dotted lines indicate frequencies that we extracted, but Kurtz et al. (2014) did not. The triangles (black and white) indicate possible dipole doublets. The upper panel is zoomed in for clarity (the oscillation mode at 17.96 d^{-1} has an amplitude ~7.2 mmag). 52

2.9 *Top:* A close-up of part of the Fourier spectrum of KIC 11721304 (black). All the marked frequencies are accepted following the criterion described in Section 2.2. *Bottom:* The period spacing as computed from the accepted frequencies. The black markers and grey dash-dotted lines indicate the frequencies for which we find a smooth spacing pattern. 56

2.10 *Top:* A small part of the light curve of KIC 11721304. *Bottom:* The Fourier spectrum (black) of KIC 11721304. The grey areas indicate the locations of the linear combinations of the oscillation frequencies, which arise because of the asymmetry of the light curve of the star in the top panel. 57

2.11 *Top:* A close-up of the Fourier transform of the light curve of KIC 6678174 (black) and the accepted frequencies in the region where the detected period spacing series is located. The frequencies which were accepted for $\alpha = 0.5$ are marked with full grey lines, and the ones for which $\alpha < 0.5$ are marked with dotted lines. *Bottom:* The period spacing as computed for the (accepted) frequencies shown in the top. The white markers indicate the spacings for frequencies accepted for $\alpha < 0.5$, while the dotted lines indicate the regions where there are likely frequencies missing. 58

3.1 Histograms representing the distribution of the atmospheric parameter values obtained for the single stars and the single-lined binaries in our sample. 69

3.2 The differences between the spectroscopically derived values and the KIC values of the fundamental parameters T_{eff} (top), log g (middle) and $[M/H]$ (bottom), as a function of the spectroscopic values. Linear fits of the relations are represented by the solid black lines. 71

3.3 The period spacing patterns of the slowly rotating star KIC 9751996. *Left:* the pulsation series in a period échelle diagram. The prograde (black circles), zonal (black triangles) and retrograde (black squares) dipole modes are marked separately, while the other pulsation modes are shown in grey. *Top right:* the prograde (dash-dot lines), zonal (full lines) and retrograde (dashed lines) modes in the Fourier spectrum. *Bottom right:* the period spacing patterns, using the same symbols as before. The dotted lines indicate missing frequencies. 73

3.4 The prograde (left) and retrograde (right) period spacing patterns of KIC 8375138. The used symbols are the same as in Fig. 3.3. . 74

3.5 The prograde (left) and retrograde (right) period spacing patterns of KIC 2710594. The used symbols are the same as in Fig. 3.3. . 75

3.6 The retrograde period spacing patterns of KIC 11668783. The used symbols are the same as in Fig. 3.3. 76

3.7 Illustration of some of the photometric parameters from the period spacing patterns (shown here for KIC 10224094) for the statistical analysis: $\langle P\rangle$ is the mean pulsation period, P_{max} is the longest pulsation period, $\langle \Delta P\rangle$ is the mean spacing, and $\langle \frac{\mathrm{d}\Delta P}{\mathrm{d}P}\rangle$ is the mean derivative (computed from the polynomial fit, here shown in red). Finally, Δ_{res} is a measure of the difference between the polynomial fit and the period spacing pattern, defined in Equation (3.1). 78

3.8 The average period spacing values of the different stars with respect to the logarithm of their $v \sin i$ values. 79

3.9 Observed values (white dots) for the dominant frequency f_g, with lines connected to the values predicted by the multivariate models (black squares) described in Table 3.3 for the rotation velocity $v \sin i$ (*top*) and the temperature log T_{eff} (*bottom*). The bivariate model fits listed in the left part of Table 3.3 are shown by the full lines. 80

3.10 Same as Fig. 3.9, but for the pulsation period P_{max} instead of the frequency f_g. 80

3.11 (log T_{eff},log g)-diagrams with the sample stars for which period spacing patterns with downward patterns were found. The white dots indicate the single stars, whereas the black squares are the single-lined binaries. The full lines mark the instability strip taken from Dupret et al. (2005) (with $\alpha_{\text{MLT}} = 2.0$). The light grey and dark grey areas are the instability strips for the main-sequence γ Dor stars presented by Bouabid et al. (2011), with $\alpha_{\text{ov}} = 0$ and $\alpha_{\text{ov}} = 0.2$ respectively. The marker sizes indicate the longest pulsation period P_{max} in the spacing patterns (*top*), the rotation velocity $v \sin i$ (*middle*) and the g-mode frequency f_g with the highest amplitude (*bottom*). The average error bars on the data points are shown in the bottom right corner. 86

4.1 Distributions of the asymptotic period spacing values $\Delta\Pi_l$ for spherical degree $l = 1$ and 2 computed for the MESA evolution tracks with the input parameters provided in Table 4.1. The ages and evolution rates of the stellar models were taken into account in computing the distributions. 90

4.2 Illustration of our method to derive the rotation rate f_{rot} and asymptotic spacing $\Delta\Pi_l$ from an observed period spacing pattern (black dots). An equidistant spacing series (grey squares) is defined, rotationally shifted (white squares), and fitted to the observed pattern using χ^2-minimisation, optimising for the variables l, m, $\Delta\Pi_l$, and f_{rot}. 91

4.3 *Top:* the input period spacing pattern (black dots and grey triangles) with the best-fitting pattern (white squares) as obtained from the χ^2-minimisation in Figure 4.5 assuming (l,m) = (1,1). The black part of the input patterns was used to determine f_{rot} and $\Delta\Pi_l$, while the grey section was excluded. *Bottom:* the residuals of the fit. 94

4.4 Best χ^2-values for the synthetic data shown in Figure 4.2 for each (l, m) combination, as a function of the asymptotic spacing $\Delta\Pi_l$. The black and light grey lines correspond to $l = 1$ and $l = 2$, respectively, while the modes with $m = 0$ are indicated with dashed lines, $m = 1$ with full lines, and $m = 2$ with the dash-dotted line. 94

4.5 $\log(\chi^2_{\rm red})$ for the simulated period spacing series assuming $l = 1$ as a function of the asymptotic period spacing $\Delta\Pi_l$ and the rotation rate $f_{\rm rot}$. The white dot indicates the input values, while the white cross and the red boundary indicate the solution and its 1σ-uncertainty margins, respectively. 95

4.6 $\log(\chi^2_{\rm red})$ for the observed period spacing series of KIC 9751996, assuming $l = 1$, as a function of the asymptotic period spacing $\Delta\Pi_l$ and the rotation rate $f_{\rm rot}$. The white crosses indicate the best-fit solutions. *Top:* the χ^2-distribution that we find by only analysing the detected prograde series. *Bottom:* the χ^2-distribution obtained by fitting the prograde, zonal, and retrograde spacing series simultaneously. 96

4.7 Observed period spacing patterns (black dots and grey triangles) for the retrograde (top), zonal (middle), and prograde (bottom) modes of KIC 9751996. The black parts of the input patterns were used to determine $f_{\rm rot}$ and $\Delta\Pi_l$, while the grey sections were excluded. The white squares indicate the modes of the optimal model in the grid when all three series are fitted simultaneously. 97

4.8 *Top:* Observed period spacing patterns (black dots and grey triangles) for the prograde (left) and retrograde (right) modes of KIC 12066947. The black part of the pattern was used to determine $f_{\rm rot}$ and $\Delta\Pi_l$, while the grey section was excluded. The white squares indicate the model fit, assuming these are gravito-inertial modes and using the $f_{\rm rot}$ and $\Delta\Pi_l$ values obtained from the analysis of the marked prograde series. The white diamonds indicate the model computed for Rossby modes using the same $f_{\rm rot}$ and $\Delta\Pi_l$ values, assuming $m = -1$ and $k = -2$ in the k-based indexing scheme by Lee & Saio (1997). *Bottom:* The residuals of the fit to the prograde period spacing series. . 98

4.9 Part of the frequency spectrum of KIC 7365537. The light grey area shows the location of the pulsation modes that form the detected period spacing pattern of this star. The dashed line shows the value of the derived rotation frequency $f_{\rm rot}$, while the dotted line indicates the isolated high-amplitude mode we found. 99

4.10 Dominant pulsation frequency $f_{\mathrm{dom,corot}}$ in the corotating frame as a function of the rotation frequency f_{rot} for the identified g-mode pulsations of 40 stars in the sample. The thick vertical lines do not represent error bars, but indicate the full extent of the detected spacing series. The dashed red line shows where the pulsations pass from the superinertial regime (above the line) into the subinertial regime (below the line). 101

4.11 Absolute value of the spin parameter s for the detected period spacing series of the stars in our sample as a function of the rotation frequency f_{rot}. The dashed red line shows where the pulsations pass from the superinertial regime (below the line) into the subinertial regime (above the line). The symbols are the same as in Figure 4.10, and the thick vertical again do not represent error bars, but indicate the full extent of the detected spacing series. 102

4.12 Section of the Fourier spectra of the three slowest rotating stars in our sample. These are our only stars in the superinertial regime, and all three are hybrid γ Dor/δ Sct candidates with variability between $5\,\mathrm{d}^{-1}$ and $8\,\mathrm{d}^{-1}$. 103

4.13 Correlation between the spectroscopic $v \sin i$ values and the values of the rotation rate f_{rot} . The black line indicates the corresponding linear fit, for which the coefficients are listed in Table 4.3. The symbols are the same as in Figure 4.10. For all of the stars a series of prograde dipole modes was detected. If another series was detected as well, the symbol of the corresponding mode identification was used. 106

4.14 Estimates of the inclination angles of the observed stars, derived from the spectroscopic $v \sin i$ values and the rotation rates f_{rot}. Hereby it was assumed that the stars rotate rigidly and have a stellar radius R_* of $2.0 \pm 0.5\,R_\odot$. The black dashed line indicates an inclination angle i of 90°. The symbols are the same as in Figure 4.10. For all of the stars a series of prograde dipole modes was detected. If another series was detected as well, the symbol of the corresponding mode identification was used. 107

4.15 The prevalence of the radial orders n of the pulsations in the detected period spacing patterns. Following the computation of the rotation frequency f_{rot} and the mode identification, radial orders were derived using Equation 1.14. 107

4.16 The average pulsation period $\langle P\rangle$, period spacing $\langle \Delta P\rangle$ and slope $\langle \frac{\mathrm{d}\Delta P}{\mathrm{d}P}\rangle$ of the observed $(l,m)=(1,1)$ pulsation patterns in the inertial reference frame, with respect to the derived rotation rates f_{rot}. The grey shaded areas indicate the expected relation for the radial orders n observed in our data, assuming $\Delta\Pi_{l=1}=3100\,\mathrm{s}$. The intensity of the shaded regions corresponds to the prevalence of the different values of n, as illustrated in the histogram in Figure 4.15: dark grey refers to a higher likelihood to observe a radial order n. 108

4.17 The pulsation periods of the observed (l,m) = (1,1) series in our sample, in the co-rotating reference frame, with respect to the observed temperature T_{eff}. The black markers indicate the dominant pulsation of each series, while the vertical lines show the extent of the corresponding pulsation patterns. The closed loops show the period ranges of the unstable (l,m) = (1,1) g-modes, computed by Bouabid et al. (2013) for equatorial rotation velocities $v_{eq}=0\,\mathrm{km\,s^{-1}}$ (black), $30\,\mathrm{km\,s^{-1}}$ (dark grey), $60\,\mathrm{km\,s^{-1}}$ (grey) and $90\,\mathrm{km\,s^{-1}}$ (light grey). 109

4.18 Near-core (circles) and envelope (triangles) rotation frequencies of BAF (cyan) core-hydrogen burning stars (including the γ Dor stars in this work), as well as of subgiants (green), of hydrogen-shell (red) and core-helium (orange) red giants, as a function of their log g (a proxy of their age), as deduced from photometry assembled by the *Kepler* satellite. The plot is an update of Figure 4 in Aerts (2015) to which we refer for the input data, with the stars from Table D.2 in this text and from Triana et al. (2015), Moravveji et al. (2016), Schmid & Aerts (2016) and Murphy et al. (2016) added to it. Dotted lines connect values of the same star. The plot covers the mass range from 0.8 to $3.3\,\mathrm{M}_{\odot}$. Figure courtesy of C. Aerts. 110

5.1 χ^2-values for the computed models for KIC 9751996, as a function of the input parameters, assuming the exponential overshooting. The dashed lines indicate the χ^2-values at the boundaries of the 1σ-uncertainty region. 119

5.2 Same as Figure 5.1, but for the models with step overshooting. 120

5.3 χ^2-values for the computed models for KIC 9751996, as a function of the convective core mass *(top)*, asymptotic spacing $\mathit{\Delta\Pi}_{l=1}$ *(middle)* and rotation frequency f_{rot} *(bottom)* assuming the exponential overshooting. The dashed lines indicate the χ^2-values at the boundaries of the 1σ-uncertainty region. 121

5.4 Same as Figure 5.3, but for the models with step overshooting. 122

5.5 *Top:* The observed period spacing patterns for KIC 9751996 (black dots) with the best fitting model (red line) assuming exponential overshooting. From top to bottom, the observed patterns have $(l, m) = (1, -1)$, (1,0) and (1,1), respectively. *Bottom:* The residuals of the fit in the top panel. 123

5.6 Same as Figure 5.5, but for the best fitting model with step overshooting. 124

C.1 The period spacing patterns of KIC 2710594. 153

C.2 The period spacing patterns of KIC 3448365. 153

C.3 The period spacing patterns of KIC 4757184. 154

C.4 The period spacing patterns of KIC 4846809. 154

C.5 The period spacing patterns of KIC 5114382. 154

C.6 The period spacing patterns of KIC 5350598. 155

C.7 The period spacing patterns of KIC 5522154. 155

C.8 The period spacing patterns of KIC 5708550. 155

C.9 The period spacing patterns of KIC 5788623. 156

C.10 The period spacing patterns of KIC 6185513. 156

C.11 The period spacing patterns of KIC 6425437. 156

C.12 The period spacing patterns of KIC 6468146. 157

C.13 The period spacing patterns of KIC 6468987. 157

C.14 The period spacing patterns of KIC 6678174. 157

C.15 The period spacing patterns of KIC 6778063. 158

C.16 The period spacing patterns of KIC 6935014. 158

C.17 The period spacing patterns of KIC 6953103. 158

C.18 The period spacing patterns of KIC 7023122. 159
C.19 The period spacing patterns of KIC 7365537. 159
C.20 The period spacing patterns of KIC 7380501. 159
C.21 The period spacing patterns of KIC 7434470. 160
C.22 The period spacing patterns of KIC 7583663. 160
C.23 The period spacing patterns of KIC 7746984. 160
C.24 The period spacing patterns of KIC 7867348. 161
C.25 The period spacing patterns of KIC 7939065. 161
C.26 The period spacing patterns of KIC 8364249. 161
C.27 The period spacing patterns of KIC 8375138. 162
C.28 The period spacing patterns of KIC 8645874. 162
C.29 The period spacing patterns of KIC 8836473. 162
C.30 The period spacing patterns of KIC 9210943. 163
C.31 The period spacing patterns of KIC 9419694. 163
C.32 The period spacing patterns of KIC 9480469. 163
C.33 The period spacing patterns of KIC 9595743. 164
C.34 The period spacing patterns of KIC 9751996. 164
C.35 The period spacing patterns of KIC 10224094. 164
C.36 The period spacing patterns of KIC 10256787. 165
C.37 The period spacing patterns of KIC 10467146. 165
C.38 The period spacing patterns of KIC 11080103. 165
C.39 The period spacing patterns of KIC 11099031. 166
C.40 The period spacing patterns of KIC 11294808. 166
C.41 The period spacing patterns of KIC 11456474. 166
C.42 The period spacing patterns of KIC 11668783. 167
C.43 The period spacing patterns of KIC 11721304. 167
C.44 The period spacing patterns of KIC 11754232. 167

C.45 The period spacing patterns of KIC 11826272. 168

C.46 The period spacing patterns of KIC 11907454. 168

C.47 The period spacing patterns of KIC 11917550. 168

C.48 The period spacing patterns of KIC 11920505. 169

C.49 The period spacing patterns of KIC 12066947. 169

C.50 The period spacing patterns of KIC 12458189. 169

D.1 Dominant pulsation frequency $f_{dom,inert}$ in the inertial frame as a function of the rotation frequency f_{rot} for the identified g-mode pulsations of 40 stars in the sample. The thick vertical lines indicate the full extent of the detected spacing series. The full black line indicates where f_{inert} is equal to f_{rot}. 177

List of Tables

2.1 A least-squares fit for the additional p-mode frequencies ($*$) which we found compared to the analysis by Kurtz et al. (2014), and for the other frequencies which are part of the same multiplets. Δf is the spacing between the given frequency and the preceding one. The provided errors are the formal error margins from the least-squares fit. 54

2.2 Atmospheric parameter values obtained for the four γ Dor stars analysed in this study. The provided errors are the 1-σ values obtained from the chi-square statistics. 55

3.1 The estimates for the orbital periods and system velocities of the binaries KIC 3222854 and KIC 8693972. 65

3.2 The orbital solutions for the binary systems KIC 3952623, KIC 7867348 and KIC 11754232. (See the main text for details.) 66

3.3 Results of the multiple linear regression. We list the coefficients of the covariates for the different model fits as well as the p-values (obtained from a t-test) and the R^2 values. 82

3.3 Continued. 83

4.1 Parameter values of the computed grid of 1170 MESA evolutionary tracks, consisting of some 900,000 models. 90

4.2 Parameter values of the simulated period spacing pattern. *Top:* the input parameters of the MESA evolution track. *Bottom:* the parameters of the model for which the pulsation periods were computed. 93

4.3 Results of the linear regression analysis. We list the coefficients of the covariates for the different correlations with their errors, as well as their p-values (obtained from a t-test) and R^2 values. 106

5.1 Parameter ranges considered in the analysis of KIC 9751996 with the genetic algorithm MPIKAIA, both for the assumption of exponential overshooting *(left)* and step overshooting *(right)*. . 117

5.2 Parameter values of the best fitting models for KIC 9751996 with their 1σ-uncertainties, assuming both exponential overshooting *(left)* and step overshooting *(right)*. 118

B.1 Pulsation frequencies of the simulated light curve in Section 2.3.1, in the inertial reference frame. 138

B.1 Continued. 139

C.1 Observation log of the stars in our sample. N_Q and N_S indicate the total number of available *Kepler* mission quarters and HERMES spectra respectively. 142

C.1 Continued. 143

C.1 Continued. 144

C.2 The global observational characteristics of the stars in our sample. We have listed information on the variability type, where the label "ROT" indicates rotational modulation, and * indicates that frequencies are found outside of the traditional range for γ Dor stars, but likely correspond to combination frequencies. Stars labelled as "γ Dor/δ Sct" are candidate hybrid γ Dor/δ Sct pulsators. In addition, stars are listed as single (S), single-lined binaries (SB1), double-lined binaries (SB2), binaries with no detected radial velocity variations (SB) and triple systems (SB3). We also report the detections of period spacing patterns and comment on their suspected nature. 145

C.2 Continued. 146

C.2 Continued. 147

C.3 Spectroscopic parameter values computed for the merged spectra of the single stars and single-lined binaries in our sample. The provided errors are the 1-σ values obtained from the χ^2-statistics. 148

C.3 Continued. 149

C.3 Continued. 150

C.4 The values of pulsation parameters and their error margins derived from the downward period spacing patterns for the multivariate analysis (see Section 3.5). Only the patterns for single stars and single-lined binaries are included in this table. . 151

C.4 Continued. 152

D.1 Pulsation periods (in days; in the inertial reference frame) of the simulated data in Section 4.4.1, with 1σ uncertainty margins. . 172

D.2 Rotation rates $f_{\rm rot}$ and asymptotic period spacings $\Delta\Pi_l$ computed from the observed period spacing patterns, as well as the mode identification and the dominant pulsation frequency for each series. For the latter we also computed the spin parameter s, listed in the final column. The pulsation mode patterns marked with "R" are retrograde modes, which are most likely Rossby modes. The pulsation modes marked with "S" are single high-amplitude peaks that were present in the frequency spectra, but clearly separate from the detected period spacing patterns. Neither the retrograde pulsation modes nor the single peaks were used in the computations. The corresponding rotation rates and asymptotic period spacings were obtained from the prograde series observed for the same star. 173

Chapter 1

Scientific framework

> *Everyone knew that stars were points of light. If they weren't, some would be visibly bigger than others. Some were fainter than others, of course, but that was probably due to clouds. In any case their purpose, according to established Discworld law, was to lend a little style to the night.*
>
> Sir Terry Pratchett in *The Science of Discworld*

The theory of stellar structure and evolution is one of the most important ingredients of modern astronomy and astrophysics. As stars interact with their environment throughout their evolution, our understanding of this theory has a direct impact on other astrophysical research fields, from exoplanet and habitability research (e.g. Gallet et al. 2016, and references therein) all the way up to galactic and cosmological evolution (e.g. Hopkins et al. 2014), etc. While some global aspects of stellar structure and evolution are currently well understood, other aspects which influence these related research domains, such as stellar rotation or the chemical mixing processes in the deep stellar interior, are largely unknown (Zahn 1992; Maeder 2009; Aerts et al. 2014). A key ingredient of theoretical models that can be studied quantitatively since recently, is the evolution of the convective core in intermediate-mass ($1M_{\odot} \lesssim M \lesssim 2M_{\odot}$) main-sequence stars.

A good way to calibrate and improve the existing stellar structure and evolution theories is asteroseismology. This relatively young field within astrophysics allows us to trace the stellar interior structure by analysing and interpreting stellar pulsations. Over the last decade, there has been a lot of progress in asteroseismology thanks to space missions such as MOST (Walker et al. 2003), CoRoT (Auvergne et al. 2009), and *Kepler* (Koch et al. 2010). These missions have a much higher duty-cycle and the space-based photometry is much more precise than what can be achieved with ground-based observing campaigns.

As can be seen in this PhD thesis, the observational study of γ Doradus stars has benefited greatly from the *Kepler* space mission. Gamma Doradus stars are intermediate-mass stars that exhibit gravity- and/or gravito-inertial modes, which probe the near-core region in the deep stellar interior (e.g. Kaye et al. 1999; Miglio et al. 2008; Bouabid et al. 2013). In this thesis, we take a major step forward in the asteroseismic modelling of γ Doradus stars to improve our understanding of the convective core properties and interior rotation of intermediate-mass stars. This would not have been possible without the high quality-data provided by the NASA *Kepler* satellite.

In the following section, we give a brief overview of the relevant physics for the study of intermediate-mass stars. We refer the interested reader to Maeder (2009) and Kippenhahn et al. (2012) for a more detailed description.

1.1 Stellar structure & evolution

1.1.1 Stellar structure

Multiple characteristics of stellar structure and evolution are not yet understood or cannot be studied yet because the required computational resources are orders of magnitude larger than what is currently available. Nevertheless, a basic description of a typical star can be relatively easily provided sufficient simplifications are made. If we ignore the effects of rotation and magnetism and assume spherical symmetry and hydrostatic equilibrium, the interior structure of a star can be described with the set of equations (1.1) to (1.5). These equations represent basic laws of physics applied to a spherically symmetric gaseous sphere, see, e.g. Kippenhahn et al. (2012), for details on their derivations. They characterize the local density $\rho(m)$, luminosity $l(m)$, pressure $P(m)$, radius $r(m)$, temperature $T(m)$ and mass fractions $X_j(m)$ of nuclei of type j inside the star. These quantities are expressed as a function of the independent mass coordinate m, where m is equal to 0 in the stellar centre ($r = 0$) and to the total stellar mass M at the surface.

$$\begin{aligned}
\frac{\partial P}{\partial m} &= -\frac{Gm}{4\pi r^4}, && (1.1)\\
\frac{\partial r}{\partial m} &= \frac{1}{4\pi r^2 \rho}, && (1.2)\\
\frac{\partial l}{\partial m} &= \epsilon_n + \epsilon_{grav} - \epsilon_\nu, && (1.3)\\
\frac{\partial T}{\partial m} &= -\frac{GmT}{4\pi r^4 P}\nabla \;=\; -\frac{GmT}{4\pi r^4 P}\left(\frac{\mathrm{d}\ln T}{\mathrm{d}\ln P}\right), && (1.4)\\
\frac{\partial X_j}{\partial t} &= \frac{m_j}{\rho}\left(\sum_i r_{ij} - \sum_k r_{jk}\right), \text{ with } j = 1, \ldots, J. && (1.5)
\end{aligned}$$

Equation (1.1) is the equation of hydrostatic equilibrium, i.e. the two forces that act upon a mass element inside the star, are caused by gravity and an outward pressure gradient, and balance each other. G is the gravitational constant. Equation (1.2) is the mass continuity equation, and describes the radial mass distribution inside the star. Equation (1.3) describes the conservation of energy. The terms $\epsilon_n(m)$ and $\epsilon_{grav}(m)$ denote the rate of energy generation per unit mass by nuclear fusion and gravitational contraction, respectively. The term $\epsilon_\nu(m)$, on the other hand, is the rate of energy drain per unit mass caused by emitted neutrinos. The energy transport in the star is given by Equation (1.4), which in the provided form also assumes hydrostatic equilibrium (given in Equation (1.1)). When the energy transport is done only by radiation, $\nabla = \nabla_{\mathrm{rad}}$ and Equation (1.4) can be simplified to

$$\frac{\partial T}{\partial m} = -\frac{GmT}{4\pi r^4 P}\nabla_{\mathrm{rad}} = -\frac{3\kappa l}{64\pi^2 ac r^4 T^3}, \qquad (1.6)$$

with $\kappa(m)$ the Rosseland mean opacity, a the radiation density constant and c the speed of light. Energy transport can also happen through convection, in which case a description of ∇ has to be provided by a suitable convection theory. This is discussed in more detail in Section 1.1.1. Finally, Equations (1.5) describe the nuclear reactions network inside the star. The mass of a nucleus of type j is given by m_j, while a reaction rate r_{jk} indicates the number of reactions per unit volume and time that transform nuclei of type j into type k. Mixing processes in the stellar interior, such as convective mixing, atomic diffusion, and rotational mixing, are not included in Equations (1.5), but they do induce transport of chemical elements between neighbouring stellar layers. These processes are usually described in separate equations — see, e.g., Kippenhahn et al. (2012). The convective and rotational mixing processes are discussed further in this introductory chapter. Atomic diffusion is less effective than these two for the stars treated here; they are hence not treated any further in this dissertation.

During the life of a star, local adjustments to the mechanical equilibrium and the energy transport typically occur on a shorter time scale than changes in the chemical composition. As a result, Equations (1.1) to (1.4) can then be solved separately from Equations (1.5) for a time t, assuming a chemical composition X_j. This is for instance the case when the star is evolving on the Main Sequence, which is the stage of core hydrogen burning. We discuss this further in Section 1.1.2.

The given set of equations (1.1) to (1.5) can be solved for the relevant quantities, if we have an expression for the equation of state (EOS), which describes the variation of the density ρ as a function of P, T and the chemical composition X_j. For an ideal gas with radiation pressure, the EOS is given by

$$P = \frac{\mathcal{R}}{\overline{\mu}}\rho T + \frac{a}{3}T^4,$$

where $\mathcal{R}$ is the gas constant and $\overline{\mu}$ the mean molecular weight. In modern stellar astrophysics the EOS is computed numerically by specialised research groups for different chemical compositions, taking into account different types of interaction forces that have an impact, e.g. pressure ionisation. The results are available in tabular form, and included in modern stellar evolution codes. A well-known example is the OPAL EOS (Rogers et al. 1996, and follow-up studies), which we will discuss further in Section 1.1.3 in the context of the stellar evolution code MESA. With the EOS as input, other quantities such as the opacity κ and the rate of energy generation $\epsilon_n(m)$ can be calculated as well. These are studied and computed by specialised research groups as well. Examples of popular opacity tables include the Opacity Project (Badnell et al. 2005) and OPAL (Iglesias & Rogers 1993, 1996). When suitable initial values and boundary conditions are taken, this in turn allows us to solve the system of Equations (1.1) to (1.5), resulting in a stellar model.

While this outline of stellar structure theory is very well known and understood, there are several complications that were not properly included in our discussion so far, such as the influence of convection and stellar rotation. Other complicating factors, such as binarity and magnetic fields, are beyond the scope of this work.

Convection

If the gradient ∇_{rad}, given in Equation (1.6), is large, this indicates that the energy transport through radiation is ineffective. In particular, when ∇_{rad} becomes large, the energy transport will be done by convection, where macroscopic mass elements with a higher temperature than their environment rise, and then dissipate. Apart from the energy transport, this also leads to very high degree of mixing in these regions.

According to the Schwarzschild criterion, convection occurs when

$$\nabla_{ad} < \nabla_{\mathrm{rad}},$$

where

$$\nabla_{ad} = \left(\frac{\mathrm{d}\ln T}{\mathrm{d}\ln P}\right)_s$$

is the adiabatic temperature variation of the mass elements. This expression can also be generalised to the Ledoux criterion, i.e., that a region in the star is convectively unstable when

$$\nabla_{ad} + \frac{\varphi}{\delta}\nabla_{\mu} < \nabla_{\mathrm{rad}}.$$

Here

$$\varphi = \left(\frac{\partial\ln\rho}{\partial\ln\mu}\right)_{P,T}; \delta = -\left(\frac{\partial\ln\rho}{\partial\ln T}\right)_{P,\mu}; \nabla_{\mu} = \left(\frac{\mathrm{d}\ln\mu}{\mathrm{d}\ln P}\right)$$

are defined for the environment of the mass elements. The chemical gradient ∇_{μ} has a stabilising effect on convection. Regions which are unstable for the Schwarzschild criterion but stable for the Ledoux criterion, are said to be semi-convective.

Convection is a three-dimensional process that is very difficult to describe in detail. In a typical one-dimensional stellar evolution code, convection is therefore treated using the well-known mixing length theory. Here the energy transport by convection is computed as a function of the mean free path ℓ_m of the macroscopic convective elements. The variable ℓ_m, in turn, is typically expressed as the mixing length parameter α_{MLT}, in units of the local pressure scale height H_p. In most cases, it is a free input parameter, and larger values for α_{MLT} result in a higher efficiency for the convective energy transport. There are various descriptions for the mixing length theory available in the literature, e.g., Böhm-Vitense (1958) and Henyey et al. (1965).

Because of the simplifications made in the mixing-length theory, not all physical aspects of convection are adequately described. As ancurrently example, the boundary of a convective region is sharp and discontinuous in the theory. In real stars a gradual transition is likely to occur, where multiple convective mass elements shoot past the boundary into the non-convective regions, because of their inertia. This can be taken into account by including a convective overshooting region at the edge of the convective zones in stellar models. Similar to the mixing length, the extent of the overshooting region is also expressed in units of the local pressure scale height, and used as a free input parameter. It can follow different prescriptions. Simple examples include the step overshoot and the exponential overshoot (Herwig 2000), where the local mixing is either constant or drops off exponentially, respectively. The introduction of the convective core overshooting region increases the amount of chemical mixing near the core boundary, which in turn brings additional fuel, such as hydrogen during the star's main-sequence evolution, into the core, extending the life of the star and effectively increasing the convective core size. This is discussed in Section 1.1.2 as well.

Alternative implementations of convection are also available, but less common. Examples are the descriptions provided by Canuto & Mazzitelli (1991) and Canuto et al. (1996). Whereas the mixing-length theory only takes into account a single possible size for the eddies in the convective regions and assumes convective turbulence is incompressible, these two theories both consider a full spectrum of turbulent eddies, but with different treatments of the energy input rate.

Rotation

Stellar rotation can also have a major impact on stellar structure and evolution, as explained in detail by Maeder (2009). However, because the calculations of stellar structure can be complex and computationally demanding, the influence of rotation is often ignored or severely simplified. Ideally, rotation is treated using two- or three-dimensional models. In stellar evolution codes, which are often one-dimensional to keep the computational cost manageable, stellar rotation and the resulting mixing processes are assumed to occur while keeping spherical symmetry. These processes are then described by a radial coordinate. Differential rotation and mixing then takes place between concentric shells in the theoretical model (for the mathematical treatment, see, e.g. Zahn 1992).

Stellar rotation impacts the stellar structure and evolution on several different levels. The centrifugal force leads to the flattening of a rotating star towards its equator, breaking the spherical symmetry. Differential stellar rotation also induces various extra mixing processes, which influence the chemical stratification inside the star. These mixing mechanisms can be classified as either dynamical or secular processes, depending on whether they are adiabatic and act on the dynamical time scale, or they act on the Kelvin-Helmholtz time scale, allowing thermal adjustments via radiative processes, respectively. The rotational mixing mechanisms that are often considered, are typically based on meridional circulation, rotational shear, and the interaction between the stellar rotation and convective (in)stabilities (Heger et al. 2000). If the local angular momentum in a star increases radially outwards, an upward displaced convective mass element has a lower angular momentum than its environment. This in turn pushes the displaced mass element back down to its original position, effectively suppressing the convective motion. On the other hand, if the local angular momentum in a star decreases radially outwards, such a displaced mass element will be moved further upward. The full interactions between stellar rotation and convection are currently not yet understood (Maeder 2009), though recently progress has been made for both low-mass stars (e.g. Matt et al. 2011) and massive stars (e.g. Rogers 2015).

Other less understood aspects include the angular momentum transport inside the star throughout its evolution. From recent asteroseismic studies based on *Kepler* data, it is apparent that the angular momentum transport in evolved low-mass stars is a lot more efficient than what is predicted by the stellar models (e.g. Beck et al. 2012; Mosser et al. 2012, 2013; Kurtz et al. 2014; Saio et al. 2015; Murphy et al. 2016).

1.1.2 Stellar evolution of intermediate-mass stars

A star is formed when a molecular cloud in the interstellar medium contracts under the influence of its own gravitational force. During this process, the molecular cloud breaks up into fragments, and the gravitional energy which is released due to the contraction of the clouds, is partially absorbed by the gas and the dust, heating up the material. Each individual cloud fragment continues to contract adiabatically, and a protostar develops in the centre. The rest of the material forms a disc which feeds the growing protostar and may eventually lead to the formation of a planetary system. Meanwhile, the temperature in the core of the star keeps rising, until it is sufficiently high to start hydrogen core burning. The nuclear fusion of hydrogen into helium in the stellar core provides enough heat to support the outward pressure gradient that counteracts the gravitational force. The required counter balance to gravity was previously supported by the gravitational energy, released by the cloud's contraction but is no longer needed and the star stops contracting. It has arrived at the so-called zero-age main sequence.

Throughout the main-sequence evolution of a star, hydrogen burning continues to take place in the stellar core. The two main nuclear reaction chains which regulate this process are the proton-proton chains (hereafter pp-chains) and the CNO-cycle. Following the pp-chains, hydrogen is fused into helium via direct proton-proton interactions. These reactions occur when the temperature $T \gtrsim 5 \cdot 10^6\,\mathrm{K}$, and are the dominant fusion process for the hydrogen burning in low-mass stars, i.e. with $M \lesssim 1\,M_\odot$. In higher-mass stars, with $M \gtrsim 2\,M_\odot$ the temperature in the centre T_c is higher, and hydrogen fusion process is instead dominated by the CNO-cycle. In these reactions, various isotopes of C, N and O serve as catalysts for the hydrogen fusion, and throughout the process most of these atoms will be transmuted into ^{14}N. The CNO-cycle is also more sensitive to the temperature. While the reaction efficiency of the pp-chains $\sim T^6$ at $T = 5 \cdot 10^6\,\mathrm{K}$ and $\sim T^{3.5}$ at $T = 20 \cdot 10^6\,\mathrm{K}$, we have $\sim T^{18}$ at $T = 20 \cdot 10^6\,\mathrm{K}$ for the reaction efficiency of the CNO-cycle (Kippenhahn et al. 2012). As a result, hydrogen burning following the CNO-cycle will be more concentrated towards the centre of the star. This also has consequences for the energy transport and consequently the stellar structure. While high-mass main sequence stars have a convective core and a radiative envelope, low-mass stars have a radiative core and a convective envelope.

In the intermediate-mass stars ($1\,M_\odot \lesssim M \lesssim 2\,M_\odot$), the onset of the convective core is strongly influenced by the local opacity κ and the energy produced by the CNO-cycle with respect to the pp-chains. During the main sequence evolution, the mass fraction of hydrogen in the stellar core is slowly depleted, and because the opacity $\kappa \sim (1 + X)$ in the core, the opacity reduces as well. For the higher mass stars in this range, this leads to smaller values of ∇_{rad} and a shrinking convective core as the star evolves. However, at the same time the temperature in the core increases, so the relative importance of the CNO-cycle with respect to the pp-chains increases too, leading to a larger energy production rate ϵ_n. For stars on the lower end of the intermediate-mass range, this results in an increase in ∇_{rad} and a growing convective core (e.g. Mitalas 1972; Crowe & Mitalas 1982; Miglio et al. 2008; Silva Aguirre et al. 2011). This is illustrated in Figures 1.1 and 1.2. In the first figure, we see stellar evolution tracks on the main sequence for various initial stellar masses ($1.2\,\mathrm{M}_\odot$, $1.4\,\mathrm{M}_\odot$, $1.6\,\mathrm{M}_\odot$, $1.8\,\mathrm{M}_\odot$ and $2.0\,\mathrm{M}_\odot$). The second figure shows the evolution of the convective core as a function of the hydrogen mass fraction X_c in the stellar core, together with the total luminosity from both the pp chain and the CNO cycle hydrogen burning. We can see that, as long as the CNO cycle produces (much) less energy than the pp chains, the convective core increases. This growth stalls when the energy production of both processes is comparable, and the convective core size decreases when the energy production from the CNO cycle is (much) larger.

In theoretical models, the precise properties and evolution of the gradient ∇_{rad} not only depend on the star's initial mass, chemical composition and internal mixing processes, but also on their numerical treatment, e.g., the

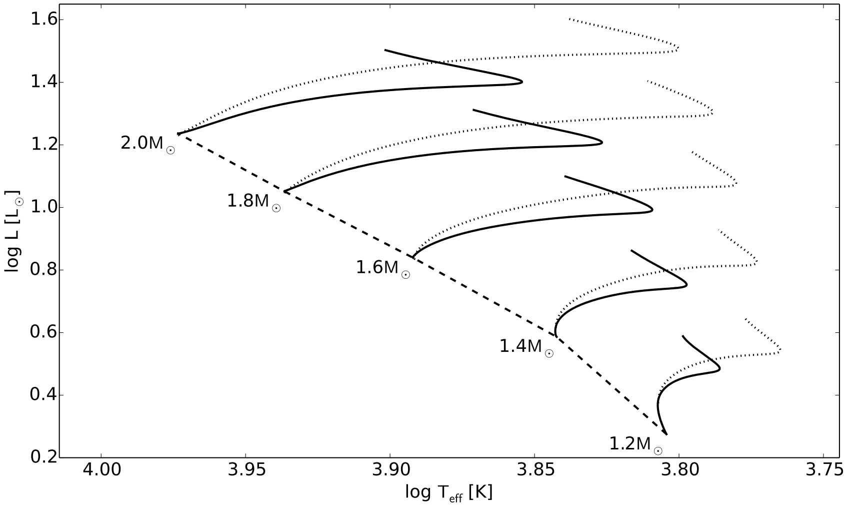

Figure 1.1: Evolution tracks in the Hertzsprung-Russell diagram for stars with an initial mass M of $1.2\,\mathrm{M}_\odot$, $1.4\,\mathrm{M}_\odot$, $1.6\,\mathrm{M}_\odot$, $1.8\,\mathrm{M}_\odot$ and $2.0\,\mathrm{M}_\odot$. The full black lines are the evolution tracks for exponential overshooting with $f_{ov} = 0.0075$, while the dotted evolution tracks correspond to $f_{ov} = 0.030$. The dashed line indicates the ZAMS. The tracks were computed with MESA v7385 (for a description of the input physics, see Section 1.1.3), assuming initial hydrogen fraction $X = 0.71$, metallicity $Z = 0.014$, mixing-length parameter $\alpha_{\mathrm{MLT}} = 1.8$ and extra diffusive mixing $D_{\mathrm{mix}} = 1\,\mathrm{cm}^2\,\mathrm{s}^{-1}$.

chosen (local) mesh grid (Miglio et al. 2008). Furthermore, as convective overshooting has to be included in theoretical modelling in combination with the mixing length theory (see Section 1.1.1), the interaction between the CNO hydrogen burning cycle and the pp-chains has an impact on the overshooting as well. The impact of the convective core overshooting on the main sequence evolution is also illustrated in Figure 1.1, which shows several intermediate-mass evolution tracks for exponential overshooting with $f_{ov} = 0.0075$ and 0.030, respectively. As mentioned in Section 1.1.1, convective core overshooting increases the chemical mixing near the boundary of the convective core, which introduces more hydrogen into the core, lengthening the star's life. This is the reason that in Figure 1.1, the main-sequence evolution tracks computed for larger core overshooting values are longer.

After the hydrogen in the stellar core of an intermediate-mass star has been fully depleted, hydrogen burning will take place in a shell surrounding the helium core, and the star slowly moves up the red giant branch (RGB). The

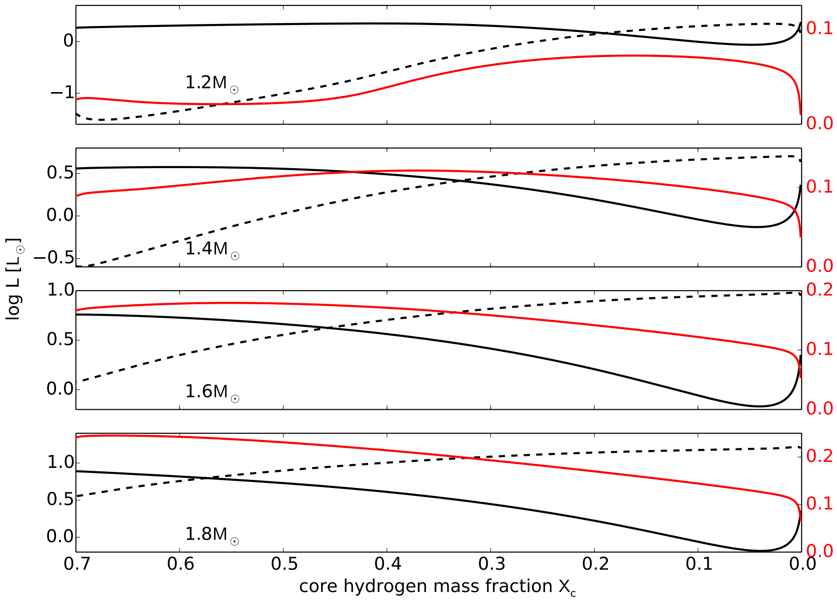

Figure 1.2: The evolution of the convective core mass as a function of the central hydrogen mass fraction X_c (full red line), together with the luminosity which originates from the pp-chain hydrogen burning (full black line) and the CNO cycle (dashed black line). The models correspond to the evolution tracks in Figure 1.1 with the same mass ($1.2\,\mathrm{M}_\odot$,$1.4\,\mathrm{M}_\odot$, $1.6\,\mathrm{M}_\odot$ and $1.8\,\mathrm{M}_\odot$) and $f_{ov} = 0.0075$.

convective envelope expands and the core contracts, until the temperature in the core is sufficient to burn helium into carbon and oxygen. In the mass range considered here, the helium burning starts explosively with a helium flash due to degeneracy of the electrons. Once the degeneracy is lifted, the burning happens quietly and the star settles at the horizontal branch. As a CO core develops, and the helium burning continues in a shell, the star climbs up the Asymptotic Giant Branch (AGB) and undergoes radial pulsations with large amplitude. These bring gas from the envelope to circumstellar distances where dust grains can form. Consequently, a strong dust-driven wind develops, which strips away most of the envelope, until finally the hot CO core is exposed and the star becomes a white dwarf. The dispersed gas of the stellar envelope can be ionised by the radiation from the core, and becomes a planetary nebula surrounding the slowly cooling white dwarf.

Various aspects that are relevant for stellar structure and evolution, such as stellar rotation, diffusive mixing, and mass loss, are currently not well understood and complicate the theory (cf. Section 1.1.1). Most importantly, stellar rotation induces chemical mixing. On the main sequence, this leads to additional transport of hydrogen into the stellar regions where nuclear hydrogen burning takes place, effectively increasing the star's lifetime. Other aspects, such as the efficiency of the convection (related to the value of the mixing length parameter $\alpha_{\rm MLT}$ in the models) or the convective overshooting also affect chemical mixing, and by implication the star's life. To determine the full extent of the impact of these phenomena, they have to be studied further.

1.1.3 The stellar evolution code MESA

Modules for Experiments in Stellar Astrophysics[1] (MESA) is an open-source one-dimensional stellar evolution code, developed by Bill Paxton and his collaborators at UCSB (Paxton et al. 2011, 2013, 2015). It consists of various modules, each of which deals with different aspects of theoretical stellar models, such as the equation of state, the chemical composition, opacity tables, etc. Apart from the extensive default options, which can be called and controlled using an inlist of parameters, MESA also allows the user to incorporate his/her own algorithms or replace parts of the default code. This makes the code highly customizable, and a good tool to test new stellar physics.

The computation of a stellar evolution track can be started from the pre-main sequence, the zero-age main sequence or a pre-computed model. The stellar model is then solved for explicitly at each time step, taking into account the chosen input parameters. The code uses both adaptive mesh refinement for the stellar models, as well as an adaptive time step. The solutions for the equation of state and a variety of opacities, chemical mixtures and nuclear reaction networks have all been calculated beforehand, and are accessible in table form within the MESA installation. During the computations, the required values and profiles are obtained by interpolation in these tables.

In this work, we used MESA v7385 to compute basic stellar models with five input parameters: the mass M, metallicity Z, initial hydrogen mass fraction X, extra diffusive mixing D, and the convective core overshooting. Within this setup, the ranges of the extra diffusive mixing and the convective core overshooting are totally unknown for γ Doradus stars. The age of the star was taken into account by keeping track of the core hydrogen mass fraction X_c in our models.

---

[1] `http://mesa.sourceforge.net/`

As mentioned before in Section 1.1.2, stellar rotation induces chemical mixing. However, the strength of these mixing processes is badly constrained and their numerical treatment in one-dimensional models is difficult. First, the relevant differential equations are ideally solved implicitly as a function of time, but are treated explicitly in MESA. Second, these are three-dimensional processes implemented in one-dimensional models. Consequently, they are scaled using free input parameters, similar to the treatment of convection within the mixing-length theory. We have therefore opted to only consider non-rotating MESA models. The influence of rotational mixing on the chemical stratification inside the star was taken into account with the constant extra diffusive mixing parameter D in the radiative zone, which also includes the non-rotational diffusive mixing in this region.

Convective instabilities were evaluated using the Ledoux criterion and treated using the mixing length theory. The mixing length parameter α_{MLT} was kept fixed at 1.80, while the parameter α_{sc}, which regulates the efficiency of the semiconvection, was fixed at 0.01, where both are expressed in terms of the local pressure scale height. These are typical values, taken from the literature (e.g. Dupret et al. 2005; Pápics et al. 2014). The chosen value of 1.80 for α_{MLT} is similar to the value used to treat the convection in the Sun in helioseismology (e.g. Trampedach et al. 2014). For the convective core overshooting, we considered two formalisms: the step overshooting and the exponential overshooting. Both descriptions use the level D_{mix} of the mixing processes at the convective core boundary as input. However, because this value goes to zero in the numerical models, MESA requires the value of D_{mix} to be taken at a user-specified distance inside the convective core. Throughout this work, we have taken the mixing coefficient D_{mix} at a distance of $0.001\,H_p$ inside the convective core.

Finally, the chosen chemical mixture was the one of the Sun computed by Asplund et al. (2009), and we relied on the OPAL type I tables for the opacity (Rogers & Nayfonov 2002).

An example of a typical MESA inlist, used in this work, can be found in Section A.1 in Appendix A.

1.2 Asteroseismology

Asteroseismology is a tool in modern astronomy and astrophysics that allows us to probe the interior structure of stars by analysing and modelling stellar pulsations. Classical snapshot astrophysical observations can only provide information about the stellar atmosphere, and provide only limited constraints on the stellar interior. In contrast, time series of high-precision photometric or spectroscopic observations of a pulsating star allow us to discern brightness variations or radial velocity variations at the stellar surface, that are caused by stellar pulsations. Because these pulsations travel through and are influenced by the stellar interior, a detailed analysis of such time resolved observations provides direct constraints on the properties of theoretical stellar structure models.

The precision of these observational constraints is highly dependent on the quality and quantity of the data. A high duty-cycle, high signal-to-noise ratio and long time series of observations are typically required to obtain reliable observational values for pulsation frequencies and amplitudes. As discussed in 1.3, these requirements are more easily fulfilled for space-based than for ground-based observations. Consequently, accurate seismic modelling of observed stars is now possible since the operations of space missions such as MOST (Walker et al. 2003), CoRoT (Auvergne et al. 2009), and *Kepler* (Koch et al. 2010). These implied breakthroughs in our knowledge of stellar physics over the past couple of years, extensively improving upon what was known in asteroseismology before space photometry.

In this section we provide a short overview of the relevant aspects of asteroseismology, and refer the interested reader to Unno et al. (1989) and Aerts et al. (2010) for more detailed overviews. Since then, several review papers have appeared summarising new insights, including but not limited to Chaplin & Miglio (2013), Aerts (2015), and Hekker & Christensen-Dalsgaard (2016).

1.2.1 Stellar pulsations

The set of equations (1.1) to (1.5) which we discussed in Section 1.1.1 describe a stellar model in equilibrium. During a star's evolution, there will often be physical processes that pull the star away from its perfect equilibrium, causing it to oscillate around its equilibrium state. While the impact of these pulsations is typically small and the previous discussion on evolution remains globally valid, it is instructive to study the stellar pulsations in order to probe the stellar structure in particular evolutionary phases. By applying linear perturbation theory to equations (1.1) to (1.5), it is found that the pulsations can typically be described with spherical harmonic functions. In a non-rotating spherically symmetric star, the displacement $\boldsymbol{\xi}$ of local mass elements caused by a pulsation with frequency f_n and quantum numbers n, l and m is given by

$$\begin{aligned}
\xi_{n,r}\left(r,\theta,\phi,t\right) &= a_n\left(r\right)Y_l^m\left(\theta,\phi\right)e^{-2\pi i f_n t},\\
\xi_{n,\theta}\left(r,\theta,\phi,t\right) &= b_n\left(r\right)\frac{\partial Y_l^m\left(\theta,\phi\right)}{\partial\theta}e^{-2\pi i f_n t},\\
\xi_{n,\phi}\left(r,\theta,\phi,t\right) &= \frac{b_n\left(r\right)}{\sin\theta}\frac{\partial Y_l^m\left(\theta,\phi\right)}{\partial\phi}e^{-2\pi i f_n t}.
\end{aligned}$$

Here $\boldsymbol{\xi}$ is described in spherical coordinates, whose symmetry axis is chosen to coincide with the rotation axis of the star. The quantities $a_n\left(r\right)$ and $b_n\left(r\right)$ are the amplitudes of the radial and horizontal components, respectively. Their ratio at the stellar surface, $b_n\left(R\right)/a_n\left(R\right)$ is determined by the boundary condition adopted for the pulsation equations and can be approximated as

$$\frac{b_n\left(R\right)}{a_n\left(R\right)} \simeq \frac{GM}{f_n^2R^3}$$

(cf. Eq. (3.161) in Aerts et al. 2010, Chapter 3). $Y_l^m\left(\theta,\phi\right)$ is a spherical harmonic function given by

$$Y_l^m\left(\theta,\phi\right) = \left(-1\right)^m\sqrt{\frac{2l+1}{4\pi}\frac{\left(l-m\right)!}{\left(l+m\right)!}}P_l^m\left(\cos\theta\right)\exp\left(im\phi\right),$$

where P_l^m is a Legendre function. The quantum numbers n, l and m denote the geometry of the pulsation: the radial order n is related to the number of radial nodes, the spherical degree l stands for the number of surface nodal lines and the azimuthal order m is the number of surface nodal lines that pass through the symmetry axis of the star. This is illustrated in Figure 1.3. As a result, we have that $l \geq |m|$. Traditionally, pulsation modes with $l = |m|$ are referred to as sectoral modes, while pulsations with $0 \leq |m| \leq l$ are called tesseral modes and pulsations with $m = 0$ are zonal modes. Similarly, pulsations with $l = 0$ are labelled radial modes, as opposed to non-radial modes with $l \neq 0$. The modes with spherical degree $l = 1$ are also referred to as dipole modes, whereas pulsations with $l = 2$ are called quadrupole modes, and so on.

The quantum numbers n, l and m have a strong impact on the characteristics of the pulsations. In an observational asteroseismic study, a correct geometric mode identification, i.e., the derivation of the values of n, l and m, is therefore paramount.

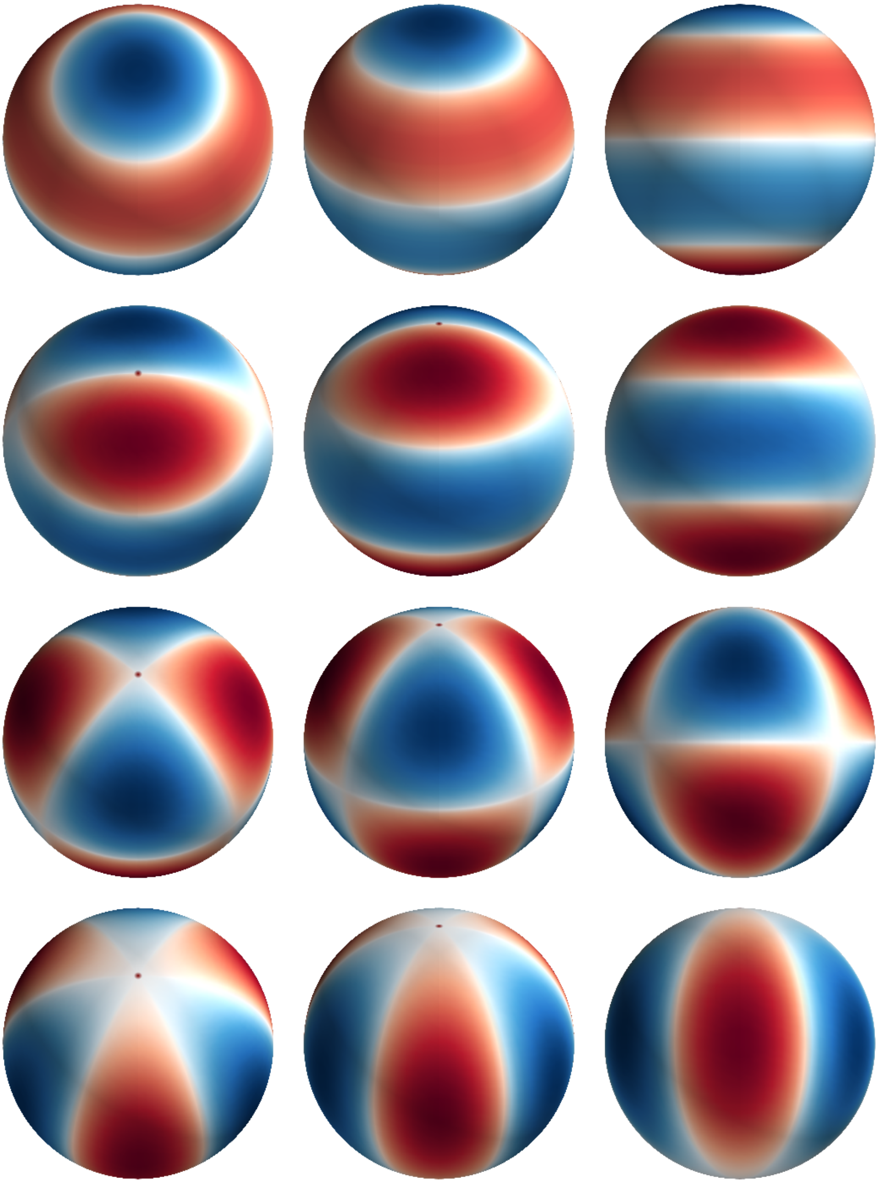

Figure 1.3: A snapshot of stellar pulsations with spherical degree $l = 3$ and different azimuthal orders m. They have $m = 0$ *(top row)*, $m = \pm 1$ *(2^{nd} row)*, $m = \pm 2$ *(3^{rd} row)*, $m = \pm 3$ *(bottom row)* respectively, at inclination angles of 30° *(left column)*, 60° *(middle column)* and 90° *(right column)*. The pulsations vary sinusoidally in time. At the chosen moment in the pulsation cycle, the blue and red sections are moving radially outwards and inwards, respectively. The surface nodal lines are shown in white. Figure courtesy of C. Aerts.

Pressure modes

Stellar pulsations may also be categorised according to their dominant restoring force. Pressure modes (p-modes) or acoustic modes are pulsations where the local pressure is the dominant restoring force. While they are typically most sensitive to the outer layers of the star, pulsations with low values of the degree l still travel deep into the star, and are sensitive to the density. For various classes of pulsating stars, observational scaling relations exploiting this fact for low-order radial modes ($l = 0$) exist (e.g. Breger 1990). This is discussed for δ Sct stars in Section 1.2.2. In addition, frequencies of low-degree p-mode pulsations with the same value for l are expected to be approximately equidistant in the asymptotic regime (where $n \gg l$), assuming a non-rotating star. Tassoul (1980, 1990) showed that for p-modes

$$f_{nl} = \mathit{\Delta}\nu\left(n + \frac{l}{2} + \tilde{\alpha}\right) + \epsilon_{nl}. \tag{1.7}$$

Here f_{nl} is the frequency of the pulsation mode with radial order n and degree l, $\tilde{\alpha}$ a constant of order unity and ϵ_{nl} is a small correction connected with the core properties of the star. The large separation $\mathit{\Delta}\nu$ is the frequency spacing between modes with the same value for l and consecutive values for n, given in turn by

$$\mathit{\Delta}\nu = \left(2\int_0^R \frac{\mathrm{d}r}{c(r)}\right)^{-1}, \tag{1.8}$$

where R is the stellar radius, r the local distance from the stellar centre and $c(r)$ the sound speed. In Equation (1.7) the parameters $\tilde{\alpha}$ and ϵ_{nl} also depend on the local chemical composition. While the exact nature of these offsets are not yet completely understood, research on the topic is ongoing. Recently, Trampedach et al. (2017) compared the theoretical p-mode frequencies for both one-dimensional and three-dimensional models of sun-like stars, and found that the former systematically overestimate the pulsation frequencies.

Gravity modes

For gravity-mode or g-mode pulsations, buoyancy is the dominant restoring force. As a consequence, these modes can only propagate in the radiative regions of a star, because buoyancy is precisely what enables convection as well. As opposed to the p-modes, g-modes are most sensitive to the properties of the deep stellar interior, and cannot be purely radial in nature. Furthermore, for a non-rotating chemically homogeneous star with a convective core and a radiative envelope, the g-mode pulsations are expected to be equidistant in period in the asymptotic regime. It was shown by Tassoul (1980) that

$$P_{nl} = \frac{\Pi_0}{\sqrt{l\,(l+1)}}\,(n + \alpha_{l,g})\,, \tag{1.9}$$

where

$$\Pi_0 = 2\pi^2 \left(\int_{r_1}^{r_2} N \frac{\mathrm{d}r}{r} \right)^{-1} . \tag{1.10}$$

Here P_{nl} is the period of the pulsation with radial order n and degree l, $\alpha_{l,g}$ is a constant depending on the boundaries r_1 and r_2 of the mode trapping region, and r again the distance from the stellar centre. N is the Brunt-Väisälä frequency or the buoyancy frequency, i.e. the frequency with which a vertically displaced mass element oscillates. Equation (1.10) is graphically illustrated in Figure 1.4, where we show the evolution of Π_0 for a $1.6\,M_\odot$ stellar model on the main sequence in the top panel, along with the integrand in Equation (1.10) at selected stages of the stellar evolution in the bottom three panels. Consequently, the spacing value $\Delta\Pi$ between modes with the same degree l and consecutive orders n is given by

$$\Delta\Pi_l = \frac{\Pi_0}{\sqrt{l\,(l+1)}}. \tag{1.11}$$

As a result, the expected period spacings for different l-values in a non-rotating, chemically homogeneous star have fixed ratios.

Various aspects of stellar structure and evolution that are not taken into account in this simple approximation, have a large impact on the period spacing series. As explained in Section 1.1.2, the convective core in intermediate-mass stars can either grow or shrink during the stellar evolution. A growing convective core leads to a discontinuity in the chemical composition at its boundary, while a receding convective core leaves behind a μ-gradient zone near the core. Miglio et al. (2008) showed that the variation of the local average molecular weight leads to modifications of the g-mode resonance cavity and to so-called mode-trapping. This mode trapping translates into characteristic dips in the period spacing pattern. The amplitude of the dips is connected with the steepness of the chemical gradient, whereas the periodicity of the dips indicates its location. This is illustrated in Figure 1.5, where we show the dipole mode period spacing patterns calculated with the pulsation code GYRE v4.3 (Townsend & Teitler 2013, ; discussed in Section 1.2.3) for MESA models of a $1.6\,\mathrm{M}_\odot$ star at different phases of its evolution, with $X = 0.71$, $Z = 0.014$, step core overshoot $\alpha_{\mathrm{ov}} = 0.3$ and diffusive mixing $D_{\mathrm{mix}} = 1\,\mathrm{cm}^2\,\mathrm{s}^{-1}$. Miglio et al. (2008) further studied the impact of chemical mixing, such as convective core overshooting and extra diffusive mixing. The authors found that the mixing processes wash out the chemical gradient, which reduces the presence of the dips in the spacing pattern and decreases the average period spacing value, though there might still be dips

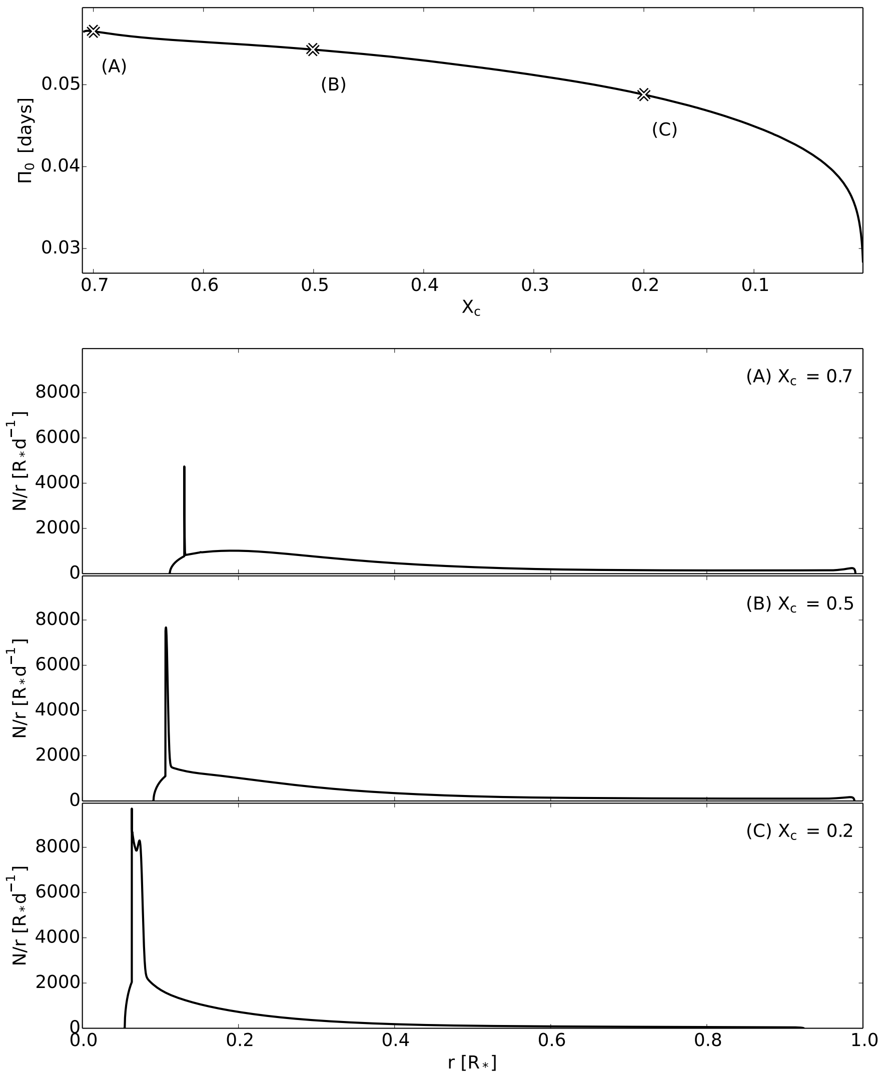

Figure 1.4: *Top panel:* The evolution of the parameter Π_0 for a $1.6\,\mathrm{M}_\odot$ stellar model on the main sequence, with input parameters $X = 0.71$, $Z = 0.014$, step core overshoot $\alpha_{\rm ov} = 0.3$ and diffusive mixing $D_{\rm mix} = 1\,\mathrm{cm}^2\,\mathrm{s}^{-1}$. *Bottom three panels:* The integrand used in Equation (1.10) for the computation of the parameter Π_0 at the selected stages of the stellar evolution indicated in the top panel.

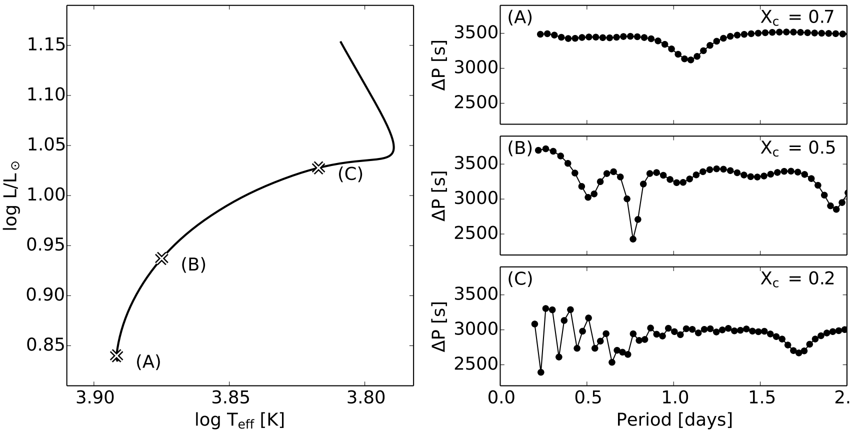

Figure 1.5: *Left:* Part of a $1.6\,\mathrm{M}_\odot$ evolution track, with $X = 0.71$, $Z = 0.014$, step core overshoot $\alpha_{\rm ov} = 0.3$ and diffusive mixing $D_{\rm mix} = 1\,\mathrm{cm}^2\,\mathrm{s}^{-1}$. *Right:* Period spacing patterns computed for dipole modes of the marked models on the evolution track in the left plot. For each the hydrogen content of the core (X_c) is provided.

present in the period spacing pattern depending on the level of efficiency of the mixing.

Bouabid et al. (2013) further extended the work of Miglio et al. (2008), and studied the influence of both mixing processes and rotation. The results that the authors obtained for the mixing processes, converge to those found by Miglio et al. (2008) when rotation is ignored. The influence of rotation was found to vary from mode to mode. The period spacings of prograde modes, which travel in the direction of rotation, exhibit a downward slope in the period spacing pattern for a rotating star, because of the positive rotational frequency shift added to the oscillation frequencies in an inertial frame. The same effect is observed for zonal modes, though it is not as strong as for prograde modes. Retrograde modes, which travel in the opposite direction of rotation, have an upward slope. These effects are illustrated in Figure 1.6 for the dipole g-mode pulsations of the same model shown in Figure 1.5 at $X_c = 0.5$. Extra mixing was taken into account by increasing the diffusive mixing to $D_{\rm mix} = 100\,\mathrm{cm}^2\,\mathrm{s}^{-1}$, while the frequency shifts resulting from rotation were computed using the traditional approximation (TA) of pulsations implemented in GYRE v4.3. The influence of TA will be discussed further later in this Section, while the GYRE code is discussed in more detail in Section 1.2.3.

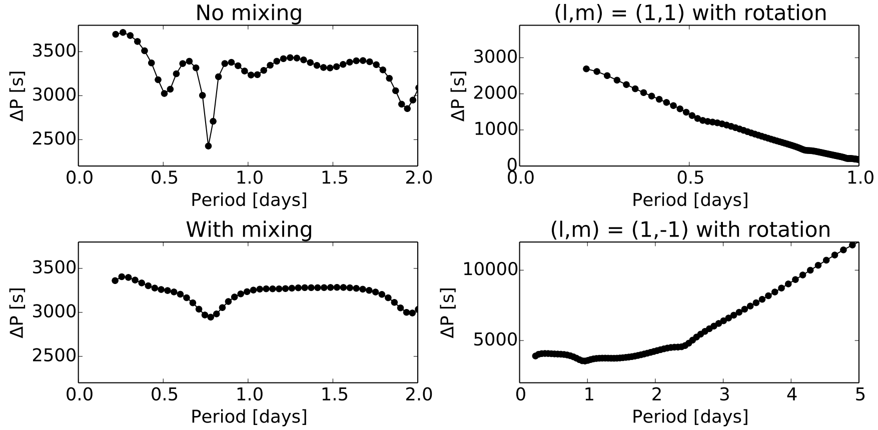

Figure 1.6: Period spacing patterns computed for dipole modes of a 1.6 $M_\odot$ star with $X_c = 0.5$. *Left:* spacing patterns with and without extra diffusive mixing, with $D_{\rm mix} = 100\,{\rm cm^2\,s^{-1}}$. *Right:* spacing patterns including the effect of extra diffusive mixing for a star rotating with $v_{\rm eq} = 73\,{\rm km\,s^{-1}}$, i.e., $f_{\rm rot} = 0.8\,{\rm d^{-1}}$, for the prograde (top) and retrograde (bottom) modes. We note the difference of the scales on the x- and y-axes.

Following these theoretical predictions, a detailed analysis of observed period spacing patterns is an efficient way to constrain the interior stellar structure. Such successful modelling based on g-mode period spacings detected in space photometry has been accomplished for various types of pulsating stars (cfr. Section 1.2.2), such as slowly pulsating B-type stars (e.g. Degroote et al. 2010; Savonije 2013; Pápics et al. 2014; Moravveji et al. 2015, 2016; Triana et al. 2015) and sdB stars (e.g. Reed et al. 2011; Foster et al. 2015; Reed et al. 2016), thanks to data from the space missions CoRoT and *Kepler*. Over the course of this PhD research, period spacing patterns have been detected for multiple A- and F-type stars as well (e.g. Chapellier et al. 2012; Kurtz et al. 2014; Bedding et al. 2015; Saio et al. 2015; Keen et al. 2015; Murphy et al. 2016), in addition to the detections presented in this dissertation (see Chapter 3). Other earlier detailed searches led to a failure to detect this important diagnostic (Hareter 2012; Breger et al. 2012) because of too poor frequency resolution of the data or too rapid rotation of the star.

The properties of gravity-mode pulsations in intermediate-mass stars are discussed further in Section 1.2.2.

The impact of rotation

While the discussion about stellar pulsations so far mostly assumed non-rotating stars, it is well-known that the influence of rotation on stellar pulsations is significant.

Indeed, as we discussed before in Section 1.1.1 and 1.1.2, stellar rotation has a major impact on stellar structure and evolution. This in turn impacts the resonance cavities for the pulsations travelling through the star, affecting both the pulsation frequencies and eigenfunctions.

However, rotation also influences stellar pulsations directly. For (very) slowly rotating stars this effect can again be derived by applying a 1st-order perturbative analysis to the set of equations (1.1) to (1.5), but including a rotational velocity field (Ledoux 1951; Lynden-Bell & Ostriker 1967). Assuming rigid rotation, this results in a rotational multiplet of pulsation frequencies given by

$$f_{nlm} = f_{nl} + m(1 - C_{nl}) f_{\mathrm{rot}}. \tag{1.12}$$

Here f_{nlm} is the observed pulsation frequency for a mode with radial order n, spherical degree l and azimuthal order m for a star rotating with frequency f_{rot}, while f_{nl} is the pulsation frequency for modes with order n and degree l in the non-rotating case. The additional term "$m f_{\mathrm{rot}}$" on the right hand side of Equation (1.12) gives the impact of the change of reference frame (from the co-rotating frame of the star to the observer's inertial frame). The Ledoux constant C_{nl} represents the 1st-order influence due to the Coriolis force, and has different values for p- and g-modes. For high-order p-modes ($n \gg l$), C_{nl} is close to zero, but for high-order g-modes it is given by

$$C_{nl} = \frac{1}{l(l+1)}.$$

As we can see, rotation lifts the degeneracy occurring for the non-rotating case. The frequencies of prograde modes, which travel in the direction of the rotation, will become larger in the inertial reference frame, while the frequencies of retrograde modes, which travel in the opposite direction, will become smaller in the inertial reference frame. In this work, we adopt the convention that $m > 0$ ($m < 0$) for prograde (retrograde) modes. Zonal modes, with $m = 0$, are unaffected by the rotation when only first-order effects are taken into account, and have $f_{nl0} = f_{nl}$.

In the case of higher rotation rates, the situation is more complex. For p-modes, 2nd- and 3rd-order perturbative methods are used (e.g. Dziembowski & Goode 1992; Soufi et al. 1998; Goupil 2011). Apart from a more accurate treatment of the Coriolis force, these also include an approximation of the impact of the centrifugal force.

For the low-frequency g-modes, on the other hand, the Coriolis force becomes part of the restoring force of the pulsations itself if the spin parameter $|s| \gtrsim 1$, with

$$s = \frac{2 f_{\text{rot}}}{f_{\text{co}}}, \tag{1.13}$$

where f_{rot} ($= \varOmega/2\pi$) and f_{co} are the stellar rotation frequency and the pulsation frequency in the corotating frame, respectively. In this situation, the g-mode pulsations are called gravito-inertial pulsations. If the value of $|s| \lesssim 1$ for a pulsation, it is said to be in the superinertial regime. If $|s| \gtrsim 1$, we are working in the subinertial regime.

In the subinertial regime various types of pure interial pulsations, which have the Coriolis force as the only restoring force, can also be present. Here we limit ourselves to a concise summary, and refer the interested reader to the literature for more extensive discussions on their characteristics (e.g. Papaloizou & Pringle 1978; Lee & Saio 1997; Townsend 2003b; Mathis 2011). Rossby modes or r-modes are retrograde modes which originate from the conservation of specific vorticity, combined with the influence of the stellar curvature (Saio 1982). They propagate in a stably stratified medium, and take on the appearance of rotationally modified g-modes for increasing rotation rates. However, one of the characteristic properties of r-modes is that they have pulsation frequencies smaller than the rotation rate in the inertial reference frame. In other words, as seen in the corotating reference frame Rossby modes travel in the direction opposite from the stellar rotation, but more slowly than the star rotates. Kelvin modes, on the other hand, are prograde inertial modes. Like Rossby modes, they also originate from the conservation of specific vorticity, but here it is the density stratification inside the star which plays a role, rather than the stellar curvature. Finally, Yanai modes are a mixed form of Rossby modes and rotationally modified g-modes. Their dominant behaviour may resemble that of either of these two pulsation types, depending on the physical conditions.

To take the impact of rotation into account, the traditional approximation is often used to describe the pulsations (Eckart 1960; Lee & Saio 1987, 1997; Townsend 2005). In the traditional approximation, one assumes that *(i)* the star is spherically symmetric, and *(ii)* the latitudinal component of the rotation vector can be neglected. While this particular assumption may not always be applicable, gravity modes and gravito-inertial modes are mostly sensitive to the stellar properties near the convective core, as discussed earlier. Here the rotational deformation of the star remains limited. This is illustrated in Figure 1.7, which shows the Brunt-Väisälä frequency N and the rotational kernel K_{nl} for the lowest- and highest-order mode of the stellar model discussed in Section 4.4.1. Both functions correlate with the sensitivity of the pulsations to the different regions in the star and peak near the convective core boundary. The rotational kernel K_{nl} specifically indicates the sensitivity of the pulsations to the local stellar rotation profile. Ballot et al. (2012) showed that the traditional approximation continues to perform adequately if the spin parameter $|s| \leq 2$ (see Ballot et al. 2012, Figure 2). It can further be shown that within the traditional approximation, an asymptotic pulsation period series can be rewritten for a rotating star as

$$P_{nkm,co} = \frac{\Pi_0}{\sqrt{\lambda_{k,m,s}}}(n + \alpha_g), \tag{1.14}$$

where $P_{nkm,co}$ is the pulsation period of order n, classification parameter k, and azimuthal order m in the corotating frame (e.g. Berthomieu et al. 1978; Ballot et al. 2012; Bouabid et al. 2013). Here, $\lambda_{k,m,s}$ is the eigenvalue of the Laplace tidal equation depending on k, m, and the spin parameter s, while the phase term α_g depends on the internal stellar properties at the boundaries of the pulsation mode cavity. The classification parameter k was defined by Lee & Saio (1997), and allows us to classify all the different gravity, gravito-inertial and inertial modes, including those which do not have an equivalent in the non-rotating case. For Rossby modes, we have $k \leq -2$, while the pulsations with $k = -1$ are retrograde Yanai modes. Pulsations with a non-rotating equivalent have $k \geq 0$, and $l = k + |m|$. In the limit of a non-rotating star, $s = 0$ and $\lambda_{k,m,s}$ approaches $l(l+1)$, so Equation 1.14 reduces to Equation 1.9. Whenever in this work a geometric identification for g-mode pulsations in a rotating star is provided with values for l and m, these pulsations have $k > 0$, and the given value for l corresponds to the one obtained in this limit.

The variation of the eigenvalue $\lambda_{k,m,s}$ as a function of the spin parameter s for some of the different pulsation types is illustrated in Figure 1.8, where it is assumed that $|m| = 1$. In this figure, the retrograde and prograde modes have $s < 0$ and $s > 0$, respectively.

It was also shown in the literature that, under the influence of the Coriolis force, gravito-inertial modes are concentrated towards the equator (e.g. Longuet-Higgins 1968; Lee & Saio 1997; Townsend 2003a), and can be expressed mathematically with Hough functions rather than spherical harmonic functions. As a result, the geometrical cancellation effects will be more pronounced for these pulsation modes, making it harder to detect them. This is illustrated in Figure 1.9, where we compare a $(l, m) = (1, 1)$ pulsation mode for a non-rotating star and for a star rotating at 50 % of its critical rotation rate. The spin parameter of the pulsation was taken to be $s = 6$, and the resulting equatorial constraint on the pulsation was computed using Equation (51) from Townsend (2003b). This expression gives us the polar dependence $\Theta(\theta)$ of the radial pulsation component in the asymptotic regime,

$$\Theta(\theta) = \exp\left(\frac{ms\cos^2\theta}{2}\right).$$

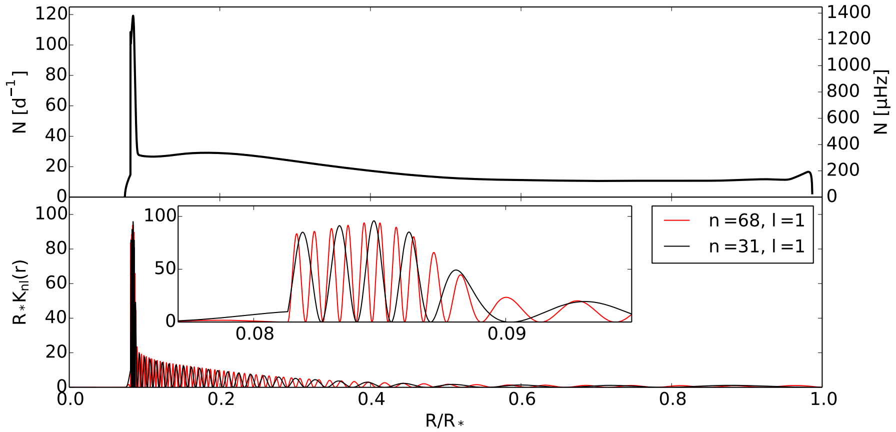

Figure 1.7: Brunt-Väisälä frequency N (*top*) and the rotational kernel K_{nl} (*bottom*) for the lowest- and highest-order mode of the stellar model discussed in Section 4.4.1. The inset shows a zoom of K_{nl}. Both functions correlate with the sensitivity of the gravity-mode pulsations to the different regions inside the star.

While the pulsation affects (almost) the entire surface of the non-rotating star, a significant fraction of the surface of the rotating star does not exhibit any pulsational variability. This effect is present for all gravito-inertial pulsations, but it is smallest for Rossby modes and for prograde sectoral modes, the latter being the equivalent of Kelvin modes for high values of the spin parameter s (e.g. Townsend 2003b).

These approaches still have limitations. Within the framework of the traditional approximation, the gravito-inertial mode pulsations still do not propagate into the convective core, whereas in real stars this may be expected: while buoyancy cannot act as a restoring force in the convective core, the complete Coriolis force can (Ballot et al. 2012; Prat et al. 2016b). In the case of p-modes, the rotationally split multiplets not only become asymmetric for higher rotation rates, but overlap with each other as well. A failure to precisely predict the rotationally shifted pulsation frequencies, often prevents mode identification and hence a detailed asteroseismic analysis. Consequently, for moderate to fast rotating stars two-dimensional models are required for a proper analysis. Examples of two-dimensional pulsation codes include ACOR (adiabatic code of oscillation including rotation; Ouazzani et al. 2012, 2017), and TOP (two-dimensional oscillation program; e.g. Reese et al. 2013). These codes are currently not publicly available.

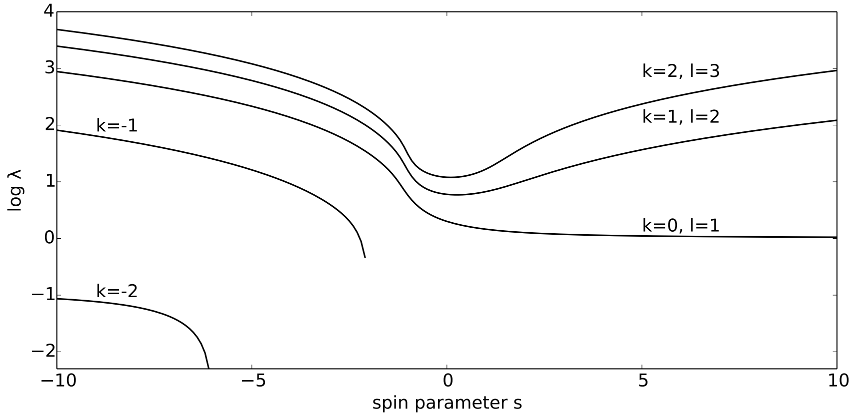

Figure 1.8: The variation of the eigenvalue $\lambda_{k,m,s}$ as a function of the spin parameter s for various pulsations with $m = 1$. In this figure, the retrograde and prograde modes have $s < 0$ and $s > 0$, respectively. The classification parameter k indicates the type of pulsation mode (Lee & Saio 1997). If $k \geq 0$, the indicated pulsations have an equivalent in the non-rotating star, for which $l = k + |m|$. If $k \leq -2$, the pulsation is a Rossby wave, and the pulsations with $k = -1$ are retrograde Yanai modes.

Finally, it is worth noting that stellar pulsations and waves are expected to have an impact on stellar rotation as well. Numerical simulations by Rogers et al. (2013) for a $3M_\odot$ core-hydrogen burning star have shown that internal gravity waves (IGW), i.e., gravity-waves in the deep stellar interior stochastically excited at the convective core boundary, can contribute significantly to the transport of angular momentum inside stars with a convective core and a radiative envelope. The principles of this mechanism had been worked out before by, e.g., Lee & Saio (1993), Zahn et al. (1997), and Pantillon et al. (2007). In addition, Rogers (2015) demonstrated for eight main-sequence stars with measured differential rotation from asteroseismology that angular momentum transport by IGW can explain the observed rotation profiles. Similarly, Belkacem et al. (2015) have suggested that pulsations with a mixed p-mode and g-mode character could be responsible for the observed spin-down of the core in evolved red giants.

Excitation mechanisms

In general, stellar pulsations are damped as they occur in a star. Thus, excitation mechanisms, which pump energy into these pulsations, are required to explain

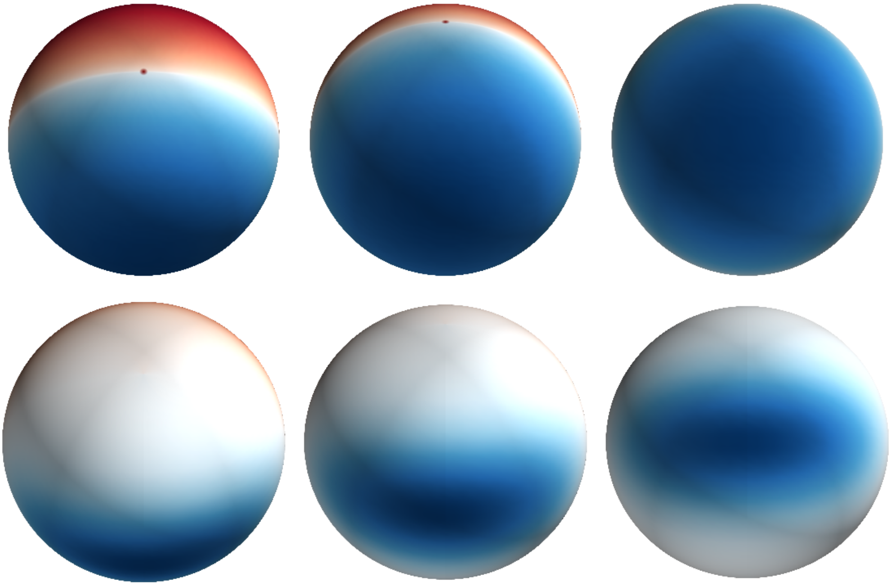

Figure 1.9: *Top:* A snapshot of a $(l, m) = (1, 1)$ mode pulsation in a non-rotating star, at inclination angles of 30° *(left)*, 60° *(middle)* and 90° *(right)*. The assigned colour coding has the same meaning as in Figure 1.3. *Bottom:* A snapshot of the same pulsation mode, with $(l, m) = (1, 1)$ and at the same inclination angles, but in a star rotating at 50 % of its critical rotation rate. The spin parameter of the pulsation was taken to be $s = 6$, and the resulting equatorial constraint on the pulsation was computed using Equation (51) from Townsend (2003b).

the existence of observable stellar pulsations. There are various known pulsation excitation mechanisms, which can typically be subdivided in two main groups: stochastic excitation by convective motions and heat-engine mechanisms.

Stochastically excited modes can often be found in stars with an outer convective layer, such as cool main-sequence stars and red giants. Here, part of the kinetic energy of the convective mass elements is converted into pulsation mode energy: the star resonates in one or more of its eigenfrequencies. Stochastically excited pulsations have relatively small amplitudes (of the order of $\mathrm{cm\,s^{-1}}$ to $\mathrm{m\,s^{-1}}$ in velocity and parts-per-million (ppm) in flux) and short lifetimes before they are damped, typically on the order of days (e.g. Belkacem et al. 2006a,b). Furthermore, stochastic excitation of gravity modes has also been suggested and studied by Samadi et al. (2010) for massive main-sequence stars. Such modes were subsequently detected by Neiner et al. (2012) in the fast rotating Be star HD51452, but with amplitude properties contradicting the predictions made by Samadi et al. (2010). Mathis et al. (2014) subsequently demonstrated that rotation, through the Coriolis force, modifies the stochastic excitation of gravity- and gravito-inertial modes, causing strong coupling between these modes and the rotating turbulent convective regions, enhancing in this way the mode amplitudes and bringing theory into agreement with observations.

Heat-driven pulsators, on the other hand, have internal layers that act as a heat engine. Often these are partial ionisation regions where the local opacity κ undergoes cyclic variations. Normally, the compression of stellar material leads to an increase of the local temperature, which results in a reduction of the opacity κ following Kramer's law,

$$\kappa \sim \rho T^{-7/2}.$$

However, in partial ionisation regions most of the energy released during the compression may lead to the ionisation of the local stellar material instead. This then results in an increase of the density ρ and the opacity κ, trapping the flux coming from the stellar interior. Consequently, the local pressure increases, the local occupied volume expands and the density drops again. This leads the local ionised material to recombine and the opacity κ becomes smaller as well. The previously trapped radiation is released. The pressure decreases in turn, and the whole cycle starts all over again. Because of the typically strong influence of the opacity κ on this mode excitation mechanism, it is often also referred to as the κ-mechanism. It is responsible for the excitation of the p-modes in δ Sct stars, with the main driving occurring in the HeII partial ionisation zone (see Section 1.2.2).

Another example of a heat-driving mechanism is the convective flux blocking mechanism (Guzik et al. 2000; Dupret et al. 2005). In this case, the pulsating stars have a thin outer convective envelope (CE) on top of a radiative zone. As the flux passes from the inner radiative region to the CE, it is converted from radiative flux to convective flux, but the CE does not (sufficiently) react to radiative flux variations at the bottom of the layer. This means that, if there is a rise in the radiative flux at the bottom of the CE, the corresponding energy will be trapped below the CE, and because local luminosity and density variations in this region are in phase, this gives rise to stellar pulsations with periods on the order of the thermal relaxation time τ_{th} at the bottom of the CE. Here,

$$\tau_{\mathrm{th}} = \int_m^M \frac{T c_v \mathrm{d}m}{l},$$

where m is the mass at the bottom of the convective envelope, M is the stellar mass, and T, c_v and l are the temperature, heat capacity at constant specific volume and luminosity, respectively. In simple terms, τ_{th} is the time interval during which the star radiates an amount of energy equal to the thermal energy stored in the stellar layers outside the mass coordinate m.

The convective flux blocking mechanism is responsible for the excitation of g-modes in γ Doradus stars (see Section 1.2.2), though recently the κ mechanism has been linked to these stars as well (Xiong et al. 2016). While Guzik et al. (2000) and Dupret et al. (2005) did not take stellar rotation into account in their computations, Bouabid et al. (2013) analysed the convective flux blocking mechanism in γ Doradus stars more thoroughly, by conducting a non-adiabatic study including the effects of rotation via the traditional approximation. The authors confirmed the convective flux blocking mechanism to be a valid mode excitation mechanism, and further noted that rotation can shift the observed pulsation frequencies out of the classical range.

While other mode excitation mechanisms, such as the ϵ-mechanism and tidal excitation, do not play a role in this work, they are important in other types of stars. In the ϵ-mechanism the pulsation excitation is caused by the temperature dependence of the nuclear reaction rates. It has been suggested as the excitation mechanism of, e.g., gravity-mode pulsations in both SNII-progenitors (Moravveji et al. 2012) and He-rich sdB-stars (Miller Bertolami et al. 2013). Tidally induced pulsations occure in the stellar components of eccentric binary systems, and various detections have been reported (e.g. Welsh et al. 2011; Hambleton et al. 2013; Guo et al. 2017).

1.2.2 A zoo of pulsating stars

The diversity in excitation mechanisms results in a wide variety of observed classes of pulsating stars. These are spread all over the Hertzsprung-Russell diagram, as shown in Figure 1.10. Furthermore, thanks to the continuing improvements in both quality and quantity of asteroseismic observations (discussed in Section 1.3), both newly discovered classes of pulsating stars as well as newly discovered characteristics continue to be reported. A discussion on all these different classes of pulsators would take us too far, and we limit ourselves to a description of γ Doradus stars and δ Sct stars. We refer to Aerts et al. (2010) for an overview of commonly known types of pulsating stars. Two examples of more recently discovered (sub)classes of pulsators can be found in Mowlavi et al. (2013) and Soszyński et al. (2016). Mowlavi et al. (2013) reported the discovery of a new class of g-mode pulsators, which are located between the slowly pulsating B-type stars (SPBs) and δ Sct stars in the Hertzsprung-Russell diagram. It was suggested by Salmon et al. (2014) that these are actually fast-rotating SPB stars whose pulsation frequencies are rotationally shifted.

Meanwhile, Soszyński et al. (2016) describe a new subclass of double-mode RR Lyrae stars in the Large and Small Magellanic Clouds.

Gamma Doradus stars

The variability of the star γ Doradus was first observed by Cousins et al. (1989); Cousins (1992). After a failed attempt to explain the observations with stellar spots (Balona et al. 1994) and the discovery of similar variability in 9 Aur, HD 96008 and HD 164615 (Krisciunas et al. 1993), they were found to be a previously unknown class of pulsating stars. Subsequently, scientific interest in them grew further, and the stars were characterised by Kaye et al. (1999).

Gamma Doradus stars (hereafter γ Dor stars) are intermediate-mass stars ($1.4\,M_\odot \lesssim M_* \lesssim 2.0\,M_\odot$) on or near the main sequence that exhibit multiple gravity- and/or gravito-inertial mode pulsations. Typical temperatures $T_{\rm eff}$ and luminosities log $L/L_\odot$ range from 6500 K to 7500 K and 0.7 to 1.85, respectively. As we discussed in Section 1.1, this mass range covers (part of) the transition between low-mass stars with a radiative core and a convective envelope, and high-mass stars with a convective core and a radiative envelope. The gravity- and gravito-inertial modes in these stars are excited by the convective flux blocking mechanism at the bottom of the convective envelope (Guzik et al. 2000; Dupret et al. 2005, as explained in Section 1.2.1), and are most sensitive to the properties of the near core regions. Thus, the analysis of the g-modes allows us to directly constrain the properties and evolution of the convective core in this stellar mass range.

Earlier studies of the γ Dor stars in the literature relied on spectroscopic and multicolour photometric observations. Because the amplitudes of γ Dor type pulsations are small (brightness variations < 50 mmag, radial-velocity amplitudes $< 5\,\mathrm{km\,s^{-1}}$), and the typical range of pulsation frequencies (from 0.2 to 3 d^{-1}) is close to the day-night cycle of the Earth's rotation, it is especially challenging to obtain reliable observations for these stars. Despite these complications, on the order of 100 bona fide γ Dor type pulsators were identified in 2011 using ground-based data and observations from the Hipparcos satellite (e.g. Henry et al. 2011, and references therein), not including the γ Dor stars found in galactic open clusters (e.g. Arentoft et al. 2007). In addition, several lists of γ Dor candidates can be found in the literature as well (e.g. Kahraman Aliçavuş et al. 2016, and references therein). Thorough analyses of individual stars were done based on time series of ground-based multi-colour photometric observations (e.g. Cuypers et al. 2009) or spectroscopic observations (e.g. Brunsden et al. 2012a,b; Davie et al. 2014). In most cases, the observed pulsations were found to be prograde dipole modes, though retrograde and

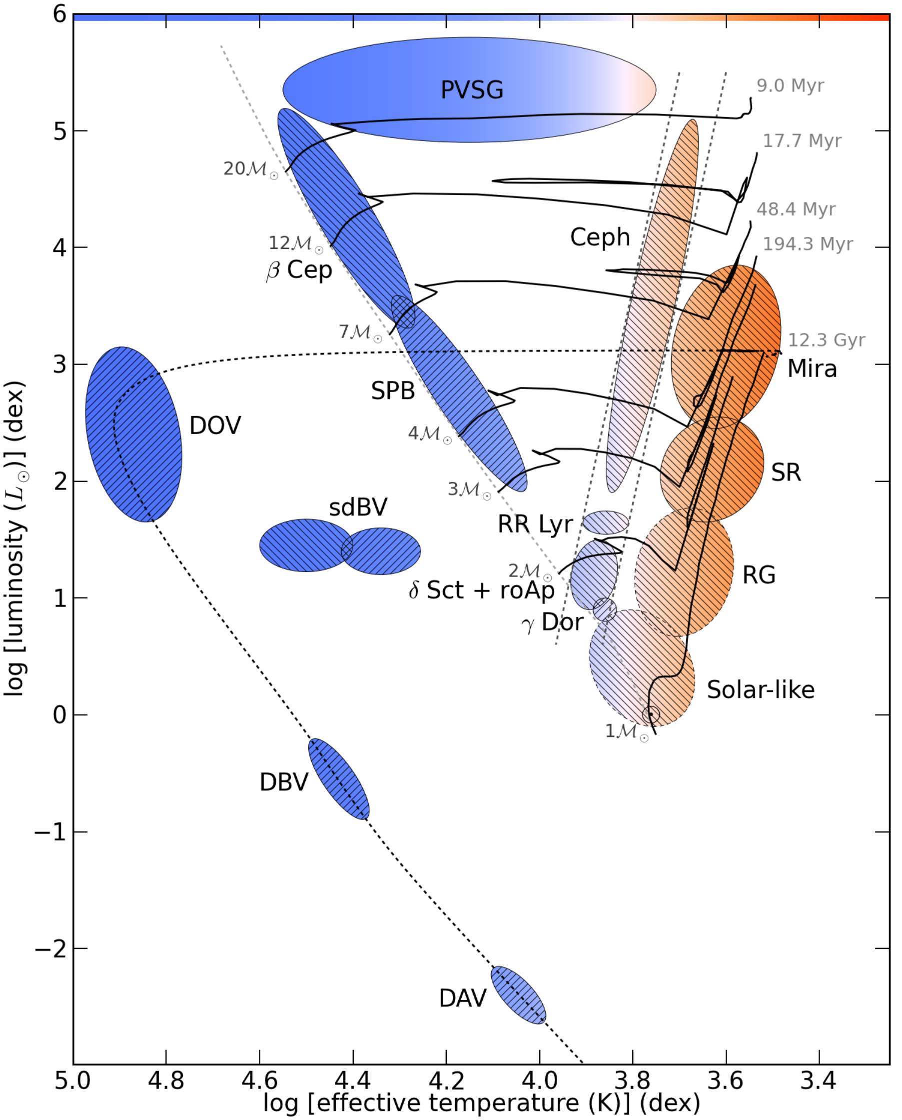

Figure 1.10: An overview of different known classes of pulsating stars across the Hertzsprung-Russell diagram. The evolutionary tracks are taken from Schaller et al. (1992) and Driebe et al. (1998). Initial masses and evolutionary time scales are added in grey. The hatching corresponds to the dominant character of the pulsation modes, with forward and backward slanting representing p- and g-modes, respectively. The colour indicates the spectral type. The two vertical dashed lines mark the position of the classical instability strip, whereas the zero-age main sequence is represented by the light-grey dashed line. Figure courtesy of P. I. Pápics, adapted from a similar figure made by J. Christensen-Dalsgaard.

quadrupole modes have also been detected. This is in line with the theoretical expectations given in Section 1.2.1.

Since the launch of space missions (discussed in Section 1.3), asteroseismic research of γ Dor stars has experienced a large boost, because space-based observations are typically more precise and do not suffer from the Earth's day-night cycle. Consequently, the number of detected γ Dor pulators has skyrocketed during the past few years (e.g. Uytterhoeven et al. 2011; Tkachenko et al. 2013a; Bradley et al. 2015).

Delta Sct stars

Delta Sct stars have been known and studied for over a century. An overview of these pulsators was given by Breger (2000a). They are intermediate-mass stars ($1.5 \lesssim M_* \lesssim 2.5$) on or near the main sequence, and exhibit pressure mode pulsations, with possible pulsation periods in the range from 15 minutes to 8 hours. The temperature $T_{\rm eff}$ typically varies between about 6600 K and 8500 K, while luminosities $\log L/L_\odot$ range from 0.6 to 2. The pulsations are excited by the κ mechanism in the second partial ionisation zone of helium (see Section 1.2.1). The amplitudes of the brightness and velocity variations due to the pulsations are smaller than 0.3 mag and $10\,\mathrm{km\,s^{-1}}$, respectively.

Before the launch of space missions, extensive ground-based observations of δ Sct stars already led to several interesting results. The well-known period-density relation (Breger 1990), which expresses the correlation between low-order pulsation periods and the star's mean density, is related to the theoretically expected equidistance of pulsation frequencies with consecutive radial orders (explained in Section 1.2.1). Coordinated observation campaigns of δ Sct stars such as 4 CVn led to the discovery of amplitude modulation of the pulsation modes (Breger 2000b).

Space-based observations resulted in an explosive growth in the number of known δ Sct stars. For many of them amplitude modulation was again observed (e.g. Bowman et al. 2016), and semi-analytical relations between the large separation (defined in Section 1.2.1) and the mean stellar density were reported (Suárez et al. 2014; García Hernández et al. 2015).

However, the space missions led to the most notable progress for the hybrid γ Dor/δ Sct pulsators. From the possible values for $T_{\rm eff}$ and $\log L/L_\odot$ for both types of pulsators, it is clear that their instability strips partially overlap (see also Figure 1.10). Dupret et al. (2005) showed that indeed, stars located in this overlapping region in the Hertzsprung-Russell diagram, can be expected to exhibit both g- and p-modes. Because gravity-modes are sensitive to the properties of the deep stellar interior and the pressure modes to those of the outer layers of the star, much can be learned from these hybrid pulsators, such as core-to-surface rotation rates. These data, in turn, can be used to constrain angular momentum transport in theoretical models (e.g. Kurtz et al. 2014). Before the era of the space missions, only a handful of these stars were known (e.g. Handler et al. 2002). Since then, several dozens of candidate pulsators have been reported (e.g. Hareter 2012; Bradley et al. 2015).

Interestingly, many of the observed γ Dor stars, δ Sct stars, and hybrid pulsators seem to lie outside of the theoretically predicted instability strips. This implies that the current theory of pulsation mode excitation needs to be revised. Recent work by Xiong et al. (2016) was a step in this direction. However, it should be noted that in the existing theory, the properties of the outer convective layer, i.e. the mixing parameter α_{MLT}, has a large impact. By changing the value of α_{MLT}, the location of the instability strips of the γ Dor stars and δ Sct stars can be shifted. Furthermore, the atmospheric parameter values of the stars used in these studies are often derived from photometry, which tend to be less reliable than those determined from spectroscopic observations. More research is therefore required before conclusions on the borders of the instability strips can be drawn.

1.2.3 The stellar pulsation code GYRE

GYRE[2] is a one-dimensional stellar pulsation code, developed by Richard Townsend and his collaborators (Townsend & Teitler 2013). Similar to MESA (described in Section 1.1.3), GYRE is an open source modular code. Based on a given equilibrium stellar model, GYRE solves the set of linear stellar pulsation equations for both the pulsation frequencies and the corresponding eigenfunctions. Other quantities or profiles, such as the normalised moment of inertia of the computed pulsations, can also be computed. The provided equilibrium model can be *(i)* a numerical model, computed with an evolutionary code such as MESA, *(ii)* a polytropic model based on a solution of the Lane–Emden equation, and *(iii)* an analytic model based on explicit expressions for the structure coefficients. GYRE is particularly well integrated within MESA, as it is always included as one of the modules of the stellar evolution code. In addition, blueprints of the interface between the two codes are included in GYRE by default, so different versions of the codes can be relatively easily combined.

The GYRE code is constantly under development, and currently allows the user to do the computations in different frameworks. The pulsation frequencies

---

[2] `http://bitbucket.org/rhdtownsend/gyre`

themselves can, for instance, be computed in either the adiabatic or the nonadiabatic regime. The stellar rotation, on the other hand, can be treated with the 1^{st} order perturbative approach or the traditional approximation. It can be included via either differential rotation profiles in a numerically computed input model, or an imposed rigid rotation rate.

In this work we use the adiabatic module of GYRE v4.3. The impact of uniform stellar rotation on the gravito-inertial mode pulsations is taken into account using the traditional approximation, which is already implemented in the GYRE code.

An example of a typical GYRE inlist used in this work, can be found in Section A.2 in Appendix A.

1.3 Observations

Because asteroseismology requires accurate values for the pulsation frequencies of a star, there are very stringent requirements for the observations, in terms of the precision, total observation time and duty cycle. So although a lot has been accomplished using ground-based observations, it is clear they have a strong disadvantage compared to space-based data. For an average photometric observation run at a ground-based observatory, a precision of mmag can be reached despite the influence of the Earth atmosphere, and while a total data set can cover years, the Earth's day-night cycle and the usually high oversubscription of telescopes leads to very low duty cycles. In some cases, multi-site campaigns were set up to improve the overall quality of the data set, but these are difficult to organise.

As a result, the photometric observations from space-based telescopes, such as MOST, CoRoT, and *Kepler*, provided a large boost to the study of asteroseismology. The typical precision is μmag, much better than what is typically obtained from ground-based observations, and duty cycles are $\gtrsim 90\%$ for observation times going from tens to hundreds of days. Consequently, we can now observe up to hundreds of pulsation frequencies for individual targets, rather than the handful of frequencies which could be determined from dedicated ground-based observations (e.g. Cuypers et al. 2009, for a long-term effort of studying γ Dor stars). Furthermore, the measured pulsation frequencies are extremely precise, which allows us to do detailed seismic modelling of observed stars.

In this work, we make use of the data provided by the original *Kepler* space mission, which had a total observation time of about four years, and complement them with high-resolution spectra taken with the HERMES spectrograph at the ground-based Mercator telescope.

1.3.1 *Kepler* space photometry

Kepler is a NASA space mission, which operated from 2009 to 2013. While its main goal was to observe Earth-sized exoplanets in the habitable zone around solar-like stars using the transit method, the complementary science included observing variable stars with a higher precision and a higher cadence than has ever been possible (Koch et al. 2010; Gilliland et al. 2011). To this end, the 0.95-m Schmidt telescope was placed in an Earth-trailing heliocentric orbit (ETHO). This has the advantage that *(i)* the telescope does not pass through the South-Atlantic Anomaly or the Earth's shadow, *(ii)* there is no varying earthshine, and *(iii)* no torque on the spacecraft resulting from atmospheric drag or gravity gradient. This in turn results in much more precise photometric observations than what can typically be achieved otherwise.

The original *Kepler* space mission had a fixed 115 deg^2 field-of-view in the constellations Lyra and Cygnus, which was projected onto a 95 megapixel focal plane composed of 42 science CCDs and four guidance sensor CCDs. Up to 170 000 stars were observed simultaneously in long cadence, with a default cadence of one measurement per 29.43 minutes. Meanwhile, a maximum of up to 512 stars could be observed in short cadence, i.e., with a cadence of 58.86 seconds. The measurements were white light photometry, with the observed passband ranging from 423 to 897 nm.

The *Kepler* space telescope is a very sensitive instrument. During the original mission, the brightness of the observed stars lay primarily between 9th and 15th mag, and for a 12th mag star a noise level on the order of 30 ppm on 6.5 hours observation time was achieved. In addition, the overall duty cycle of this space mission was more than 90%, partly thanks to the ETHO.

The data obtained during the original *Kepler* mission can be found at both the MAST[3] (Mikulski Archive for Space Telescopes) and KASOC[4] (Kepler Asteroseismic Science Operations Center) websites. This includes both the raw pixel data, as well as data which have been reduced using a variety of standard pipelines.

In May 2013 the second reaction wheel of the spacecraft failed, after another reaction wheel had already stopped working in July 2012. Because a minimum of three operational wheels was required to maintain the stability of the telescope,

---

[3] `http://archive.stsci.edu/kepler/data_search/search.php`

[4] `http://kasoc.phys.au.dk/`

the original field-of-view could no longer be observed. Since then, the telescope has been repurposed as the K2 mission, and is now oriented along the ecliptic plane, with a long side of the telescope facing the Sun (Howell et al. 2014; Vanderburg & Johnson 2014). Here the missing stabilisation is provided by the radiation pressure from the Sun and the periodic firing of the thrusters every six hours. The K2 mission provides the opportunity to observe a variety of types of stars in various campaign target fields in the ecliptic plane, that were rare or absent in the original *Kepler* field. However, because the orientation of the spacecraft is limited by its orientation relative to both the field of view and the Sun, the maximum observation time per field of view is limited to 75 days. While this is adequate for pulsating stars with short periods, e.g., δ Sct stars, it is insufficient to detect period spacing patterns in the pulsation frequency spectra of relatively long-period pulsators, such as γ Dor stars.

1.3.2 HERMES spectroscopy

Spectroscopy is very valuable in the study of variable stars. On one hand, the observations of spectra provide detailed information about the physical conditions in the stellar atmospheres, placing constraints on the effective temperature $T_{\rm eff}$, the surface gravity $\log g$, the surface metallicity [M/H] and the projected surface rotation velocity $v \sin i$. This information gives us to location of the observed star in the Hertzsprung-Russell diagram or the Kiel diagram. In combination with either photometric or spectroscopic time series of observations, this information is vital to determine the class membership of an observed pulsator. Furthermore, if the observed star is part of a multiple system, periodic variations of the radial velocity v_r will impact the spectroscopic observations via the Doppler effect

$$\frac{\Delta\lambda}{\lambda} = \frac{v_r}{c},$$

where $\frac{\Delta\lambda}{\lambda}$ is the relative wavelength shift caused by the radial velocity of the observed star. While we work with *Kepler* photometry in this study and only use spectroscopy to characterise the studied stars, it is worth noting that the Doppler effect can also be used to trace the radial velocity variations at the stellar surface caused by the pulsations. However, this type of analysis requires hundreds of high signal-to-noise ratio spectra, and the resulting data set typically suffers from the usual drawbacks of ground-based observations.

HERMES (High Efficiency and Resolution Mercator Echelle Spectrograph; Raskin et al. 2011) is a fibre-fed prism-cross-dispersed échelle spectrograph at the 1.2-m Mercator telescope[5] (Observatorio del Roque de los Muchachos, La

---

[5] `www.mercator.iac.es`

Palma, Canary Islands, Spain). It covers the wavelength range from 377 nm to 900 nm, and has two optical fibres, allowing the researcher to observe in either the low resolution mode ($R \sim 63000$) or the high-resolution mode ($R \sim 85000$).

The HERMES instrument is optimised for the study of variable stars, where time series of observations are required. It has a peak efficiency of 28%, so that small variations in the spectra may be observed or relatively faint stars with $m_V \sim 12$ mag can be studied, even though the Mercator telescope is small (with a 1.2 m mirror). While the high-resolution mode has been optimised for efficiency, low-resolution observations are optimised for instrument stability, e.g. include simultaneous ThArNe-exposures, which improves the radial velocity precision.

A very efficient standard reduction pipeline, HermesDRS, is available, and continuously kept up-to-date. The pipeline is written in python, and includes bias subtraction, flat fielding, wavelength calibration using a ThArNe spectrum, order merging and removal of cosmic hits. At the time of writing, the 6^{th} version of the HermesDRS is in use.

1.4 Goal and outline of the thesis

The goal of this thesis is to do a seismic study of intermediate-mass stars with both a convective core and a convective envelope, separated by a radiative region. Specifically, we aim to constrain the stellar rotation in the deep stellar interior, the size and shape of the convective core (i.e., the convective core overshooting), and the extra diffusive mixing processes in the radiative near core regions.

To this end, we analyse a sample of 70 γ Dor star candidates in the original *Kepler* field of view, which was composed by Tkachenko et al. (2013a). We developed a method to detect period spacing patterns in g-mode spectra, which we present in Chapter 2. In Chapter 3, we take a closer look at the stars in our sample. By combining the photometric observations of the *Kepler* space mission (Section 1.3.1) with spectroscopic observations, we re-evaluate their possible classification as γ Dor stars. We then look for period spacing patterns in the photometric data of the confirmed γ Dor pulsators, using the method presented in Chapter 3, and combine the information with the other available data to characterise the sample. In Chapter 4, we further analyse the detected period spacing patterns of the stars in our sample to derive their interior rotation rates and obtain a mode identification for the observed pulsations. These results are then compared with the sample characteristics discussed in Chapter 3, which allows us to do ensemble modelling of the stars. Finally, we give our conclusions in Chapter 5, and show that this work provides an excellent base for future detailed theoretical modelling of γ Dor stars, with a specific focus on differential rotation and rotational mixing.

Chapter 2

The detection of gravity-mode period spacing patterns

This chapter was based on

Detecting non-uniform period spacings in the *Kepler* photometry of γ Doradus stars: methodology and case studies

T. Van Reeth, A. Tkachenko, C. Aerts, P. I. Pápics, P. Degroote, J. Debosscher, K. Zwintz, S. Bloemen, K. De Smedt, M. Hrudkova, G. Raskin, H. Van Winckel

Astronomy & Astrophysics, 574, A17, 10 pp. (2015)

Author contributions

Timothy Van Reeth did the spectroscopic analysis with the GSSP code under the guidance of Andrew Tkachenko, and Conny Aerts suggested the use of échelle diagrams for the detection of period spacing patterns, the validation of the method on a synthetic data set and the use of a flow chart in the publication. Andrew Tkachenko, Conny Aerts, Peter Pápics, and Konstanze Zwintz have participated in many helpful discussions on the nature and observational properties of γ Dor stars. Pieter Degroote, Jonas Debosscher and Steven Bloemen provided some of the codes that were used in this work, specifically for the extraction and data reduction of the light curves from the raw *Kepler* pixel data, and for the frequency extraction from the light curves. The other co-authors were responsible for the spectroscopic observations at the Mercator telescope. Timothy Van Reeth did the data reduction, came up with the detection method for period spacing patterns in the case of moderate to fast rotators, and developed the analytic description for the simulation of γ Dor light curves. Timothy Van Reeth wrote the draft text; Andrew Tkachenko and Conny Aerts improved the text prior to submission.

Abstract

Context. The analysis of stellar oscillations is one of the most reliable ways to probe stellar interiors. Recent space missions such as *Kepler* have provided us with an opportunity to study these oscillations with unprecedented detail. For many multi-periodic pulsators such as γ Dor stars, this led to the detection of dozens to hundreds of oscillation frequencies that could not be found from ground-based observations.
Aims. We aim to detect non-uniform period spacings in the Fourier spectra of a sample of γ Dor stars observed by *Kepler*. Such detection is complicated by both the large number of significant frequencies in the space photometry and by overlapping non-equidistant rotationally split multiplets.
Methods. Guided by theoretical properties of gravity-mode oscillation of γ Dor stars, we developed a period-spacing detection method and applied it to *Kepler* observations of a few stars, after having tested the performance from simulations.
Results. The application of the technique resulted in the clear detection of non-uniform period spacing series for three out of the five treated *Kepler* targets. Disadvantages of the technique are also discussed, and include the disability to distinguish between different values of the spherical degree and azimuthal order of the oscillation modes without additional theoretical modelling.
Conclusions. Despite the shortcomings, the method is shown to allow solid detections of period spacings for γ Dor stars, which will allow future asteroseismic analyses of these stars.

2.1 Introduction

While various theoretical studies have been conducted on the internal structure of A- to F-type main-sequence stars, there have been few possibilities to verify the theoretical models observationally (e.g. Miglio et al. 2008, and references therein). γ Dor pulsators have potential in this respect, since theoretical modelling of their gravity-mode patterns would allow us to probe their internal structure (Miglio et al. 2008; Bouabid et al. 2013).

In this chapter, we present our initial proof-of-concept study, in which we developed a method for detecting non-uniform period spacing patterns in the frequency spectra of γ Dor pulsators (Section 2.2), guided by some general theoretical expectations and previous observational studies of such stars, as explained in Section 1.2.1. We test the method on simulated light curves and apply it to *Kepler* data of five γ Dor stars in Section 2.3. Finally, we summarise the methodology and conclude that our new methodology justifies a long-term PhD project to fully exploit the seismic potential of carefully selected γ Dor stars, the results of which are included in this thesis.

2.2 Methodology to identify period spacings

Pulsation frequencies are usually obtained from time series of either photometric or spectroscopic data using iterative prewhitening. Hereby pulsation frequencies and amplitudes are determined one-by-one from the Fourier spectrum and optimised by fitting the model

$$F(t_i) = c + \sum_{j=1}^{n_f} A_j \sin\left[2\pi\left(f_j t_i + \phi_j\right)\right]$$

to the light curve, where A_j, f_j and ϕ_j are the amplitudes, frequencies and phases of the n_f considered pulsations, while t_i indicates the points in time for which observed data are available. This model is re-evaluated for every additional extracted pulsation frequency, until a predetermined stop criterion is reached (e.g. Degroote et al. 2009; Aerts et al. 2010). Historically, prewhitened pulsation frequencies are accepted when their amplitude is at least four times larger than the local noise level in the Fourier transform, i.e., the signal-to-noise ratio $\mathrm{S/N} \geq 4$ (Breger et al. 1993). However, because of the high precision of the data, this traditional stop criterion is not necessarily suitable in the framework of space-based photometric observations in general, and particularly not in the search for period spacings of g-mode pulsators (e.g. Balona 2014). It would lead to the extraction of frequency values that are seriously influenced by the preceding prewhitening. This is illustrated with simulations mimicking a typical *Kepler* light curve of a γ Dor star in our sample in Figure 2.1. A lot of low-amplitude peaks are derived from the power spectrum of the simulated light curve and its subsequent prewhitening, while they are unrelated to the simulated signal. For this reason, recent analyses of *Kepler* photometry either do not use a stop criterion for the frequency analysis (e.g. Kurtz et al. 2014), or

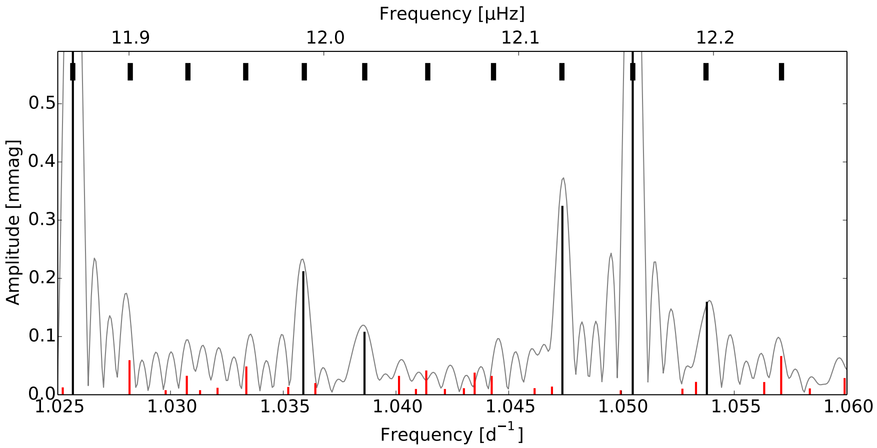

Figure 2.1: Part of the Fourier transform (grey) of a simulated light curve (described later on in Section 2.3.1). The full black vertical lines indicate the frequencies which were extracted using traditional prewhitening with $\mathrm{S/N} \geq 15$, while the red vertical lines indicate the remaining frequencies which were extracted with $\mathrm{S/N} \geq 4.0$. The thick black markers indicate the frequencies which were used as input. These were all extracted with our new definition based on the comparison criterion.

rely on a higher cutoff value than four times the local noise level. In Figure 2.1, we show all frequencies whose amplitudes have a S/N level above fifteen as an example.

The suitable S/N cut-off value varies strongly from star to star, and is not known a priori. The reason is that for such high-quality data, noise is no longer the limiting factor for the accuracy of the result. Rather, small uncertainties in the frequency, amplitude and phase values when fitting sine functions to the light curve give rise to a residual signal. These residuals modulate the subsequently extracted frequency values and their influence keeps increasing during the iterative prewhitening procedure. This is our motivation to deduce a new stop criterion based on the comparison of the extracted frequencies with the original Fourier spectrum of the light curve. Hereafter, we call this the *comparison criterion.*

We first compute the amplitude A_f of the extracted frequency f by fitting a sine function with that frequency to the light curve. Then we compare A_f to the local amplitude A_{loc} of the Fourier spectrum for the frequency f, and only accept the extracted frequency if both amplitudes agree within a specified

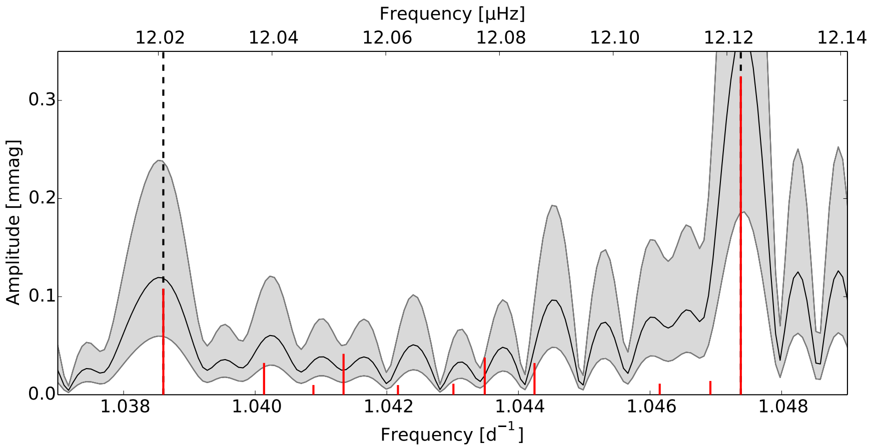

Figure 2.2: The Fourier transform (full black curve) of a simulated light curve. Using the presented comparison criterion, the frequency extraction is aborted when the amplitude of an extracted frequency (full red vertical lines) does not agree with the original Fourier transform within a specified margin (grey area). The accepted frequencies (for the specified margin) are marked with dashed lines.

margin (see Figure 2.2):

$$\alpha \leq \frac{A_f}{A_{loc}} \leq \frac{1}{\alpha}. \tag{2.1}$$

Here α is given a reasonable value, which we found to be 0.5 for most stars. When the considered frequency peak does not fulfil this requirement, the frequency extraction is aborted. This means that, even if one of the following frequencies would fulfil the requirement again, it is still not accepted, because it is preceded in the prewhitening by a frequency that failed this test. While it is likely that, with this criterion, the residuals of the light curve will still contain a lot of signal, the modulation of this signal by the preceding prewhitening may no longer be negligible. By taking $\alpha = 0.5$, we are able to keep the number of detected false frequencies down to a minimum. For most γ Dor stars the extracted frequencies are a good starting point for modelling, in the sense that they are sufficient to look for part of the period spacing series expected to be present in the data.

Detecting non-uniform period spacings can be rather complicated, especially if two different series with a different average spacing overlap. However, there are several aspects which may facilitate the detection. It is for example well-known that the visibility of a stellar oscillation mode depends on its degree l and order m, and on the inclination angle and rotational velocity of the star (e.g. Chadid et al. 2001). As a result, many of the visible oscillation modes are likely to have similar values for l and m while differing in radial order. As we already noted in Sections 1.2.1 and 1.2.2, we expect prograde sectoral modes with low l values to be the most easily visible (Townsend 2003a). In addition, early F- to late A-type main-sequence stars are typically moderate to fast rotators. While this means that the rotational splitting of oscillation frequencies will be asymmetric and thus difficult to detect (especially considering the high density of the frequency spectra), it also entails that when the star is sufficiently fast rotating, its frequency splitting will be larger than the frequency region where the pulsation frequencies of similar slowly rotating pulsators would be located. As a result, we can distinguish different groups of frequencies within the frequency spectra. Within each group, most frequencies have the same l and m values, but these differ for different groups. Finally, many γ Dor pulsators have strongly asymmetric light curves, which is indicative of non-linear effects (e.g. Balona et al. 2011; Kurtz et al. 2015). As a result, several of the peaks we detect in the Fourier spectrum, correspond to combinations of oscillation frequencies rather than frequencies of individual pulsations (e.g. Balona 2012; Pápics 2012; Bowman et al. 2016; Murphy et al. 2016; Pápics et al. 2017). We exclude these combination frequencies from the period spacing search.

One of the most efficient ways to detect period spacings for a typical γ Dor star is to order the accepted oscillation periods and determine the spacings between them. It is likely that at least some adjacent accepted frequency peaks have the same values for l and m, making them part of the same (possibly non-uniform) period spacing series. When, on the other hand, the studied γ Dor star is a slow rotator, the rotational splitting will likely be too small for this detection method to work. However, in this case we can look for spacings and/or splittings using other traditional methods, such as échelle diagrams (e.g. Grec et al. 1983; Mosser et al. 2013; Bedding et al. 2015; Keen et al. 2015; Schmid et al. 2015) because the spacing pattern will be more regular. Échelle diagrams are not useful for stars rotating such that their rotational frequency shifts no longer result in quasi-equidistant spacing patterns. Because of the expected non-uniform nature of the period spacings, detected spacing patterns should always be evaluated visually by the researcher.

After looking for period spacings, we iterate over the algorithm: we go back to the frequency extraction, but choose a different value for α. By iteratively choosing smaller values (e.g. from 0.4 to 0.05) we can extract more frequencies and systematically look for additional frequency peaks which match the found period spacing series. If no period spacings were detected (yet), it is possible that choosing a smaller value for α will help, though one must keep in mind that more noise peaks will be included as well, such that the probability of detecting spurious period spacings will be higher. Going back to Figure 2.1, we show the frequencies extracted with this proposed criterion compared to the classical signal-to-noise criterion for a simulated light curve. While the remaining low-amplitude input frequencies are also extracted with the classical criterion, the number of additional false frequencies is too high to allow for a reliable selection of the input frequencies.

A summary of our method is shown schematically in Figure 2.3. The different steps of the method are further illustrated by applications on simulated data in the next Section. The current version of our code does not allow us to formally identify l and m, with the exception of stars for which we detect rotational multiplets. This can only be achieved from comparing the detected series with theoretical model predictions, as will be done in Chapter 4.

2.3 Applications

2.3.1 Simulations

We evaluate our method on simulated data with two goals. First, we test that computing the differences between subsequent oscillation periods is a robust method for the detection of spacings for moderate to fast rotators. For slowly rotating stars, on the other hand, the use of échelle diagrams is more advantageous. Secondly, we show that the slope in the period spacing pattern induced by the rotation for prograde or retrograde modes is clearly detectable. For these tests, simulations simplified with respect to the complex physics of γ Dor stars are sufficient. We therefore generated normalised light curves mimicking the results obtained by Miglio et al. (2008) and Bouabid et al. (2013):

$$F(t) \quad = \quad A\left(\left[1+\sum_i a_i \sin\left(2\pi f_i t+\phi_i\right)\right]^{2.2}-1\right)+\sigma. \qquad (2.2)$$

Here, f_i and ϕ_i are the frequency and phase of a particular oscillation mode i, A is the overall amplitude of the light curve, a_i scales the amplitude of the pulsation mode i, and σ represents a level of Gaussian white noise, similar to what is observed in the *Kepler* data. The value for A is chosen arbitrarily, but typically on the order of a few mmag, so that the scale of the variability in the simulated light curve is representative for those of real γ Dor type observations. The power 2.2 was used to simulate the asymmetry which is often seen in γ Dor light curves (see also Balona et al. 2011). A typical set of frequencies f_i was computed with GYRE for the MESA model shown earlier in Figure 1.5 with $X_c = 0.5$. These calculations were done for both dipole and quadrupole modes taking into account the frequency shifts caused by rotation ($f_{\mathrm{rot}} = 0.8\,\mathrm{d}^{-1}$) with

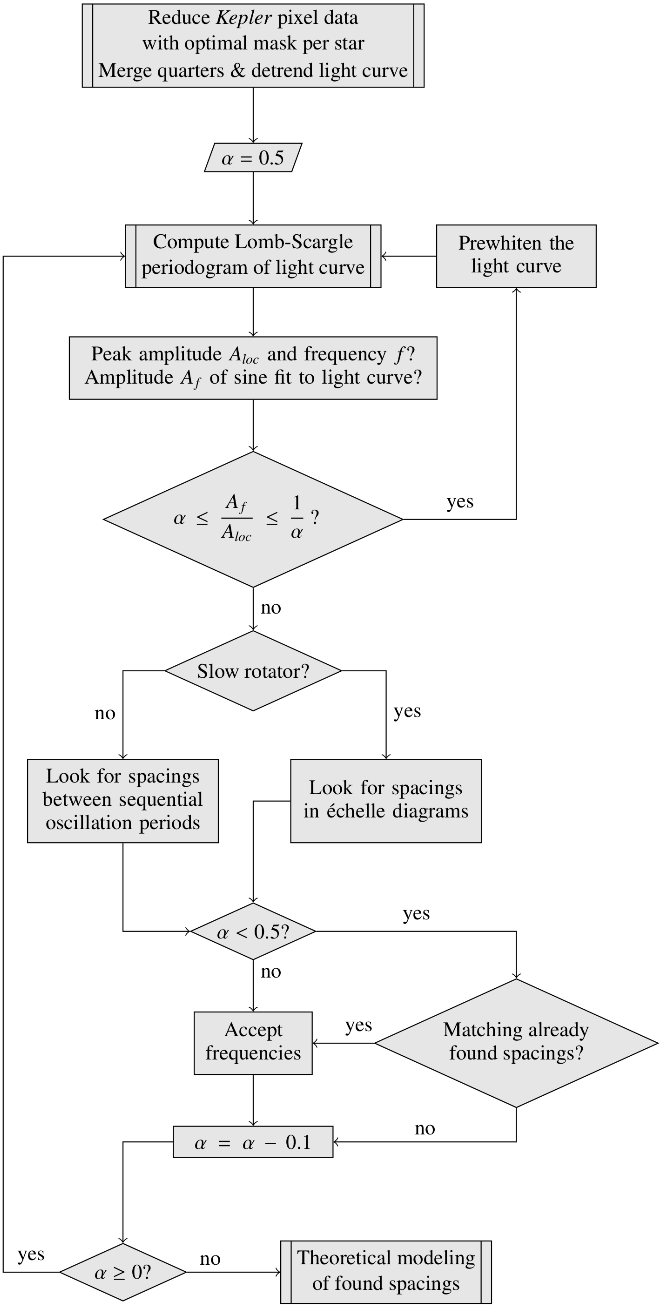

Figure 2.3: Schematic summary of the methodology described in Section 2.2. While the values of α provided here work well for most γ Dor stars, they can of course be customised for individual stars.

the traditional approximation. The full list of frequencies is available in the appendix in Table B.1. The light curve was simulated using the time stamps of real *Kepler* observations and converted to magnitude scale.

We extracted the oscillation frequencies from the simulated data using the prewhitening method as described earlier (Degroote et al. 2009) in combination with the comparison criterion defined in Section 2.2, using $\alpha = 0.5$. The errors of the frequency values were determined using the method by Schwarzenberg-Czerny (2003), which is based on the statistical errors resulting from a non-linear least-squares fit corrected for the correlated nature of the data. Since we included the effects of a moderate rotation velocity in this simulation, we searched for period spacing patterns by ordering the oscillation periods monotonically and by computing the differences between subsequent values. The results are shown in Figure 2.4, together with the spacing patterns corresponding to the input frequencies. Since we cut off the iterative prewhitening relatively quickly, we only detected a fraction of the input frequencies. This is also illustrated in Figure 2.5, where we show the fraction of detected input frequencies with respect to the number of prewhitened frequencies as well as the relative increase in the number of extracted noise and combination frequencies. By using a comparison criterion with $\alpha = 0.5$, the number of such detected false frequencies is small. Indeed, close inspection of the results for the simulated light curve revealed that all of the additional extracted frequencies at this point in the prewhitening are actually combination frequencies. Two of these were located within the period spacing series of the sectoral quadrupole modes, triggering the stop criterion. As such, the algorithm allows for the detection of period spacing patterns at a high level of confidence.

In a second step we iteratively decreased the value of α from 0.4 to 0.1. This allowed us to extract more oscillation frequencies, which we could match with the period spacings that were already detected. As shown in Figure 2.4, this allowed us to extend the period spacing series without including noise peaks.

As we already mentioned, period spacing patterns corresponding to different l and m values are more likely to overlap for slowly rotating stars. In this case, the use of échelle diagrams is more robust for the detection of period spacings. This is illustrated in Figure 2.6, where we show overlapping prograde and retrograde dipole pulsation series, computed for the same theoretical model as the one used throughout Section 2.3.1, but with a much smaller rotation rate f_{rot} of $0.08\,\mathrm{d}^{-1}$. When all the pulsation periods are naively assumed to belong to the same series, i.e., have the same values for l and m, the resulting period spacing pattern is a mess (as can be seen in the bottom left panel of Figure 2.6). However, in the échelle diagram both series are clearly distinguishable.

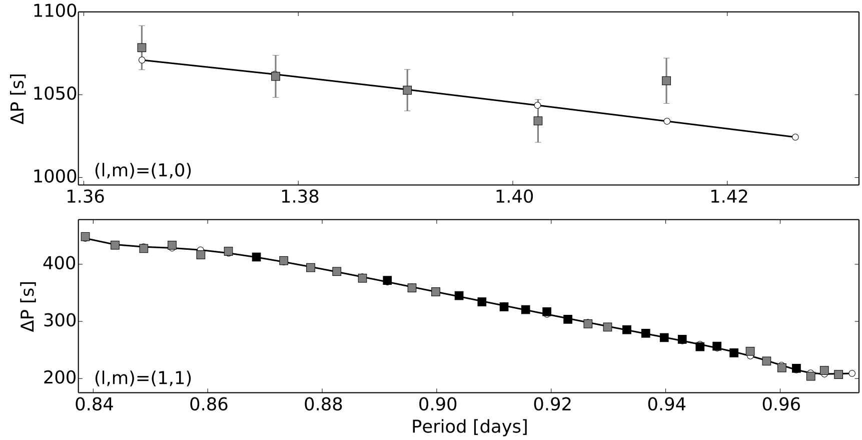

Figure 2.4: The period spacings corresponding to several input frequencies in a simulated data set. The found spacings with $\alpha = 0.5$ are indicated by black squares, while spacings found for other values of α (from 0.4 to 0.1) are represented by grey squares. The original input period spacings are indicated by white dots. This is shown for both zonal (top) and prograde (bottom) dipole modes.

2.3.2 A well-studied *Kepler* star: KIC 11145123

We applied our method to the hybrid δ Sct / γ Dor pulsator KIC 11145123, which was studied by Kurtz et al. (2014). The authors showed the star to be a slow rotator ($P_{\rm rot} \sim 100\,$d), exhibiting almost-uniform period spacings. A large number of rotationally split multiplets were clearly visible in the frequency spectrum, making this star a good test case for our approach.

For this star there are about four years (Q0-Q17) of *Kepler* data available. Given that the light curves obtained with the standard extraction algorithm and provided by the MAST (Mikulski Archive for Space Telescopes) were shown to complicate the analyses for g-mode pulators and lead to a fake instrumental low frequencies (Debosscher et al. 2013; Tkachenko et al. 2013a), we applied the light curve extraction code developed by Steven Bloemen (one of the co-authors of the original publication) to the pixel data. The code is based on the use of customised masks, which allows us to include the signal from more pixels, thereby reducing the influence of instrumental trends. The light curves of each individual quarter were subsequently detrended by changing the scale of the extracted light curves to magnitude and subtracting a 1^{st}- or 2^{nd}-order polynomial, and concatenated. The outliers of the light curves were removed

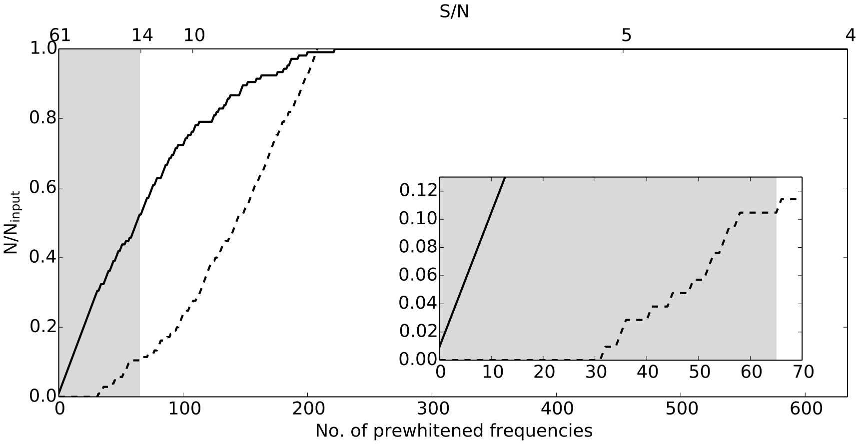

Figure 2.5: Fraction of extracted to input frequencies as a function of the number of prewhitened frequencies (full black line). The dashed grey line indicates the relative number of detected combination and noise frequencies as a function of the number of prewhitened frequencies when ignoring the comparison criterion. The upper axis provides the signal-to-noise ratio of the last extracted frequency. The shaded area indicates the number of accepted frequencies when adopting the comparison criterion with $\alpha = 0.5$, for which the number of extracted noise peaks remains modest, and the majority of the frequencies indicated by the dashed line are combination frequencies.

manually.

The pulsation frequencies of KIC 11145123 were extracted in the same way as for the simulated data, i.e. we performed prewhitening in combination with our comparison criterion described in Section 2.2. Since this star is such a slow rotator, we used the obtained frequency values in combination with échelle diagrams to look for period spacings and rotational splitting. As we can see in Figure 2.7, we clearly detected part of the spacings and multiplets present in the data. Based on these initial results, we extracted and accepted additional frequencies, allowing us to extend the detected non-uniform period spacing series shown in Figure 2.7.

We were able to detect the same g-mode frequencies series as found by Kurtz et al. (2014), who used a classical prewhitening analysis without a stop criterion and considered only the 61 frequencies with the highest amplitude for their analysis. We could also detect most of the p-mode multiplets reported by these authors, as illustrated in Figure 2.8. This is promising, given that our method

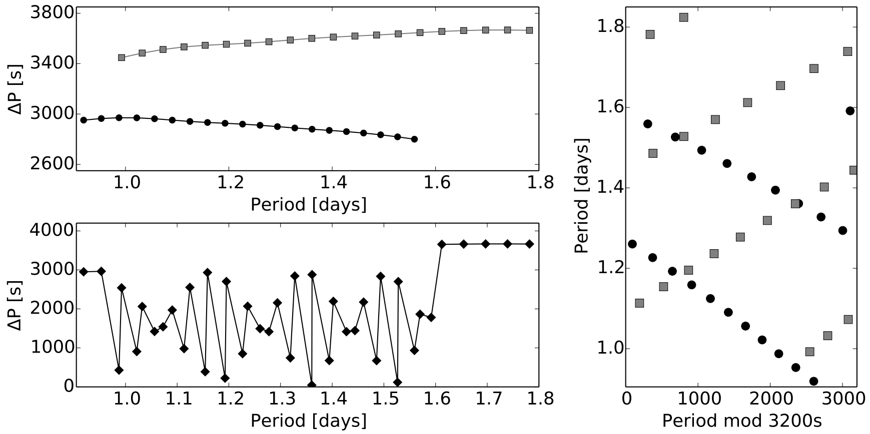

Figure 2.6: *Top left:* Period spacing patterns for simulated prograde (black dots) and retrograde (grey squares) dipole modes. The theoretical model used in this simulation is the same as the one used throughout Section 2.3.1, but with a much smaller rotation rate $f_{\rm rot}$ of $0.08\,{\rm d}^{-1}$. *Bottom left:* the period spacing pattern computed for the same pulsation periods, but assuming they are all part of the same series, i.e., have the same values for l and m. *Right:* the period échelle diagram for both simulated dipole mode series.

was developed with the sole aim to detect non-uniform period spacing patterns of g-modes. We also detected two (dipole) p-mode doublets, i.e. multiplets without a central peak, which were not listed by Kurtz et al. (2014) (Figure 2.8). On the other hand, we did not detect one of the p-mode triplets found by Kurtz et al. (2014) in the sense that one of the frequencies listed by the authors ($f = 23.516\,{\rm d}^{-1}$) was not extracted by us, independently of the value for α. Interestingly, the non-extracted frequency is part of one of the two multiplets which Kurtz et al. (2014) could not identify as modes with $l \leq 2$ for their best stellar model, which has a mass of $1.46\,{\rm M}_{\odot}$. Instead, these were listed as $l = 6$. We also found an additional frequency between the incomplete triplet and a quintuplet, as shown in the bottom plot in Figure 2.8. The inclusion of this additional frequency leads to the detection of a larger multiplet. The extracted frequencies and splittings we found in addition to those reported by Kurtz et al. (2014) are listed in Table 2.1 and can be used in future modelling of this star.

The application of our method to the light curve of KIC 11145123 has allowed us to accurately detect both the period spacing patterns and the rotational frequency splitting present in the data. We also found that the presented comparison criterion might be suitable for space-based observations of other

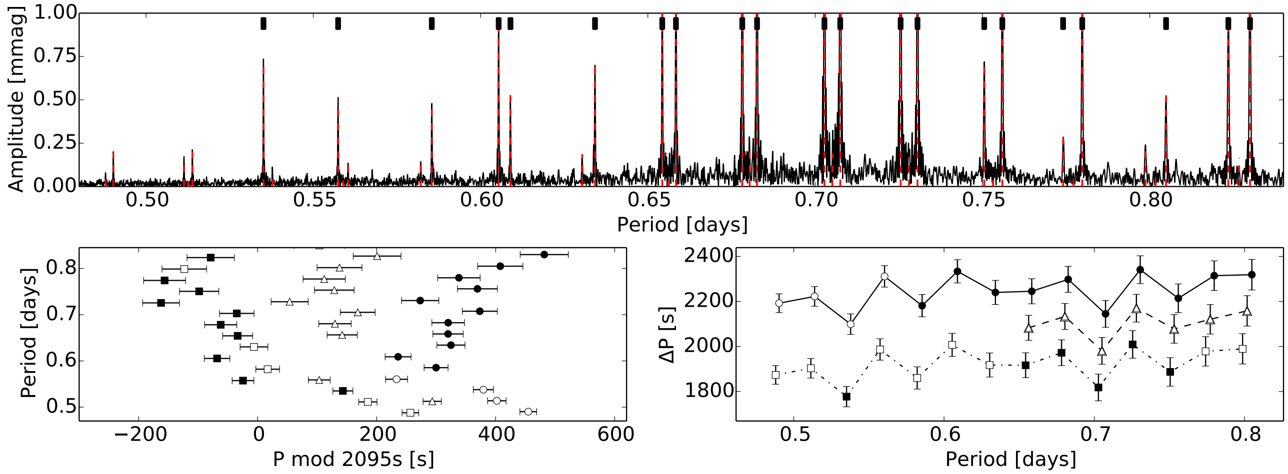

Figure 2.7: *Top:* A close-up of the Fourier transform of KIC 11145123 (black) and the accepted oscillation periods (dashed red), showing the detected period spacings. The thick black markers indicate the frequencies that were extracted for $\alpha = 0.5$. The amplitudes of some of the modes are $\sim$3 mmag, but the Figure is zoomed in for clarity. *Bottom left:* A close-up of the échelle diagram showing the detected prograde (squares), retrograde (circles) and zonal (triangles) dipole modes. The frequencies that were extracted with $\alpha = 0.5$ are marked in black. *Bottom right:* The detected period spacings. For clarity, we shifted the spacings of the prograde and retrograde modes 150 s downwards and upwards, respectively.

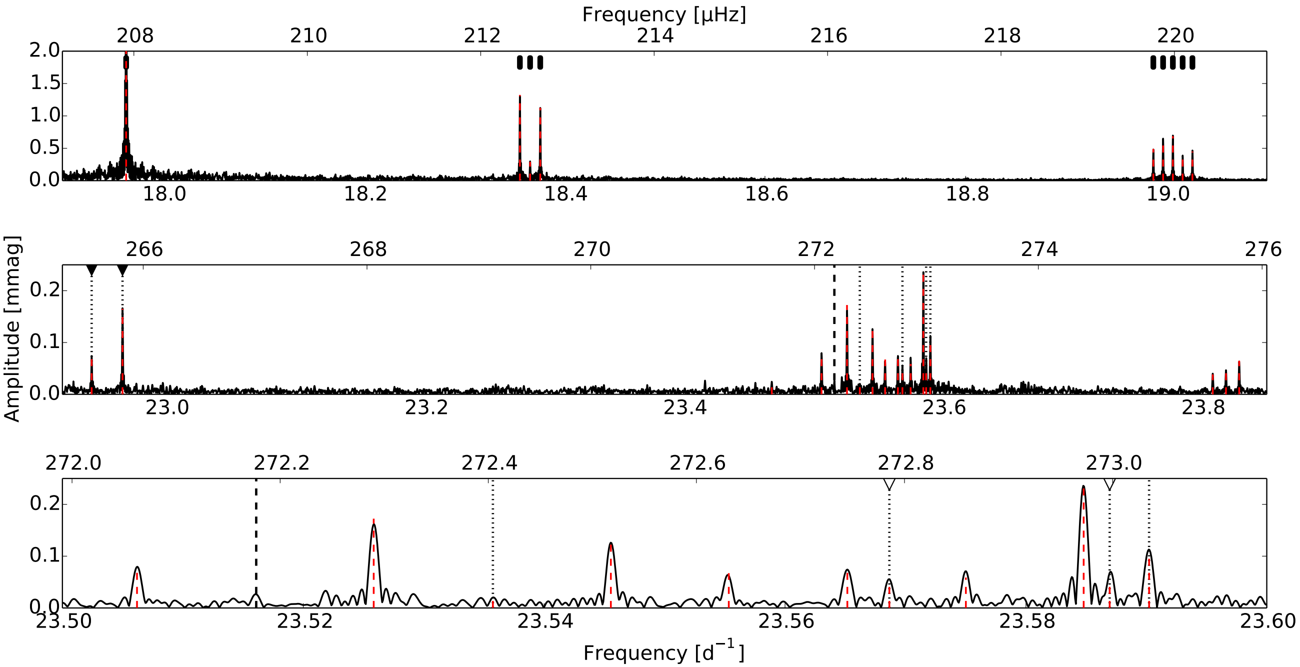

Figure 2.8: Sections of the p-mode frequency spectrum of KIC 11145123 (black), with the detected frequencies marked by a dashed red line. Frequencies found for $\alpha = 0.5$ are marked with thick black markers, whereas the one found by Kurtz et al. (2014) but not by us is indicated by a dashed line. The dotted lines indicate frequencies that we extracted, but Kurtz et al. (2014) did not. The triangles (black and white) indicate possible dipole doublets. The upper panel is zoomed in for clarity (the oscillation mode at 17.96 d^{-1} has an amplitude $\sim$7.2 mmag).

types of variable stars, when combined with an adapted spacing pattern detection algorithm. However, this PhD thesis is restricted to γ Dor stars.

2.3.3 Four γ Dor stars in the *Kepler* field

Subsequently, we applied the proposed method to four of the γ Dor pulsators from the sample presented by Tkachenko et al. (2013a), for which we have both high-resolution spectroscopy and *Kepler* photometry at our disposal. This analysis was an important test to find out if our developed methodology was suitable to embark upon a much larger long-term study of the entire sample in Tkachenko et al. (2013a). For each of those four stars we have collected high-resolution spectra, which were obtained with the HERMES spectrograph (cf. Section 1.3.2). These spectra were reduced with the dedicated HERMES pipeline, and subsequently normalised in two steps by fitting a cubic and linear spline through the flux continuum respectively, as described by Pápics et al. (2012). Outliers in the spectra resulting from cosmic hits were identified by comparing the local flux with the median value in the surrounding spectral region (of 40 pixels). If the difference exceeded 5σ, where σ is determined as the local signal-to-noise (S/N) ratio in the spectrum, the flux point was replaced by the median value. We applied the improved least-squares deconvolution (LSD) algorithm, as described by Tkachenko et al. (2013c), to the individual spectra of each star using a line mask with typical parameter values for a γ Dor star ($T_{\mathrm{eff}} = 7000\,\mathrm{K}$; $\log g = 4.0$; $[M/H] = 0.0$; $\zeta = 2\,\mathrm{km\,s^{-1}}$). The line mask was computed with the spectrum synthesis synthV code (Tsymbal 1996), which makes use of a spectral line list (obtained from the VALD database, Kupka et al. (1999)) and a predefined grid of atmospheric models computed with the LLmodels code (Shulyak et al. 2004). This code allows us to calculate LTE plane-parallel stellar model atmospheres for early and intermediate type of stars, whereby line contributions to the opacity are taken into account individually rather than via a statistical approach. This resulted in high S/N average line profiles, which were then checked for global Doppler shifts and the presence of a signal from a possible companion. No such signatures were present in these data, which confirmed that the four stars are single objects (see Table 2.2). We computed an average spectrum and analysed it to determine the fundamental and atmospheric parameters by means of the spectrum synthesis method implemented in the Grid Search in Stellar Parameters (GSSP) code (Lehmann et al. 2013; Tkachenko et al. 2013b; Tkachenko 2015). The values of the temperature T_{eff}, surface gravity $\log g$, metallicity $[M/H]$, microturbulence ζ and rotational velocity $v \sin i$ are determined from a χ^2-minimization for the observed spectra with respect to synthetic spectra within an arbitrary large wavelength range. The synthetic spectra are computed for different values of

Table 2.1: A least-squares fit for the additional p-mode frequencies ($*$) which we found compared to the analysis by Kurtz et al. (2014), and for the other frequencies which are part of the same multiplets. Δf is the spacing between the given frequency and the preceding one. The provided errors are the formal error margins from the least-squares fit.

	Frequency [d^{-1}]	Amplitude [mmag]	Phase [2π]	Δf [d^{-1}]	Remarks
$*$	22.94259 (0.00003)	0.074 (0.006)	-0.30 (0.08)	-	-
$*$	22.96643 (0.00002)	0.165 (0.008)	0.46 (0.05)	0.02383 (0.00004)	$\Delta f/2 = 0.01192$ (0.00002)
	23.50619 (0.00003)	0.068 (0.006)	-0.29 (0.09)	-	-
	23.52585 (0.00002)	0.172 (0.008)	-0.43 (0.04)	0.01965 (0.00004)	$\Delta f/2 = 0.00983$ (0.00002)
$*$	23.53574 (0.00007)	0.027 (0.005)	0.47 (0.18)	0.00990 (0.00007)	-
	23.54554 (0.00002)	0.128 (0.007)	0.37 (0.05)	0.00980 (0.00007)	-
	23.55533 (0.00003)	0.067 (0.006)	0.46 (0.09)	0.00979 (0.00004)	-
	23.56517 (0.00003)	0.079 (0.006)	-0.07 (0.08)	0.00984 (0.00004)	-
	23.57502 (0.00004)	0.059 (0.006)	0.18 (0.10)	0.00984 (0.00005)	-
	23.58480 (0.00001)	0.239 (0.009)	-0.16 (0.04)	0.00978 (0.00004)	-
$*$	23.56866 (0.00005)	0.045 (0.005)	0.08 (0.12)	-	-
$*$	23.58695 (0.00004)	0.046 (0.006)	-0.39 (0.12)	0.01829 (0.00006)	$\Delta f/2 = 0.00915$ (0.00003)
$*$	23.59023 (0.00002)	0.109 (0.007)	-0.06 (0.06)	-	-

Table 2.2: Atmospheric parameter values obtained for the four γ Dor stars analysed in this study. The provided errors are the 1-σ values obtained from the chi-square statistics.

KIC	T_{eff} $[K]$	log g [dex]	$[M/H]$ [dex]	$v \sin i$ $[\mathrm{km\,s^{-1}}]$	ξ $[\mathrm{km\,s^{-1}}]$
4749989	7320 (55)	4.24 (0.21)	0.13 (0.06)	204 (8)	3.33 (0.22)
6678174	7105 (90)	3.77 (0.33)	0.01 (0.10)	27.4 (1.6)	2.3 (0.4)
8611423	7135 (105)	4.21 (0.30)	0.10 (0.08)	20.7 (1.5)	1.86 (0.34)
11721304	7160 (82)	4.13 (0.28)	0.08 (0.08)	28.3 (1.5)	2.15 (0.33)

the listed parameters using a combination of the synthV code (Tsymbal 1996), the LLmodels code (Shulyak et al. 2004) and information obtained from the VALD database (Kupka et al. 1999), i.e. similar to how the LSD line mask was computed. In this study we took the spectral range between 4700 Å and 5800 Å, which includes the H_β-line. For a typical γ Dor star, the Balmer lines are mostly sensitive to T_{eff} (e.g. Gray 1992), thus putting strong constraints on this parameter. In addition, the advantages of using the average spectra are that (i) they have higher signal-to-noise ratios than the individual spectra, and (ii) line profile deformations due to the pulsations are largely smoothed out. The obtained values are listed in Table 2.2 and place the four stars in the γ Dor strip, as provided by, e.g., Bouabid et al. (2013).

For KIC 6778174 and KIC 8611423 about two years of photometric observations (Q0-Q1, Q10-Q17) were obtained with *Kepler*, while for KIC 4749989 (Q0-Q5, Q7-Q9, Q11-Q13, Q15-Q17) and KIC 11721304 (Q0-Q17) about three and four years of observations are available, respectively. The pixel data were extracted, reduced and analysed in the same way as the data for KIC 11145123, as described in Section 2.3.2, and unless mentioned otherwise, α was taken to be 0.5. Using the obtained frequency values to compute the period spacing, we discuss the patterns for each star individually.

KIC 11721304

For KIC 11721304 we have detected a period spacing pattern with a clear slope, as shown in Figure 2.9. The average period spacing (1200 s) is small compared to typical values for a non-rotating γ Dor star. These are of the order of 3000 s ($l = 1$) to 2000 s ($l = 2$), which implies that the pulsations in the detected series

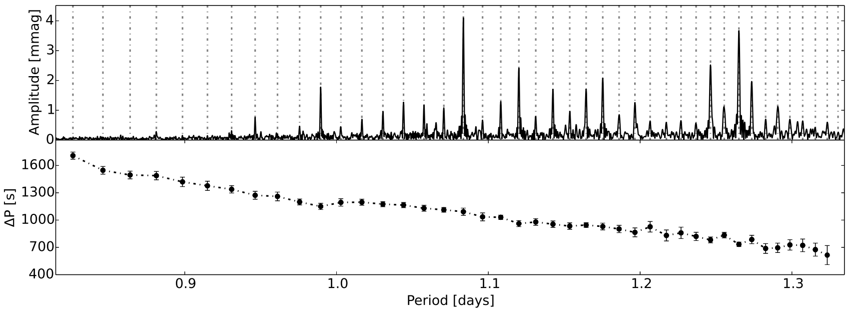

Figure 2.9: *Top:* A close-up of part of the Fourier spectrum of KIC 11721304 (black). All the marked frequencies are accepted following the criterion described in Section 2.2. *Bottom:* The period spacing as computed from the accepted frequencies. The black markers and grey dash-dotted lines indicate the frequencies for which we find a smooth spacing pattern.

are prograde modes. The downward trend of the spacing pattern supports this interpretation.

In addition to the pulsation frequencies belonging to this spacing pattern, more frequencies were detected in the same range. These likely correspond with modes of different wavenumbers l and m, but firm conclusions about this requires detailed future modelling, taking into account various mixing processes.

We mentioned in Section 2.2 that many γ Dor stars have asymmetric light curves and that this leads to the appearance of linear combinations of the frequencies in their Fourier spectra. In general, we have to make sure that we did not include any of these combination frequencies in the period spacing series. This is not an issue in the case of KIC 11721304 because the combination frequencies are located sufficiently far from the detected period spacing series in the frequency domain (Figure 2.10).

KIC 6678174

In the case of KIC 6678174, there is also a clear detection of a period spacing series, though the length of the found series is relatively short (Figure 2.11). Similar to the period spacing series we detected for KIC 11721304, there are no apparent dips present in the pattern. This seems to indicate that either the star is close to the ZAMS, close to the TAMS, or that there is a reasonable

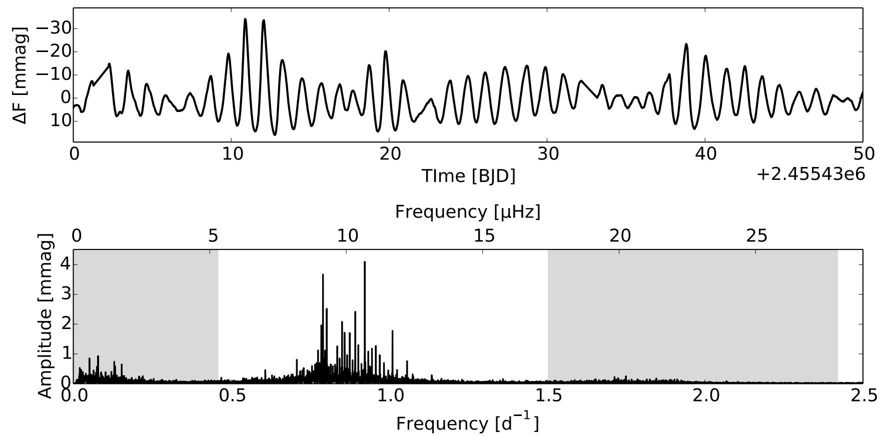

Figure 2.10: *Top:* A small part of the light curve of KIC 11721304. *Bottom:* The Fourier spectrum (black) of KIC 11721304. The grey areas indicate the locations of the linear combinations of the oscillation frequencies, which arise because of the asymmetry of the light curve of the star in the top panel.

degree of extra mixing present inside the star. An in-depth individual study of this star is required to formulate a firm conclusion.

KIC 4749989 and KIC 8611423

For KIC 4749989 and KIC 8611423, reliable period spacing patterns could not be detected.

Based on the atmospheric parameter values provided in Table 2.2, we conclude that KIC 4749989 is a fast rotator. Because low-frequency pulsations are equatorially confined at higher rotation rates (Townsend 2003a,b), they typically have smaller observable amplitudes than in a more slowly rotating star. Oscillations with intrinsically small amplitudes may therefore no longer be detectable, and the uncertainties on the observed pulsation frequencies are larger. As a result, there are too few well-constrained pulsation frequencies to allow a firm detection of a period spacing pattern.

For KIC 8611423, on the other hand, a very large number of frequencies is detected. As a consequence, it is difficult to establish which of these, if any, are intrinsic pulsation frequencies with the same (l,m) values and form a period spacing pattern. In this case, candidate series which are consistent with the

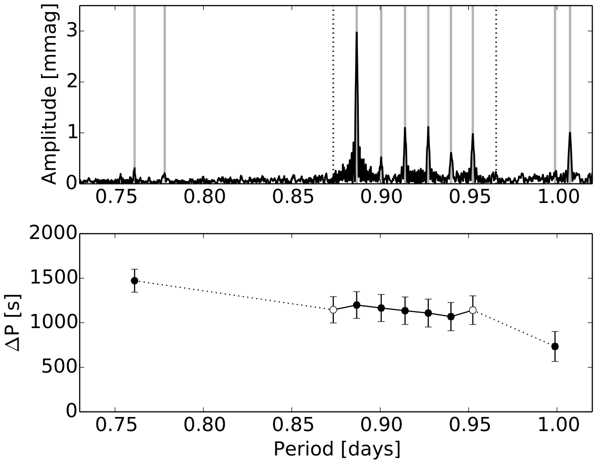

Figure 2.11: *Top:* A close-up of the Fourier transform of the light curve of KIC 6678174 (black) and the accepted frequencies in the region where the detected period spacing series is located. The frequencies which were accepted for $\alpha = 0.5$ are marked with full grey lines, and the ones for which $\alpha < 0.5$ are marked with dotted lines. *Bottom:* The period spacing as computed for the (accepted) frequencies shown in the top. The white markers indicate the spacings for frequencies accepted for $\alpha < 0.5$, while the dotted lines indicate the regions where there are likely frequencies missing.

star's $v \sin i$ value ($20.7 \pm 1.5\,\mathrm{km\,s^{-1}}$) may be detected, but cannot be confirmed with certainty.

2.4 Discussion and conclusions

In this proof-of-concept we have developed a method to detect reliable period spacings in the complex frequency spectra of γ Dor stars. The various steps are as follows:

1. Extract the frequencies from the light curve using a prewhitening method.
2. Adopt a conservative stop criterion for the prewhitening procedure; we propose to use what we termed the comparison criterion given in Eq. (2.1), where $\alpha = 0.5$ was found to be a suitable value for γ Dor stars for the first iteration.

3. Make a distinction between moderate to fast versus slow rotators when searching for the period spacing patterns. For the former, order the extracted oscillation periods monotonically and compute the differences between subsequent values to search for period spacings. For slow rotators, échelle diagrams were found to be the most robust method to search for period spacing patterns.
4. Iterate over the method while lowering the value for α, allowing to extract more frequencies from the data. If period spacings were already detected, use these as a guide to check which additional frequency values are reliable and to avoid the influence of frequencies due to noise. If no period spacings were detected yet, the extraction of additional frequency peaks at lower α could lead to a detection, though it is important to keep in mind that the detection of false frequencies due to noise also becomes more likely.

In the present initial study, we have taken a closer look at the results for KIC 11145123, a hybrid pulsator presented by Kurtz et al. (2014), and at four single γ Dor stars from the sample presented by Tkachenko et al. (2013a). The purpose of analysing these five stars was to determine if the results of our method justify an in-depth analysis of the entire sample. From the application of our method on KIC 11145123 we deduced that the method excels in the exclusion of noise peaks. Because of this star's slow rotation, we detected the frequency splittings and the period spacings using échelle diagrams. For two of the other four stars we studied, KIC 6678174 and KIC 11721304, we were able to detect period spacings that are completely in line with theoretical expectations as presented in Miglio et al. (2008) and Bouabid et al. (2013). The analysis of KIC 11721304 was particularly successful, resulting in a series of 35 pulsation periods, hinting towards strong mixing processes. The frequency analysis of the two additional stars did not lead to firm conclusions.

It is important to keep in mind that the method cannot be automated and it remains necessary for the user to check carefully any detected period spacing pattern. As such, the user should be familiar with the basic aspects of the theoretical expectations for non-uniform period spacings. Detected spacings should then be verified and interpreted in terms of interior physics using extensive grids of theoretical pulsation properties from a combination of stellar evolution and pulsation codes. Such modelling will also allow us to assign values to the pulsation parameters l and m, as will be shown in the following chapters.

The final conclusion of our proof-of-concept study is that the capability of our newly developed method to search period spacing patterns of gravity-mode pulsators is such that it justifies full exploitation of such diagnostics for the entire γ Dor sample in Tkachenko et al. (2013a). Indeed, even if we can find period spacing patterns in only half of the sample stars, it will be a major step forward given that such diagnostics is available for only a handful of stars while the identification of high-order g-modes holds great potential for the probing of near-core physics of intermediate-mass stars, as discussed in Chapter 1.

Chapter 3

A *Kepler* Guest Observer γ Dor sample selection and its characterisation

This chapter was originally published as

Gravity-mode period spacings as seismic diagnostic for a sample of γ Doradus stars from Kepler space photometry and high-resolution ground-based spectroscopy

T. Van Reeth, A. Tkachenko, C. Aerts, P. I. Pápics, S. A. Triana, K. Zwintz, P. Degroote, J. Debosscher, S. Bloemen, V. S. Schmid, K. De Smedt, Y. Fremat, A. S. Fuentes, W. Homan, M. Hrudkova, R. Karjalainen, R. Lombaert, P. Nemeth, R. Østensen, G. Van De Steene, J. Vos, G. Raskin, H. Van Winckel

The Astrophysical Journal Supplement Series, 218 (2), 27, 32 pp. (2015)

Author contributions

Timothy Van Reeth did the spectroscopic analysis with the GSSP code under the guidance of Andrew Tkachenko, and Conny Aerts suggested the multivariate correlation analysis. Andrew Tkachenko, Conny Aerts, Peter Pápics, Santiago Triana and Konstanze Zwintz have participated in many helpful discussions on the nature and observational properties of γ Dor stars. Pieter Degroote, Jonas Debosscher and Steven Bloemen provided some of the codes that were used in this work, specifically for the extraction and data reduction of the light curves from the raw *Kepler* pixel data, and for the frequency extraction from the light curves. The other co-authors were responsible for many of the spectroscopic observations at the Mercator telescope. Timothy Van Reeth did the data reduction, detection and analysis of the binary systems, and detection of the period spacing patterns. He also selected the parameters to be used in the multivariate correlation and did the analysis. Timothy Van Reeth wrote the draft text; Andrew Tkachenko and Conny Aerts improved the text prior to submission.

Abstract

γ Dor stars are gravity-mode pulsators of spectral type A or F. Such modes probe the deep stellar interior, offering a detailed fingerprint of their structure. Four-year high-precision space-based *Kepler* photometry of γ Dor stars has become available, allowing us to study these stars with unprecedented detail. We selected, analysed, and characterized a sample of 67 γ Dor stars for which we have *Kepler* observations available. For all the targets in the sample we assembled high-resolution spectroscopy to confirm their F-type nature. We found thirteen multiple star systems, among which four single-lined binaries, four double-lined binaries, two triple systems and three objects with composite spectra but no detected radial velocity variations. We estimated the orbital parameters whenever possible. For the single stars and the single-lined binaries, fundamental parameter values were determined from spectroscopy. We searched for period spacing patterns in the photometric data and identified this diagnostic for 50 of the stars in the sample, 46 of which are single stars or single-lined binaries. We found a strong correlation between the spectroscopic $v \sin i$ and the period spacing values, confirming the influence of rotation on γ Dor-type pulsations as predicted by theory. We also found relations between the dominant g-mode frequency, the longest pulsation period detected in series of prograde modes, $v \sin i$, and log $T_{\rm eff}$.

3.1 Introduction

Tkachenko et al. (2013a) presented a sample of 69 γ Dor candidates in the *Kepler* field of view. The selection of these stars was based on the automated supervised machine-learning classification method applied by Debosscher et al. (2011) to all *Kepler* Q1 light curves, i.e. observations of about 150 000 stars. This statistical classification is based on the amplitudes, frequencies and relative phases of the three dominant pulsations, and their harmonics. While this type of analysis is invaluable when working with such a rich database, some types of variability cannot be differentiated based on a superficial analysis of white-light photometry, e.g., the variability of γ Dor stars and SPB stars. Tkachenko et al. (2013a) therefore carried out a complementary selection based on 2MASS colour information, which allowed them to determine the approximate location of the stars in the Hertzsprung-Russell diagram and select the best candidates. The authors further restricted the final selection of γ Dor candidates to the brightest stars, to make sure ground-based spectroscopic observations were possible for all sample targets. We have also added another γ Dor star, KIC 5000454, to this sample. This target was originally classified as an SPB star candidate, but was identified as a γ Dor star based on spectroscopic observations. Subsequently, further photometric observations of these stars were taken with the *Kepler* space telescope in Guest Observer programs.

In this chapter we study this sample of 70 γ Dor candidates in full depth. We have collected all available high-precision *Kepler* photometry of all stars and we gathered high-resolution spectroscopy to make a full observational characterization of the sample. In Section 3.2, we discuss the available data and the applied data reduction methods. In Section 3.3, we evaluate the γ Dor-type nature of the targets and check for binarity. We also list the fundamental parameter values derived from the spectroscopy. We then look for period spacing patterns in the photometric data in Section 3.4 using the method presented in Chapter 2 and check for correlations with the spectroscopic parameter values (Section 3.5), before coming to our conclusions (Section 3.6).

3.2 Observations and data reduction

Tkachenko et al. (2013a) had already obtained spectra for 36 stars in the sample with the HERMES spectrograph (cf. Section 1.3.2). Several more spectra were taken afterwards, and we applied for observation time in 2014 at the same telescope. For each star in our sample we collected high-resolution spectra that were taken between May and August in 2011, 2013, and 2014. The total number of spectra and observation times are listed per star in the Appendix in Table C.1.

The obtained spectra were reduced with the HERMES pipeline (release 5, i.e., the most recent version at the time of the original publication) and subsequently normalised following the method by Pápics et al. (2012), as explained in Section 2.3.3.

In addition to the spectroscopic observations, all the stars in our sample have been observed by the *Kepler* mission with long cadence (i.e. with an integration time of 29.43 minutes; cf. Section 1.3.1). For the majority of stars, data are available for all eighteen quarters (Q0-Q17), while the shortest obtained light curves cover eight quarters. The available quarters are also listed for each star in Table C.1.

Because the standard light curve extraction algorithm, provided by the Mikulski Archive for Space Telescopes (MAST), is known to result in residual instrumental signal in the low frequency region (Debosscher et al. 2013; Tkachenko et al. 2013a), we apply the light curve extraction algorithm developed by Steven Bloemen (one of the co-authors of the original publication) as explained in Section 2.3.2.

We then extracted the frequencies from the reduced light curves by an iterative prewhitening method based on the Lomb-Scargle periodogram, as described in detail in Chapter 2. Observed oscillation frequencies above the Nyquist frequency were evaluated by comparing their amplitudes with those of possible aliases. Following Murphy et al. (2013), the frequency with the highest amplitude was retained.

3.3 Spectroscopic analysis

Visual inspection of the available spectra revealed that two of the targets, KIC 5772452 and KIC 7516703, are in fact K-type stars in a binary systems, and the variability in their light curves was found to correspond to rotational modulation. These stars have therefore been discarded for the rest of this work. In addition, one of the stars in the sample, KIC 10080943, had already been identified as a double-lined binary by Tkachenko et al. (2013a). This star has been monitored extensively in spectroscopy meanwhile and reveals tidally-excited as well as free oscillations. Given that some of its modes are of different origin than those of the other sample stars, it has been analysed separately in the framework of the PhD thesis of Valentina Schmid (Schmid et al. 2015; Schmid & Aerts 2016). This leaves us with 67 stars for the current study.

3.3.1 Binarity

In a first step in our data analysis we checked the targets in our sample for binarity. We applied the improved least-squares deconvolution (LSD)

Table 3.1: The estimates for the orbital periods and system velocities of the binaries KIC 3222854 and KIC 8693972.

	KIC 3222854	KIC 8693972
P [days]	$\gtrsim 100$	$\sim$ 60, 90, 120 or 180
γ $[km\, s^{-1}]$	-39.5	-5.9
σ_γ	1.7	3.9

algorithm (Tkachenko et al. 2013c) to the individual spectra of each star as described in Section 2.3.3. The resulting high S/N average line profiles were then checked for global Doppler shifts and the presence of a signal from a possible companion. This resulted in the detection of four single-lined binaries (KIC 6468146, KIC 7867348, KIC 10467146, KIC 11754232), four double-lined binaries (KIC 3222854, KIC 3952623, KIC 6367159, KIC 8693972), two triple systems (KIC 6467639, KIC 6778063) and three objects for which we have spectral contributions from both components, but no detected radial-velocity variations. This is also listed in Table C.2.

The radial velocities of the different components of a binary were obtained by taking the centre of gravity of their LSD profile, and can be found on the website[1] describing this work. For some of the detected single- and double-lined binaries we have obtained a sufficient number of observations to cover the binary orbit. For KIC 3222854 and KIC 8693972 we were able to derive only an order of magnitude estimate of the orbital period P_{orbit}, as listed in Table 3.1. For KIC 3952623, KIC 7867348, and KIC 11754232 these values were sufficiently accurate to allow us to determine values for the remaining spectroscopic orbital parameters (eccentricity e, the angle ω between the ascending node and the periapsis, the time T_0 of periastron passage, the system velocity γ, velocity amplitudes K_j and the projected semi-major axes $a_j \sin i$) as well, which are listed in Table 3.2. The radial velocity variations of the two triple systems proved to be complicated to unravel. Here a more detailed analysis is required, which is outside the scope of this work.

We also applied the frequency modulation (FM) method (Shibahashi & Kurtz 2012) and the phase modulation (PM) method (Murphy et al. 2014) to the pulsation frequencies extracted from the *Kepler* light curves. These methods exploit the impact of the Doppler effect on the pulsation frequencies and relative phases, respectively, which can be observed thanks to the high precision of the *Kepler* data. They both require that

$$f_{\text{orbit}} \ll f_{\text{puls}} \ll f_{\text{obs}},$$

---

[1] `https://fys.kuleuven.be/ster/Projects/gamma-doradus`

Table 3.2: The orbital solutions for the binary systems KIC 3952623, KIC 7867348 and KIC 11754232. (See the main text for details.)

	KIC 3952623			KIC 7836348	KIC 11754232
method	spectroscopy	FM method	PM method	spectroscopy	spectroscopy
P_{orbit} [days]	19.515	19.5	19.526	10.0132	214.9
σ_P	0.006	0.2	0.001	0.0006	0.6
e	0.17	0	0.191	0.23	0.55
σ_e	0.04	-	0.001	0.03	0.01
ω [2π]	1.65	-	1.5481	1.05	4.52
σ_ω	0.1	-	0.0006	0.11	0.03
T_0 [BJD]	2456442.8	-	-	2455685.96	2456417.23
σ_{T_0}	0.3	-	-	0.15	1.38
K_1 [$km\,s^{-1}$]	30	30.08	19.36	9.3	17.8
σ_{K_1}	0.8	-	0.04	0.2	0.2
K_2 [$km\,s^{-1}$]	52.5	-	-	-	-
σ_{K_2}	1.4	-	-	-	-
$a_1 \sin i$ [AU]	0.053	0.054	-	0.0083	0.294
$\sigma_{a_1 \sin i}$	0.001	-	-	0.0002	0.004
$a_2 \sin i$ [AU]	0.093	-	-	-	-
$\sigma_{a_2 \sin i}$	0.003	-	-	-	-
γ [$km\,s^{-1}$]	-15.7	-	-	-26	13.5
σ_γ	2.5	-	-	0.2	0.4

where f_{orbit} is the orbital frequency, f_{puls} is the pulsation frequency and f_{obs} is the cadence of the observations. As Murphy et al. (2014) pointed out, the FM method is most sensitive for the detection of relatively short-period binaries, because the Doppler shift of pulsation frequencies scales with the radial velocity of the pulsating star, and for wider binaries this shift becomes comparable to the frequency resolution. The PM method provides a direct measure of the time delay because of the orbital motion of the pulsating star. The detection of this time delay requires splitting up the light curve in time intervals of suitable length P_{int}, i.e., $P_{\mathrm{puls}} \ll P_{\mathrm{int}} \ll P_{\mathrm{orbit}}$. Hence the PM method is more likely to be successful for the detection of long-period binaries and lower-frequency pulsations than the FM method. In the case of KIC 3952623, we were able to confirm the spectroscopic results with both the FM and PM methods, as listed in Table 3.2, though the PM method leads to an underestimate of the velocity amplitude due to the relatively short orbital period. Neither method provided a satisfactory result for the other observed binaries. There are several possible explanations. Firstly, the typical γ Dor pulsation period has a value between 0.3 and 3 days, so that the difference between P_{puls} and P_{orbit} is small for short-period binaries. Secondly, as we will see in Section 3.4, we often observe period spacing patterns with a value between 0.001 and 0.035 d, depending on the rotation velocity and the spherical degree l of the mode. The corresponding spacings in the frequency domain are close to the ones we would obtain for a binary orbit above 20 d. Aside from KIC 3952623, there are indications of the presence of the expected signal for KIC 11754232, but unfortunately we have only eight quarters of data available for this star, which prevented a reliable analysis.

Out of the thirteen targets that we found to be multiple star systems, seven are identified as γ Dor/δ Sct hybrid candidate pulsators (out of eleven hybrid candidates in the studied sample of 67 targets). While this could mean that several of these binary systems consist of a γ Dor and a δ Sct star, we cannot exclude the possibility that one (or both) of the components are hybrid pulsators. Indeed, three hybrids are identified as single-lined binaries, and from the application of the FM method to KIC 3952623 we conclude that the studied δ Sct pulsations belong to the brightest component. This indicates this star is a hybrid as well, considering the relatively high amplitudes of the γ Dor pulsations.

3.3.2 Fundamental parameters

In the second part of the spectroscopic analysis, we focused on the stars which have been classified as either single stars or single-lined binaries. The spectra of these stars were corrected for any radial velocity variations (in the case of the single-lined binaries) and merged, as described earlier in Section 2.3.3. This resulted in a single spectrum for each star, which we subsequently used to determine the fundamental spectroscopic parameter values.

We again use the Grid Search in Stellar Parameters (GSSP) code for the spectral analysis, as discussed in Section 2.3.3, to determine the values of the temperature T_{eff}, surface gravity log g, metallicity $[M/H]$, microturbulence ζ and projected rotational velocity $v \sin i$. We again focused on the observed spectra in the range between 4700 Å and 5800 Å, which includes the H_{β}-line.

The obtained parameter values are listed in Table C.3 and some sample distributions are illustrated in Fig. 3.1. As we can see, T_{eff} typically has a value near 7100 K, while log g is close to 4.1. The metallicity, $[M/H]$, is on average slightly higher than the solar metallicity, while ζ typically has a value between 2 and $3.5\,\text{km}\,\text{s}^{-1}$. These are in close agreement with the parameters we had chosen for the LSD line mask in Section 3.3.1. The metallicity values previously computed by Tkachenko et al. (2013a) are on average slightly below the solar value, because ζ was kept fixed at $2\,\text{km}\,\text{s}^{-1}$ in that study, whereas we included it as a free parameter. We also find that most γ Dor stars in our sample are slow to moderate rotators compared to their Keplerian break-up velocity $v_c = \sqrt{2GM_*/3R_*}$, where M_* and R_* are the stellar mass and radius. For a $1.6\,M_{\odot}$ star with a $1.9\,R_{\odot}$ radius we find $v_c = 327\,\text{km}\,\text{s}^{-1}$. Typical values for γ Dor stars are on the order of $300\,\text{km}\,s^{-1}$, while the stars in our sample have $v \sin\, i$ ranging from roughly $10\,\text{km}\,\text{s}^{-1}$ to $200\,\text{km}\,\text{s}^{-1}$.

A comparison of the spectroscopically derived parameters values of T_{eff}, log g and $[M/H]$ with the values found in the *Kepler* input catalogue (KIC)(Brown et al. 2011), which are derived from spectral energy distribution (SED) fitting, is shown in Fig. 3.2. It is found that, apart from a few outliers, the T_{eff} values in the *Kepler* catalogue are reasonably reliable, while the deviations of the surface gravity and metallicity values seem to be correlated to the actual parameter values. This relation is similar to the one found by Tkachenko et al. (2013c).

3.4 Period spacing patterns in the *Kepler* photometry

Having confirmed the γ Dor nature for the vast majority of the targets in our sample and having identified the binaries, we used the extracted pulsation frequencies to look for period spacings by means of the methodology described in Chapter 2. This resulted in the *detection of period spacings for 50 of the 67 studied targets.* These are listed in Tables C.2 and C.4. The found spacing

Figure 3.1: Histograms representing the distribution of the atmospheric parameter values obtained for the single stars and the single-lined binaries in our sample.

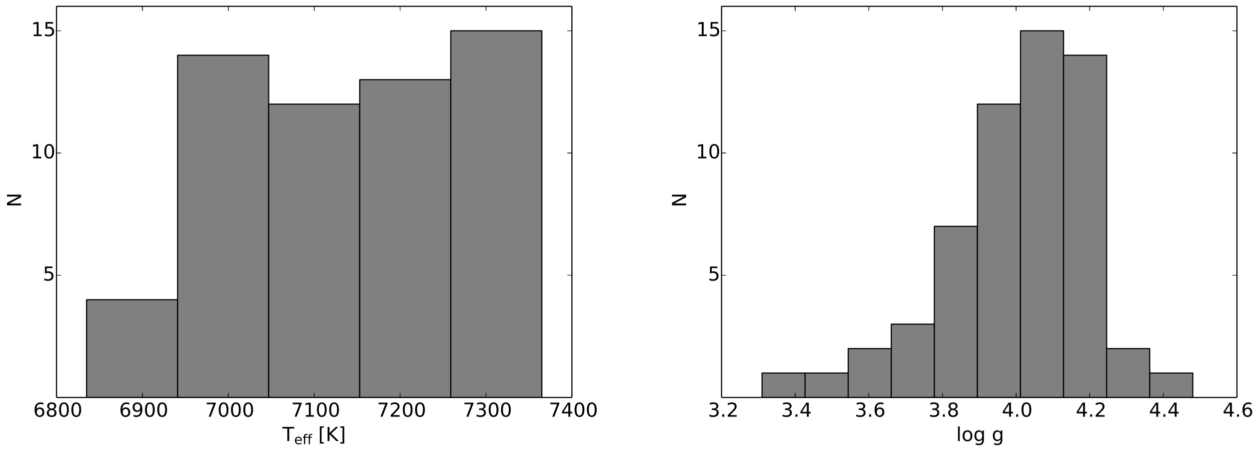

Figure 3.1: Continued.

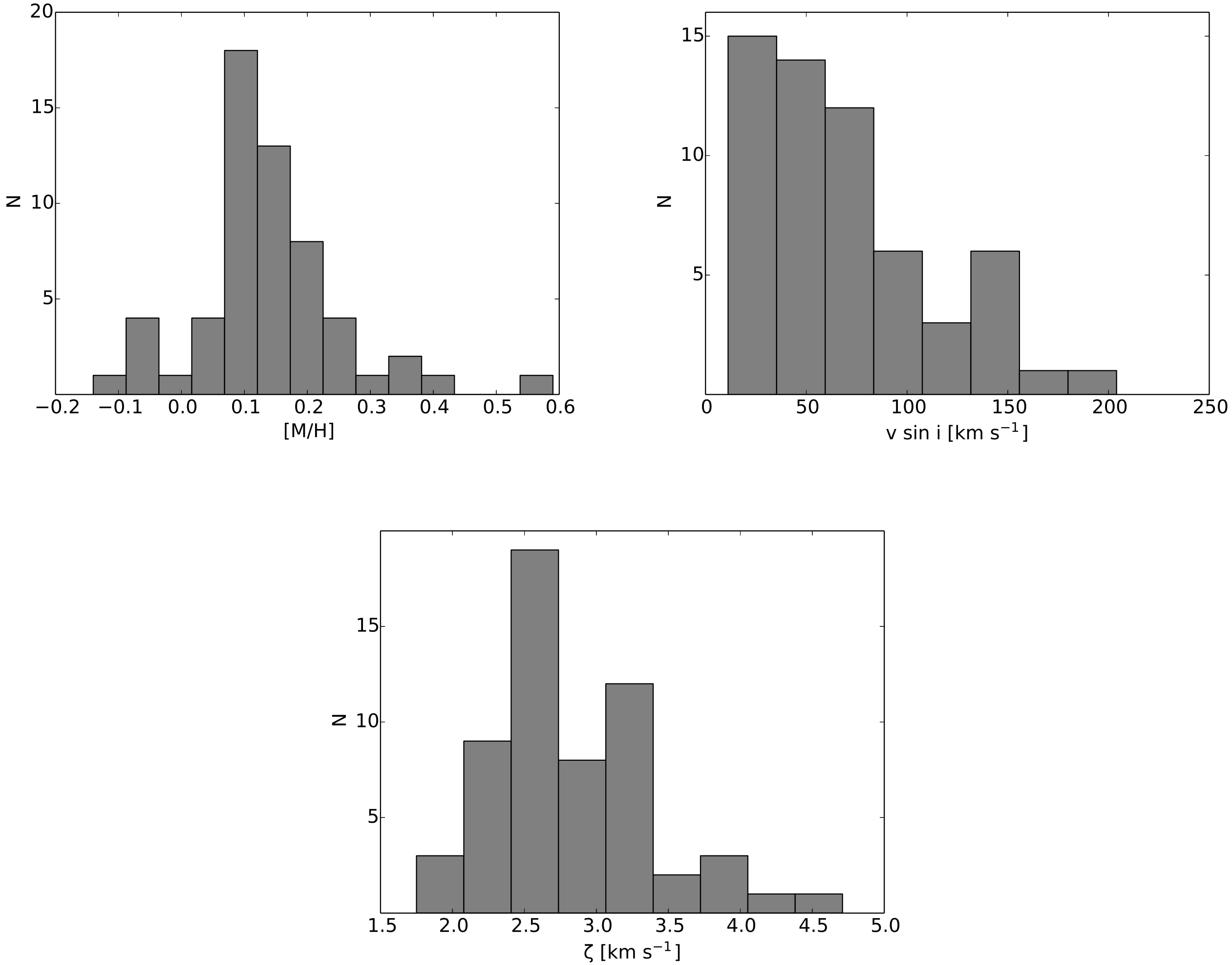

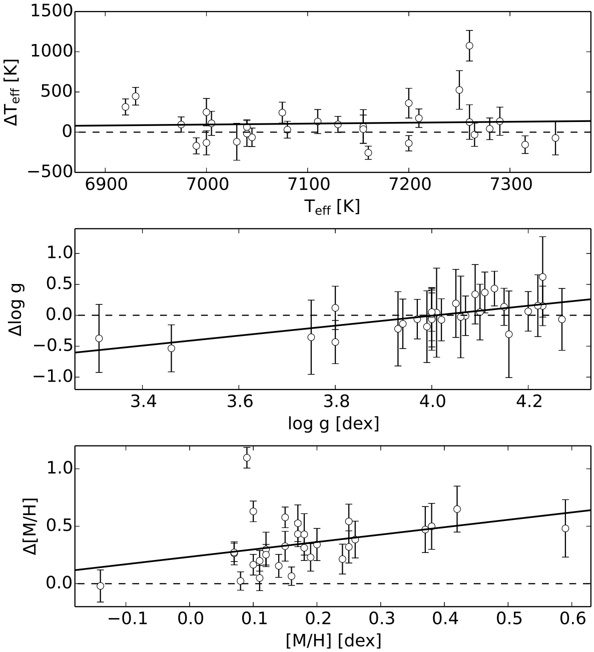

Figure 3.2: The differences between the spectroscopically derived values and the KIC values of the fundamental parameters $T_{\rm eff}$ (top), log g (middle) and $[M/H]$ (bottom), as a function of the spectroscopic values. Linear fits of the relations are represented by the solid black lines.

patterns are all shown in Appendix C. A selection can also be found in Figs. 3.3 to 3.6.

Most of the period spacing patterns have a clear slope. This has been observed before (cf. Chapter 2, Bedding et al. 2015) and is a consequence of frequency shifts due to rotation. Interestingly, most of the detected period spacing patterns seem to be complementary to the ones presented by Bedding et al. (2015). These authors considered slowly rotating stars without spectroscopic confirmation that it actually concerns F-type stars, while our method is also suitable to detect the period spacing patterns of the moderate to fast rotating stars in our sample. While this difference is clearly visible in the increasingly strong downward slopes of many of the detected patterns, there are also several detected spacing series with an upward slope.

As discussed in Section 1.2.1, the period spacing patterns with a downward slope are either prograde or zonal modes. Given that zonal modes are expected to be more susceptible to trapping in an equatorial waveguide under the influence of the Coriolis force (Townsend 2003a), we expect most, if not all, of the detected modes to be prograde. According to theory, spacing series with an upward slope correspond to retrograde modes that are shifted in the frequency domain because of the stellar rotation. It is expected that the average period spacing value of retrograde modes increases for higher rotation rates (Bouabid et al. 2013), as found for KIC 11145123 (Kurtz et al. 2014), KIC 9244992 (Saio et al. 2015) and KIC 9751996 (see Fig. 3.3). Nevertheless, for several stars, such as e.g. KIC 8375138 (see Fig. 3.4), the observed mean period spacing value for the series with the upward slope is smaller than it would be if the star did not rotate. The reason is that for these stars, the rotation frequency is so high relative to the pulsation frequencies of the retrograde modes in the co-rotating frame, that the retrograde modes are shifted below zero in the inertial reference frame. When observed, pulsation frequencies are assumed to be positive, so that when the retrograde modes are observed, these are in fact mirrored over $0\,\mathrm{d}^{-1}$ in the Fourier spectrum, and we end up with a spacing pattern such as the one seen in Fig. 3.4. While Bouabid et al. (2013) already mentioned that this might occur, we find this to be fairly common since we identify this phenomenon for no less than ten stars with a detected period spacing pattern exhibiting both prograde and retrograde modes.

For six stars in our sample, such as KIC 11668783 illustrated in Fig. 3.6, we find a period spacing pattern connected with retrograde modes only, all of which having similar characteristic amplitude patterns in the sense that the mode amplitude grows as the pulsation period increases and drops sharply (see Figs. 3.4 and 3.5). The amplitude comb of KIC 8375138 as seen in Fig. 3.4 reveals dips in the amplitudes in an otherwise monotonically growing period series.

Even though many of the observed period spacing patterns are reasonably smooth, there are also several patterns which show regular dips. This is particularly visible for the pulsation spacing pattern of KIC 2710594, shown in Fig. 3.5. Finally, several of the stars for which we find period spacing patterns are hybrid γ Dor/δ Sct candidates, most notably KIC 8645874, KIC 9751996 and KIC 11754232 (listed in Table C.2). Not only are these single stars or single-lined binaries (KIC 11754232), they are also slow rotators and have a relatively rich pulsation spectrum in the higher frequency range. If the suspected δ Sct nature of the higher frequency modes is confirmed, these are interesting targets to probe the interior stellar rotation profile, as done in Kurtz et al. (2014), Saio et al. (2015), and Murphy et al. (2016).

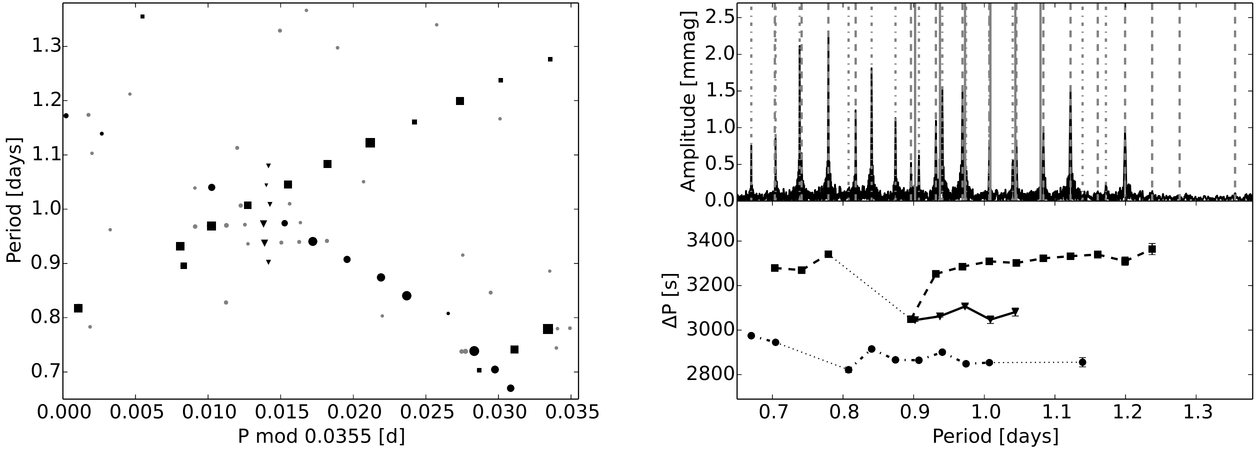

Figure 3.3: The period spacing patterns of the slowly rotating star KIC 9751996. *Left:* the pulsation series in a period échelle diagram. The prograde (black circles), zonal (black triangles) and retrograde (black squares) dipole modes are marked separately, while the other pulsation modes are shown in grey. *Top right:* the prograde (dash-dot lines), zonal (full lines) and retrograde (dashed lines) modes in the Fourier spectrum. *Bottom right:* the period spacing patterns, using the same symbols as before. The dotted lines indicate missing frequencies.

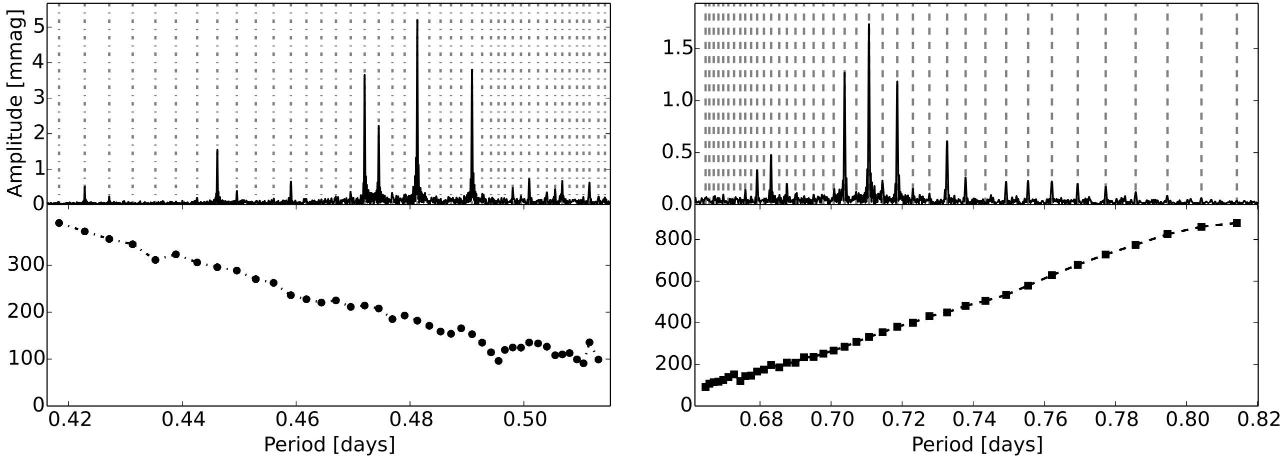

Figure 3.4: The prograde (left) and retrograde (right) period spacing patterns of KIC 8375138. The used symbols are the same as in Fig. 3.3.

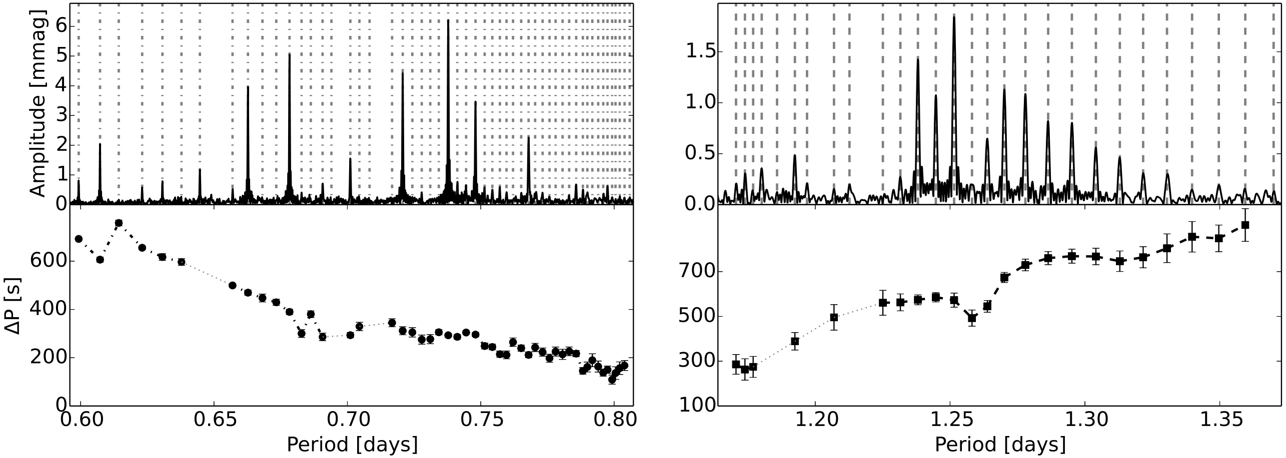

Figure 3.5: The prograde (left) and retrograde (right) period spacing patterns of KIC 2710594. The used symbols are the same as in Fig. 3.3.

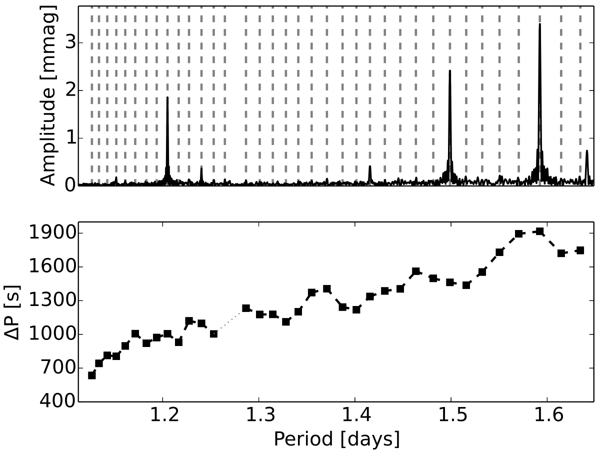

Figure 3.6: The retrograde period spacing patterns of KIC 11668783. The used symbols are the same as in Fig. 3.3.

3.5 Statistical analysis of the sample properties

Among the 50 stars for which we found period spacing patterns, 42 are single stars and four are single-lined binaries. We have therefore 46 stars for which we have both spectroscopic and pulsational parameters based on period spacings, allowing us to look for possible correlations between their properties and compare those qualitatively with the relations predicted by theory.

In order to properly take into account the characteristics of the period spacing patterns in the analysis, we limited ourselves to the patterns with a downward slope, because these are by far the most frequently detected, i.e., in 40 stars. We derived various quantities from them, as illustrated in Fig. 3.7. The mean pulsation period of the g-modes that are part of the found series is denoted as $\langle P \rangle$, while $\langle \varDelta P \rangle$ is the mean spacing value of the pattern. In addition, we have the mean derivative $\mathrm{d}(\varDelta P)/\mathrm{d}P$ of the pattern, which is actually computed from a fitted 2^{nd} order polynomial (shown in red in Fig. 3.7) as this allows us to avoid the influence of any irregularities or dips in the spacing series.

We also took into account the parameter $\varDelta_{\mathrm{res}}$, which is given by

$$\varDelta_{\mathrm{res}} = \frac{1}{n} \sum_{i=1}^{n} \left(\frac{\varDelta P_i - m_i}{m_i} \right)^2 . \tag{3.1}$$

Here n is the number of data points in the observed period spacing series, and m_i are the values of the previously fitted 2^{nd} order polynomial for the pulsation periods P_i. Thus, $\varDelta_{\mathrm{res}}$ is a measure of the residuals of the polynomial fit to the period spacing series as a proxy of the smoothness of the found pattern. The parameter P_{max}, on the other hand, is the longest detected pulsation period of the downward spacing pattern. We here consider it to be indicative of the cut-off frequency for which the radiative damping of the pulsations in the g-mode cavity becomes dominant over the excitation (Dupret et al. 2005; Bouabid et al. 2013). In general, it is the interplay between the non-adiabatic excitation and damping that determines whether a mode will be excited to detectable amplitude or not. Hereby, one should take into account "advective damping", i.e., damping caused by the non-zero divergence of the wave flux, which may occur for modes with a period above the cutoff. For a given stellar region, such advective damping corresponds to mechanical energy transfer beyond the region's boundary. In a rotating star, the excitation mechanism's efficiency can be enhanced by the Coriolis force (Townsend 2000). The observed quantity P_{max} is therefore not only of interest to deduce the boundaries of the γ Dor instability strip, but also to derive the physical conditions that determine the delicate balance between damping and excitation of the modes.

The other included parameters in our analysis are the frequency f_g and the amplitude A_g of the dominant g-mode as well as the obtained spectroscopic stellar parameters. While it would have been valuable to also include the frequency f_p and the amplitude A_p of the δ Sct p-mode with the highest amplitude or a proxy for the acoustic cutoff frequency for the hybrid γ Dor/δ Sct stars, there are not enough hybrids in the sample for a meaningful statistical analysis based on these quantities. Similarly, the number of sample stars with retrograde modes is also too small for such a study.

We searched linear relations between the different established parameters, where we took the logarithm for those quantities whose range is two or more orders of magnitude. These are the twelve parameters listed in Tables C.3 and C.4 for the 40 single stars or single-lined binaries with a downward period spacing pattern. We performed several multivariate analyses, each time choosing one of the available parameters as the dependent variable Y and taking the others as covariates X_i. In order to make sure that there was no offset in the parameter relation, we subtracted the mean values of all the parameters prior to the regression analysis. The latter was based on forward selection and backward elimination (e.g., Aerts et al. 2014, for a similar application). With the forward selection method, we add covariates one at a time as long as their addition implies a significantly better model fit, starting with the one showing the strongest correlation with the chosen dependent variable. In the case of the backward elimination, we start with all covariates under study and remove those

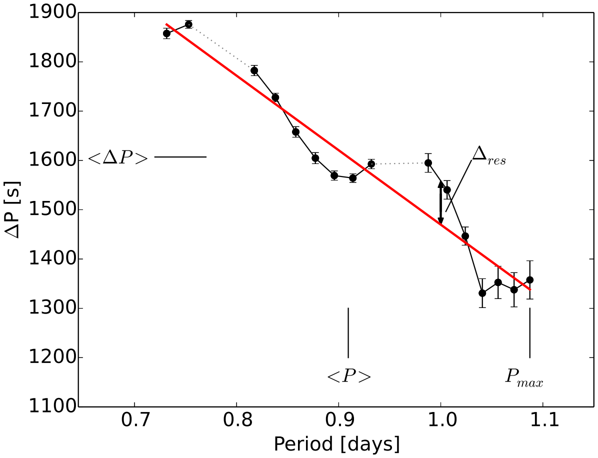

Figure 3.7: Illustration of some of the photometric parameters from the period spacing patterns (shown here for KIC 10224094) for the statistical analysis: $\langle P \rangle$ is the mean pulsation period, P_{max} is the longest pulsation period, $\langle \mathit{\Delta} P \rangle$ is the mean spacing, and $\langle \frac{\mathrm{d}\mathit{\Delta} P}{\mathrm{d}P} \rangle$ is the mean derivative (computed from the polynomial fit, here shown in red). Finally, $\mathit{\Delta}_{\mathrm{res}}$ is a measure of the difference between the polynomial fit and the period spacing pattern, defined in Equation (3.1).

showing insignificant correlation with the dependent variable. The significance tests for each individual covariate were done using a t-test, while the evaluation of each step of the fit was based on the coefficient of determination R^2, i.e., the fraction of the variance of the dependent variable explained by the model. A summary of the multiple regression results is provided in Table 3.3.

The clearest result from these analyses is the strong correlation between the stellar rotation and the found period spacing, as predicted by theory (Bouabid et al. 2013) and already discussed in Sections 1.2.1, 1.2.1 and 3.4. The faster a star is rotating, the larger the rotational shifts of the pulsation frequencies, which for prograde modes translates into a period spacing pattern with a steeper downward slope and consisting of more closely spaced, shorter pulsation periods. The bivariate relation between the mean period spacing and $\log(v \sin i)$ is shown in Fig. 3.8.

Secondly, we found that the value of the dominant mode frequency, f_g, is strongly correlated with the values of $v \sin i$ and $\log T_{\mathrm{eff}}$, as shown in Fig. 3.9. As listed in Table 3.3, the R^2-value we obtain for the bivariate model based

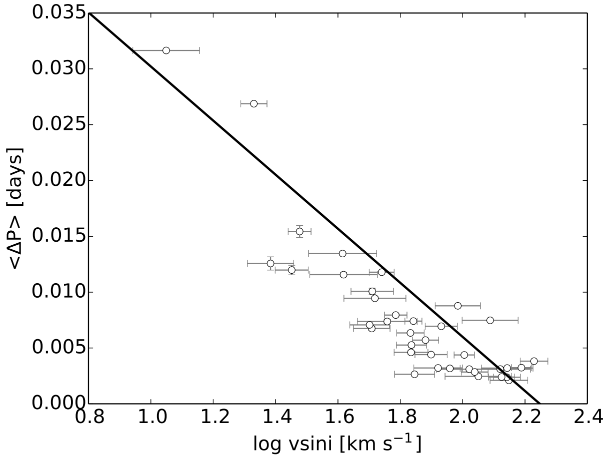

Figure 3.8: The average period spacing values of the different stars with respect to the logarithm of their $v\sin i$ values.

on f_g and $v\sin i$ is 0.468. When we include log $T_{\rm eff}$ as well, the value of R^2 increases to 0.665 for the trivariate model fit, given by

$$f_g \;=\; 30.9(6.6)\cdot\log T_{\rm eff} + 0.0103(0.0013)\cdot v\sin i - 118.23(0.32),$$

where the frequency f_g is expressed in d^{-1}, $T_{\rm eff}$ in Kelvin and $v\sin i$ in $\mathrm{km\,s^{-1}}$. The relation was found for both the forward and the backward modelling and is clearly appropriate. However, there are two unknowns causing variance in this trivariate model that we cannot take into account at present: the inclination angle i of the star and the spherical degree l of the pulsation modes. This may explain some of the scatter in Fig. 3.9.

It is noteworthy that the trend between f_g and log $T_{\rm eff}$ is opposite to the one found for B-type g-mode pulsators, which do not have an outer convective envelope and are, in general, slower rotators than the sample we studied here (De Cat & Aerts 2002; Aerts et al. 2014). However, the two correlations are not directly comparable because the instability strip of SPB stars is much more extended along the main sequence than the γ *Dor* instability strip. The latter is confined to a much more narrow log $T_{\rm eff}$ range than the SPB instability region. Therefore the main contributor to the above mentioned trend for γ *Dor* stars, is the stellar radius, whereas this is the initial mass for SPB pulsators.

We also found a bivariate relation between f_g and the spectroscopically derived microturbulent velocity ζ. This is not surprising because the overall pulsational

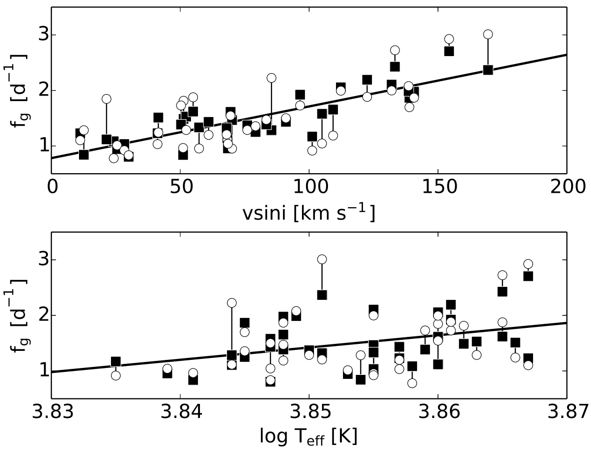

Figure 3.9: Observed values (white dots) for the dominant frequency f_g, with lines connected to the values predicted by the multivariate models (black squares) described in Table 3.3 for the rotation velocity $v \sin i$ (*top*) and the temperature $\log T_{\rm eff}$ (*bottom*). The bivariate model fits listed in the left part of Table 3.3 are shown by the full lines.

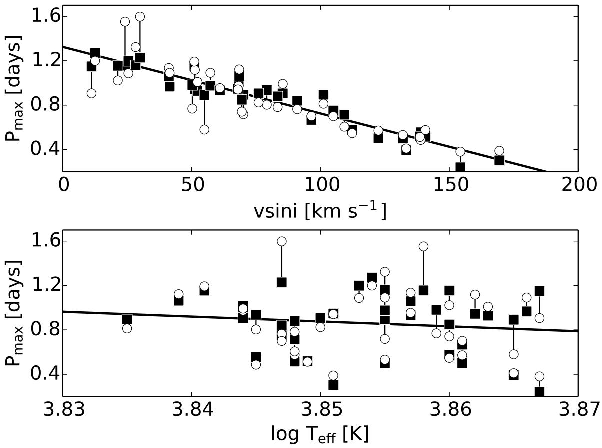

Figure 3.10: Same as Fig. 3.9, but for the pulsation period $P_{\rm max}$ instead of the frequency f_g.

line broadening, which is dominated by the mode with frequency f_g, is captured by ζ. Indeed, we could not perform line-profile modelling due to the individual pulsation modes as it would require time-resolved spectroscopy covering the phases of each and every g-mode (e.g., Aerts et al. 2010, Chapter 6). Hence, the overall pulsational broadening is included in the simple broadening function parametrized with ζ (Cf. Morel et al. 2006).

Finally, we also found a bivariate relation between f_g and $\langle P \rangle$, which indicates that the period spacing patterns are typically found in frequency regions around the dominant g-mode frequency.

The correlations between f_g and the other variables also apply to $P_{\rm max}$ to almost the same extent, as can be seen in Table 3.3 and as illustrated in Fig. 3.10. The main difference is that the correlation between $P_{\rm max}$ and $v \sin i$ is stronger than between f_g and $v \sin i$, while the correlation with log $T_{\rm eff}$ is weaker. Thus, rotation seems to have a larger impact on the period $P_{\rm max}$ than on the frequency of the dominant mode.

Table 3.3: Results of the multiple linear regression. We list the coefficients of the covariates for the different model fits as well as the p-values (obtained from a t-test) and the R^2 values.

Explanatory variables	Separate models			Multivariate models		
	Estimate (σ)	p-value	R^2	Estimate (σ)	p-value	R^2
			Models for the dependent variable $\langle\frac{\mathrm{d}\Delta P}{\mathrm{d}P}\rangle$			
$\log(v\sin i)$	-0.032(0.004)	0.025	0.606	-	-	-
			Models for the dependent variable $\langle P\rangle$			
Intercept	-	-	-	77.09	-	0.501
$\log(v\sin i)$	-0.45(0.10)	0.0001	0.350	-0.52(0.09)	< 0.0001	
$\log T_{\mathrm{eff}}$	-5.8(4.2)	0.313	0.050	-10.4(3.2)	0.0346	
			Models for the dependent variable $\langle\Delta P\rangle$			
$\log(v\sin i)$	-0.024(0.002)	< 0.0001	0.796	-	-	-
			Models for the dependent variable f_g			
Intercept	-	-	-	-118.23(0.32)	-	

Table 3.3: Continued.

Explanatory variables	Separate models			Multivariate models		
$v \sin i$	0.0093(0.0016)	< 0.0001	0.468	0.0103(0.0013)	< 0.0001	0.665
$\log T_{\text{eff}}$	22.1(10.5)	0.142	0.104	30.9(6.6)	0.0047	
ζ	0.61(0.14)	< 0.0001	0.346	-	-	-
$\langle P \rangle$	-1.93(0.28)	< 0.0001	0.549	-	-	-
	Models for the dependent variable $P_{\max}$					
Intercept	-	-	-	39.50(0.14)	-	0.773
$v \sin i$	-0.0060(0.0006)	< 0.0001	0.703	-0.0064(0.0006)	< 0.0001	
$\log T_{\text{eff}}$	-4.4(5.9)	0.550	0.015	-10.0(2.9)	0.0292	
ζ	-0.33(0.07)	0.0079	0.358	-	-	-
$\langle P \rangle$	1.31(0.08)	< 0.0001	0.876	-	-	-
$\langle \frac{\mathrm{d}\Delta P}{\mathrm{d}P} \rangle$	18.4(2.8)	0.0130	0.526	-	-	-
f_g	-0.38(0.06)	< 0.0001	0.505	-	-	-

3.6 Discussion and conclusions

This chapter offers an observational asteroseismic analysis of 67 of the γ Dor stars in the sample presented by Tkachenko et al. (2013a). Thanks to the available combination of *Kepler* photometry and ground-based high-resolution spectroscopy, we were able to carry out a detailed statistical analysis. We found thirteen of the 67 stars to be members of a multiple star system. We computed the stellar parameters for all single stars and single-lined binaries in the sample and found them to be consistent with the typical values expected for γ Dor stars. Most of the stars in our sample are slow to moderate rotators with respect to their breakup velocity.

For 50 stars in the sample we were able to detect period spacings using the methodology described in Chapter 2. The found spacing patterns are in line with theoretical expectations (Miglio et al. 2008; Bouabid et al. 2013). For several of the stars we detected periodic dips in the period spacing versus period relations, as predicted by Miglio et al. (2008). These dips are caused by the presence of a chemical gradient near the edge of the convective core. For many of the sample stars, the period spacing patterns are smooth, pointing either to extremely young stars or, more likely, to the presence of mixing processes inside the star that have diminished or even washed out the chemical gradient. A priori one could expect to see a correlation between the smoothness of the period spacing patterns and the observed rotation velocity. In this chapter, such a correlation would be reflected between the values of $\varDelta_{\mathrm{res}}$ and $v \sin i$, but we could not find a significant relation between the two parameters. It is likely that, if such a correlation exists, the uncertainties on the values of $\varDelta_{\mathrm{res}}$ are too large.

In order to determine the precise cause of the smooth patterns, detailed forward seismic modelling is required for each individual star. In addition, each of the found spacing patterns reveals a clear slope. This is as predicted theoretically and points towards frequency shifts of the g-modes due to rotational effects, resulting in a downward or upward slope for prograde and retrograde modes, respectively.

Our results based on the *Kepler* time series photometry were further confronted with the spectroscopic parameters of the pulsators. We searched for correlations between the seismic quantities for the stars exhibiting period spacing patterns with a downward slope, since only these constitute a large enough sample to perform multivariate linear regressions. We found a strong correlation between $v \sin i$ and the average period spacing, confirming the influence of rotation on γ Dor-type pulsations as predicted by theory. In addition, we found a correlation between the dominant g-mode frequency and both $v \sin i$ and log T_{eff}. Similarly,

$P_{\rm max}$ correlates with $v \sin i$ and log $T_{\rm eff}$.

While our sample contains only eleven hybrid γ Dor/δ Sct candidate pulsators, these constitute an interesting sub-sample for various reasons. First, seven of these stars were found to be in a multiple star system. In these cases, it is possible the γ Dor and the δ Sct-type pulsations originate from different component. However, for four of them this is unlikely, as three were identified as single-lined binaries, while in the case of KIC 3952623 the observed γ Dor and δ Sct variability were both found to likely originate from the brighter primary component.

Two of the single stars (KIC 8645874 and KIC 9751996) and one of the single-lined binaries (KIC 11754232) were found to be slow rotators. Interestingly, some of the recently studied hybrid γ Dor/δ Sct pulsators are also very slow rotators (Kurtz et al. 2014; Bedding et al. 2015; Saio et al. 2015; Murphy et al. 2016). On the other hand, the hybrid star KIC 4749989 is a fast rotator, similar to KIC 8054146 (e.g. Breger et al. 2012).

We compared the locations of the sample stars in the Kiel diagram with the γ Dor instability strips determined by Dupret et al. (2005) and Bouabid et al. (2011) (as shown in Figure 3.11). Given the large uncertainties on log g, the positions are compatible with the strips, although most of our sample stars clearly cluster around the blue edge. In addition, it is clear the single-lined binaries have lower values for log g than the single stars, although this difference is still smaller than the average $1\,\sigma$-uncertainty. This can possibly be explained by the light dilution effect, i.e., the light contributed by the secondary to the continuum flux. In this temperature range, the value of log g is obtained from the metal lines, and the values given for the metallicity [M/H] in Table C.3 in Appendix C are also lower for the single-lined binaries than for the single stars. The symbol sizes in Figure 3.11 indicate the longest pulsation period $P_{\rm max}$ in the spacing patterns (*top*), the rotation velocity $v \sin i$ (*middle*) and the g-mode frequency f_g with the largest amplitude (*bottom*). The quantity $P_{\rm max}$ is of interest to understand γ Dor instability, in the sense that modes with even longer period are more sensitive to radiative damping and/or wave energy leakage.

While we found a correlation between f_g as well as $P_{\rm max}$ and log $T_{\rm eff}$ in Section 3.5, this is not obvious from the figure because of the strong influence of $v \sin i$ on these two quantities and due to the large errors of log g. We do see from the symbol sizes that a higher rotation velocity typically correlates with a higher frequency f_g and a lower period $P_{\rm max}$, as found from the forward and backward regression.

Our sample study constitutes a very rich observational data base to pursue

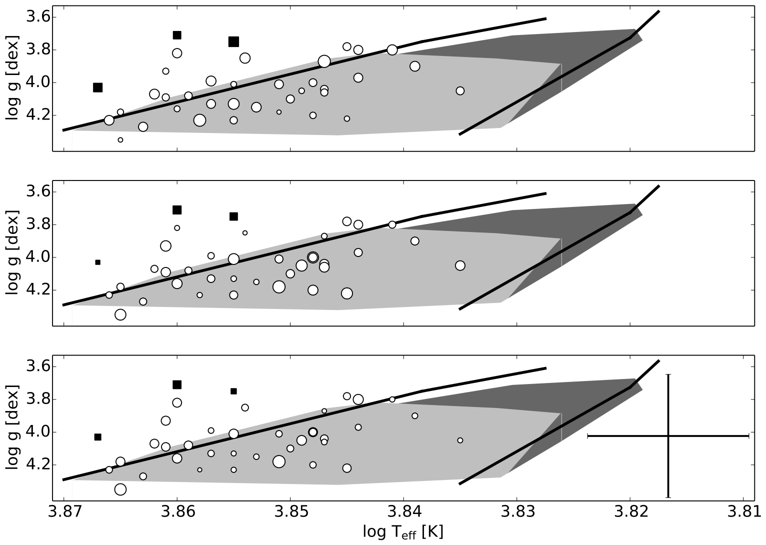

Figure 3.11: ($\log T_{\rm eff}$,$\log g$)-diagrams with the sample stars for which period spacing patterns with downward patterns were found. The white dots indicate the single stars, whereas the black squares are the single-lined binaries. The full lines mark the instability strip taken from Dupret et al. (2005) (with $\alpha_{\rm MLT} = 2.0$). The light grey and dark grey areas are the instability strips for the main-sequence γ Dor stars presented by Bouabid et al. (2011), with $\alpha_{\rm ov} = 0$ and $\alpha_{\rm ov} = 0.2$ respectively. The marker sizes indicate the longest pulsation period $P_{\rm max}$ in the spacing patterns (*top*), the rotation velocity $v \sin i$ (*middle*) and the g-mode frequency f_g with the highest amplitude (*bottom*). The average error bars on the data points are shown in the bottom right corner.

forward asteroseismic modelling of γ Dor stars. All the necessary data to perform such stellar modelling is provided to the community through `https://fys.kuleuven.be/ster/Projects/gamma-doradus`.

Chapter 4

Mode identification and interior rotation rate from ensemble modelling

This chapter was based on

Interior rotation of a sample of γ Doradus stars from ensemble modelling of their gravity-mode period spacings

T. Van Reeth, A. Tkachenko, C. Aerts

Astronomy & Astrophysics, 593, A120, 13 pp. (2016)

Author contributions

Timothy Van Reeth developed the method to derive the rotation rate and mode identification, identified the Rossby waves, compared the detections to the theoretical predictions made by Bouabid et al. (2013), and set up the computations with MESA and GYRE. Andrew Tkachenko did the computations of the theoretical models on the computer cluster in Tautenburg, and Conny Aerts proposed repeating the multivariate correlation analysis and made the graphical overview of the observed surface gravities and rotation rates of the BAF stars. Both Andrew Tkachenko and Conny Aerts have also participated in many helpful discussions. Timothy Van Reeth wrote the draft text; Andrew Tkachenko and Conny Aerts improved the text prior to submission.

Abstract

Context. γ Dor stars are known to exhibit gravity- and/or gravito-intertial modes that probe the inner stellar region near the convective core boundary. The non-equidistant spacing of the pulsation periods is an observational signature of the stellar evolutions and current internal structure and is heavily influenced by rotation.
Aims. We aim to constrain the near-core rotation rates for a sample of γ Dor stars for which we have detected period spacing patterns.
Methods. We combined the asymptotic period spacing with the traditional approximation of stellar pulsation to fit the observed period spacing patterns using χ^2-optimisation. The method was applied to the observed period spacing patterns of a sample of stars and its results were used for ensemble modelling.
Results. For the majority of stars with an observed period spacing pattern we successfully determined the rotation rates and the asymptotic period spacing values, although the uncertainties on the latter were typically large. This also resulted directly in the identification of the modes that correspond to the detected pulsation frequencies, which for most stars were prograde dipole gravity and gravito-inertial modes. The majority of the observed retrograde modes were found to be Rossby modes. We also discuss the limitations of the method that are due to the neglect of the centrifugal force and the incomplete treatment of the Coriolis force.
Conclusions. Despite its current limitations, the proposed method was successful to derive the rotation rates and to identify the modes from the observed period spacing patterns. It forms the first step towards detailed seismic modelling based on observed period spacing patterns of moderately to rapidly rotating γ Dor stars.

4.1 Introduction

In this chapter we focus on the period spacing patterns detected in Chapter 3 for our sample of 67 γ Dor stars and aim to derive the stellar internal rotation rates and the asymptotic period spacing value of the series. This serves as a first step for further detailed analyses of differential rotation, similar to the studies that have previously been carried out in slow rotators among g-mode pulsators and that have recently been interpreted in terms of angular momentum transport by internal gravity waves (e.g. Triana et al. 2015; Rogers 2015).

We present a grid of theoretical models, which we use as a starting point (Section 4.2), and explain our method to derive the rotation frequency (Section 4.3). The method is illustrated with applications on synthetic data (Section 4.4.1), a slowly rotating star with rotational splitting, KIC 9751996, and a fast rotator with a prograde and a retrograde period spacing series, KIC 12066947 (Section 4.4.2). We then analyse the sample as a whole (Section 4.4.3) before moving on to the discussion and conclusions (Section 4.5).

4.2 Grid of stellar models and pulsation frequencies

We first computed a rough grid of theoretical stellar models to gain further insight into the internal structure and properties of γ Dor stars. To allow for a complete understanding of the models and the impact of their input parameters, the models were purposely kept relatively simple, and we limited ourselves to the setup described in Section 1.1.3. The varying parameter values of the models in the grid are given in Table 4.1.

For each of the models in our grid we also computed the asymptotic period spacing $\Delta\Pi_l$ given in Equation (1.11). While $\Delta\Pi_l$ is smaller for higher values of l (as can be seen in Equation 1.11), $\Delta\Pi_l$ also changes as the star evolves. We therefore calculated the probability of observing different spacing values using the stellar ages in our grid models. As shown in Figure 4.1, we typically expect $\Delta\Pi_l$ values of about $3100\,s$ and $1800\,s$ for $l = 1$ and $l = 2$, respectively, which in turn implies that Π_0 is of the order of $4400\,s$. In addition, there are strong linear correlations for $\Delta\Pi_l$ between models with different values of M, Z, X, $f_{\rm ov}$, and $\alpha_{\rm ov}$, assuming a fixed hydrogen abundance X_c in the convective core.

As shown by Bouabid et al. (2013) and as we observed in Chapter 3, gravity-mode period spacing patterns are heavily influenced by rotation. We therefore introduced the influence of rotation on the pulsation periods using the traditional approximation, following the explanation given in Section 1.2.1. For each of the models in our grid, we computed the $l = 1$ and $l = 2$ mode frequencies for radial orders ranging from 5 to 120.

4.3 Method

As we have discussed in the Introduction in Section 1.2.1, the influence of rotation on the pulsation frequencies depends on the values of l and m, while

parameter	begin	end	step size
mass M $[M_\odot]$	1.4	2.0	0.05
metallicity Z	0.010	0.018	0.004
exp. core overshooting $f_{\rm ov}$	0.001	0.03	0.0075
step core overshooting $\alpha_{\rm ov}$	0.01	0.3	0.075
initial hydrogen abundance X_i	0.69	0.73	0.02

Table 4.1: Parameter values of the computed grid of 1170 MESA evolutionary tracks, consisting of some 900,000 models.

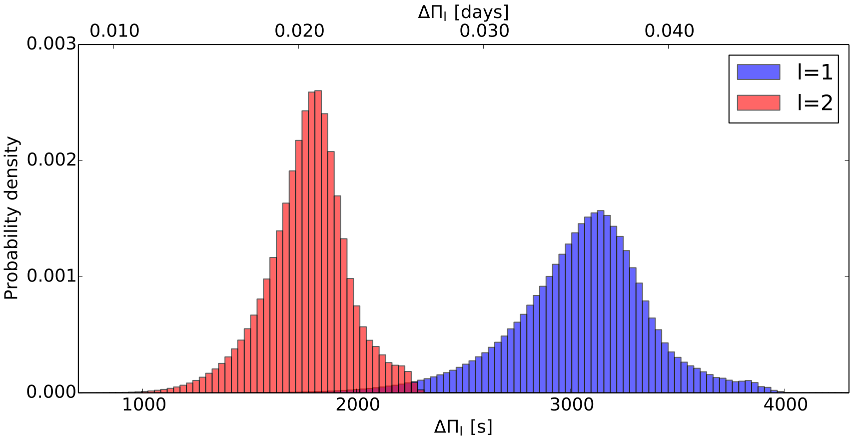

Figure 4.1: Distributions of the asymptotic period spacing values $\Delta\Pi_l$ for spherical degree $l = 1$ and 2 computed for the MESA evolution tracks with the input parameters provided in Table 4.1. The ages and evolution rates of the stellar models were taken into account in computing the distributions.

the asymptotic spacing $\Delta\Pi_l$ is dependent on the value of l (Eq. 1.11). It is therefore necessary to have a pulsation mode identification if we wish to constrain the rotation profile of the observed star properly.

To derive a reliable estimate of the rotation rate of a γ Dor star with one or more observed period spacing patterns, we considered all the possible combinations of l and m values for the mode identification of the GYRE pulsation frequencies computed for the MESA models in our grid. For each combination of l and m, we computed the asymptotic spacing value $\Delta\Pi_l$, as expressed in Eq. (1.11) and subsequently corrected it in the framework of the traditional approximation according to Eq. (1.14). This is illustrated graphically in Figure 4.2. Because the application of a rotational frequency shift does not introduce dips into the

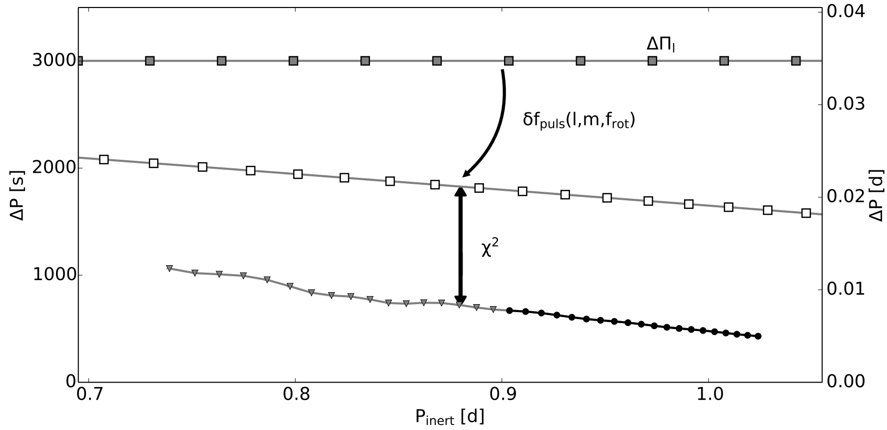

Figure 4.2: Illustration of our method to derive the rotation rate $f_{\rm rot}$ and asymptotic spacing $\Delta\Pi_l$ from an observed period spacing pattern (black dots). An equidistant spacing series (grey squares) is defined, rotationally shifted (white squares), and fitted to the observed pattern using χ^2-minimisation, optimising for the variables l, m, $\Delta\Pi_l$, and $f_{\rm rot}$.

period spacing patterns, we did not need to take them into account at this point. A uniform period spacing series is sufficient for our needs.

The pulsation frequencies in this series were then rotationally shifted using the traditional approximation, as described by Eq. (1.14) and assuming the star is rigidly rotating. The values of the pulsation periods in the inertial reference frame are then obtained by

$$P_{\rm inert} = \frac{1}{f_{\rm co} + m f_{\rm rot}}. \tag{4.1}$$

This introduced a slope into the model spacing series, as shown in Figure 4.2. The resulting pattern was subsequently fitted to the observed period spacing series using χ^2-minimisation, optimising for the variables $\Delta\Pi_l$ and $f_{\rm rot}$. Finally, we selected the best solution for all studied l and m values, taking into account the theoretical expectations for the asymptotic spacing $\Delta\Pi_l$, as shown in Figure 4.1 and derived from our model grid in Section 4.2. From this fit, we then obtained estimates for the rotation rate $f_{\rm rot}$ and the asymptotic spacing $\Delta\Pi_l$, as well as a mode identification.

4.4 Applications

4.4.1 Synthetic data

To illustrate our method, we first analyse a simulated period spacing pattern. The simulated data were computed using the MESA and GYRE codes with the input values provided in Table 4.2, further taking $(l,m) = (1,1)$. For the computation of the evolution track itself the influence of rotation was not taken into account. The rotation was only included in the GYRE computations using the traditional approximation module. The computed pattern is shown in Figure 4.3 and the values of the pulsation periods are listed in Appendix D in Table D.1.

The results of our analysis are shown in Figures 4.3 to 4.5. In Figure 4.3 we fitted the simulated data nicely when we excluded the dips in the pattern from the analysis and assumed $(l,m) = (1,1)$. However, similarly good results were obtained when we treated the pulsations as (2,1) modes or (2,2) modes during our analysis, as illustrated in Figure 4.4. In other words, we cannot obtain a unique mode identification based solely on the obtained χ^2-values. This problem is solved when we recall the expected values of the asymptotic spacing $\Delta\Pi_l$ for different values of l, which we previously showed in Figure 4.1. The values for $\Delta\Pi_l$ we found are clearly far too high for $l = 2$. We can therefore safely identify the simulated data as (1,1) modes, and obtain $f_{\rm rot} = 0.664 \pm 0.013\,{\rm d}^{-1}$ and $\Delta\Pi_{l=1} = 3020 \pm 190\,{\rm s}$.

It is important to exclude any significant dips in the period spacing structure from this analysis. In our technique, we do not take the influence of chemical gradients in the stellar interior into account. As shown by Miglio et al. (2008), these gradients result in non-uniform deviations from the asymptotic spacing series. Because we can only observe a small part of a period spacing pattern, any non-uniform variations in the pattern will change the measured mean spacing and/or the measured slope of the pattern. This, in turn, will influence our analysis. By ignoring significant non-uniform variations in the period spacing structure, we limit their influence on the analysis, so that we obtain results that are correct within or on the order of 1σ. For our simulated data set this is illustrated with the 2-dimensional χ^2-distribution shown in Figure 4.5. While we ignored the large dip in the period spacing structure (as seen in Figure 4.3), the remaining non-uniform variations still affected the analysis. As a result, there is a small offset between the input values of the data set and the 1σ-confidence interval for the obtained solution.

Furthermore, we also note that in the derivation of Equation (1.14) it is assumed we are working with pulsations in the asymptotic regime, where $n \gg l$. In

Table 4.2: Parameter values of the simulated period spacing pattern. *Top:* the input parameters of the MESA evolution track. *Bottom:* the parameters of the model for which the pulsation periods were computed.

parameter	values
mass M $[M_\odot]$	1.63
metallicity Z	0.016
initial hydrogen abundance X_i	0.71
mixing length parameter $\alpha_{\rm MLT}$	1.8
step core overshooting $\alpha_{\rm ov}$	0.18
mixing coefficient D $[{\rm cm}^2{\rm s}^{-1}]$	0.8
$T_{\rm eff}$ [K]	7047
$\log g$ [dex]	4.34
$[M/H]$ [dex]	0.094
$v_{\rm eq}$ $[{\rm km\,s}^{-1}]$	69.38
$f_{\rm rot}$ $[{\rm d}^{-1}]$	0.674
$\Delta\Pi_{l=1}$ [s]	3186.5
central hydrogen abundance X_c	0.357

other words, the period spacing patterns corresponding to any excited low-order pulsation may exhibit strong non-uniform variations. This can be seen in Figures 1.5 and 1.6 in Chapter 1. Thus, by excluding non-uniform variations in the period spacing patterns from the analysis, we automatically limit the application of our method to its valid range.

4.4.2 Slow and fast rotator

KIC 9751996

In our sample we have one slowly rotating star, KIC 9751996, for which we detected period spacing series with rotational splitting, delivering immediately the m-values of the modes. To additionally validate our proposed method, we have applied it to KIC 9751996. In a first step, we only analysed the prograde period spacing pattern to test the reliability of our method. Assuming $(l,m) = (1,1)$, this led us to find $f_{\rm rot} = 0.07 \pm 0.02\,{\rm d}^{-1}$, which is shown in the top panel of Figure 4.6. However, assuming $l = 1, m = 0$ for the treated series, we found $f_{\rm rot} = 0.19 \pm 0.03\,{\rm d}^{-1}$ for a similar χ^2 value. The challenge in this case is that the shift and slope in the period spacing pattern are almost negligibly small compared to the non-uniform period spacing variations as a result of a chemical gradient. This was resolved when we fit the prograde, zonal, and

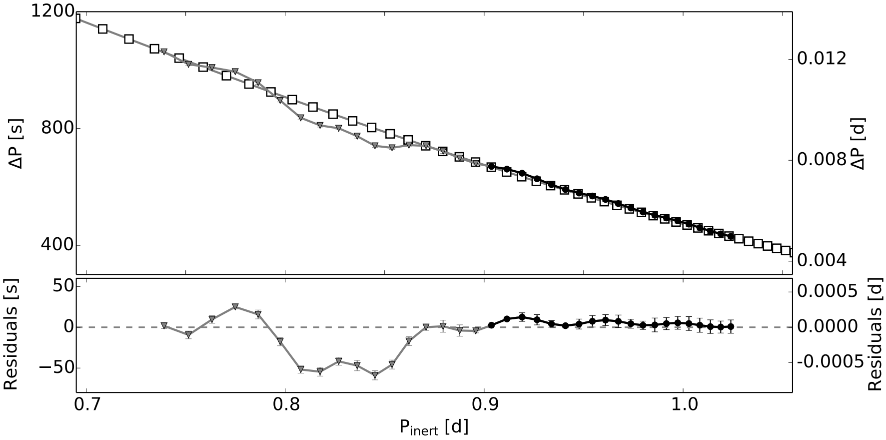

Figure 4.3: *Top:* the input period spacing pattern (black dots and grey triangles) with the best-fitting pattern (white squares) as obtained from the χ^2-minimisation in Figure 4.5 assuming $(l,m) = (1,1)$. The black part of the input patterns was used to determine $f_{\rm rot}$ and $\Delta\Pi_l$, while the grey section was excluded. *Bottom:* the residuals of the fit.

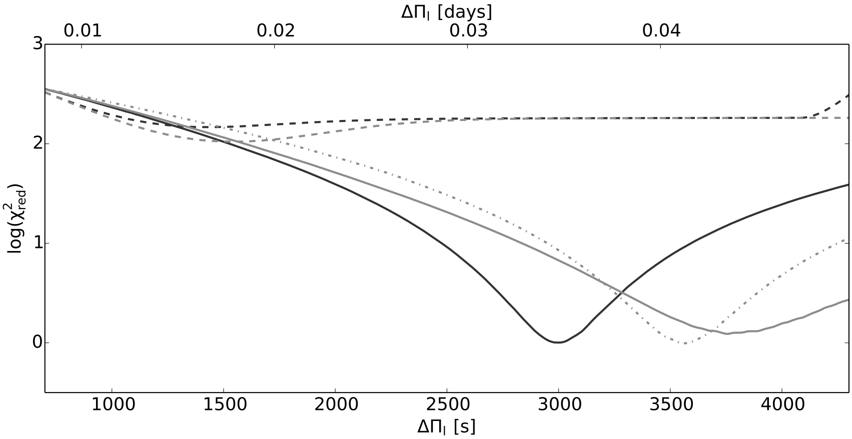

Figure 4.4: Best χ^2-values for the synthetic data shown in Figure 4.2 for each (l, m) combination, as a function of the asymptotic spacing $\Delta\Pi_l$. The black and light grey lines correspond to $l = 1$ and $l = 2$, respectively, while the modes with $m = 0$ are indicated with dashed lines, $m = 1$ with full lines, and $m = 2$ with the dash-dotted line.

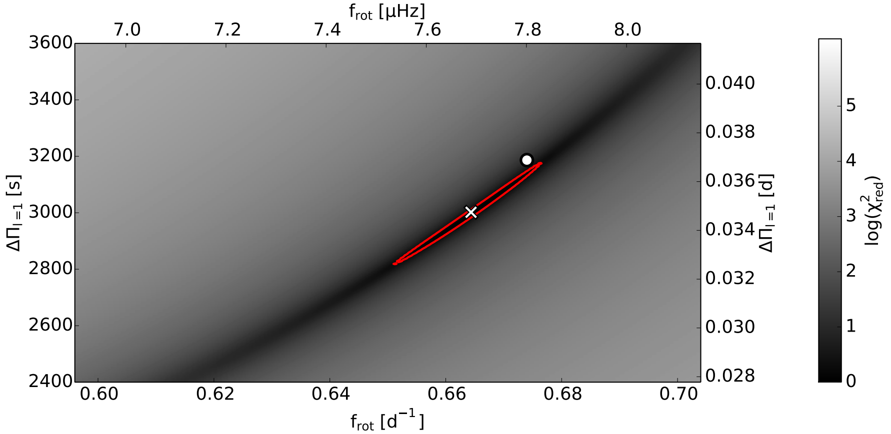

Figure 4.5: $\log(\chi^2_{\mathrm{red}})$ for the simulated period spacing series assuming $l = 1$ as a function of the asymptotic period spacing $\Delta\Pi_l$ and the rotation rate f_{rot}. The white dot indicates the input values, while the white cross and the red boundary indicate the solution and its 1σ-uncertainty margins, respectively.

retrograde dipole modes simultaneously, as shown in Figure 4.7. Not only did this allow us to formally identify the (l, m, n) values of the modes, it also resulted in a much higher precision for the rotation rate $f_{\mathrm{rot}} = 0.070 \pm 0.001\,\mathrm{d}^{-1}$ and the spacing $\Delta\Pi_{l=1} = 3086 \pm 12\,\mathrm{s}$ (see Figure 4.6). Interestingly, we have another independent indication for this derived rotation rate. In the series of the prograde and retrograde modes, we have pulsation periods that do not seem to follow the pattern at values of 0.8 days and 0.9 days, respectively. These modes are likely trapped, which has influenced their pulsation period. When the periods of these retrograde and prograde modes are converted into their values in the corotating reference frame using the derived rotation rate, we find that the pulsation periods are almost equal, which is consistent with the interpretation of trapped pulsation modes.

KIC 12066947

Next we also analysed the period spacing patterns of KIC 12066947, a fast-rotating star for which both a prograde and a retrograde period spacing series were detected. While we were able to fit the pattern of prograde modes to derive a rotation rate f_{rot}, the observed retrograde series presented us with a challenge. We found these to correspond with Rossby modes rather than “classical” gravity or gravito-inertial modes. This is illustrated in the top panel

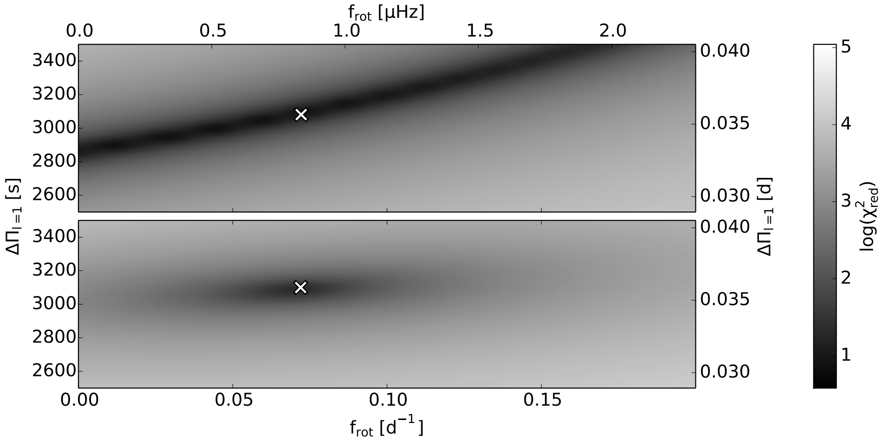

Figure 4.6: $\log(\chi^2_{\rm red})$ for the observed period spacing series of KIC 9751996, assuming $l = 1$, as a function of the asymptotic period spacing $\Delta\Pi_l$ and the rotation rate $f_{\rm rot}$. The white crosses indicate the best-fit solutions. *Top:* the χ^2-distribution that we find by only analysing the detected prograde series. *Bottom:* the χ^2-distribution obtained by fitting the prograde, zonal, and retrograde spacing series simultaneously.

of Figure 4.8, where we show the observed period spacing patterns for the detected prograde and retrograde series, as well as the spacings predicted by the most suitable model in the grid, by assuming the values for $f_{\rm rot}$ and $\Delta\Pi_l$ obtained by modelling the prograde series. To calculate the period series for the Rossby modes, Π_0 was derived from $\Delta\Pi_l$ using Eq. (1.11), and this value was subsequently filled into Eq. (1.14). The appropriate eigenvalues λ were computed using the asymptotic approximation derived by Townsend (2003b), that is, Eq. (37) in that study. This equation is valid when $\lambda \neq m^2$, as is the case here. The expected values of λ for Rossby modes are three to four orders of magnitude smaller than for retrograde gravito-inertial modes, which allowed us to identify the observed pulsations. However, as Townsend (2003b) pointed out, the asymptotic approximation does not converge well to the numerical solution for these modes. The possibility of computing Rossby modes had not yet been included in the publicly available version of GYRE at the time of the original publication. As a consequence, we were unable to perform a reliable quantitative analysis of the retrograde series at this point and focused on the analysis of the prograde series to derive $f_{\rm rot}$. However, several qualitative arguments can be made in favour of Rossby modes as a correct identification. From the upward slope and the small average period spacing of the observed

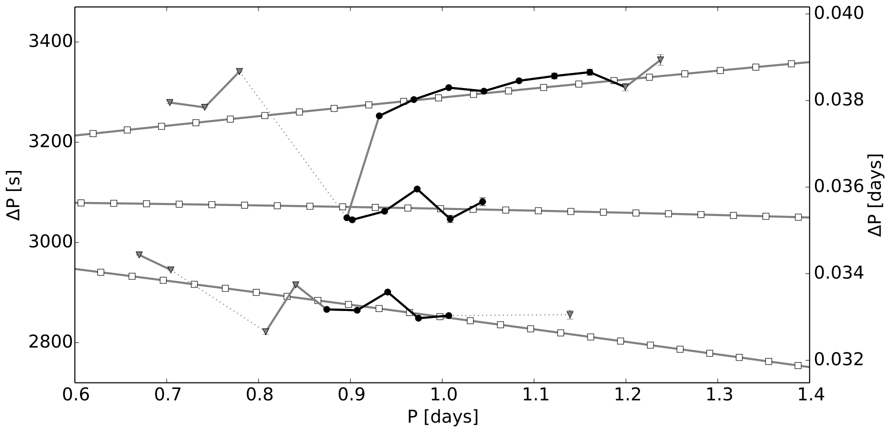

Figure 4.7: Observed period spacing patterns (black dots and grey triangles) for the retrograde (top), zonal (middle), and prograde (bottom) modes of KIC 9751996. The black parts of the input patterns were used to determine f_{rot} and $\Delta\Pi_l$, while the grey sections were excluded. The white squares indicate the modes of the optimal model in the grid when all three series are fitted simultaneously.

pattern, we derive that these modes are retrograde in the corotating frame with $|f_{\mathrm{co}}| < f_{\mathrm{rot}}$, which is completely in line with theoretical expectations. Furthermore, the observed spin parameter values are higher for the retrograde than for the prograde modes: the values of the dominant modes of the two series are 15.8 ± 0.4 and 7.7 ± 0.1, respectively. This indicates that in the corotating frame the pulsation frequencies of the retrograde modes are smaller than those of the prograde modes, which in turn can be explained by the low values of the eigenvalues λ. Finally, Townsend (2003b) also noted that, compared to the retrograde gravito-inertial modes, Rossby modes are less equatorially confined as the stellar rotation rate increases. As a result, the latter can be expected to be less influenced by the geometrical cancellation effects, although the effect is still present. For KIC 12066947, we find that the dominant prograde and Rossby modes are confined within equatorial bands with a width of 77.2° and 53.5°, respectively.

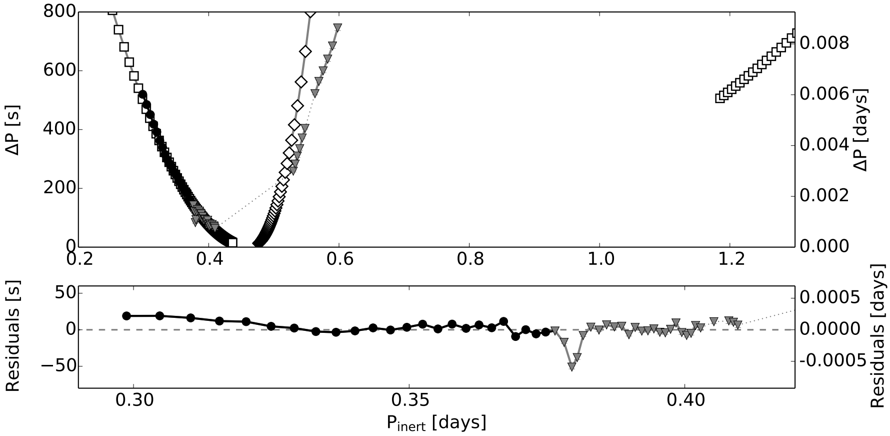

Figure 4.8: *Top:* Observed period spacing patterns (black dots and grey triangles) for the prograde (left) and retrograde (right) modes of KIC 12066947. The black part of the pattern was used to determine $f_{\rm rot}$ and $\Delta\Pi_l$, while the grey section was excluded. The white squares indicate the model fit, assuming these are gravito-inertial modes and using the $f_{\rm rot}$ and $\Delta\Pi_l$ values obtained from the analysis of the marked prograde series. The white diamonds indicate the model computed for Rossby modes using the same $f_{\rm rot}$ and $\Delta\Pi_l$ values, assuming $m = -1$ and $k = -2$ in the k-based indexing scheme by Lee & Saio (1997). *Bottom:* The residuals of the fit to the prograde period spacing series.

4.4.3 Sample study

Subsequently, we also applied our method to the other stars in our sample. This led to the mode identification and determination of the rotation rate $f_{\rm rot}$ for the period spacing series of 40 stars in our sample. Six additional sample stars only exhibit retrograde modes and fast rotation, and cannot be quantitatively analysed with our current methodology. The difference of the best χ^2-value for different (l,m) combinations is too small for the remaining stars, therefore no unique solution could be determined.

For the 40 stars that were successfully analysed, the results are listed in Appendix D in Table D.2. The vast majority of these stars were found to exhibit prograde dipole modes. For fourteen targets in the sample we detected multiple series. In principle, these are prime targets to look for differential rotation. However, for ten of them the second detected period spacing pattern corresponds to Rossby modes, for which we still need to develop a suitable computational tool to arrive at appropriate numerical values, as discussed in Section 4.4.2.

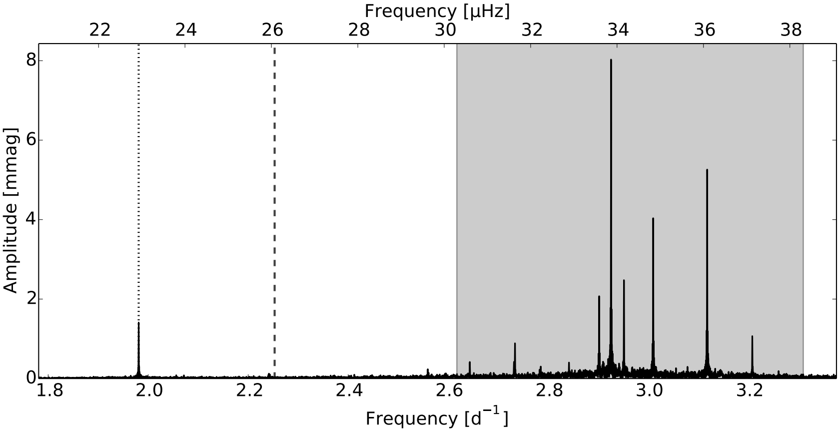

Figure 4.9: Part of the frequency spectrum of KIC 7365537. The light grey area shows the location of the pulsation modes that form the detected period spacing pattern of this star. The dashed line shows the value of the derived rotation frequency $f_{\rm rot}$, while the dotted line indicates the isolated high-amplitude mode we found.

For the remainder of this study, we assign the values of $f_{\rm rot}$ and $\Delta\Pi_l$ that we obtained from the prograde series to the retrograde series of the same star. Because formal mode identification of these retrograde pulsations is currently not possible, they are marked as “R” in Table D.2. For two other stars we have both a zonal and prograde dipole series, while for a third we have prograde dipole and quadrupole modes. Finally, KIC 9751996, the slowly rotating star we discussed in Section 4.4.2 is the only target for which we have a series of rotationally split multiplets. For each of these last four stars, we were able to use the multiple detected period spacing patterns to refine the obtained $f_{\rm rot}$ and $\Delta\Pi_l$.

There are several stars for which a single high-amplitude mode was detected that does not belong to a period spacing series and that differs from the rotation frequency. In Figure 4.9 we show the frequency spectrum of KIC 7365537 as an example. For these modes the identification in Table D.2 is marked “S”. Because our method cannot be applied to these single modes, we again used the values of $f_{\rm rot}$ and $\Delta\Pi_l$ that were derived from the prograde series in the same star in the subsequent analysis. The selection of series of modes in some stars versus the presence of single modes in others also provides much information about their respective stellar structure. It has been suggested by Dziembowski & Pamyatnykh (1991) that such single high-amplitude modes might be caused by mode trapping effects. However, detailed theoretical modelling of each of these individual stars is required to confirm this or come up with an alternative explanation.

Figure 4.10 illustrates the frequency $f_{\rm dom,corot}$ of the dominant mode of each detected series in the corotating frame with respect to the computed rotation frequency. An alternative version of Figure 4.10 in the inertial reference frame is included in Appendix D in Figure D.1. For the majority of the stars, we obtain values of $f_{\rm dom,corot}$ between 0.15 and $0.75\,{\rm d}^{-1}$. This can be linked to the convective flux blocking excitation mechanism. Dupret et al. (2005) and Bouabid et al. (2013) remarked that for the mode excitation mechanism to be efficient, the thermal time scale $\tau_{\rm th}$ at the bottom of the convective envelope has to be similar to the pulsation periods in the corotating frame. From this information and the content of Figure 4.10, we can also derive that the detected retrograde spacing series and single modes most likely have azimuthal order $m = -1$ because only $|m| = 1$ led to similar $f_{\rm dom,corot}$ values for the series of different stars. While these results are consistent, we note that the observed pulsation periods in the corotating frame are typically longer than the theoretical values computed by Bouabid et al. (2013). For the retrograde Rossby modes this can be linked to the correspondingly low eigenvalues λ of the Laplace tidal equation. However, the same discrepancy is observed for the prograde modes as well, although to a lesser degree. This discrepancy may point towards limitations of the current theory of mode excitation in γ Dor stars for moderate to fast rotators or may be caused by the limited applicability of the traditional approximation for these rotation rates. Further research on this topic is required.

In Figure 4.11 we show the spin parameter s, as defined in Eq. (1.13) and listed in the last column of Table D.2, as a function of the measured rotation frequency $f_{\rm rot}$. The spin parameter s is a measure of the effect of rotation on the pulsation frequency and is inversely proportional to the pulsation frequency $f_{\rm co}$ in the corotating frame. Once again, the Rossby modes (shown as dark blue dots) have low values for the eigenvalue λ. In addition, although both prograde sectoral modes and Rossby modes are less easily confined in a band around the equator, the effect is still significant for these high values of s (Townsend 2003b). In addition, our observed values of s are on average much higher than the values quoted in theoretical papers in the literature (e.g. Townsend 2003a; Ballot et al. 2012). This implies that many of the stars in our sample are seen at moderate to high inclination angles.

Figure 4.12 shows the three slowest rotating stars in our sample in greater detail, one of which is KIC 9751996, which has been discussed in Section 4.4.2. These three stars have comparable properties. They are slow rotators, placing them in the superinertial regime, and they are hybrid γ Dor/δ Sct candidates. Each

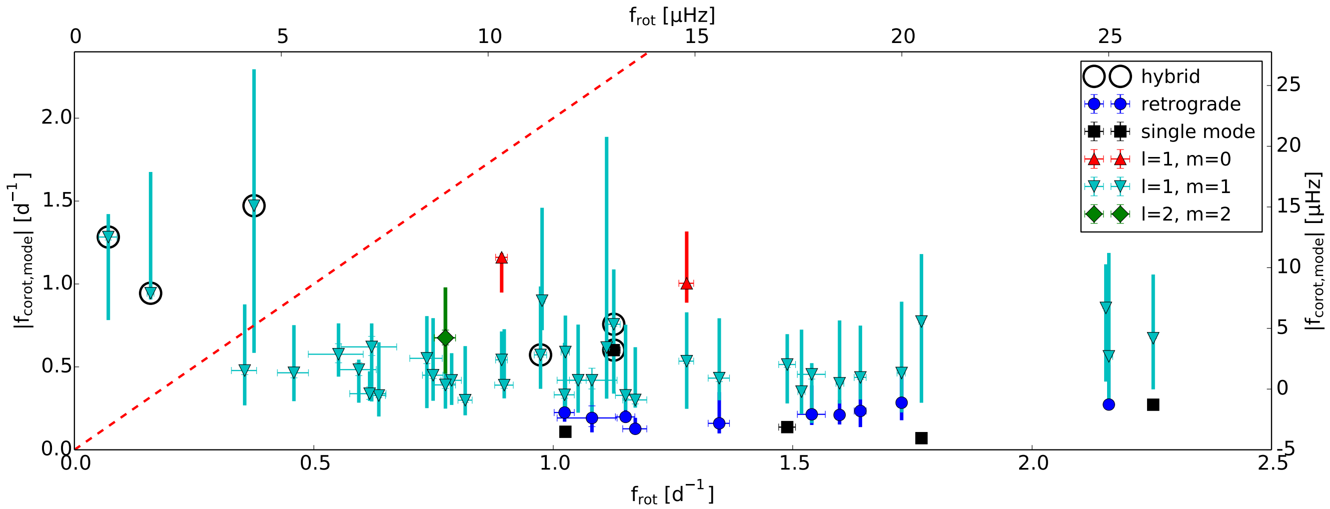

Figure 4.10: Dominant pulsation frequency $f_{\mathrm{dom,corot}}$ in the corotating frame as a function of the rotation frequency f_{rot} for the identified g-mode pulsations of 40 stars in the sample. The thick vertical lines do not represent error bars, but indicate the full extent of the detected spacing series. The dashed red line shows where the pulsations pass from the superinertial regime (above the line) into the subinertial regime (below the line).

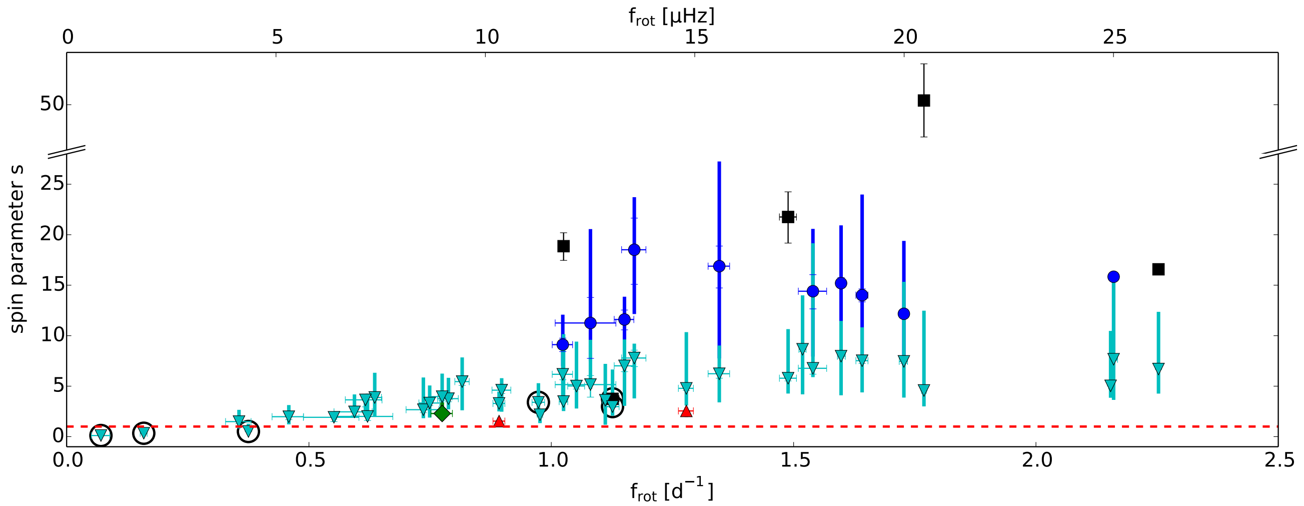

Figure 4.11: Absolute value of the spin parameter s for the detected period spacing series of the stars in our sample as a function of the rotation frequency $f_{\rm rot}$. The dashed red line shows where the pulsations pass from the superinertial regime (below the line) into the subinertial regime (above the line). The symbols are the same as in Figure 4.10, and the thick vertical again do not represent error bars, but indicate the full extent of the detected spacing series.

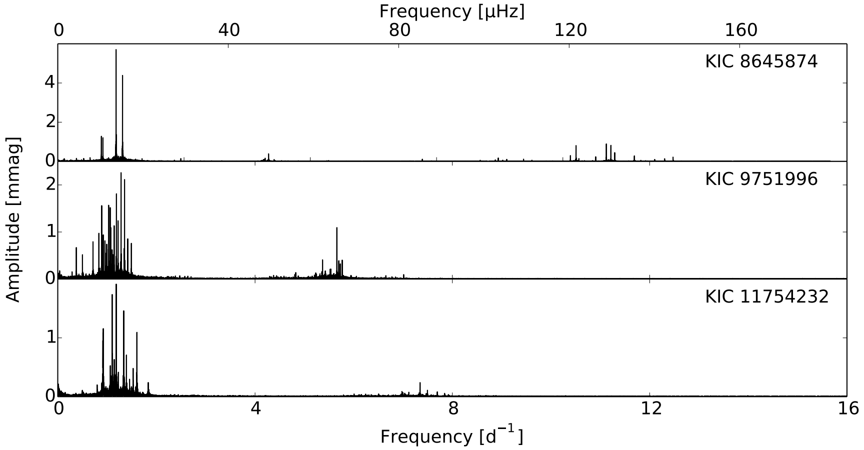

Figure 4.12: Section of the Fourier spectra of the three slowest rotating stars in our sample. These are our only stars in the superinertial regime, and all three are hybrid $\gamma\,$Dor/$\delta\,$Sct candidates with variability between $5\,\mathrm{d}^{-1}$ and $8\,\mathrm{d}^{-1}$.

of them exhibits variability in the frequency range between $5\,\mathrm{d}^{-1}$ and $8\,\mathrm{d}^{-1}$. These striking similarities suggest that there is a link between the low stellar rotation rates and their (possibly) hybrid properties, marking them interesting targets for follow-up research. During the last two years, other similar slowly rotating hybrid $\gamma\,$Dor/$\delta\,$Sct pulsators have been reported and studied in the literature as well (Kurtz et al. 2015; Saio et al. 2015; Murphy et al. 2016; Gizon et al. 2016).

Statistical analysis

Finally, we also searched for correlations between the parameter values of our stars, similar to the multivariate statistical analysis that was carried out in Chapter 3 and listed in Table C.3 in Appendix C. In this work, we again used the spectroscopic fundamental parameter values obtained in Chapter 3. We also included the detected values of the variables f_{rot}, $\Delta\Pi_l$, $R\sin i = v\sin i/f_{\mathrm{rot}}$ and the dominant pulsation frequency f_{dom} (in the corotating and the inertial reference frame). For consistency, we focused on the parameter values derived from the identified prograde dipole mode series of 40 stars in the sample. The results of our multivariate statistical study are summarised in Table 4.3.

Most of the correlations presented in Chapter 3 were indicative of the strong relation between the observed gravity-mode pulsations and the stellar rotation.

In retrospect, these can now be linked to the identification of most pulsations as prograde dipole gravity, gravito-inertial, or retrograde Rossby modes with $|m| = 1$. In particular, those previous results are echoed in our current work by the detected correlations between $f_{\rm rot}$ and $v \sin i$, and $f_{\rm rot}$ and $f_{\rm dom,inert}$. The strong correlation between $f_{\rm rot}$ and $v \sin i$ is illustrated in Figure 4.13. We can also obtain estimates for the inclination angles of the observed stars from the derived rotation frequencies and the spectroscopic $v \sin i$ values, if we assume that they are rotating rigidly and if we have estimates for the stellar radii. As a first step, we computed the average stellar radius for the grid of models which we discussed before in Section 4.2, and found $\langle R_* \rangle = 2.0 \pm 0.5\,R_\odot$. Adopting for all stars in the ensemble, we obtained the inclination angle estimates shown in Figure 4.14. These are completely in line with our expectations: overall, the stars are seen from a relatively high inclination angle, most likely because of the equatorial confinement of stellar pulsations at higher values for the spin parameter s. The distribution of inclination angles $i \gtrsim 30°$ is quite broad. Furthermore, two of the stars for which lower inclination angle estimates were found, KIC 4846809 and KIC 9595743, are also the stars for which we detected zonal dipole modes. This is consistent with expectations for the geometrical cancellation effects of the pulsations. We stress that these inclination estimates cannot be but a first rough initial estimate and that better estimates require a through seismic estimate of the stellar radius for each of the individual stars separately, rather than this global ensemble analysis.

The previously detected correlations between $v \sin i$ and the mean period spacing $\langle \Delta P \rangle$, the mean pulsation period $\langle P \rangle$ and the mean slope $\langle \frac{{\rm d}\Delta P}{{\rm d}P} \rangle$ of the observed series discussed in Chapter 3 are now also reflected in similar correlations with $f_{\rm rot}$. As illustrated in Figures 4.15 and 4.16, we do find a level of scatter in the relationship between these parameters and the rotation rate $f_{\rm rot}$, originating from the broad variety of radial orders of the detected modes, the limited lengths of some of the observed series, and from non-uniform variations in the period spacing patterns covered by our sample. Moreover, we assumed a constant rotation rate throughout the stars to deduce $f_{\rm rot}$, which is simplistic compared to observations (e.g. Kurtz et al. 2014) and predictions based on numerical simulations (Rogers 2015). Allowing for a variety of non-uniform interior rotation profiles will likely complicate the correlations.

These results are in line with the recent study by Ouazzani et al. (2017). The authors proposed using the slope of an observed period spacing pattern, derived from a simple linear fit, as a direct measure for the core rotation rate $f_{\rm rot}$. From our findings, we can confirm the validity of this relation. However, as noted by Ouazzani et al. (2017) as well, additional information about the average pulsation period and average period spacing is required when real stars are analysed. This is particularly important when pulsations with higher radial orders n

are studied. In addition, there are several aspects of the study by Ouazzani et al. (2017), which was conducted simultaneously to the work presented in this Chapter, that are complementary to our own. For instance, the authors relied on two-dimensional stellar models to validate their method, and directly compared the results to ones obtained with the tradiational approximation, which we use. Ouazzani et al. (2017) find a significant impact on the morphology of the period spacing patterns on a frequency-by-frequency basis. However, the authors only observe a small impact on global parameters such as the slope, average pulsation period and average period spacing of an observed pattern, on the order of the impact of chemical mixing and stratification. This is a reassuring validation of our approach in this Chapter, considering their two-dimensional models also include the effect of, e.g., the centrifugal force, which cannot be taken into account within the traditional approximation. One exception to this result are the period spacing patterns of retrograde gravito-inertial modes, for which the differences between the two approaches are already noticeable at moderate rotation rates.

In the previous Chapter we also reported a smaller contribution of $T_{\rm eff}$ to the multivariate correlation with $f_{\rm dom,inert}$ and $v\sin i$, but this contribution drops when we replace $v\sin i$ with $f_{\rm rot}$. While a weak correlation between $R\sin i = v\sin i/2\pi f_{\rm rot}$ and $T_{\rm eff}$ is still present, we would like to point out that a more meaningful comparison can be made between $T_{\rm eff}$ and the pulsation periods of the detected pulsation series in the co-rotating frame. This can be seen in Figure 4.17, where the predictions by Bouabid et al. (2013) for different rotation velocities are also shown. A detailed non-adiabatic study lies outside the scope of this work, but it is interesting to note that the observed pulsation periods are typically longer than the theoretical predictions, even when the relatively higher rotation rates of the observed stars are taken into account. The outlier in Figure 4.17 is KIC 9480469, which has a temperature $T_{\rm eff}$ of $7250 \pm 240\,$K. These uncertainty margins are the largest of all the stars in our sample. This implies that KIC 9480469 may very well have a lower value for $T_{\rm eff}$ than what is shown in Figure 4.17.

Furthermore, a weak correlation was found between $f_{\rm rot}$ and log g, indicating that as the star evolves and its radius increases, the surface gravity and the rotation rate both decrease. This is reflected on a larger sample in Figure 4.18, which shows the rotation rates of different types of stars as a function of log g (used as a proxy of age). Although the BAF core-hydrogen burning stars in Figure 4.18 may be too massive to be the progenitors of the subgiants and the red giants, the large difference in rotation rate between the stars at different evolutionary stages is striking.

In contrast, we did not find correlations between the asymptotic spacing $\Delta\Pi_l$ and any of the other parameters. The uncertainty margins on the value of

Table 4.3: Results of the linear regression analysis. We list the coefficients of the covariates for the different correlations with their errors, as well as their p-values (obtained from a t-test) and R^2 values.

Explanatory variable	Dependent variable	Intercept	Estimate	p-value	R^2
f_{rot} [d^{-1}]	$v \sin i$ [km s^{-1}]	0(16)	74(5)	< 0.0001	0.859
f_{rot} [d^{-1}]	$f_{\mathrm{dom,inert}}$ [d^{-1}]	0.7(0.3)	0.90(0.08)	< 0.0001	0.780
f_{rot} [d^{-1}]	$\langle P \rangle$ [d]	0.9(0.1)	-0.22(0.06)	< 0.0001	0.630
f_{rot} [d^{-1}]	$\langle \Delta P \rangle$ [d]	0.017(0.005)	-0.009(0.002)	< 0.0001	0.508
f_{rot} [d^{-1}]	$\langle \frac{\mathrm{d}\Delta P}{\mathrm{d}P} \rangle$	-0.013(0.006)	-0.013(0.001)	< 0.0001	0.479
T_{eff} [K]	$R \sin i$ [$R_\odot$]	573(10)	-0.08(0.02)	0.0001	0.357
log g [dex]	f_{rot} [d^{-1}]	-5.8(0.4)	1.7(0.4)	0.0002	0.332

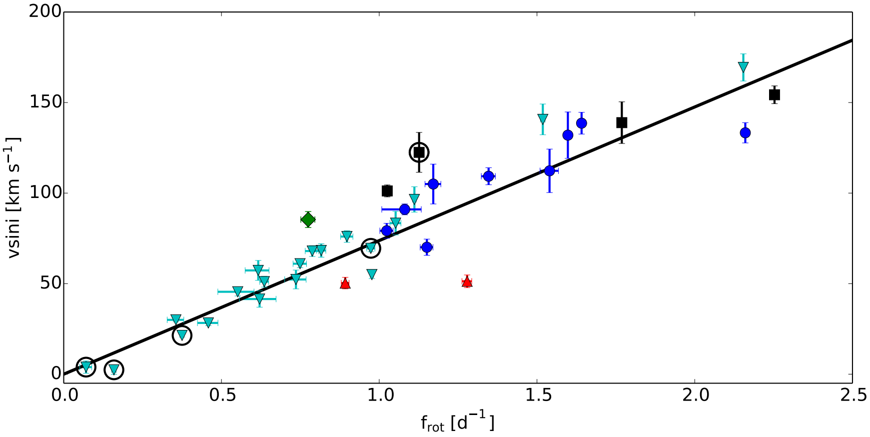

Figure 4.13: Correlation between the spectroscopic $v \sin i$ values and the values of the rotation rate f_{rot} . The black line indicates the corresponding linear fit, for which the coefficients are listed in Table 4.3. The symbols are the same as in Figure 4.10. For all of the stars a series of prograde dipole modes was detected. If another series was detected as well, the symbol of the corresponding mode identification was used.

$\Delta\Pi_l$ are likely too large for a proper correlation to be unravelled. Multivariate correlations were not detected either.

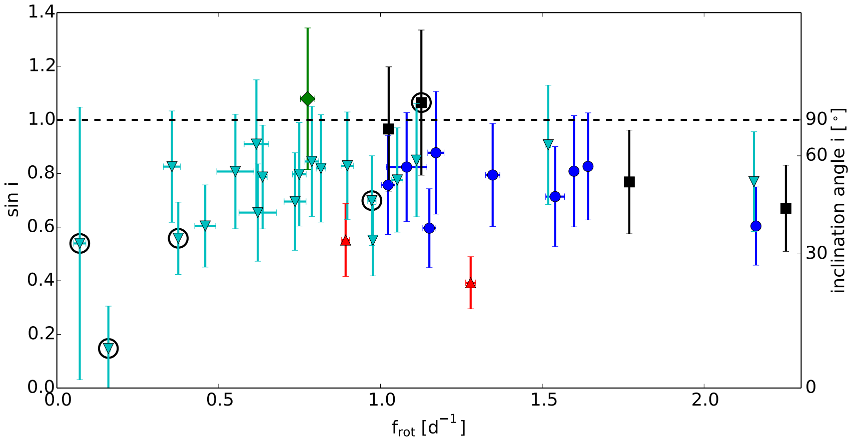

Figure 4.14: Estimates of the inclination angles of the observed stars, derived from the spectroscopic $v \sin i$ values and the rotation rates $f_{\rm rot}$. Hereby it was assumed that the stars rotate rigidly and have a stellar radius R_* of $2.0 \pm 0.5\, R_\odot$. The black dashed line indicates an inclination angle i of 90°. The symbols are the same as in Figure 4.10. For all of the stars a series of prograde dipole modes was detected. If another series was detected as well, the symbol of the corresponding mode identification was used.

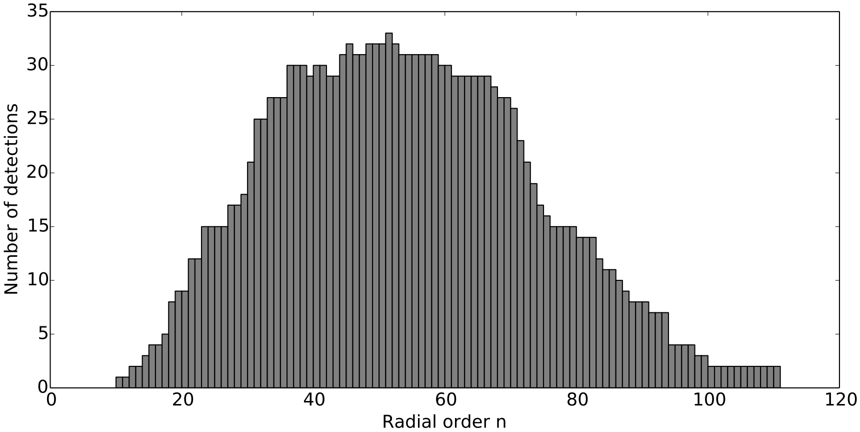

Figure 4.15: The prevalence of the radial orders n of the pulsations in the detected period spacing patterns. Following the computation of the rotation frequency $f_{\rm rot}$ and the mode identification, radial orders were derived using Equation 1.14.

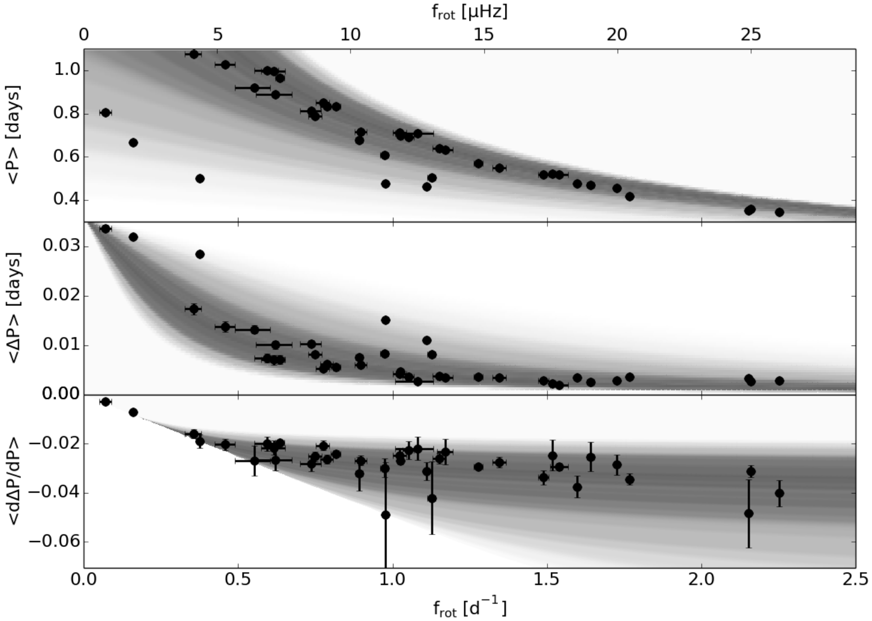

Figure 4.16: The average pulsation period $\langle P \rangle$, period spacing $\langle \Delta P \rangle$ and slope $\langle \frac{\mathrm{d}\Delta P}{\mathrm{d}P} \rangle$ of the observed $(l, m) = (1, 1)$ pulsation patterns in the inertial reference frame, with respect to the derived rotation rates f_{rot}. The grey shaded areas indicate the expected relation for the radial orders n observed in our data, assuming $\Delta\Pi_{l=1} = 3100\,\mathrm{s}$. The intensity of the shaded regions corresponds to the prevalence of the different values of n, as illustrated in the histogram in Figure 4.15: dark grey refers to a higher likelihood to observe a radial order n.

4.5 Discussion and conclusions

We have presented a method to derive the near-core interior rotation rate f_{rot} from an observed period spacing pattern and to perform mode identification for the pulsations in the series. In a first step, we considered all combinations of l and m values for mode identification. For each pair of l and m, we considered the asymptotic spacing $\Delta\Pi_l$ and computed the corresponding equidistant model period spacing pattern as described by Tassoul (1980). Using the traditional approximation, the frequencies of the model pattern were then shifted for an assumed rotation rate f_{rot} and the chosen l and m. The best-fit values of $\Delta\Pi_l$, f_{rot}, l, and m were then determined by fitting the model pattern to the observed period spacing series using least-squares optimisation and taking into account

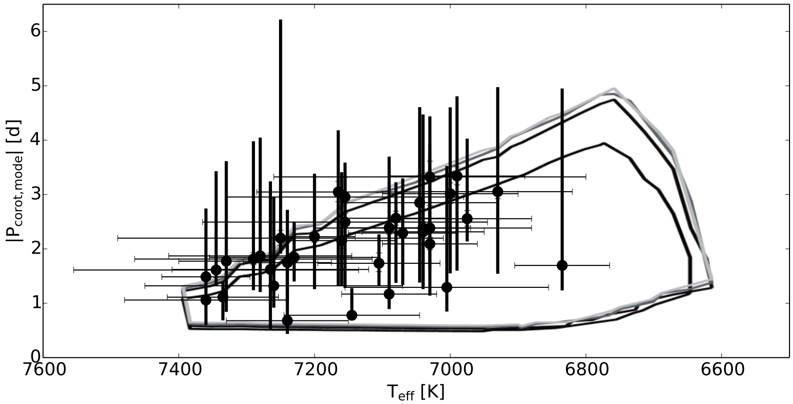

Figure 4.17: The pulsation periods of the observed (l, m) = (1,1) series in our sample, in the co-rotating reference frame, with respect to the observed temperature T_{eff}. The black markers indicate the dominant pulsation of each series, while the vertical lines show the extent of the corresponding pulsation patterns. The closed loops show the period ranges of the unstable (l, m) = (1,1) g-modes, computed by Bouabid et al. (2013) for equatorial rotation velocities $v_{eq} = 0\,\text{km}\,\text{s}^{-1}$ (black), $30\,\text{km}\,\text{s}^{-1}$ (dark grey), $60\,\text{km}\,\text{s}^{-1}$ (grey) and $90\,\text{km}\,\text{s}^{-1}$ (light grey).

that different values of $\Delta\Pi_l$ are expected for different values of l.

In most cases this method was reasonably successful. For slow rotators it may be difficult to find the correct value for the azimuthal order m, although this problem is solved when multiple series with different l and m values are considered. By fitting these series simultaneously, not only did we obtain the mode identification, but the values for $\Delta\Pi_l$ and f_{rot} were also much more precise than when we did not detect multiplets. When we considered a moderate to fast rotator, the retrograde modes were found to be Rossby modes, which arise from the interaction between the stellar rotation and toroidal modes. We used the asymptotic approximation derived by Townsend (2003b) to compute their eigenvalues λ of the Laplace tidal equation. A complete numerical treatment of these modes is required to exploit them quantitatively. A complete and detailed analysis of such stars with multiple gravity-mode period spacings will allow us to study possible differential rotation in γ Dor stars, ultimately leading to proper observational constraints on rotational chemical mixing and angular momentum transport mechanisms. It is noteworthy that our method was meanwhile also applied to five newly discovered rotating slowly pulsating B stars (Pápics et al.

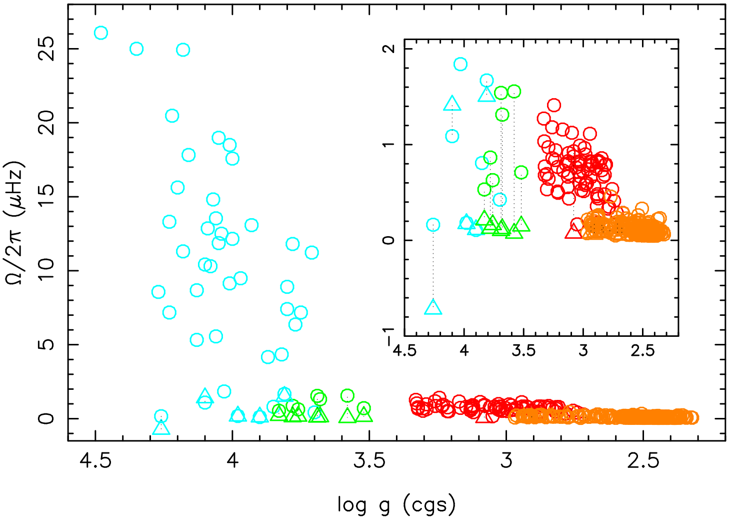

Figure 4.18: Near-core (circles) and envelope (triangles) rotation frequencies of BAF (cyan) core-hydrogen burning stars (including the γ Dor stars in this work), as well as of subgiants (green), of hydrogen-shell (red) and core-helium (orange) red giants, as a function of their log g (a proxy of their age), as deduced from photometry assembled by the *Kepler* satellite. The plot is an update of Figure 4 in Aerts (2015) to which we refer for the input data, with the stars from Table D.2 in this text and from Triana et al. (2015), Moravveji et al. (2016), Schmid & Aerts (2016) and Murphy et al. (2016) added to it. Dotted lines connect values of the same star. The plot covers the mass range from 0.8 to 3.3 $M_\odot$. Figure courtesy of C. Aerts.

2017).

From the ensemble modelling of the gravity-mode period spacings of the stars in our sample, we found that there is a wide range in the stellar rotation rates. Interestingly, only three out of forty targets were found to be in the superinertial regime. These three stars, KIC 8645874, KIC 9751996, and KIC 11754232, are hybrid γ Dor/δ Sct candidates that exhibit variability in the frequency range from 5 d^{-1} to 8 d^{-1}. This indicates that these low stellar rotation rates are most likely linked to their possibly hybrid character, making them prime targets for further asteroseismological analysis. The other stars were found to be in the subinertial regime. Their pulsation frequencies in the corotating frame are typically confined in the narrow range between 0.15 and 0.75 d^{-1}. This is in agreement with the theoretical expectation that γ Dor pulsation frequencies in the corotating frame are approximately on the thermal time scale $\tau_{\rm th}$ at the bottom of the convective envelope (Bouabid et al. 2013). However, this frequency range does not agree with the predicted values by Bouabid et al. (2013). With the exception of the three stars in the superinertial regime, we found that on average the observed modes have longer pulsation periods in the corotating frame than theory predicts. This is also reflected in the high spin parameter values we derived for many of the stars. The high spin parameters detected for the retrograde Rossby modes are linked to the low eigenvalues λ of these modes, as already found on theoretical grounds by Townsend (2003b).

The global results for the mode identification are consistent with existing spectroscopic studies. The majority of the modes were found to be prograde dipole modes. This is in line with the results obtained by Townsend (2003a) for heat-driven gravity modes in slowly pulsating B stars. In addition, we found single high-amplitude modes, as opposed to a series, to be present in several stars. They are consistent with retrograde Rossby modes with $m = -1$. They are most likely heavily influenced by mode trapping, and as a result contain valuable information about the internal structure of these stars.

We conducted a linear regression analysis on the combined spectroscopic and photometric parameter values for the sample. The strong correlation between $v \sin i$ and $f_{\rm rot}$ independently confirmed the reliability of the obtained rotation rates. We also detected weak correlations between $R \sin i = v \sin i / 2\pi f_{\rm rot}$ and $T_{\rm eff}$ and between $\log g$ and $f_{\rm rot}$. As a star with a convective core evolves on the main sequence, its radius increases, and its temperature and rotation rate decrease. The impact of $T_{\rm eff}$ can also be seen when compared with the periods of the excited pulsations in the co-rotating frame. Furthermore, the ranges of the observed pulsation periods seem to be larger than those predicted by Bouabid et al. (2013), though detailed research is required to confirm this assessment and determine possible causes.

Despite the limitations of the traditional approximation, the results we obtained in this work are consistent with those obtained by Ouazzani et al. (2017) using two-dimensional models, and offer the first estimates of the interior rotation frequencies for a large sample of γ Dor stars. The high observed spin parameter values indicate that the pulsations are constrained in a waveguide around the equator (Townsend 2003a,b), which in turn implies that most of the stars are seen at moderate to high inclination angles. This is indeed what we could indirectly derive from the relation between the observed $v \sin i$ and $f_{\rm rot}$ values in Figure 4.13. From the grid of theoretical models in Section 4.2, we find radii between $1.3\,R_\odot$ and $3\,R_\odot$. For most stars in our sample, this results in inclination angle estimates above $30\,^\circ$. Two of the stars for which lower inclination angle estimates were found, KIC 4846809 and KIC 9595743, are also the stars for which we detected zonal dipole modes. This is consistent with expectations for the geometrical cancellation effects of the pulsations.

These ensemble analyses now form an ideal starting point for detailed asteroseismic modelling of individual targets in the sample. This, in turn, will allow us to place constraints on the shape and extent of the convective core overshooting and the diffusive mixing processes in the radiative near-core regions, and by extension on the evolution of the convective core itself as it was recently achieved for a hybrid δ Sct / γ Dor binary (Schmid & Aerts 2016) and also for a slowly (Moravveji et al. 2015) and a moderately (Moravveji et al. 2016) rotating gravity-mode pulsator of $\sim 3.3\,M_{\odot}$.

Chapter 5

Summary, ongoing research and future prospects

5.1 Summary

The goal of this thesis was to do a seismic study of intermediate-mass stars with both a convective core and a convective envelope, separated by a radiative region. Specifically, we aimed to constrain the stellar rotation in the deep stellar interior, the size and shape of the convective core (i.e., the convective core overshooting), and the extra diffusive mixing processes in the radiative near core regions.

To this end, we have developed a method to detect period spacing patterns in the gravity-mode frequency spectra of γ Dor stars, for which high-precision space-based photometric observations were obtained. In a first step, we applied a new evaluation criterion to the prewhitened pulsation frequencies, based on a comparison between the extracted pulsation signal and the original Fourier transform of the light curve. Because of the low noise level of space-based data, the classical stop criterion for iterative prewhitening, based on the signal-to-noise ratio, is insufficient. Our comparison criterion allowed us to classify the extracted frequencies according to the likelihood that they are influenced by the prewhitening procedure itself. Starting with the most reliable frequencies, we added frequencies while looking for period spacing patterns. For slowly rotating stars, the échelle diagram was found to be the most robust method. For moderate to fast rotators, observable series are typically well separated, and we could find consecutive significant pulsation periods that belong to the same pulsation pattern.

We then studied a sample of 70 γ Dor candidates in the original *Kepler* field of view, which was originally composed by Tkachenko et al. (2013a). For all of the stars in this sample we had both high-precision *Kepler* space-based photometric observations and high-resolution HERMES spectroscopy at our disposal. By analysing these data, we were able to confirm that 68 of the stars are indeed γ Dor stars. The two others were found to be rotationally modulated K-type stars in binary systems. One other target in the sample, KIC 10080943, was studied in detail separately in the framework of the PhD thesis of Valentina Schmid (Schmid et al. 2015; Schmid & Aerts 2016).

Thirteen of the 67 targets were found to be part of a multiple star system, four of which were single-lined binaries, four were double-lined binaries, two were triple systems and there were three binaries with no detected radial velocity variations. We computed atmospheric parameter values for all single stars and single-lined binaries in the sample from the available spectroscopic data, and found them to be consistent with the typical values expected for γ Dor stars. Most of the stars in our sample were found to be relatively slow to moderate rotators with respect to their Keplerian breakup velocity.

After applying our method to the available *Kepler* data of these stars, we were able to find period spacing patterns, in line with theoretical expectations (Miglio et al. 2008; Bouabid et al. 2013), for 50 stars in the sample. We then conducted a multivariate linear correlation analysis between various parameters describing the morphology of the period spacing patterns and the atmospheric parameters derived from the spectroscopic data. Strong correlations were observed between the projected rotational velocity $v \sin i$ and the global properties of the pattern, in line with theoretical expectations (Bouabid et al. 2013). Furthermore, correlations were observed between the $v \sin i$ value, the effective temperature $T_{\rm eff}$ and the dominant gravity-mode pulsation frequency f_g.

We exploited the strong relation between the observed period spacing patterns and the stellar rotation. Based on the asymptotic theoretical predictions for high-order g-modes (Tassoul 1980) and the impact of stellar rotation (using the traditional approximation; Bouabid et al. 2013), we defined basic model period spacing patterns that do not take into account the impact of possible chemical stratification inside the star. The patterns were derived from an extensive grid of stellar models and their pulsation spectra, computed with the codes MESA and GYRE. Our procedure turned out to be sufficient to obtain a reasonable estimate of the interior stellar rotation rate and mode identification for the analysed period spacing pattern. We successfully applied this analysis technique to the 50 targets in our sample for which we have detected period spacing patterns, which resulted in measured internal rotation rates and pulsation mode identification for 40 of them. The vast majority of the dominant pulsation series in the different stars were found to be prograde dipole modes. This is in line with both the theoretical expectations and the findings from ground-based spectroscopy, and explains the correlations which we found in the multivariate correlation analysis, revealing a strong correlation between the rotation rates f_{rot} and the spectroscopic $v \sin i$ values. In addition, the application of this method to the stars in our sample also led to the discovery of Rossby mode pulsations in ten of our targets. While versatile, the current implementation of this method is still limited in its applicability. Because it relies on the traditional approximation, which assumes the star is a slow to moderate rotator, its application to retrograde modes of moderate to fast rotators is unreliable (Ouazzani et al. 2017). According to Ouazzani et al. (2017) the use of the traditional approximation for moderate to fast rotators is appropriate for the case of zonal and prograde modes. However, under these circumstances the star is no longer spherically symmetric, and gravito-inertial mode pulsations will likely be able to propagate into convective regions thanks to the Coriolis force (e.g. Prat et al. 2016a) which will modify the pulsation patterns. We should therefore remain cautious about the results obtained for the faster rotators in our sample. An interesting future prospect in this research domain is a treatment of stellar rotation which takes these effects into account. Recently, Prat et al. (2017) made much progress in this domain. Unfortunately, their work is currently not applicable to either Rossby waves or Kelvin waves. The use of two-dimensional rotation models (e.g. Ballot et al. 2012; Ouazzani et al. 2017) and differential rotation are also promising (e.g. Mathis 2011, and references therein).

While the previous results were obtained for our studied sample as a whole, several targets in our sample can now be studied individually, such as the hybrid γ Dor/δ Sct pulsators. Seven of the eleven hybrid γ Dor/δ Sct candidate stars were found to be in a multiple star system. This could indicate that the γ Dor and the δ Sct-type pulsations actually originate from different stars. However, for four of them this is unlikely: three were identified as single-lined binaries, and for KIC 3952623 the observed γ Dor and δ Sct variability both likely originate from the brighter primary component. KIC 8645874, KIC 9751996 and KIC 11754232 are the slowest rotating stars in our sample and they pulsate in the superinertial regime; all exhibit variability in the frequency range between $6\,\mathrm{d}^{-1}$ and $8\,\mathrm{d}^{-1}$, making them hybrid γ Dor/δ Sct pulsators as well. They are the only three stars in our sample that exhibit variability in this particular frequency range, which suggests it is linked to their low rotation rates. Our focus will be on the detailed seismic modelling of these sample stars.

5.2 Towards asteroseismic modelling of individual stars

The results obtained in this PhD thesis feed future seismic analysis of selected individual targets. We now have dozens of stars with derived spectroscopic parameters, observed period spacing series, mode identification, and a measured rotation rate in the deep stellar interior. While a detailed analysis of the faster rotating targets in this sample likely requires a two-dimensional stellar model, spherical symmetry is a reasonable assumption for the slower rotating γ Dor stars. In previous studies, observed period spacing patterns have typically been modelled by comparing them with grids of theoretical models using χ^2-minimisation (e.g. Moravveji et al. 2015, 2016; Schmid & Aerts 2016). However, such grids are very computationally intensive.

We have meanwhile embarked upon the design of a more efficient approach by means of a genetic algorithm (e.g. Charbonneau 1995). Within this technique, a group of theoretical models is randomly selected from a probability distribution on a parameter space, and evaluated by comparison with an observational data set. These are then ordered based on their goodness-of-fit, and used to build a new generation of models. This process is regulated by a crossover operator, which simulates biological reproduction, i.e., it takes the parameter values of a number of existing models and recombines them to deliver a new set of models. Hereby models with a better fit have a higher probability of “passing on” their input parameter values to the next generation. Furthermore, these algorithms typically allow for genetic “mutation”, i.e., randomly changing a (limited) fraction of the input parameter values. While it is difficult to find the global solution using a genetic algorithm, they are well-suited to find the region in parameter space that contains the global solution without covering unnecessary areas in the parameter space as in a grid-based approach.

In currently ongoing work, we have selected the slowly rotating hybrid γ Dor/δ Sct candidate KIC 9751996 for a proof-of-concept study of theoretical modelling based on our implementation of a genetic algorithm. It is the only star in our sample with clear rotational splitting in the g-mode pulsation spectrum, making it uniquely suited to study the stellar structure and rotation in its deep interior, and the interplay between them. In particular, we focus our attention on the size and shape of the convective core. We compare models with exponential core overshooting and with step core overshooting, and aim to determine which provides the best theoretical description of the observations.

We have coupled our setup for the MESA and GYRE codes, as described in Sections 1.1.3 and 1.2.3 respectively, with MPIKAIA (Metcalfe & Charbonneau 2003), a parallellised implementation of the genetic algorithm code PIKAIA

parameter	exponential overshooting		step overshooting	
	begin	end	begin	end
mass M $[M_\odot]$	1.4	2.4	1.4	2.4
metallicity Z	0.008	0.022	0.008	0.022
exp. core overshooting $f_{\rm ov}$	0.001	0.030	-	-
step core overshooting $\alpha_{\rm ov}$	-	-	0.01	0.3
initial hydrogen fraction X_i	0.69	0.73	0.69	0.73
core hydrogen fraction X_c	X_i	0.001	X_i	0.001

Table 5.1: Parameter ranges considered in the analysis of KIC 9751996 with the genetic algorithm MPIKAIA, both for the assumption of exponential overshooting *(left)* and step overshooting *(right)*.

(Charbonneau 1995). MPIKAIA is highly versatile. It allows the user to implement and optimise his or her own evaluation function. It only requires the return of a goodness-of-fit parameter value, and provides several default parameters to regulate the genetic algorithm itself. For both the exponential and the step core overshooting description, we have computed 100 generations consisting of 150 sets of theoretical pulsation frequencies, computed with GYRE for MESA models in the parameter domains given in Table 5.1. We required a final precision of three significant digits for the different input parameters to have a sufficiently fine grid mesh, selected a crossover probability of 85 % and initial, minimum and maximum mutation rates of 0.5 %, 0.1 % and 5.5 %, respectively. We also kept the best models when going to the next generation.

In our comparison, we used the inverse of a χ^2-value between the observed period spacings and the model patterns as the goodness-of-fit parameter. For each model evaluation, the rotation rate $f_{\rm rot}$ was given to GYRE as input, and optimised separately with the Levenberg-Marquardt algorithm. It is assumed that the star is rigidly rotating as in Chapter 4.

The first generation of models was selected by sampling the probability function

$$P(x_j) = \beta_n \exp\left[\sum_{i=1}^{n}\left(\frac{O_i - M_i(x_j)}{\beta_\sigma \sigma_i}\right)^2\right]$$

over the input parameter space. Here, we evaluate the n observational parameters O_i, with uncertainties σ_i, by comparing them with the values M_i given by theoretical models as a function of the input parameters x_j. The parameter $\beta_\sigma \geq 1$ broadens the distribution, to take into account possible unknown discrepancies, e.g., between the atmosphere models used in the spectroscopic analysis, and the stellar interior models that rely on an atmosphere as boundary condition. Finally, the scaling parameter β_n is used to normalise the

parameter	exponential overshooting	step overshooting
mass M $[M_\odot]$	1.55 (0.10)	1.60 (0.08)
metallicity Z	0.021 (0.006)	0.011 (0.007)
initial hydrogen fraction X_i	0.72 (0.02)	0.72 (0.02)
core hydrogen fraction X_c	0.38 (0.16)	0.59 (0.09)
exp. core overshooting $f_{\rm ov}$	0.012 (0.010)	-
step core overshooting $\alpha_{\rm ov}$	-	0.07 (0.10)
effective temperature $T_{\rm eff}$ [K]	6600 (1300)	7900 (900)
surface gravity log g	4.09 (0.15)	4.3 (0.1)
convective core mass $[M_\odot]$	0.15 (0.03)	0.17 (0.02)
Asymptotic spacing $\Delta\Pi_{l=1}$ [s]	3140 (70)	3160 (60)
Rotation frequency $f_{\rm rot}$ $[{\rm d}^{-1}]$	0.067 (0.006)	0.067 (0.003)

Table 5.2: Parameter values of the best fitting models for KIC 9751996 with their 1σ-uncertainties, assuming both exponential overshooting *(left)* and step overshooting *(right)*.

distribution. In the analysis of KIC 9751996, the chosen evaluation parameters were $T_{\rm eff}$, log g and $\Delta\Pi_{l=1}$, and the parameter $\beta_\sigma = 2$. The model values M_i were obtained by quadratic inter- and extrapolation of the grid computed in Section 4.2.

In Figures 5.1 to 5.4, we show the χ^2-values of the evaluated models as a function of the model input parameters, as well as the optimal rotation rate $f_{\rm rot}$, asymptotic spacing $\Delta\Pi_{l=1}$ and convective core mass. In Figures 5.1 and 5.3, these are shown for the exponential overshooting, and in Figures 5.2 and 5.4 for the step overshooting. Meanwhile, the period spacing patterns for the optimal solution are shown in Figures 5.5 to 5.6, while their parameter values are given in Table 5.2. The 1σ-uncertainties were computed by fitting a $2^{\rm nd}$-degree polynomial to the χ^2-distribution, and determining its intersection points with the 1σ-level of χ^2 indicated in Figures 5.1 to 5.4. As we can see, the solution found for the exponential overshooting is marginally better than the one found for the step overshooting. The uncertainties found for $f_{\rm rot}$ and $\Delta\Pi_{l=1}$ are larger than those found earlier in Chapter 4, because we now allow the morphology of the model period spacing patterns to vary as well. Furthermore, the input parameters which could be constrained best are the initial mass M, which is strongly correlated with the value for central hydrogen fraction X_c, and the extra diffusive mixing $D_{\rm mix}$, which is remarkably low.

There are multiple indications that the optimisation routine did not find the optimal solutions yet and further analysis is in order. For both the exponential

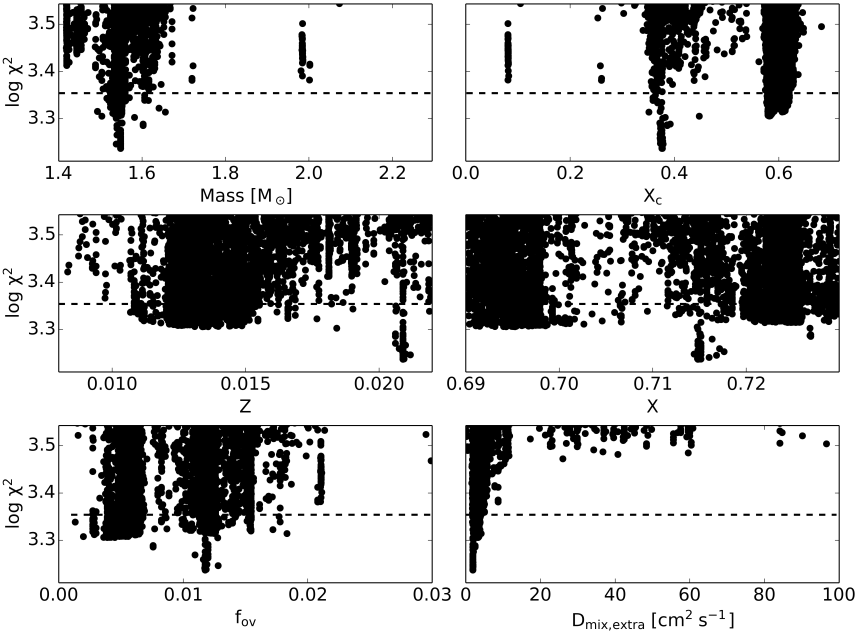

Figure 5.1: χ^2-values for the computed models for KIC 9751996, as a function of the input parameters, assuming the exponential overshooting. The dashed lines indicate the χ^2-values at the boundaries of the 1σ-uncertainty region.

and step overshooting models, the best solutions are located in the first half of the main-sequence evolution, while the observations suggest that KIC 9751996 is actually more evolved. First, while the uncertainties on the spectroscopic parameters are moderately large, the surface gravity log g is rather low, with a value of $3.85 \pm 0.24\,\mathrm{dex}$. Second, the star is slowly rotating, with $f_{\mathrm{rot}} = 0.070 \pm 0.001\mathrm{d}^{-1}$, especially compared to other γ Dor stars, which indicates a lot of angular momentum transport and dissipation has taken place over the course of its evolution. Third, the observed period spacing patterns are a lot more irregular than our best theoretical models. Because this morphology is similar for all three different series, we know it is intrinsic to the star. From a qualitative evaluation of the morphology in theoretical models we also know this type of behaviour is more likely to occur during the later evolution stages of the star on the main sequence. The fact that this is not the result provided by the genetic algorithm, could be because *(a)* the chosen setup for the algorithm is not yet optimal to the problem, *(b)* the optimal region within the evaluated χ^2-landscape is too narrow to find it, or *(c)* the input physics in our models is too

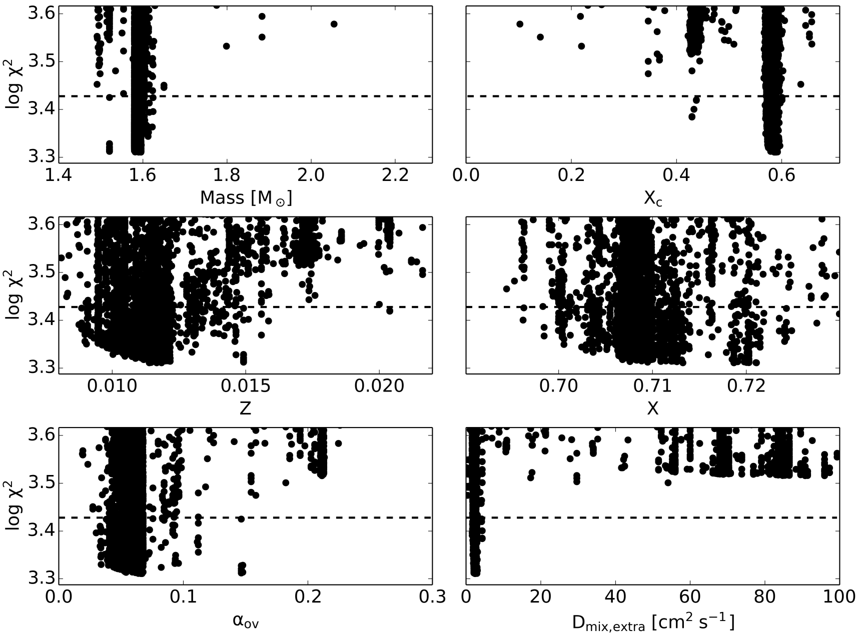

Figure 5.2: Same as Figure 5.1, but for the models with step overshooting.

simplistic, and cannot be used to reproduce the interior stellar structure to the level of the morphology of the observed pattern. The latter situation was also encountered for the slowly rotating hybrid γ Dor/δ Sct hybrids KIC 10080943 A and B (Schmid & Aerts 2016).

There are several improvements which we will test in the near future, and which are listed below in order of importance.

1. We can implement more refined input physics in our theoretical models, e.g., differential rotation, or choose different types of overshooting such as the double-exponential overshooting (Herwig et al. 2007; Battino et al. 2016). Such missing physics in our models could very well skew the results from a traditional χ^2-minimisation between the observations and our models.

2. We can limit the studied parameter domain towards more evolved models, and include the values of the spectroscopic parameters T_{eff} and $\log g$ into the model evaluation. While these parameters should not have as much

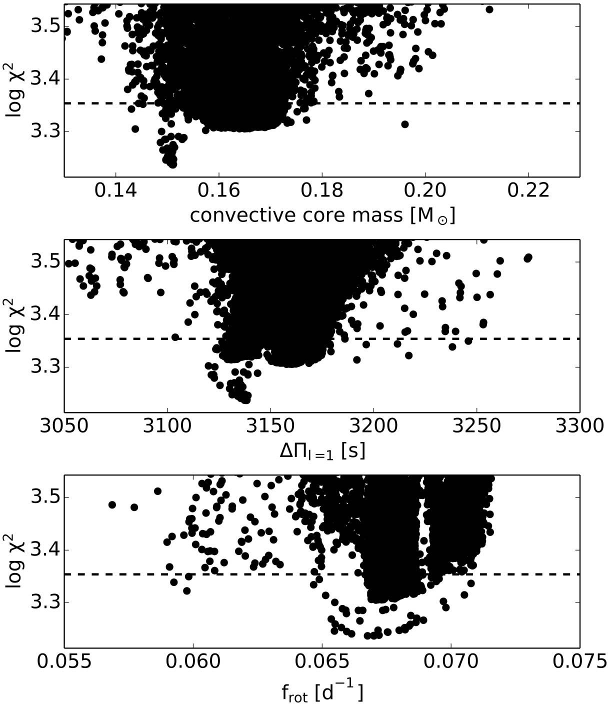

Figure 5.3: χ^2-values for the computed models for KIC 9751996, as a function of the convective core mass *(top)*, asymptotic spacing $\Delta\Pi_{l=1}$ *(middle)* and rotation frequency f_{rot} *(bottom)* assuming the exponential overshooting. The dashed lines indicate the χ^2-values at the boundaries of the 1σ-uncertainty region.

weight as the period spacing patterns in this analysis, they can help to guide the algorithm.

3. We can include the mixing length α_{MLT} as an additional free parameter. In our current set-up, it was fixed at $\alpha_{\mathrm{MLT}} = 1.8$. The strongest influence of this parameter will be on the effective temperature T_{eff}. The parameter α_{MLT} also has a significant influence on the location of the γ Dor instability strip (e.g. Dupret et al. 2005), but because we limited ourselves to an adiabatic treatment of the pulsations, this was not (yet) done in our work.

4. A higher number of models computed per generation is advisable to better sample the multi-dimensional parameter space.

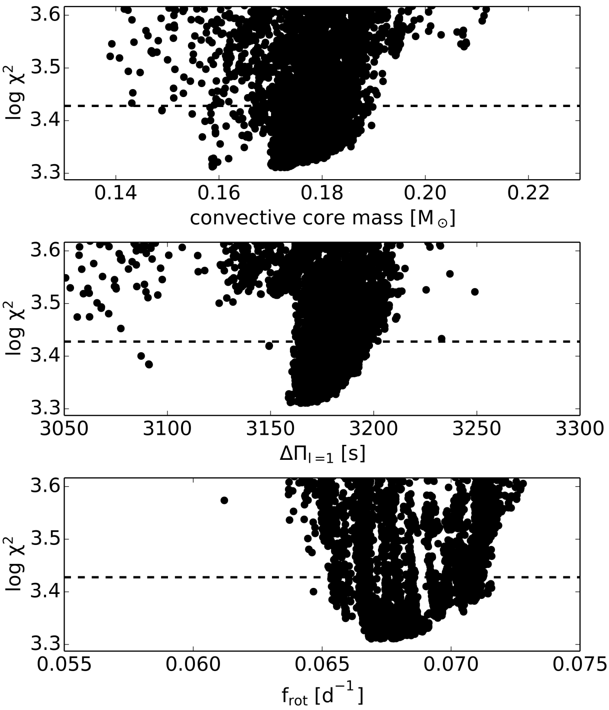

Figure 5.4: Same as Figure 5.3, but for the models with step overshooting.

5. We can consider other goodness-of-fit criteria besides the inverse χ^2-value obtained by fitting the observed period spacing patterns. Because the optimisation done by the genetic algorithm is sensitive to the relative goodness-of-fit evaluation of the different theoretical models, this will have a direct influence on the convergence to the best solution.

6. We can try to characterise the additional variability between $4.2\,\mathrm{d}^{-1}$ and $7.1\,\mathrm{d}^{-1}$, and use it to refine our modelling, although this is far from trivial.

Aside from KIC 9751996, there are other stars in our sample that are very promising for theoretical seismic modelling and will be analysed in the near future. KIC 8645874 is similar to KIC 9751996. While this star does not have any rotationally split multiplets in the g-mode regime, it does exhibit pressure modes with frequencies between $9\,\mathrm{d}^{-1}$ and $20\,\mathrm{d}^{-1}$. Rotational splitting is observed for several p-modes, and suggests differential rotation, whereby the envelope is rotating more slowly than the deep stellar interior. Furthermore, from the

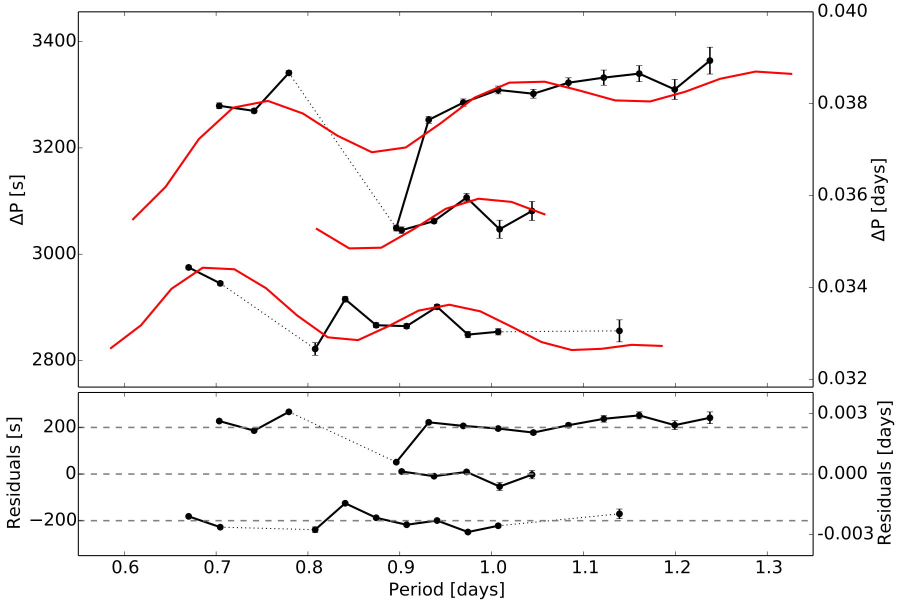

Figure 5.5: *Top:* The observed period spacing patterns for KIC 9751996 (black dots) with the best fitting model (red line) assuming exponential overshooting. From top to bottom, the observed patterns have $(l, m) = (1, -1)$, (1,0) and (1,1), respectively. *Bottom:* The residuals of the fit in the top panel.

low-order radial pressure modes, we find that this star has a large frequency separation $\sim 2.35\text{d}^{-1}$, which means that the average density is low (García Hernández et al. 2015). This confirms that KIC 8645874 is located close to the TAMS in the Hertzsprung-Russell diagram, just as we suspect is the case for KIC 9751996. KIC 11294808 is also a special case in our sample. So far, it is the only star for which we could find both prograde dipole and prograde quadrupole pulsation modes. The dips in its two observed period spacing series, caused by mode trapping, occur for the same radial orders n in both patterns. This suggests that this star is rigidly rotating in its deep interior.

5.3 Future prospects from current data

Despite all of the information we obtained from the *Kepler* data of our sample of γ Dor stars, there remains a lot to be discovered and understood. Further

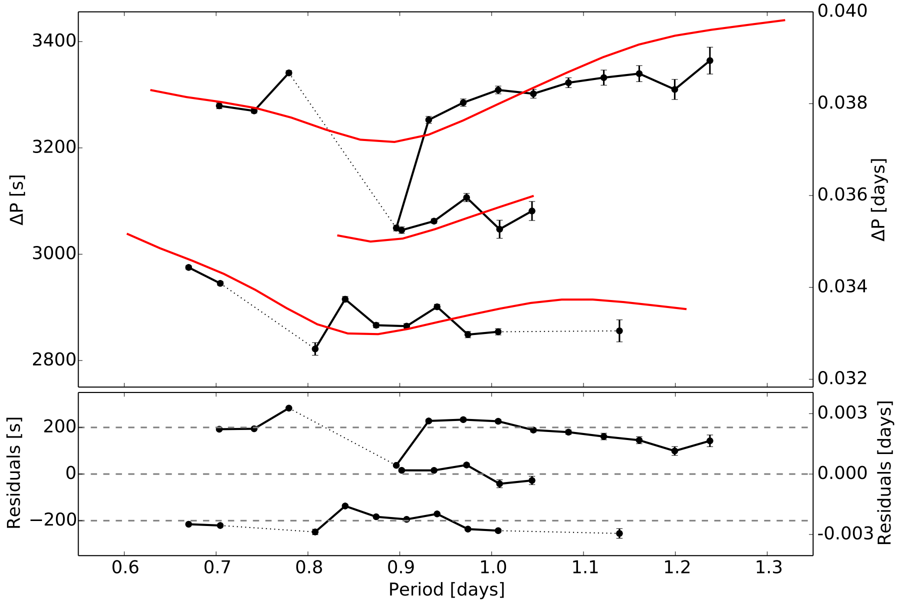

Figure 5.6: Same as Figure 5.5, but for the best fitting model with step overshooting.

analysis of the available data of our sample is therefore essential. There was, for instance, a reasonable number of stars for which we could not yet report a reliable period spacing pattern. Furthermore, a lot of frequencies in our data were labelled as combination frequencies. However, because of the high number of frequencies in these pulsation spectra, it is very well possible that several real pulsation frequencies were mislabelled. In particular, for moderate to fast rotating stars independent sectoral prograde quadrupole modes and combination frequencies of sectoral prograde dipole modes are expected to be located in the same frequency range. While it is advisable to be cautious in the analysis of such ambiguous period series, having multiple period spacing patterns for a single star provides a lot of additional information, e.g., on the rotation profile. Finally, there are other types of pulsation modes which have been predicted by theory in the literature as well, but which have not been observed yet. For instance, Lee & Saio (1997) studied the theoretical properties of low-frequency pulsations in rotating stars using the traditional approximation. Apart from the impact of stellar rotation on gravity modes and the appearance of Rossby modes, they also mentioned rotationally stabilised convective oscillations. Just like Rossby modes, these would be inertial modes, but instead of retrograde modes which propagate in a stably stratified medium, these would be prograde modes propagating in a convective region.

Given the richness of the *Kepler* data base, we have to look beyond our sample of stars as well. The targets in our sample were originally selected by Tkachenko et al. (2013a) because they are reasonably bright, have the expected 2MASS colour information, and exhibit bona fide γ Dor type variability in the photometric data. From the knowledge we gained from this project, it is likely that not all γ Dor stars were selected because (i) their colour information differs from what is expected on average, or (ii) their photometric variability is different from the standard template. Recent work done by Alejandra Sans Fuentes in the framework of her PhD thesis has for instance revealed a few γ Dor stars which are either fast rotators or exhibit both $l = 1$ and $l = 2$ modes. She applied an unsupervised clustering algorithm to the *Kepler* Q3 light curves, which resulted in the classification of a small cluster of stars that exhibit variability just outside of the traditional γ Dor range (Sans Fuentes, 2017) This is in contrast to the stars in our sample, where we do have a few fast rotating stars, but only one, KIC 11294808, was found to exhibit high amplitude quadrupole mode variability.

Another interesting path to take in future research is to apply the techniques developed in this work to other types of gravity-mode pulsators. Recently, we have also applied our mode identification algorithm to period spacing series which were detected for slowly pulsating B-type (SPB) stars, and derived values for the interior rotation rates of these stars (Pápics et al. 2017). However, this also allows for a thorough analysis of proposed new types of pulsators, such as the one observed by Mowlavi et al. (2013) and Mowlavi et al. (2016) in between the instability strips of the SPB stars and the δSct stars in the Hertzsprung-Russell diagram. The authors reported that most of these stars are fast rotators, and it was suggested by Salmon et al. (2014) that these stars are in fact SPB stars that are observed (almost) equator-on. Unfortunately, the data that are available for these stars are currently not sufficient for this type of analysis. Recently, Balona et al. (2016) similarly reported that a number of γ Dor stars observed with *Kepler* were found outside of the instability strip. Assuming the number of observable pulsations suffices, the (non-)detection and analysis of period spacing patterns in such stars could in this case provide valuable additional information.

Despite the fact that all most of these future prospects are data-driven, work also remains to be done in theoretical modelling. Throughout this work we used relatively simple theoretical models (cf. Section 1.1.3) which may very well need to be refined, as we saw in Section 5.2. This was also the conclusion of Schmid & Aerts (2016). We relied on one-dimensional models while stars are three-dimensional objects, and simplified approximations of complex processes such as convection and stellar rotation now reveal their shortcomings thanks to the high-precision asteroseismic data. We will likely need to move to higher-dimensional and more refined models to solve these puzzles, but this is far from trivial, not in the least because aside from becoming increasingly complex, such higher-dimensional models require an unrealistic amount of computation power to treat full stars, let alone stellar evolution. Despite all this, promising efforts are being made in different research domains to close the gap between the observations and the models, e.g., with three-dimensional models used to accurately study the surface effects of convection on pulsations (Trampedach et al. 2017) or with two- or three-dimensional models that treat angular momentum transport (Rogers et al. 2013; Alvan et al. 2014) or chemical mixing (Battino et al. 2016).

Another much debated aspect that can be studied is the possible presence of magnetic fields in the deep stellar interior. While the presence of surface magnetic fields in intermediate-mass Ap/Bp stars (e.g. Aurière et al. 2007) and in low-mass stars (e.g. Brown et al. 2011) is well established, both observationally and theoretically, magnetic fields in the deep stellar interior have so far been studied hypothetically (e.g. Spruit 2002; Braithwaite & Nordlund 2006). It was recently proposed that strong magnetic fields are responsible for the decreased amplitudes of dipole modes observed in a significant fraction of red giants (Fuller et al. 2015; Stello et al. 2016), but there is debate on the topic as the mixed-mode character was ignored for the inference of the interior magnetic field (Mosser et al. 2017). The detections of period spacing patterns in our sample stars, which are progenitors of red giants, may provide us with a new opportunity. Theoretical studies on the impact of a magnetic field on both internal gravity waves and angular momentum transport have been done (Mathis & de Brye 2011, 2012). Gravity and gravito-inertial modes are sensitive to this and could therefore reveal the presence or absence of a strong interior magnetic field.

Clearly, the “golden age” of observational asteroseismology has begun. During the coming years the main focus should be on building and refining the theoretical stellar models, and taking the next step towards understanding the interior stellar structure up to the precision of the *Kepler* data.

5.4 Prospects from future space missions

Given the stringent requirements on observational precision and time span for the detection and analysis of γ Dor type variability, the data in the *Kepler* database will be best suited for detailed asteroseismic analyses of γ Dor stars for years to come. However, there are several current and upcoming space missions that (will) contribute both interesting new data and with it, opportunities to advance our knowledge in asteroseismology.

As explained in Section 1.3.1, the second reaction wheel of the *Kepler* space telescope failed in May 2013. Consequently, the space telescope has been repurposed, and now observes different fields of view in the equatorial plane for about 85 days each. While this is too short to be able to analyse γ Dor stars in detail, this mission is very valuable for comparatively short-period variables, such as δ Sct stars, and rare pulsating stars, like variable O-type stars, as well as to delineate the borders of the γ Dor instability strip as a function of metallicity.

Meanwhile, the BRITE-constellation (BRIght Target Explorer) is a collaborative project between Canada, Austria and Poland (Weiss et al. 2014). It is a network of five nano-satellites, each of which is equipped with a 3.0 cm aperture. Hence, observations are limited to the brightest targets in the sky, with apparent visual magnitude m_V between $2 \leq m_V \leq 6$, and are taken in red and blue passbands. Observation runs can last up to 6 months. While this space mission is obviously on a much smaller scale than for instance the *Kepler* mission, Gössl et al. (2016) recently reported the detection of a period spacing pattern for the γ Dor star 43 Cyg with BRITE observations. Of course, the precision of the data is much worse than what is typically the case for *Kepler* data, but it does show that this space mission has some possibilities. Furthermore, the brightness of the BRITE targets make it much easier to do follow-up time-series spectroscopic campaigns for these stars.

The Transiting Exoplanet Survey Satellite (TESS; Ricker et al. 2015) is a two-year all-sky NASA mission, which will launch in March 2018. Its main goal is to look for planets orbiting bright and nearby stars using the transit detection method, i.e., the same as the *Kepler* space mission. The observation time of individual stars will range from 27 days to one year, mostly depending on the colatitude of the studied star, with stars closer to the ecliptic poles having the longer observation time. The TESS mission will provide white-light photometry, with a passband between 600 nm and 1000 nm. Full frame images will be downloaded every 30 minutes, but short cadence observations of 2 minutes will be available for 200 000 pre-selected targets. Contrary to *Kepler*, which was placed in an Earth-trailing orbit, TESS will be placed in an elliptic orbit around the Earth, with a period of 13.7 days. While the expected noise level is higher than for *Kepler* (about 200 ppm for a 10 mag star; see Figure 8 in Ricker et al. 2015), the observed stars will be more numerous, brighter and closer to Earth than typical *Kepler* targets, making it easier to organise ground-based follow-up observations.

The PLAnetary Transits and Oscillations of stars (PLATO; Rauer et al. 2014) is an ESA mission, scheduled to be launched in 2025. Its main goal is the detection and characterisation of planets down to Earth-size in the habitable zone of their host star using the photometric transit detection method. This mission will be able to observe stars in a very wide magnitude range, i.e. $4 \leq m_V \leq 16$, focusing on the brightest stars with $m_V \leq 11$ in wide fields. The large brightness again facilitates ground-based follow-up observations for the observed stars. The planned baseline observing strategy consists of two long pointings (on the order of two to three years each) at different parts of the sky, and an additional step-and-stare phase which will cover about 50% of the sky with duration between two and five months. In total, up to 1 000 000 stars are expected to be observed. Out of the four space missions mentioned here, PLATO is the most promising for observations of γ Dor stars, thanks to the long time base of its two long pointings.

Appendix A

Additional material to Chapter 1

A.1 Example of a MESA inlist (v7385)

```
 &star_job

  mesa_dir = '/home/timothy/Bin/mesa/mesa-7385'

  change_lnPgas_flag = .true.
  new_lnPgas_flag = .true.

  create_pre_main_sequence_model = .False.
  load_saved_model = .True.
  saved_model_name = 'ZAMS.mod'

  save_model_when_terminate = .true.
  save_model_filename = 'TAMS.mod'

  pgstar_flag = .false.

  kappa_file_prefix = 'a09'
  kappa_lowT_prefix = 'lowT_fa05_a09p'
  initial_zfracs = 6
/
```

```
&controls

!!! INPUT
  initial_mass = 1.5
  initial_z = 0.014
  initial_y = 0.276

  ! EXTRA DIFFUSIVE MIXING
  set_min_D_mix = .true.
  min_D_mix = 1.0
  remove_small_D_limit = 0

  ! OVER- AND UNDERSHOOTING
  D_mix_ov_limit = 5d-2
  max_brunt_B_for_overshoot = 0

  overshoot_f_above_burn_h = 0.016
  overshoot_f_above_nonburn = 0.0
  overshoot_f_below_nonburn = 0.026

  overshoot_f0_above_nonburn = 0.0
  overshoot_f0_below_nonburn = 0.001
  overshoot_f0_above_burn_h = 0.001

  step_overshoot_f_above_nonburn = 0.0
  step_overshoot_f_below_nonburn = 0.0
  step_overshoot_f_above_burn_h = 0.0

  step_overshoot_D = 0.0
  step_overshoot_D0_coeff = 1.0

  ! CONVECTION: MLT
  mixing_length_alpha = 1.8
  conv_dP_term_factor = 0
  MLT_option = 'Henyey'

  ! SEMICONVECTION
  use_Ledoux_criterion = .True.
  alpha_semiconvection = 0.01
  semiconvection_option = 'Langer_85 mixing; gradT = gradr'
```

```
!!! MESH CONTROL PARAMETERS

  xtra_coef_a_l_nb_czb = 0.015
  xtra_dist_a_l_nb_czb = 10.0
  xtra_coef_b_l_nb_czb = 0.075
  xtra_dist_b_l_nb_czb = 3.0

  xtra_coef_czb_full_on = 0.0
  xtra_coef_czb_full_off = 1.0

  num_cells_for_smooth_brunt_B = 0

  P_function_weight = 30
  T_function1_weight = 75

  mesh_delta_coeff = 0.2
  max_allowed_nz = 20000


  ! CHEMICAL GRADIENT
  mesh_dlogX_dlogP_extra(:) = 0.15
  mesh_dlogX_dlogP_full_on(:) = 1d-6
  mesh_dlogX_dlogP_full_off(:) = 1d-12

  mesh_logX_species(1) = 'he4'
  mesh_logX_min_for_extra(1) = -100
  mesh_logX_species(2) = 'n14'
  mesh_logX_min_for_extra(2) = -100

  xa_function_species(1) = 'he4'
  xa_function_weight(1) = 80
  xa_function_param(1) = 1d-2

  xa_function_species(2) = 'he3'
  xa_function_weight(2) = 20
  xa_function_param(2) = 1d-5


  refine_solution = .true.
  refine_mtx_solution = .true.
```

```
  cubic_interpolation_in_Z = .true.
  which_atm_option = 'photosphere_tables'
  create_atm_max_step_size = 0.01


  ! CONVECTIVE BOUNDARY
  conv_bdy_mix_softening_f0 = 0.003
  conv_bdy_mix_softening_f = 0.001
  conv_bdy_mix_softening_min_D_mix = 1d-3

  smooth_convective_bdy = .false.
  mesh_min_dlnR = 1d-12

  convective_bdy_weight = 1.0
  convective_bdy_dq_limit = 1d-6
  convective_bdy_min_dt_yrs = 1d-3


!!! TIME RANGE/STEP CONTROL
  varcontrol_target = 2.5d-5

  max_age = 2d10
  max_years_for_timestep = 1d7

  stop_near_zams = .False.
  Lnuc_div_L_zams_limit = 0.9d0
  xa_central_lower_limit_species(1) = 'h1'
  xa_central_lower_limit(1) = 0.001

  delta_lg_XH_cntr_min = -4
  delta_lg_XH_cntr_max = -1
  delta_lg_XH_cntr_limit = 0.01


  tol_residual_norm1 = 1d-7
  tol_max_residual1 = 1d-4
  tol_residual_norm2 = 1d99
  tol_max_residual2 = 1d99

  iter_for_resid_tol2 = 5
  iter_for_resid_tol3 = 15
```

```
!!! INPUT/OUTPUT
  write_profiles_flag = .True.
  max_num_profile_models = 4000

  photostep = 50
  profile_interval = 1
  history_interval = 1
  terminal_cnt = 10
  write_header_frequency = 1

  ! GYRE output
  write_pulse_info_with_profile = .True.
  pulse_info_format = 'GYRE'
  add_atmosphere_to_pulse_info = .true.

  star_history_name = 'history_MS.data'

/


&pgstar
/
```

A.2 Example of a GYRE inlist (v4.3)

```
 &constants
/

&model
  model_type     = 'EVOL'
  file = './LOGS/profile360.data.GYRE'
  file_format    = 'MESA'
  reconstruct_As = .False.
  uniform_rot    = .True.
  Omega_uni      = 0.0   ! in rad/s
/

&osc
  outer_bound     = 'ZERO'
  rotation_method = 'TRAD'
```

```
/

&mode
  l = 1
  m = 0
  n_pg_min = -120
  n_pg_max = -5
/

&num
  ivp_solver = 'MAGNUS_GL4'
/

&scan
  grid_type  = 'INVERSE'
  grid_frame = 'COROT_I'
  freq_units = 'PER_DAY'
  freq_frame = 'INERTIAL'
  freq_min   = 0.78
  freq_max   = 10.0
  n_freq     = 400
/

&shoot_grid
  op_type = 'CREATE_CLONE'
/

&recon_grid
  op_type = 'CREATE_CLONE'
/

&shoot_grid
  op_type = 'RESAMP_CENTER'
  n = 12
/

&recon_grid
  op_type = 'RESAMP_DISPERSION'
  alpha_osc = 5
  alpha_exp = 1
/
```

```
&shoot_grid
  op_type = 'RESAMP_DISPERSION'
  alpha_osc = 5
  alpha_exp = 1
/

&recon_grid
  op_type = 'RESAMP_CENTER'
  n = 12
/

&output
  summary_file = './ad_modes360/m150z140x071_360_summary.h5'
  summary_file_format = 'HDF'
  summary_item_list = 'beta,l,n_pg,freq,freq_units,E_norm'
  mode_prefix = './ad_modes360/m150z140x071_360_mode-'
  mode_file_format = 'HDF'
  mode_item_list = 'l,beta,n_pg,freq,freq_units,x,xi_r,xi_h,K'
  freq_units = 'PER_DAY'
/
```

Appendix B

Additional material to Chapter 2

Table B.1: Pulsation frequencies of the simulated light curve in Section 2.3.1, in the inertial reference frame.

f_{inert} $[d^{-1}]$	n	l	m	f_{inert} $[d^{-1}]$	n	l	m	f_{inert} $[d^{-1}]$	n	l	m
0.21538375	-79	1	-1	0.69531061	-66	1	0	1.07542644	-72	1	1
0.22129148	-78	1	-1	0.70109027	-65	1	0	1.07943332	-71	1	1
0.22731601	-77	1	-1	0.70702237	-64	1	0	1.08356579	-70	1	1
0.23345566	-76	1	-1	0.71311238	-63	1	0	1.08782942	-69	1	1
0.23971044	-75	1	-1	0.71936521	-62	1	0	1.09222976	-68	1	1
0.24608169	-74	1	-1	0.72578467	-61	1	0	1.09677244	-67	1	1
0.25257204	-73	1	-1	0.73237316	-60	1	0	1.10146341	-66	1	1
0.25918507	-72	1	-1	1.02566528	-88	1	1	1.10630903	-65	1	1
0.26592476	-71	1	-1	1.02821594	-87	1	1	1.11131609	-64	1	1
0.27279498	-70	1	-1	1.03077225	-86	1	1	1.11649154	-63	1	1
0.27979910	-69	1	-1	1.03333555	-85	1	1	1.12184211	-62	1	1
0.28693993	-68	1	-1	1.03593413	-84	1	1	1.12737386	-61	1	1
0.29421993	-67	1	-1	1.03861418	-83	1	1	1.13309195	-60	1	1
0.30164160	-66	1	-1	1.04140856	-82	1	1	1.13900050	-59	1	1
0.30920754	-65	1	-1	1.04432502	-81	1	1	1.14510159	-58	1	1
0.31692034	-64	1	-1	1.04735810	-80	1	1	1.15139313	-57	1	1
0.32478206	-63	1	-1	1.05050069	-79	1	1	1.15786578	-56	1	1
0.33279350	-62	1	-1	1.05374796	-78	1	1	1.16449932	-55	1	1
0.34095341	-61	1	-1	1.05709771	-77	1	1	1.17126399	-54	1	1
0.34925796	-60	1	-1	1.06054975	-76	1	1	1.17813976	-53	1	1
0.35769993	-59	1	-1	1.06410546	-75	1	1	1.18516209	-52	1	1
0.36626649	-58	1	-1	1.06776748	-74	1	1	1.19244821	-51	1	1
0.37493538	-57	1	-1	1.07153959	-73	1	1				

Table B.1: Continued.

f_{inert} $[d^{-1}]$	n	l	m	f_{inert} $[d^{-1}]$	n	l	m	f_{inert} $[d^{-1}]$	n	l	m
1.64956648	-70	2	1	2.12044268	-76	2	2	2.23158364	-63	2	2
1.65786342	-69	2	1	2.12752347	-75	2	2	2.24218278	-62	2	2
1.66640408	-68	2	1	2.13481308	-74	2	2	2.25313299	-61	2	2
1.67519815	-67	2	1	2.14231913	-73	2	2	2.26444229	-60	2	2
1.68425588	-66	2	1	2.15005095	-72	2	2	2.27611565	-59	2	2
1.69358814	-65	2	1	2.15801892	-71	2	2	2.28815239	-58	2	2
1.70320637	-64	2	1	2.16623393	-70	2	2	2.30054107	-57	2	2
1.71312201	-63	2	1	2.17470682	-69	2	2	2.31325275	-56	2	2
1.72334551	-62	2	1	2.18344830	-68	2	2	2.32623613	-55	2	2
2.09413346	-80	2	2	2.19246915	-67	2	2	2.33943278	-54	2	2
2.10040934	-79	2	2	2.20178074	-66	2	2	2.35284293	-53	2	2
2.10688757	-78	2	2	2.21139514	-65	2	2				
2.11356516	-77	2	2	2.22132514	-64	2	2				

Appendix C

Additional material to Chapter 3

Table C.1: Observation log of the stars in our sample. N_Q and N_S indicate the total number of available *Kepler* mission quarters and HERMES spectra respectively.

KIC	RA (J2000)	DEC (J2000)	m_V	N_Q	N_S	Spectroscopic observation times
2710594	19 23 33.317	+37 59 00.55	11.79	18	4	May-Aug. 2011
3222854	19 11 38.539	+38 20 43.83	12.5	18	7	Aug. 2013, July-Sept. 2014
3448365	19 30 35.779	+38 35 16.67	9.92	18	4	May-Aug. 2011
3744571	19 23 05.597	+38 48 51.91	12.03	18	4	June-July 2013
3952623	19 24 08.225	+39 00 40.25	12.09	18	14	May-July 2013, July-Aug. 2014
4547348	19 08 18.888	+39 41 36.53	11.78	18	4	May-Aug. 2011
4749989	19 31 05.251	+39 52 24.78	9.64	15	2	May-June 2011
4757184	19 38 36.922	+39 50 26.10	11.7	8	5	May-Aug. 2011
4846809	19 39 19.027	+39 55 10.70	12.36	15	4	June-July 2013
5000454	19 13 53.400	+40 10 44.76	13.56	17	3	June-July 2013
5114382	19 42 43.543	+40 15 00.66	11.55	8	4	July-Aug. 2011
5254203	18 56 08.364	+40 27 12.87	12.92	14	4	Aug. 2013, June-July 2014
5350598	19 11 54.360	+40 34 01.78	12.1	18	4	June-July 2013
5522154	19 12 23.386	+40 42 14.00	10.44	10	3	May-June 2011
5708550	19 31 03.494	+40 56 13.89	11.93	18	4	July-Aug. 2011
5772452	19 00 04.541	+41 05 17.20	12.46	14	2	Aug.-Sept. 2013
5788623	19 24 11.066	+41 00 41.47	12.07	18	4	June-July 2013
6185513	18 57 29.040	+41 30 58.10	11.89	8	4	May 2011
6342398	18 51 34.322	+41 46 35.05	12.37	14	4	May-June 2013
6367159	19 31 21.144	+41 44 55.50	12.6	18	8	Aug.-Sept. 2013, June-Aug. 2014
6425437	19 00 03.295	+41 50 16.36	11.48	14	3	May 2011
6467639	19 53 37.829	+41 49 05.02	12.02	18	12	June-July 2013, July-Aug. 2014
6468146	19 54 04.241	+41 48 31.01	9.96	18	4	July 2011, June-Aug. 2014

Table C.1: Continued.

KIC	RA (J2000)	DEC (J2000)	m_V	N_Q	N_S	Spectroscopic observation times
6468987	19 54 49.006	+41 48 13.54	12.67	18	4	Aug. 2013, June-Aug. 2014
6678174	19 10 05.712	+42 09 54.58	11.74	10	4	May-Aug. 2011
6778063	19 28 06.622	+42 15 29.60	12.18	18	9	June-July 2013, July-Aug. 2014
6935014	19 08 39.984	+42 27 11.77	10.91	18	5	May-June 2011
6953103	19 32 51.240	+42 28 46.53	12.56	18	4	Aug.-Sept. 2013, June-Aug. 2014
7023122	19 13 42.062	+42 31 13.02	10.84	18	4	May-July 2011
7365537	19 30 35.237	+42 58 10.69	9.19	18	3	May 2011
7380501	19 46 41.587	+42 59 35.34	11.98	18	4	July-Aug. 2011
7434470	19 13 57.941	+43 04 57.98	12.02	18	4	June-July 2013
7516703	19 12 48.742	+43 11 54.34	12.51	13	2	Aug.-Sept. 2013
7583663	18 46 57.458	+43 16 15.31	12.69	18	4	Aug. 2013, June-July 2014
7691618	19 39 02.666	+43 19 01.20	12.36	18	4	June-July 2013
7746984	19 18 45.175	+43 24 01.54	12.47	10	2	Aug. 2013
7867348	18 40 40.774	+43 36 17.09	10.84	18	12	May 2011, June-Aug. 2014
7939065	18 49 11.976	+43 47 53.52	12.14	18	4	May-June 2013
8364249	19 25 16.824	+44 23 46.75	11.95	18	4	July-Aug. 2011
8375138	19 40 47.623	+44 20 11.83	11.02	18	4	May-Aug. 2011
8378079	19 44 30.607	+44 22 58.04	11.84	18	3	Aug. 2011
8611423	19 03 12.216	+44 44 35.05	11.59	10	4	May-June 2011
8645874	19 53 51.715	+44 43 09.37	9.92	10	2	July 2011
8693972	19 34 44.590	+44 52 24.03	12.81	18	7	Aug.-Sept. 2013, July-Aug. 2014
8739181	19 00 06.043	+44 56 43.47	12.08	18	5	June-July 2013
8836473	19 51 12.305	+45 01 34.10	12.78	18	4	Aug. 2013, June-Aug. 2014
9210943	19 14 04.512	+45 39 08.99	11.81	18	5	May-Aug. 2011, June-Aug. 2014

Table C.1: Continued.

KIC	RA (J2000)	DEC (J2000)	m_V	N_Q	N_S	Spectroscopic observation times
9419694	19 49 57.994	+45 57 07.09	12.74	1	4	Aug. 2013, June-Aug. 2014
9480469	19 49 34.555	+46 04 20.90	12.78	15	5	Aug.-Sept. 2013, June-Aug. 2014
9595743	19 39 19.226	+46 14 57.49	12.09	11	4	June-July 2013
9751996	18 45 59.486	+46 30 43.23	10.96	10	4	May 2011
10080943	19 36 27.305	+47 05 02.29	11.81	18	27	Aug. 2011, May-July 2013, July-Oct. 2014
10224094	19 50 06.643	+47 17 06.58	11.9	15	4	July-Aug. 2011
10256787	18 53 47.189	+47 23 35.01	12.25	18	14	May-June 2013, June-Aug. 2014
10467146	19 22 06.050	+47 40 49.33	12.66	18	4	Aug.-Sept. 2013, June-Aug. 2014
11080103	19 18 50.141	+48 37 13.90	12.94	18	4	Aug.-Sept. 2013, June-Aug. 2014
11099031	19 52 37.514	+48 38 44.01	10.02	15	4	July 2011
11196370	19 38 44.486	+48 50 55.64	12.71	18	2	Aug.-Sept. 2013
11294808	19 22 45.396	+49 04 47.53	11.73	18	4	May-Aug. 2011
11456474	19 30 10.495	+49 20 28.06	12.49	18	4	Aug.-Sept. 2013, June-Aug. 2014
11668783	19 41 27.422	+49 47 41.24	12.58	18	4	Aug.-Sept. 2013, June-Aug. 2014
11721304	19 43 27.847	+49 51 25.41	11.71	18	4	July-Aug. 2011
11754232	19 05 57.926	+49 56 33.53	12.24	8	13	June-July 2013, June-Aug. 2014
11826272	19 49 50.494	+50 00 57.36	10.21	18	3	May-Aug. 2011
11907454	19 11 29.407	+50 14 29.72	11.38	18	4	May-Aug. 2011
11917550	19 34 22.565	+50 15 46.29	11.12	18	4	May-Aug. 2011
11920505	19 39 57.108	+50 13 32.09	9.88	18	2	May 2011
12066947	19 37 03.209	+50 30 20.41	10.23	10	3	May-July 2011
12458189	19 20 49.123	+51 20 09.25	11.46	18	4	May-Aug. 2011
12643786	19 13 49.205	+51 46 48.32	11.52	18	4	May-Aug. 2011

Table C.2: The global observational characteristics of the stars in our sample. We have listed information on the variability type, where the label "ROT" indicates rotational modulation, and * indicates that frequencies are found outside of the traditional range for γ Dor stars, but likely correspond to combination frequencies. Stars labelled as "γ Dor/δ Sct" are candidate hybrid γ Dor/δ Sct pulsators. In addition, stars are listed as single (S), single-lined binaries (SB1), double-lined binaries (SB2), binaries with no detected radial velocity variations (SB) and triple systems (SB3). We also report the detections of period spacing patterns and comment on their suspected nature.

KIC	class	binarity	patterns	comments
2710594	γ Dor	S	yes	Prograde and retrograde
3222854	γ Dor	SB2	no	-
3448365	γ Dor	S	yes	Prograde and retrograde
3744571	γ Dor	S	no	-
3952623	γ Dor/δ Sct	SB2	no	-
4547348	γ Dor	S	no	-
4749989	γ Dor/δ Sct	S	no	-
4757184	γ Dor	S	yes	Retrograde
4846809	γ Dor	S	yes	two patterns; downward slopes
5000454	γ Dor	S	no	-
5114382	γ Dor	S	yes	Prograde and retrograde
5254203	γ Dor	S	no	-
5350598	γ Dor	S	yes	Retrograde
5522154	γ Dor*	S	yes	Prograde
5708550	γ Dor	S	yes	Prograde
5772452	K-type (ROT)	-	-	-
5788623	γ Dor	S	yes	Prograde
6185513	γ Dor*	S	yes	Retrograde
6342398	γ Dor	S	no	-
6367159	γ Dor/δ Sct	SB2	no	-
6425437	γ Dor	S	yes	Retrograde
6467639	γ Dor/δ Sct	SB3	no	-
6468146	γ Dor/δ Sct	SB1	yes	Prograde
6468987	γ Dor	S	yes	Prograde and retrograde
6678174	γ Dor	S	yes	Prograde
6778063	γ Dor/δ Sct	SB3	yes	Prograde
6935014	γ Dor	S	yes	Prograde
6953103	γ Dor	S	yes	Prograde
7023122	γ Dor	S	yes	Prograde

Table C.2: Continued.

KIC	class	binarity	patterns	comments
7365537	γ Dor*	S	yes	Prograde
7380501	γ Dor	S	yes	Prograde
7434470	γ Dor*	S	yes	Prograde and strong single frequency
7516703	K-type (ROT)	-	-	-
7583663	γ Dor	S	yes	Prograde and retrograde
7691618	γ Dor	S	no	-
7746984	γ Dor	SB	yes	Prograde
7867348	γ Dor/δ Sct	SB1	yes	Retrograde
7939065	γ Dor*	S	yes	Prograde
8364249	γ Dor	S	yes	Prograde
8375138	γ Dor*	S	yes	Prograde and retrograde
8378079	γ Dor	S	no	-
8611423	γ Dor	S	no	-
8645874	γ Dor/δ Sct	S	yes	Prograde
8693972	γ Dor	SB2	no	-
8739181	γ Dor	S	no	-
8836473	γ Dor/δ Sct	S	yes	Prograde
9210943	γ Dor	SB	yes	Prograde and retrograde
9419694	γ Dor	S	yes	Prograde
9480469	γ Dor	S	yes	Prograde and retrograde
9595743	γ Dor	S	yes	two patterns; downward slopes
9751996	γ Dor/δ Sct	S	yes	Prograde, retrograde and zonal
10080943	γ Dor/δ Sct	SB2	-	-
10224094	γ Dor	S	yes	Prograde
10256787	γ Dor	SB	yes	Prograde
10467146	γ Dor	SB1	yes	Prograde
11080103	γ Dor	S	yes	Prograde
11099031	γ Dor*	S	yes	Prograde
11196370	γ Dor*	S	no	-
11294808	γ Dor*	S	yes	two patterns; downward slopes
11456474	γ Dor	S	yes	Prograde
11668783	γ Dor	S	yes	Retrograde
11721304	γ Dor	S	yes	Prograde
11754232	γ Dor/δ Sct	SB1	yes	Prograde
11826272	γ Dor	S	yes	Prograde

Table C.2: Continued.

KIC	class	binarity	patterns	comments
11907454	γ Dor	S	yes	Prograde and retrograde
11917550	γ Dor	S	yes	Prograde
11920505	γ Dor	S	yes	Prograde
12066947	γ Dor*	S	yes	Prograde and retrograde
12458189	γ Dor*	S	yes	Prograde
12643786	γ Dor	S	no	-

Table C.3: Spectroscopic parameter values computed for the merged spectra of the single stars and single-lined binaries in our sample. The provided errors are the 1-σ values obtained from the χ^2-statistics.

KIC	$T_{\rm eff}$ [K]	$\sigma_{T_{\rm eff}}$	log g	$\sigma_{\log\ g}$	ζ [km s^{-1}]	σ_ζ	$v \sin i$ [km s^{-1}]	$\sigma_{v \sin i}$	$[M/H]$	$\sigma_{[M/H]}$
2710594	7000	100	3.78	0.33	2.93	0.42	79.2	4.1	0.11	0.09
3448365	7030	60	4.04	0.22	2.52	0.26	91.0	3.0	0.05	0.07
3744571	7075	130	3.94	0.40	2.47	0.58	52.5	4.0	0.11	0.11
4547348	7080	105	4.02	0.34	2.54	0.44	68.5	4.0	0.10	0.09
4749989	7320	55	4.24	0.21	3.33	0.22	204.0	8.0	0.13	0.06
4757184	7285	135	4.16	0.43	1.90	0.63	36.0	3.0	0.02	0.13
4846809	7280	135	4.07	0.32	3.00	0.59	51.3	3.5	0.18	0.11
5000454	6920	100	3.46	0.38	3.91	0.50	101.0	4.4	0.07	0.10
5114382	7165	120	4.23	0.37	2.45	0.45	70.1	4.5	0.19	0.10
5254203	7350	235	4.09	0.72	3.11	1.10	42.7	6.0	0.21	0.21
5350598	7315	110	4.11	0.33	2.64	0.42	27.8	1.7	0.10	0.09
5522154	7090	70	4.18	0.26	3.15	0.36	169.4	7.5	0.08	0.08
5708550	6990	100	3.97	0.32	2.44	0.42	68.3	3.7	0.15	0.09
5788623	7210	115	4.23	0.32	2.20	0.40	24.2	1.8	0.09	0.09
6185513	7365	120	4.10	0.40	3.91	0.72	82.9	5.5	0.16	0.11
6342398	7165	165	3.95	0.49	2.61	0.60	31.6	2.9	0.17	0.13
6425437	7045	112	3.88	0.35	2.64	0.43	49.7	2.5	0.21	0.09
6468146	7240	65	3.71	0.22	3.56	0.33	69.5	1.9	-0.05	0.06
6468987	7155	210	4.01	0.72	4.08	1.10	132.0	12.8	0.38	0.20
6678174	7105	90	3.77	0.33	2.59	0.35	45.5	2.3	0.02	0.08
6935014	7090	66	4.01	0.22	2.66	0.32	68.0	3.0	0.14	0.07
6953103	7290	175	4.27	0.50	2.50	0.81	52.3	5.2	0.25	0.15
7023122	7335	82	4.18	0.30	2.81	0.43	55.0	2.2	0.04	0.08

Table C.3: Continued.

KIC	$T_{\rm eff}$ [K]	$\sigma_{T_{\rm eff}}$	log g	$\sigma_{\log\, g}$	ζ [km s^{-1}]	σ_ζ	$v \sin i$ [km s^{-1}]	$\sigma_{v \sin i}$	$[M/H]$	$\sigma_{[M/H]}$
7365537	7360	65	4.48	0.23	3.23	0.26	154.3	4.9	0.11	0.05
7380501	6930	110	3.80	0.35	2.33	0.47	51.1	3.0	0.14	0.10
7434470	7005	150	4.22	0.50	3.33	0.90	138.9	11.5	0.25	0.14
7583663	7030	230	4.06	0.66	3.38	1.20	105.0	11.0	0.42	0.20
7691618	7110	150	4.10	0.45	2.33	0.62	43.3	3.5	0.15	0.13
7867348	7030	75	3.56	0.22	2.94	0.20	17.2	1.0	-0.06	0.06
7939065	7265	145	4.09	0.48	3.38	0.78	96.5	7.0	0.24	0.13
8364249	7045	115	4.00	0.46	3.36	0.55	140.7	8.5	0.17	0.11
8375138	7070	80	4.05	0.34	3.14	0.40	138.6	6.0	0.08	0.08
8378079	7000	170	3.31	0.55	1.75	0.47	11.7	1.2	-0.14	0.14
8611423	7135	105	4.21	0.30	1.86	0.34	20.7	1.5	0.10	0.08
8645874	7240	90	3.82	0.27	3.38	0.31	21.4	0.9	-0.05	0.06
8739181	7055	120	3.59	0.40	2.24	0.44	27.4	1.8	-0.02	0.10
8836473	7260	190	3.93	0.60	4.71	1.00	122.5	11.0	0.37	0.20
9419694	7200	185	3.99	0.58	2.50	0.77	41.2	4.5	0.17	0.16
9480469	7250	240	4.16	0.70	3.74	1.25	112.3	12.0	0.59	0.25
9595743	7230	125	4.08	0.40	2.44	0.59	50.3	3.2	0.14	0.10
9751996	7145	100	3.85	0.24	3.07	0.27	12.6	0.9	0.28	0.07
10224094	7130	100	4.15	0.30	2.25	0.39	25.5	1.5	0.07	0.08
10467146	7155	175	3.75	0.60	2.85	0.80	57.3	5.5	0.12	0.15
11080103	7345	210	4.23	0.65	2.80	0.95	41.5	4.5	0.18	0.18
11099031	6835	70	4.05	0.20	2.60	0.20	101.2	3.3	0.20	0.05
11196370	7260	215	4.05	0.55	2.75	0.68	16.0	2.0	0.26	0.16
11294808	6975	95	3.80	0.35	2.95	0.44	85.4	4.4	0.12	0.09

Table C.3: Continued.

KIC	$T_{\rm eff}$ [K]	$\sigma_{T_{\rm eff}}$	$\log\ g$	$\sigma_{\log\ g}$	ζ [$\mathrm{km\,s^{-1}}$]	σ_ζ	$v\sin i$ [$\mathrm{km\,s^{-1}}$]	$\sigma_{v\sin i}$	$[M/H]$	$\sigma_{[M/H]}$
11456474	7040	160	4.00	0.50	3.21	0.79	83.4	6.5	0.20	0.14
11668783	7000	150	4.00	0.43	2.31	0.52	33.5	2.7	0.19	0.12
11721304	7160	82	4.13	0.28	2.15	0.33	28.3	1.5	0.08	0.08
11754232	7360	120	4.03	0.33	2.40	0.38	11.2	1.2	-0.05	0.09
11826272	7030	70	3.87	0.21	2.37	0.21	30.0	1.1	0.09	0.06
11907454	7040	90	4.20	0.32	2.45	0.27	109.3	4.7	0.16	0.08
11917550	7080	75	4.10	0.24	2.61	0.32	76.0	3.2	0.14	0.07
11920505	7200	60	4.13	0.19	2.55	0.19	61.0	2.2	0.10	0.05
12066947	7330	70	4.35	0.30	3.40	0.33	133.3	5.6	0.09	0.07
12458189	6895	90	3.90	0.31	2.62	0.39	68.5	3.3	0.16	0.09
12643786	7200	95	4.00	0.31	2.63	0.45	76.7	4.5	0.11	0.09

Table C.4: The values of pulsation parameters and their error margins derived from the downward period spacing patterns for the multivariate analysis (see Section 3.5). Only the patterns for single stars and single-lined binaries are included in this table.

KIC	$\langle P \rangle$ [days]	$\langle \Delta P \rangle$ [days]	$\langle \frac{\mathrm{d}\Delta P}{\mathrm{d}P} \rangle$	f_g $[d^{-1}]$	A_g [mmag]	Δ_{res}	$P_{\max}$ [days]
2710594	$0.710059^{\pm0.000106}$	$0.004405^{\pm0.000129}$	$-0.025^{\pm0.006}$	$1.35536^{\pm0.00004}$	$6.16^{\pm0.71}$	$0.81^{\pm2.02}$	$0.80391^{\pm0.00017}$
3448365	$0.708845^{\pm0.000131}$	$0.003169^{\pm0.000137}$	$-0.017^{\pm0.026}$	$1.50016^{\pm0.00004}$	$7.57^{\pm0.75}$	$0.45^{\pm6.89}$	$0.76368^{\pm0.00016}$
4846809	$0.920973^{\pm0.000197}$	$0.010070^{\pm0.000287}$	$-0.010^{\pm0.006}$	$1.81324^{\pm0.00004}$	$2.53^{\pm0.29}$	$1.82^{\pm1.21}$	$1.11765^{\pm0.00035}$
5114382	$0.670536^{\pm0.000096}$	$0.002642^{\pm0.000098}$	$-0.025^{\pm0.022}$	$0.95265^{\pm0.00006}$	$3.21^{\pm0.53}$	$0.89^{\pm5.39}$	$0.71833^{\pm0.00014}$
5522154	$0.352971^{\pm0.000009}$	$0.003819^{\pm0.000008}$	$-0.052^{\pm0.010}$	$3.00986^{\pm0.00002}$	$1.58^{\pm0.10}$	$0.31^{\pm0.15}$	$0.38857^{\pm0.00002}$
5708550	$0.832343^{\pm0.000123}$	$0.004606^{\pm0.000158}$	$-0.022^{\pm0.003}$	$1.11550^{\pm0.00005}$	$2.71^{\pm0.39}$	$1.30^{\pm2.12}$	$0.97390^{\pm0.00015}$
5788623	$1.133749^{\pm0.000558}$	$0.012569^{\pm0.000590}$	$-0.015^{\pm0.002}$	$0.77895^{\pm0.00007}$	$9.44^{\pm1.84}$	$1.97^{\pm2.67}$	$1.55211^{\pm0.00104}$
6468146	$0.608196^{\pm0.000056}$	$0.007406^{\pm0.000084}$	$-0.035^{\pm0.008}$	$1.54570^{\pm0.00001}$	$1.15^{\pm0.04}$	$1.18^{\pm0.85}$	$0.74142^{\pm0.00012}$
6468987	$0.476347^{\pm0.000058}$	$0.003106^{\pm0.000105}$	$-0.038^{\pm0.017}$	$1.99899^{\pm0.00002}$	$4.52^{\pm0.18}$	$0.19^{\pm0.76}$	$0.53144^{\pm0.00001}$
6678174	$0.917967^{\pm0.000103}$	$0.013403^{\pm0.000171}$	$-0.015^{\pm0.542}$	$1.12777^{\pm0.00007}$	$3.00^{\pm0.59}$	$3.02^{\pm55.65}$	$0.95240^{\pm0.00010}$
6935014	$0.832490^{\pm0.000104}$	$0.006348^{\pm0.000111}$	$-0.025^{\pm0.005}$	$1.20670^{\pm0.00005}$	$5.73^{\pm0.79}$	$1.88^{\pm3.21}$	$0.94147^{\pm0.00030}$
6953103	$0.812258^{\pm0.000173}$	$0.009450^{\pm0.000148}$	$-0.031^{\pm0.004}$	$1.28760^{\pm0.00004}$	$33.46^{\pm3.23}$	$1.44^{\pm1.14}$	$1.00870^{\pm0.00045}$
7023122	$0.479343^{\pm0.000024}$	$0.011788^{\pm0.000043}$	$-0.048^{\pm0.034}$	$1.87611^{\pm0.00001}$	$13.90^{\pm0.40}$	$1.27^{\pm0.43}$	$0.58005^{\pm0.00006}$
7365537	$0.344913^{\pm0.000007}$	$0.003234^{\pm0.000008}$	$-0.049^{\pm0.011}$	$2.92563^{\pm0.00001}$	$8.10^{\pm0.23}$	$0.00^{\pm0.33}$	$0.38088^{\pm0.00001}$
7380501	$0.965164^{\pm0.000137}$	$0.006745^{\pm0.000164}$	$-0.017^{\pm0.003}$	$0.96329^{\pm0.00005}$	$2.26^{\pm0.31}$	$1.12^{\pm4.95}$	$1.19243^{\pm0.00024}$
7434470	$0.417794^{\pm0.000013}$	$0.003200^{\pm0.000013}$	$-0.040^{\pm0.001}$	$1.69873^{\pm0.00001}$	$3.82^{\pm0.04}$	$1.26^{\pm0.09}$	$0.48637^{\pm0.00002}$
7583663	$0.633695^{\pm0.000072}$	$0.003101^{\pm0.000093}$	$-0.031^{\pm0.007}$	$1.04474^{\pm0.00003}$	$6.28^{\pm0.54}$	$0.90^{\pm1.44}$	$0.70027^{\pm0.00007}$
7939065	$0.462545^{\pm0.000037}$	$0.008775^{\pm0.000037}$	$-0.036^{\pm0.002}$	$1.72817^{\pm0.00003}$	$10.68^{\pm0.73}$	$0.22^{\pm0.08}$	$0.70123^{\pm0.00014}$
8364249	$0.522644^{\pm0.000017}$	$0.002100^{\pm0.000019}$	$-0.029^{\pm0.003}$	$1.86938^{\pm0.00002}$	$3.94^{\pm0.17}$	$0.57^{\pm0.96}$	$0.57555^{\pm0.00003}$
8375138	$0.469786^{\pm0.000023}$	$0.002377^{\pm0.000025}$	$-0.034^{\pm0.007}$	$2.07777^{\pm0.00002}$	$5.16^{\pm0.31}$	$0.52^{\pm0.91}$	$0.51310^{\pm0.00003}$
8645874	$0.499508^{\pm0.000019}$	$0.026876^{\pm0.000029}$	$-0.016^{\pm0.005}$	$1.84701^{\pm0.00001}$	$5.71^{\pm0.17}$	$1.15^{\pm0.06}$	$1.02248^{\pm0.00017}$
8836473	$0.505219^{\pm0.000035}$	$0.007475^{\pm0.000021}$	$-0.034^{\pm0.061}$	$1.88341^{\pm0.00003}$	$1.47^{\pm0.13}$	$0.44^{\pm0.51}$	$0.57115^{\pm0.00001}$
9419694	$0.937988^{\pm0.000193}$	$0.013458^{\pm0.000118}$	$-0.016^{\pm0.023}$	$1.03279^{\pm0.00004}$	$14.74^{\pm1.51}$	$2.02^{\pm3.78}$	$1.13479^{\pm0.00037}$

Table C.4: Continued.

KIC	$\langle P \rangle$ [days]	$\langle \Delta P \rangle$ [days]	$\langle \frac{\mathrm{d}\Delta P}{\mathrm{d}P} \rangle$	f_g $[d^{-1}]$	A_g [mmag]	Δ_{res}	$P_{\max}$ [days]
9480469	$0.518274^{\pm0.000039}$	$0.002455^{\pm0.000033}$	$-0.028^{\pm0.035}$	$1.99485^{\pm0.00003}$	$7.14^{\pm0.66}$	$0.23^{\pm3.80}$	$0.54748^{\pm0.00006}$
9595743	$0.683181^{\pm0.000099}$	$0.006987^{\pm0.000146}$	$-0.033^{\pm0.040}$	$1.72911^{\pm0.00003}$	$6.93^{\pm0.62}$	$1.09^{\pm2.68}$	$0.76882^{\pm0.00014}$
9751996	$0.858863^{\pm0.000051}$	$0.037537^{\pm0.000072}$	$0.002^{\pm0.010}$	$1.28331^{\pm0.00006}$	$2.34^{\pm0.36}$	$2.68^{\pm0.50}$	$1.19934^{\pm0.00010}$
10224094	$0.875860^{\pm0.000110}$	$0.019195^{\pm0.000134}$	$-0.017^{\pm0.010}$	$1.01242^{\pm0.00010}$	$2.81^{\pm0.71}$	$0.00^{\pm1.25}$	$1.08730^{\pm0.00031}$
10467146	$0.996770^{\pm0.000141}$	$0.007373^{\pm0.000165}$	$-0.018^{\pm0.061}$	$0.95498^{\pm0.00004}$	$3.47^{\pm0.36}$	$1.09^{\pm28.11}$	$1.09130^{\pm0.00018}$
11080103	$0.911278^{\pm0.000154}$	$0.011062^{\pm0.000194}$	$-0.019^{\pm0.016}$	$1.24139^{\pm0.00002}$	$12.13^{\pm0.75}$	$0.97^{\pm4.74}$	$1.09122^{\pm0.00017}$
11099031	$0.698765^{\pm0.000055}$	$0.004375^{\pm0.000067}$	$-0.026^{\pm0.003}$	$0.91665^{\pm0.00003}$	$1.42^{\pm0.13}$	$0.97^{\pm0.99}$	$0.81286^{\pm0.00006}$
11294808	$0.912759^{\pm0.000098}$	$0.006943^{\pm0.000118}$	$-0.043^{\pm0.023}$	$2.22475^{\pm0.00004}$	$2.32^{\pm0.22}$	$1.17^{\pm13.74}$	$0.99168^{\pm0.00013}$
11456474	$0.690040^{\pm0.000060}$	$0.003209^{\pm0.000071}$	$-0.025^{\pm0.002}$	$1.47147^{\pm0.00002}$	$4.17^{\pm0.26}$	$1.19^{\pm1.38}$	$0.78283^{\pm0.00007}$
11721304	$1.026382^{\pm0.000331}$	$0.011981^{\pm0.000430}$	$-0.020^{\pm0.002}$	$0.92287^{\pm0.00009}$	$4.10^{\pm1.03}$	$2.42^{\pm0.77}$	$1.32327^{\pm0.00053}$
11754232	$0.665339^{\pm0.000034}$	$0.031646^{\pm0.000051}$	$-0.002^{\pm0.034}$	$1.10338^{\pm0.00006}$	$2.03^{\pm0.30}$	$1.94^{\pm0.37}$	$0.90630^{\pm0.00005}$
11826272	$1.074839^{\pm0.000399}$	$0.015434^{\pm0.000543}$	$-0.018^{\pm0.001}$	$0.83370^{\pm0.00006}$	$11.61^{\pm1.94}$	$1.87^{\pm0.50}$	$1.59754^{\pm0.00086}$
11907454	$0.548784^{\pm0.000061}$	$0.002847^{\pm0.000084}$	$-0.033^{\pm0.006}$	$1.18715^{\pm0.00003}$	$4.43^{\pm0.36}$	$0.87^{\pm0.89}$	$0.60608^{\pm0.00007}$
11917550	$0.716579^{\pm0.000084}$	$0.005704^{\pm0.000104}$	$-0.028^{\pm0.003}$	$1.28768^{\pm0.00004}$	$9.21^{\pm0.87}$	$1.86^{\pm1.08}$	$0.82445^{\pm0.00018}$
11920505	$0.787720^{\pm0.000142}$	$0.007948^{\pm0.000144}$	$-0.027^{\pm0.003}$	$1.19884^{\pm0.00004}$	$13.2^{\pm1.43}$	$1.90^{\pm1.58}$	$0.95371^{\pm0.00020}$
12066947	$0.359580^{\pm0.000016}$	$0.002396^{\pm0.000017}$	$-0.040^{\pm0.003}$	$2.72379^{\pm0.00004}$	$2.77^{\pm0.30}$	$0.17^{\pm0.14}$	$0.40962^{\pm0.00003}$
12458189	$0.917404^{\pm0.000135}$	$0.005263^{\pm0.000178}$	$-0.019^{\pm0.003}$	$1.03961^{\pm0.00003}$	$4.44^{\pm0.30}$	$1.09^{\pm2.24}$	$1.12169^{\pm0.00019}$

C.1 Detected period spacing patterns

Below we provide figures of all the detected period spacing patterns for the sample stars. The used symbols are the same as the ones used in Fig. 3.3 of the main text.

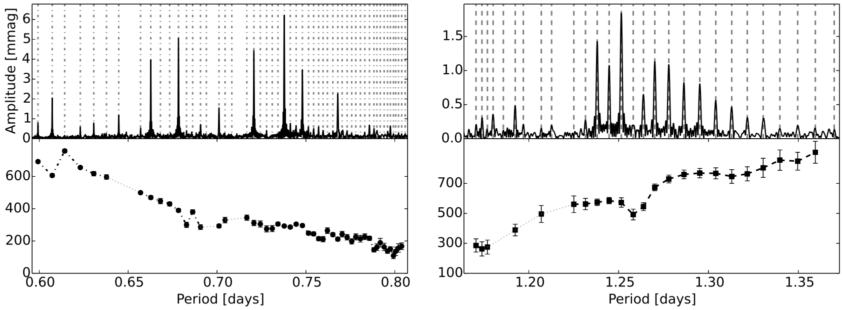

Figure C.1: The period spacing patterns of KIC 2710594.

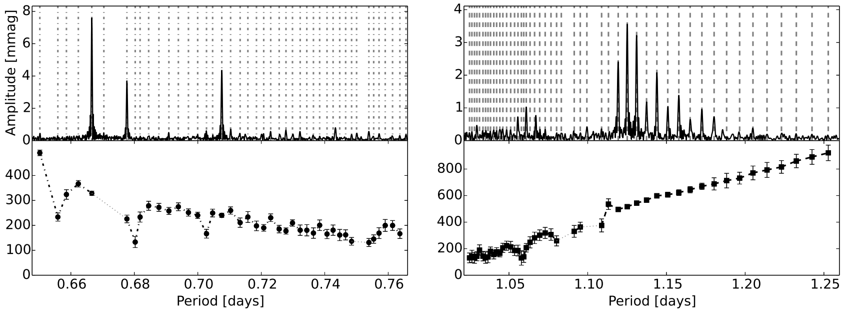

Figure C.2: The period spacing patterns of KIC 3448365.

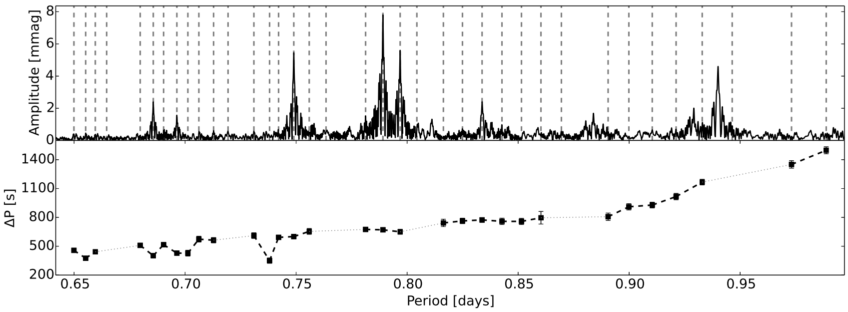

Figure C.3: The period spacing patterns of KIC 4757184.

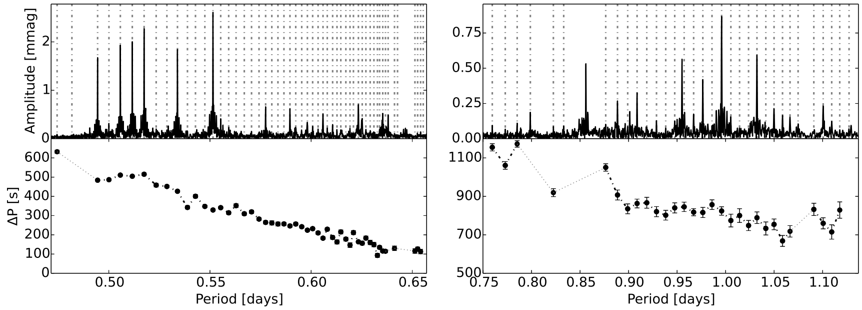

Figure C.4: The period spacing patterns of KIC 4846809.

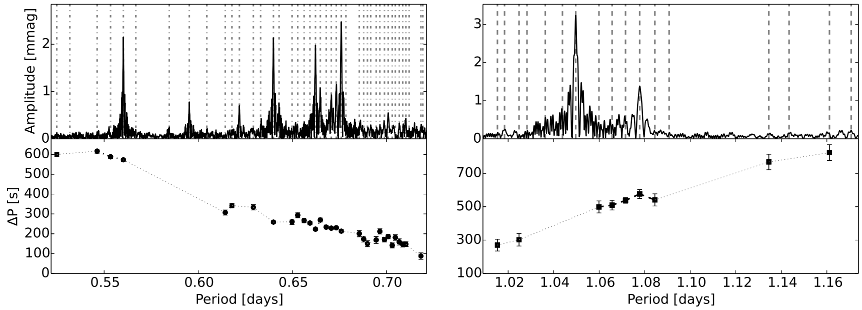

Figure C.5: The period spacing patterns of KIC 5114382.

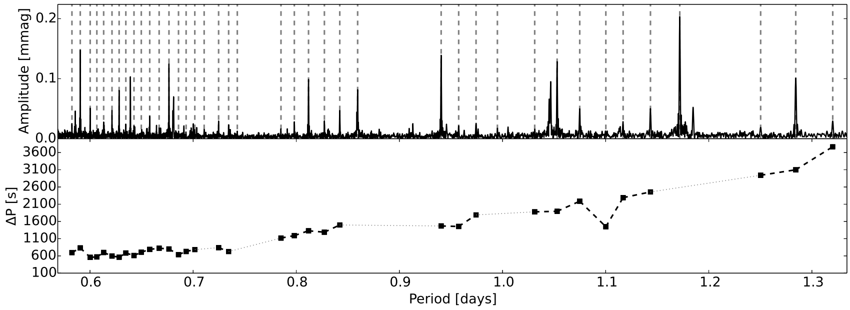

Figure C.6: The period spacing patterns of KIC 5350598.

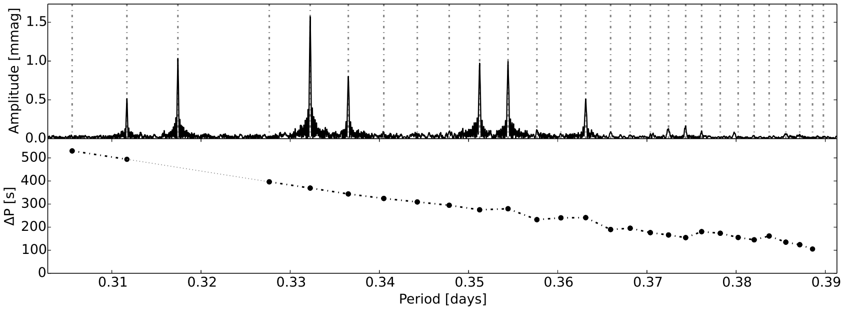

Figure C.7: The period spacing patterns of KIC 5522154.

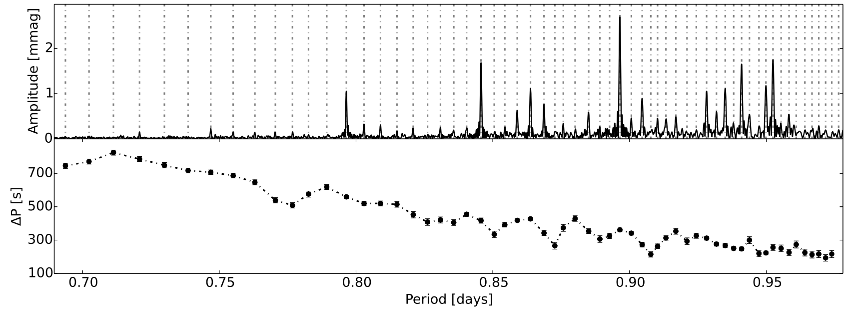

Figure C.8: The period spacing patterns of KIC 5708550.

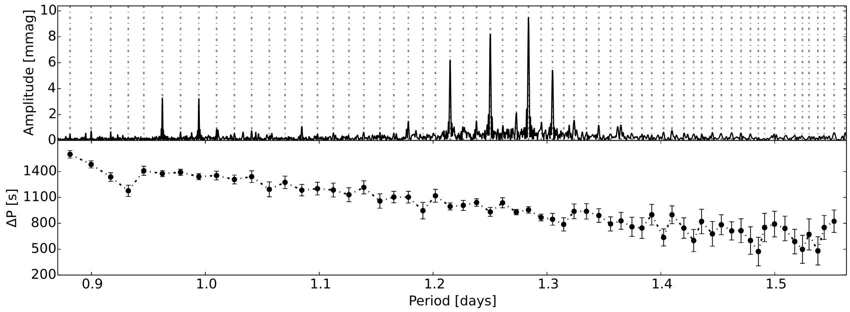

Figure C.9: The period spacing patterns of KIC 5788623.

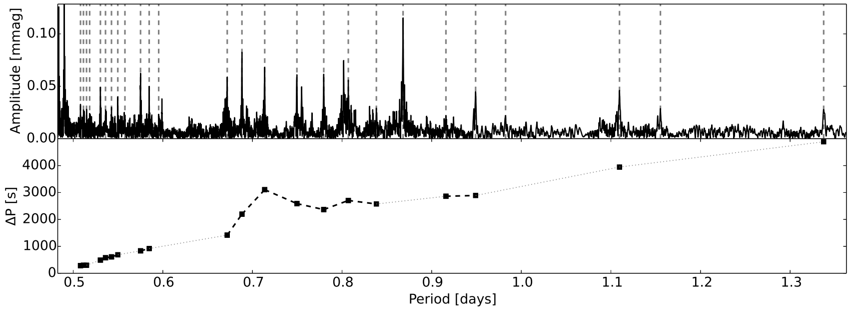

Figure C.10: The period spacing patterns of KIC 6185513.

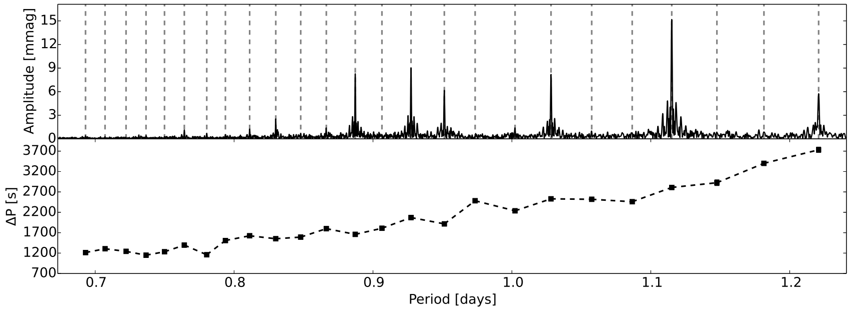

Figure C.11: The period spacing patterns of KIC 6425437.

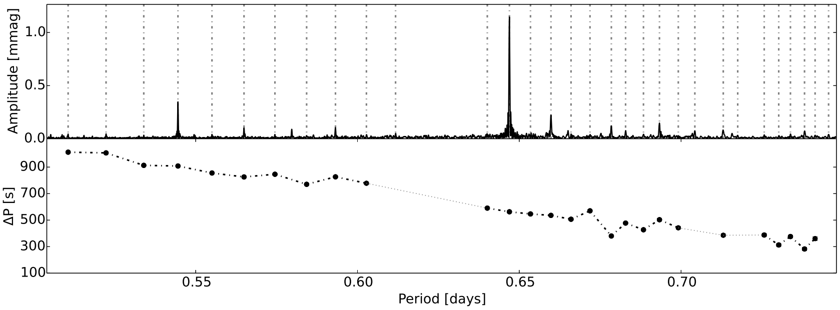

Figure C.12: The period spacing patterns of KIC 6468146.

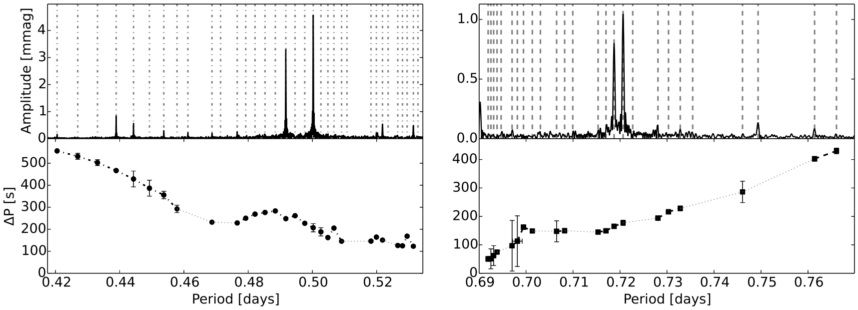

Figure C.13: The period spacing patterns of KIC 6468987.

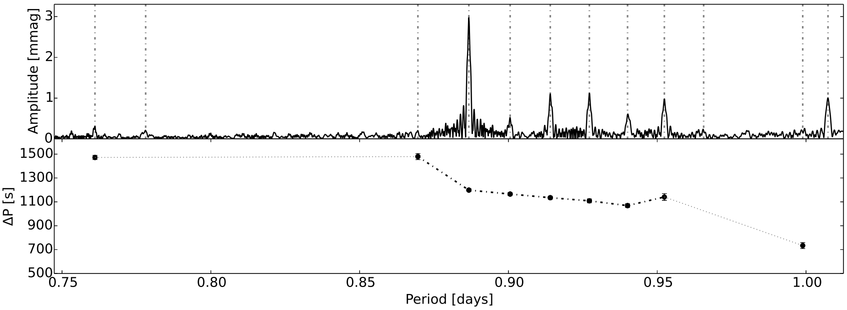

Figure C.14: The period spacing patterns of KIC 6678174.

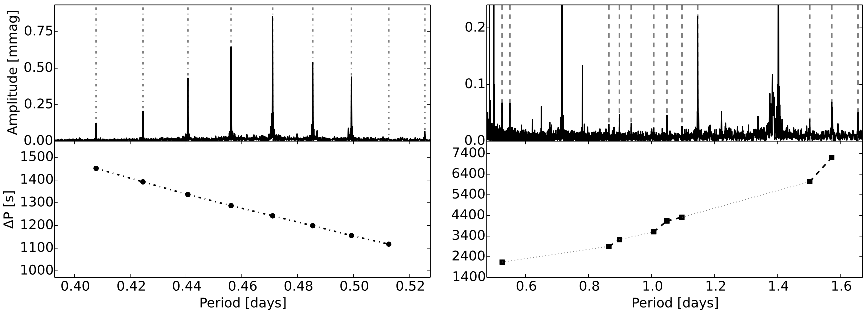

Figure C.15: The period spacing patterns of KIC 6778063.

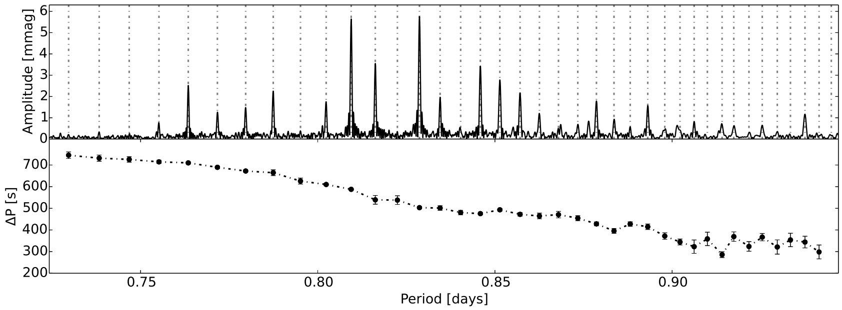

Figure C.16: The period spacing patterns of KIC 6935014.

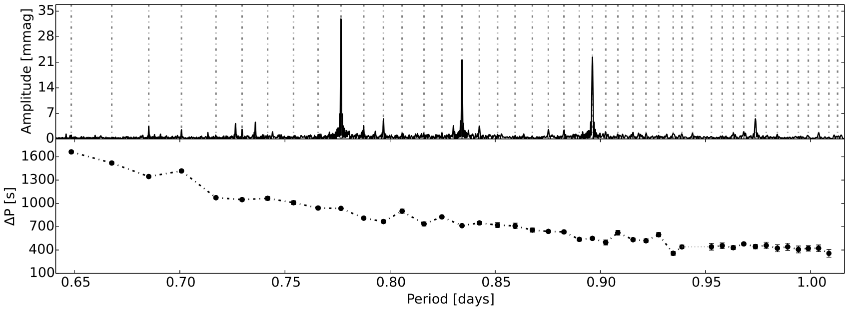

Figure C.17: The period spacing patterns of KIC 6953103.

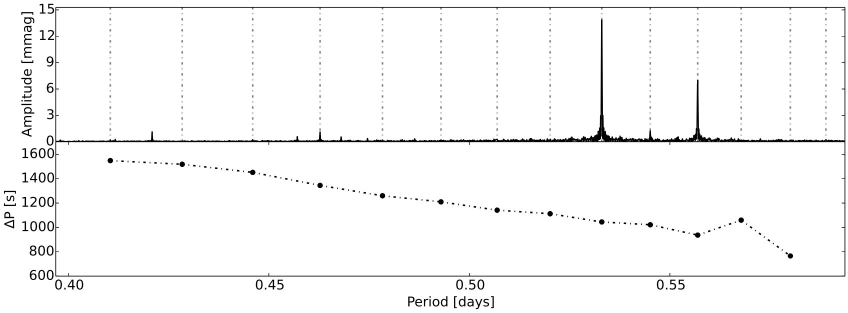

Figure C.18: The period spacing patterns of KIC 7023122.

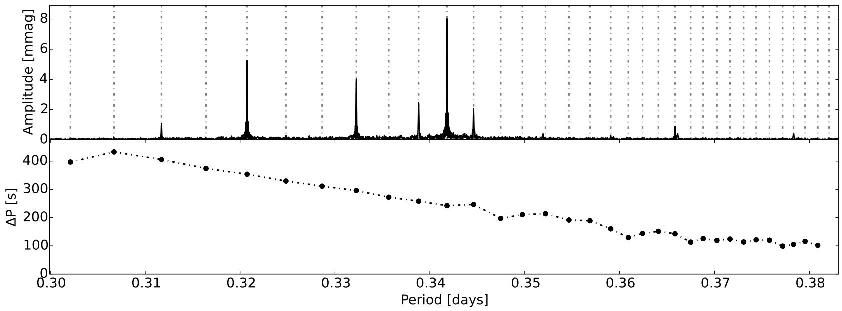

Figure C.19: The period spacing patterns of KIC 7365537.

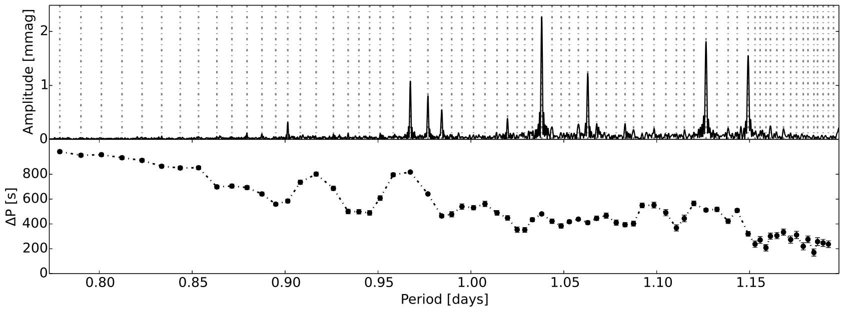

Figure C.20: The period spacing patterns of KIC 7380501.

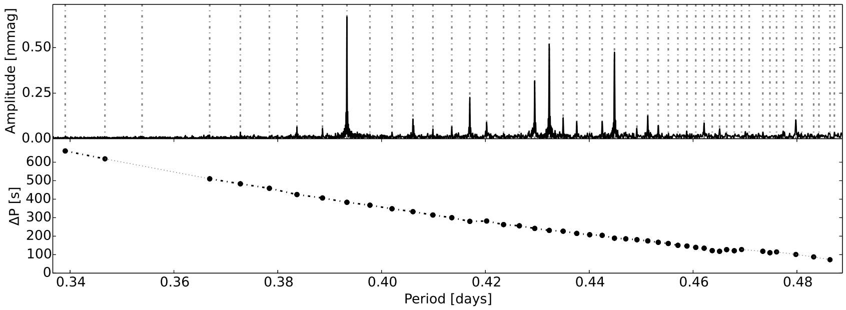

Figure C.21: The period spacing patterns of KIC 7434470.

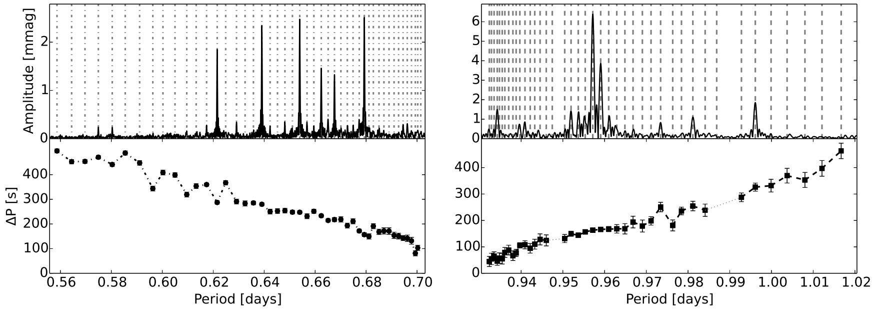

Figure C.22: The period spacing patterns of KIC 7583663.

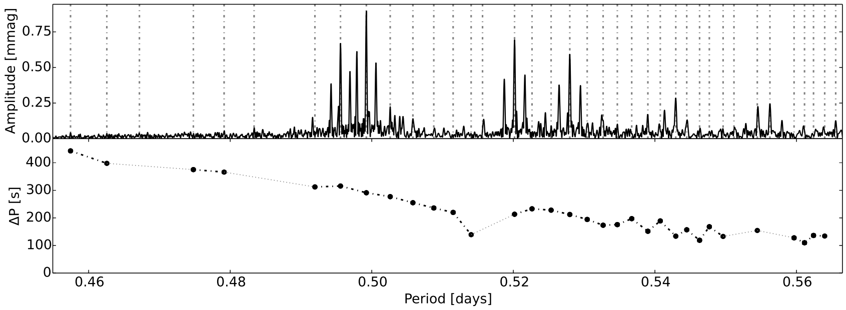

Figure C.23: The period spacing patterns of KIC 7746984.

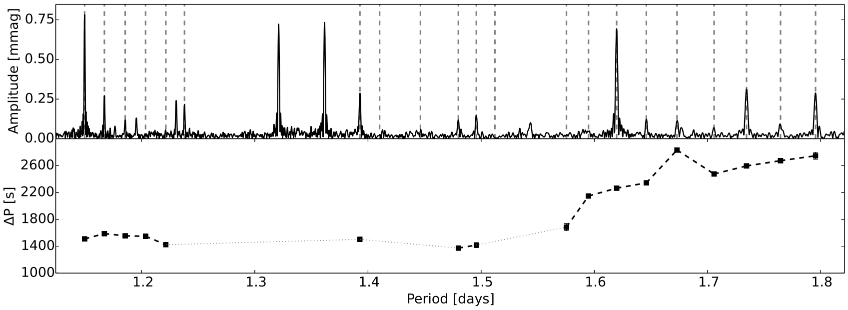

Figure C.24: The period spacing patterns of KIC 7867348.

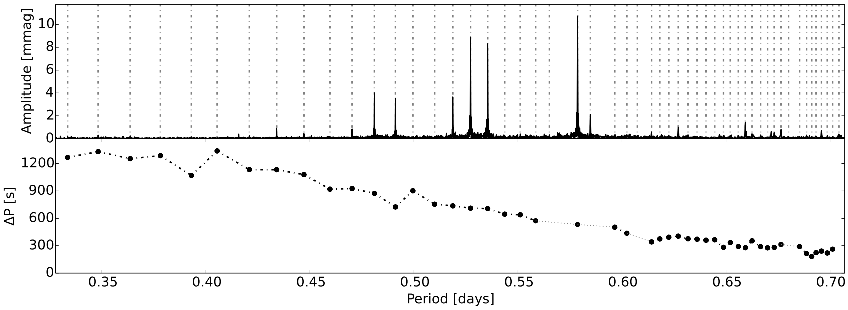

Figure C.25: The period spacing patterns of KIC 7939065.

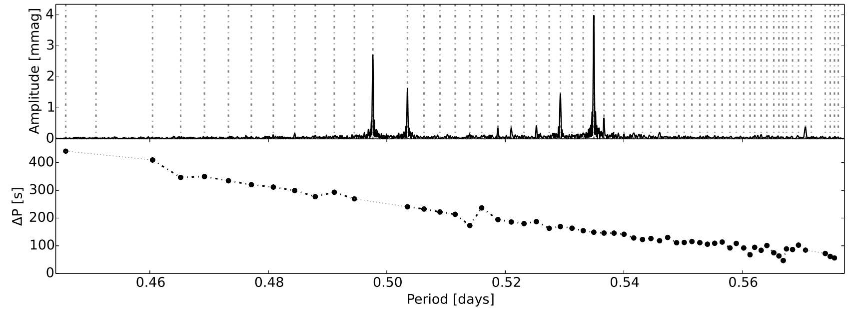

Figure C.26: The period spacing patterns of KIC 8364249.

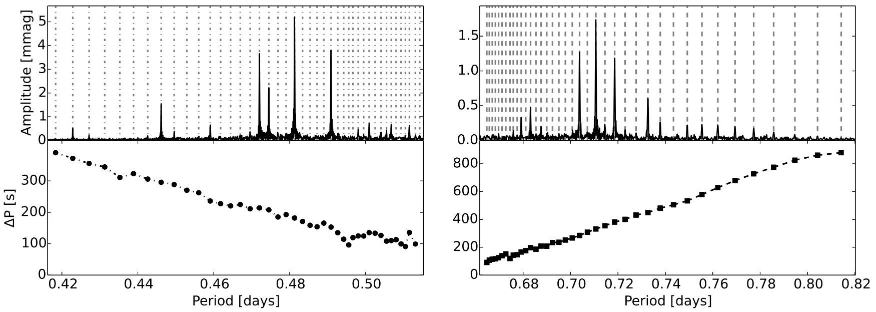

Figure C.27: The period spacing patterns of KIC 8375138.

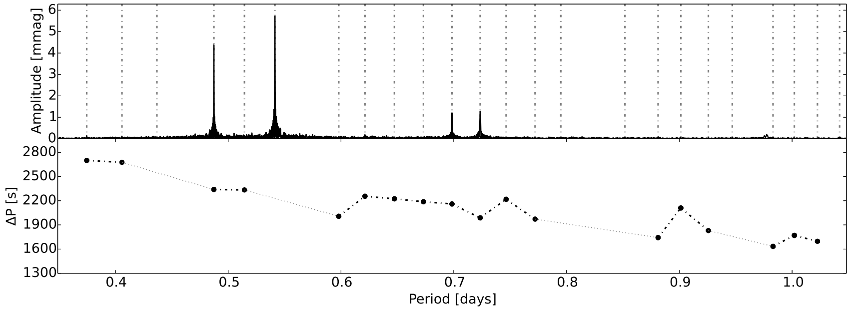

Figure C.28: The period spacing patterns of KIC 8645874.

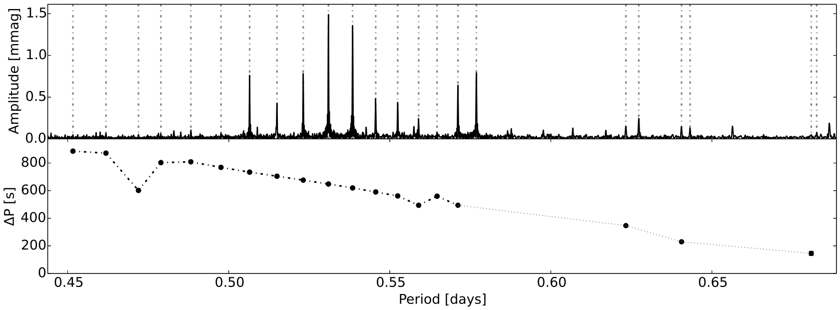

Figure C.29: The period spacing patterns of KIC 8836473.

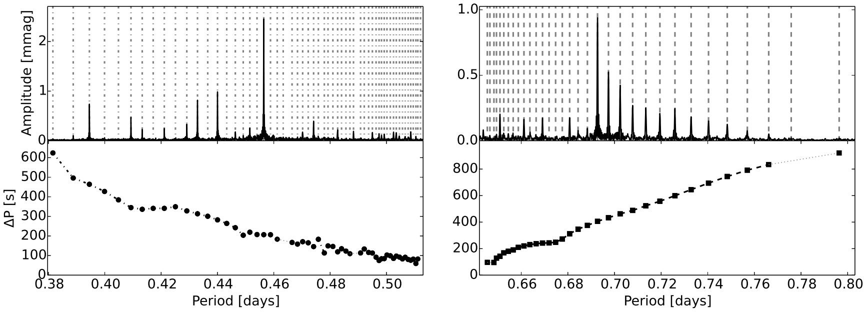

Figure C.30: The period spacing patterns of KIC 9210943.

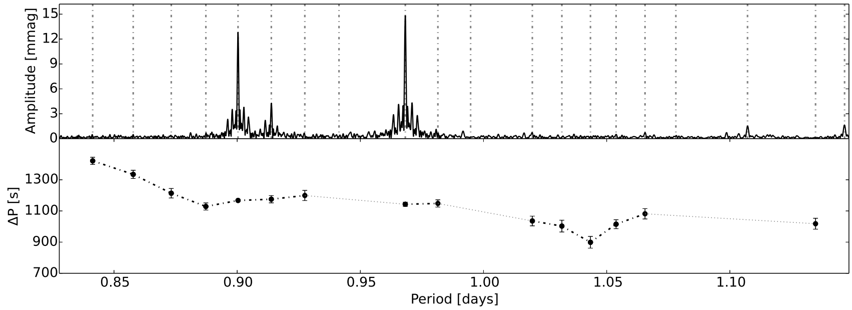

Figure C.31: The period spacing patterns of KIC 9419694.

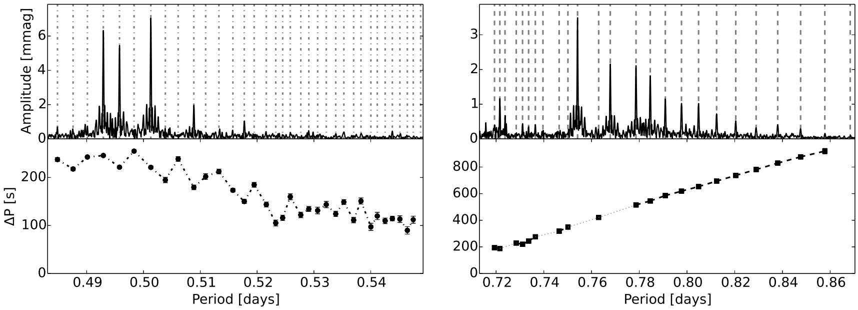

Figure C.32: The period spacing patterns of KIC 9480469.

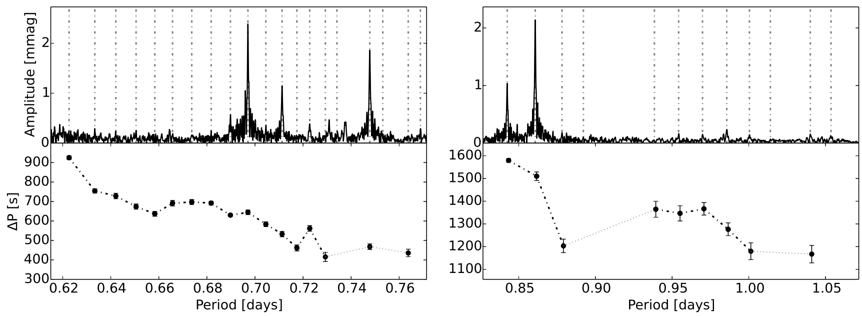

Figure C.33: The period spacing patterns of KIC 9595743.

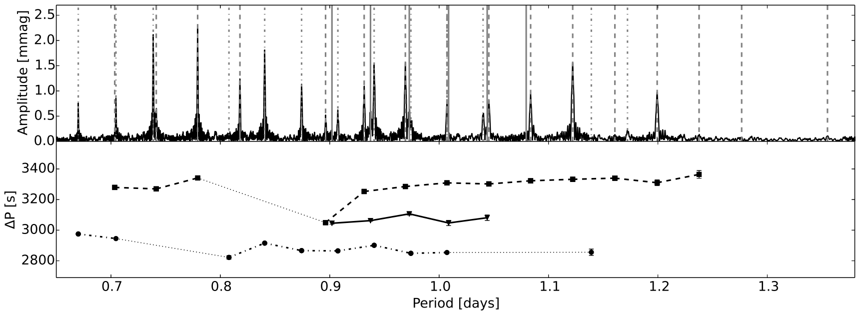

Figure C.34: The period spacing patterns of KIC 9751996.

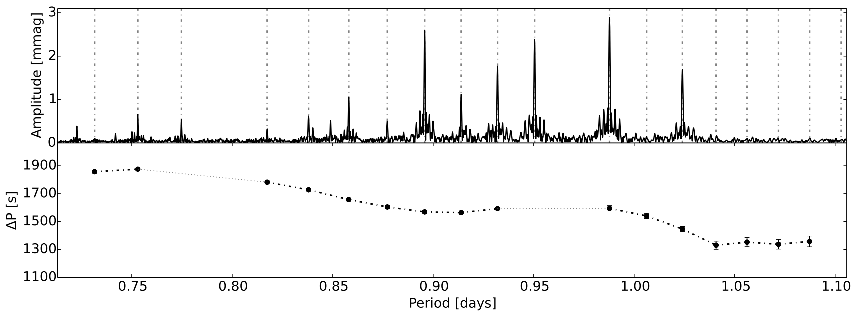

Figure C.35: The period spacing patterns of KIC 10224094.

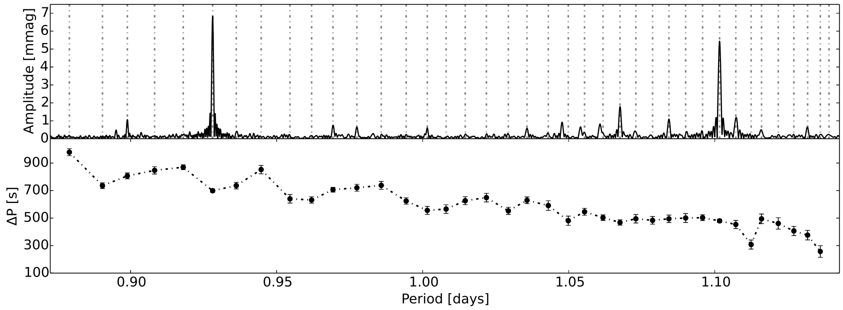

Figure C.36: The period spacing patterns of KIC 10256787.

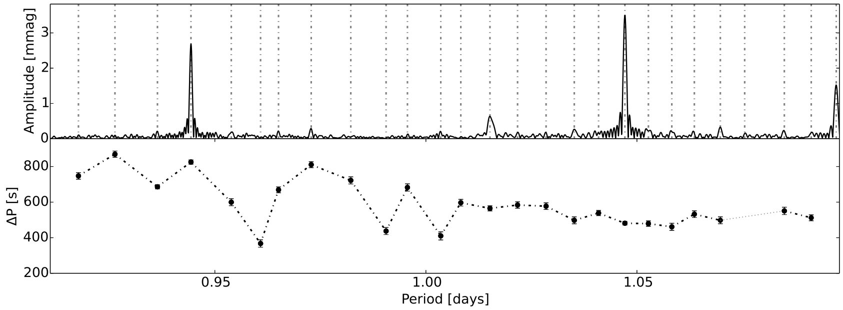

Figure C.37: The period spacing patterns of KIC 10467146.

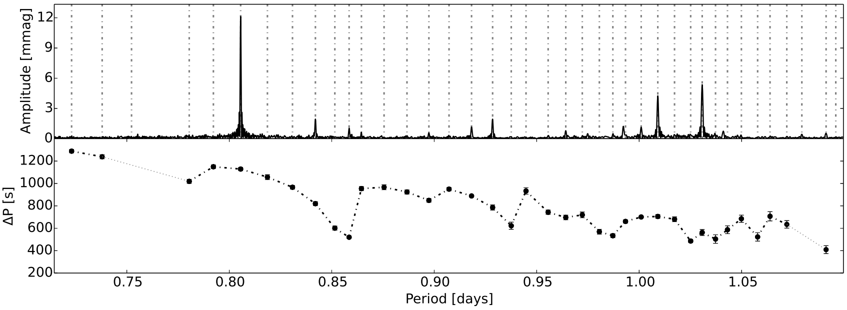

Figure C.38: The period spacing patterns of KIC 11080103.

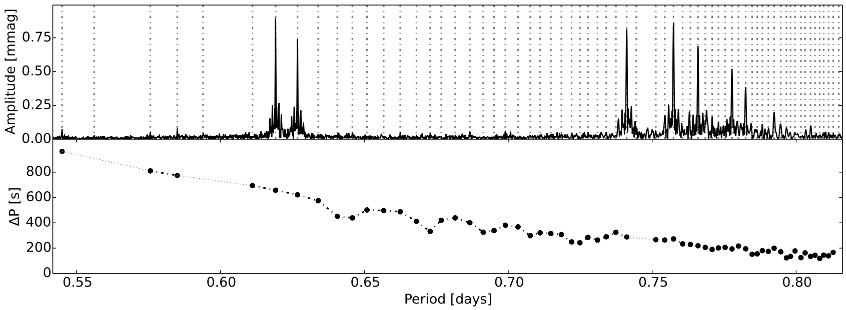

Figure C.39: The period spacing patterns of KIC 11099031.

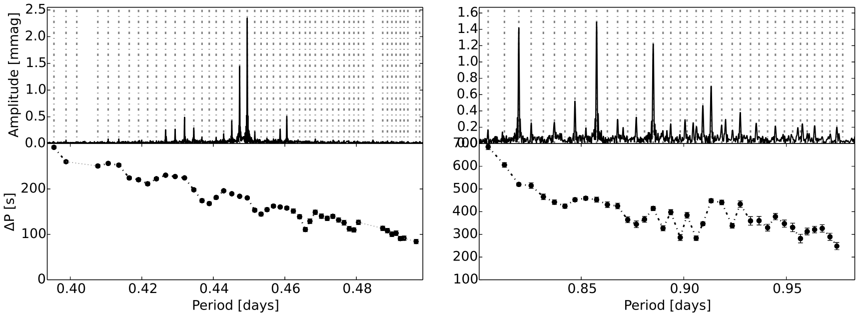

Figure C.40: The period spacing patterns of KIC 11294808.

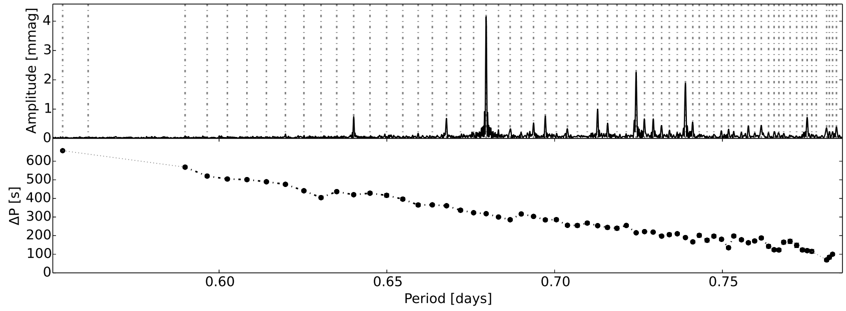

Figure C.41: The period spacing patterns of KIC 11456474.

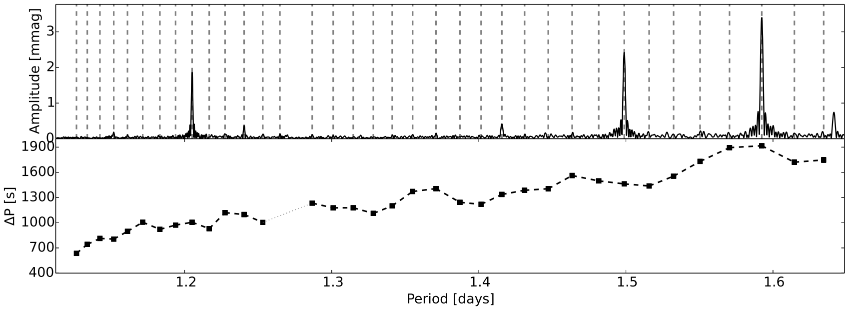

Figure C.42: The period spacing patterns of KIC 11668783.

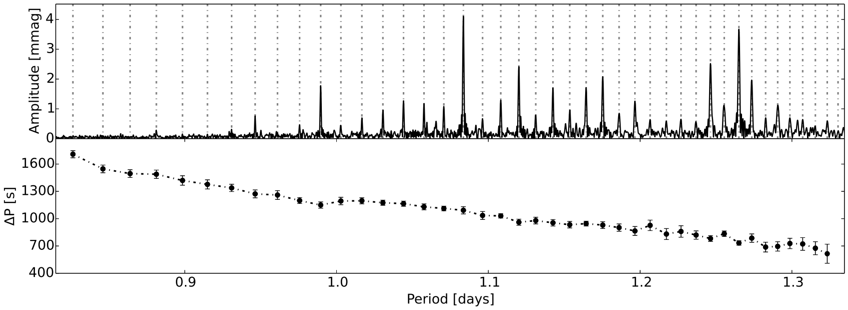

Figure C.43: The period spacing patterns of KIC 11721304.

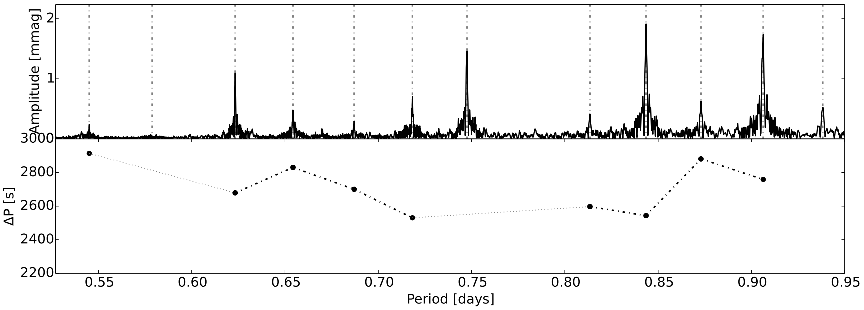

Figure C.44: The period spacing patterns of KIC 11754232.

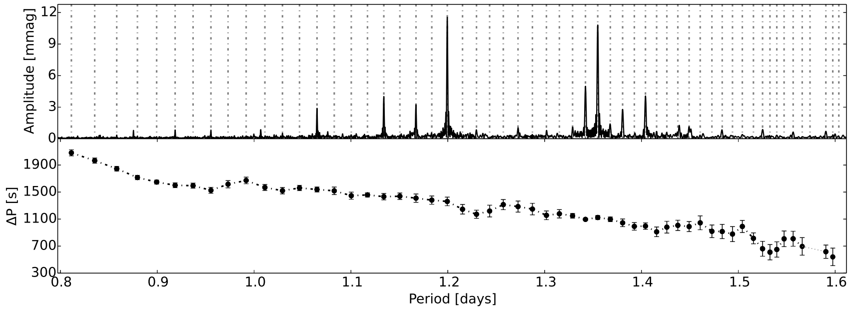

Figure C.45: The period spacing patterns of KIC 11826272.

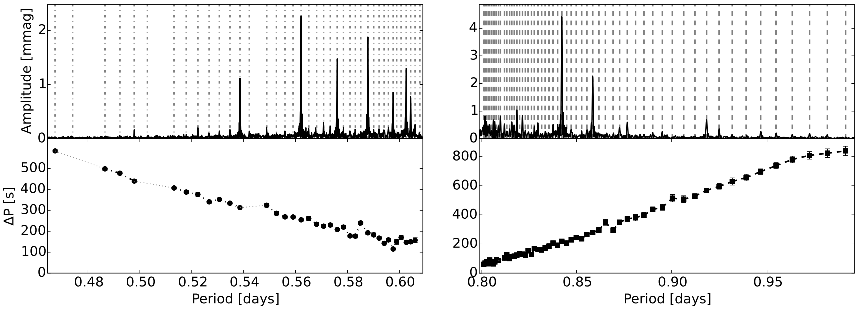

Figure C.46: The period spacing patterns of KIC 11907454.

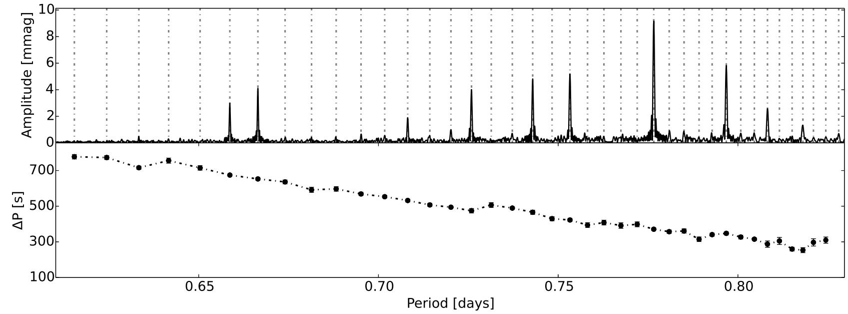

Figure C.47: The period spacing patterns of KIC 11917550.

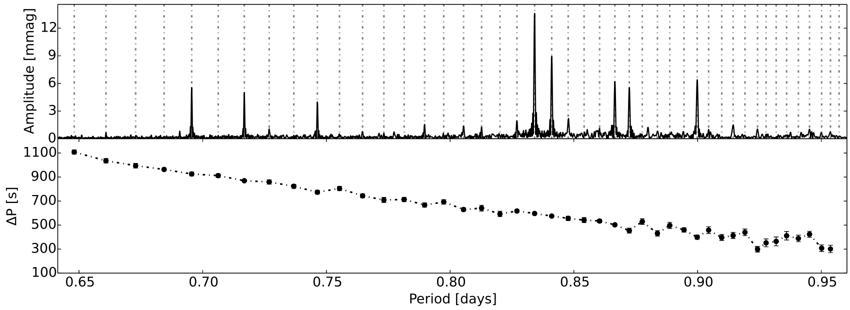

Figure C.48: The period spacing patterns of KIC 11920505.

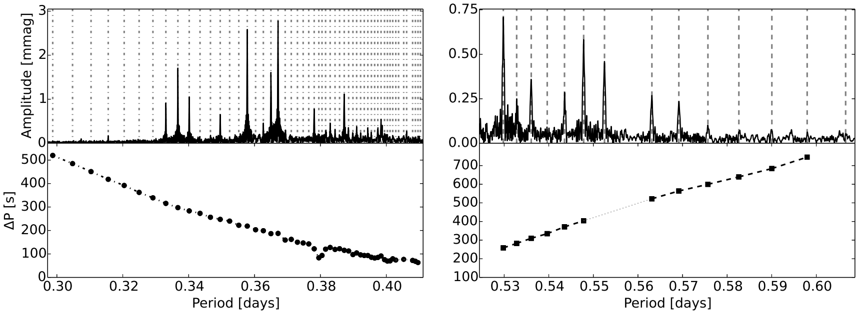

Figure C.49: The period spacing patterns of KIC 12066947.

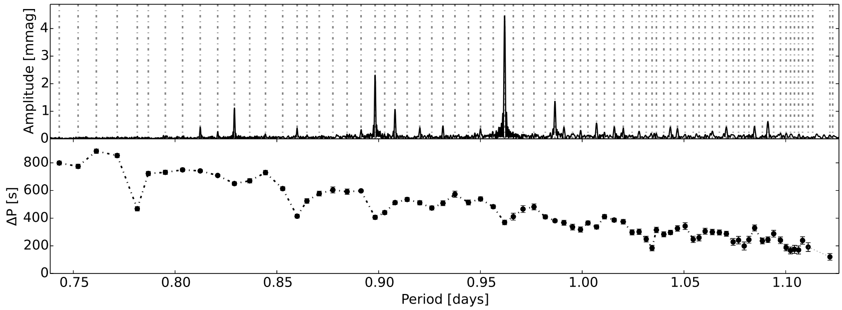

Figure C.50: The period spacing patterns of KIC 12458189.

Appendix D

Additional material to Chapter 4

Table D.1: Pulsation periods (in days; in the inertial reference frame) of the simulated data in Section 4.4.1, with 1σ uncertainty margins.

P_{inert} $[d]$	σ_P	P_{inert} $[d]$	σ_P
0.73912	0.00004	0.91909	0.00002
0.751414	0.000008	0.92658	0.00006
0.76322	0.00005	0.93385	0.00004
0.774892	0.000007	0.94088	0.00001
0.78640	0.00003	0.94772	0.00001
0.79748	0.00006	0.95442	0.00007
0.80785	0.00001	0.96100	0.00004
0.81753	0.00005	0.96745	0.00006
0.82691	0.00004	0.97373	0.00006
0.83618	0.00004	0.97984	0.00001
0.84513	0.00006	0.98579	0.00006
0.85371	0.00003	0.99161	0.00008
0.86220	0.00006	0.99732	0.00003
0.87080	0.00003	1.00292	0.00008
0.87937	0.00004	1.00839	0.00005
0.88773	0.00008	1.01372	0.00009
0.89582	0.00003	1.01891	0.00004
0.903689	0.000007	1.02400	0.00008
0.91144	0.00001	1.02898	0.00006

Table D.2: Rotation rates f_{rot} and asymptotic period spacings $\mathit{\Delta\Pi}_l$ computed from the observed period spacing patterns, as well as the mode identification and the dominant pulsation frequency for each series. For the latter we also computed the spin parameter s, listed in the final column. The pulsation mode patterns marked with "R" are retrograde modes, which are most likely Rossby modes. The pulsation modes marked with "S" are single high-amplitude peaks that were present in the frequency spectra, but clearly separate from the detected period spacing patterns. Neither the retrograde pulsation modes nor the single peaks were used in the computations. The corresponding rotation rates and asymptotic period spacings were obtained from the prograde series observed for the same star.

KIC	l	m	$f_{\mathrm{dom,inert}}$	f_{rot}	$\mathit{\Delta\Pi}_l$		$\lvert s\rvert$
			[d^{-1}]	[d^{-1}]	[s]	[d]	
2710594	1	1	$1.35536^{+0.00001}_{-0.00001}$	$1.02^{+0.02}_{-0.02}$	3370^{+330}_{-310}	$0.039^{+0.004}_{-0.004}$	$6.2^{+0.5}_{-0.5}$
	R	R	$0.79908^{+0.00002}_{-0.00002}$	$1.02^{+0.02}_{-0.02}$	3370^{+330}_{-310}	$0.039^{+0.004}_{-0.004}$	$9.1^{+0.7}_{-0.6}$
3448365	1	1	$1.500157^{+0.000009}_{-0.000009}$	$1.08^{+0.05}_{-0.07}$	3020^{+1160}_{-970}	$0.03^{+0.01}_{-0.01}$	$5.2^{+0.9}_{-1.2}$
	R	R	$0.88877^{+0.00001}_{-0.00001}$	$1.08^{+0.05}_{-0.07}$	3020^{+1160}_{-970}	$0.03^{+0.01}_{-0.01}$	11^{+4}_{-3}
4846809	1	1	$1.81324^{+0.00001}_{-0.00001}$	$1.28^{+0.01}_{-0.02}$	2930^{+140}_{-150}	$0.034^{+0.002}_{-0.002}$	$4.8^{+0.2}_{-0.2}$
	1	0	$1.00410^{+0.00002}_{-0.00002}$	$1.28^{+0.01}_{-0.02}$	2930^{+140}_{-150}	$0.034^{+0.002}_{-0.002}$	$2.55^{+0.03}_{-0.03}$
5114382	1	1	$1.47927^{+0.00002}_{-0.00002}$	$1.15^{+0.02}_{-0.02}$	3070^{+300}_{-290}	$0.036^{+0.003}_{-0.003}$	$7.0^{+0.5}_{-0.6}$
	R	R	$0.95265^{+0.00002}_{-0.00002}$	$1.15^{+0.02}_{-0.02}$	3070^{+300}_{-290}	$0.036^{+0.003}_{-0.003}$	$11.6^{+1.0}_{-0.9}$
5522154	1	1	$3.009858^{+0.000008}_{-0.000008}$	$2.154^{+0.004}_{-0.004}$	3350^{+40}_{-30}	$0.0388^{+0.0004}_{-0.0004}$	$5.03^{+0.03}_{-0.03}$
5708550	1	1	$1.11550^{+0.00001}_{-0.00001}$	$0.82^{+0.01}_{-0.02}$	3330^{+240}_{-220}	$0.039^{+0.003}_{-0.003}$	$5.5^{+0.4}_{-0.4}$
5788623	1	1	$0.77895^{+0.00001}_{-0.00001}$	$0.40^{+0.04}_{-0.05}$	2800^{+480}_{-440}	$0.032^{+0.006}_{-0.005}$	$2.1^{+0.4}_{-0.5}$
6468146	1	1	$1.545700^{+0.000005}_{-0.000005}$	$0.97^{+0.01}_{-0.01}$	3000^{+110}_{-110}	$0.035^{+0.001}_{-0.001}$	$3.4^{+0.1}_{-0.1}$
6468987	1	1	$1.998989^{+0.000004}_{-0.000004}$	$1.598^{+0.009}_{-0.008}$	3730^{+120}_{-100}	$0.043^{+0.001}_{-0.001}$	$8.0^{+0.2}_{-0.2}$

KIC	l	m	$f_{\rm dom,inert}$	$f_{\rm rot}$	$\mathit{\Delta\Pi}_l$		$\lvert s\rvert$
			[d^{-1}]	[d^{-1}]	[s]	[d]	
	R	R	$1.387598^{+0.000009}_{-0.000009}$	$1.598^{+0.009}_{-0.008}$	3730^{+120}_{-100}	$0.043^{+0.001}_{-0.001}$	$15.2^{+0.5}_{-0.6}$
6678174	1	1	$1.12777^{+0.00002}_{-0.00002}$	$0.55^{+0.05}_{-0.06}$	3370^{+710}_{-620}	$0.039^{+0.008}_{-0.007}$	$1.9^{+0.4}_{-0.4}$
6935014	1	1	$1.20670^{+0.00001}_{-0.00001}$	$0.79^{+0.02}_{-0.02}$	3180^{+310}_{-300}	$0.037^{+0.004}_{-0.003}$	$3.8^{+0.3}_{-0.3}$
6953103	1	1	$1.287597^{+0.000008}_{-0.000008}$	$0.74^{+0.03}_{-0.04}$	3560^{+490}_{-440}	$0.041^{+0.006}_{-0.005}$	$2.7^{+0.3}_{-0.3}$
7023122	1	1	$1.876108^{+0.000003}_{-0.000003}$	$0.977^{+0.005}_{-0.005}$	3380^{+40}_{-30}	$0.0391^{+0.0004}_{-0.0004}$	$2.17^{+0.03}_{-0.03}$
7365537	1	1	$2.925633^{+0.000004}_{-0.000004}$	$2.253^{+0.003}_{-0.003}$	3340^{+30}_{-30}	$0.0387^{+0.0003}_{-0.0003}$	$6.70^{+0.04}_{-0.04}$
	S	S	$1.981016^{+0.000006}_{-0.000006}$	$2.253^{+0.003}_{-0.003}$	3340^{+30}_{-30}	$0.0387^{+0.0003}_{-0.0003}$	$16.6^{+0.2}_{-0.2}$
7380501	1	1	$0.96329^{+0.00001}_{-0.00001}$	$0.64^{+0.01}_{-0.01}$	2860^{+180}_{-170}	$0.033^{+0.002}_{-0.002}$	$3.9^{+0.2}_{-0.3}$
7434470	1	1	$2.542409^{+0.000006}_{-0.000006}$	$1.769^{+0.005}_{-0.005}$	3020^{+50}_{-50}	$0.0349^{+0.0006}_{-0.0005}$	$4.57^{+0.04}_{-0.04}$
	S	S	$1.698729^{+0.000001}_{-0.000001}$	$1.769^{+0.005}_{-0.005}$	3020^{+50}_{-50}	$0.0349^{+0.0006}_{-0.0005}$	50^{+3}_{-4}
7583663	1	1	$1.47213^{+0.00001}_{-0.00001}$	$1.17^{+0.02}_{-0.03}$	3120^{+390}_{-360}	$0.036^{+0.005}_{-0.004}$	$7.8^{+0.8}_{-0.9}$
	R	R	$1.044741^{+0.000008}_{-0.000008}$	$1.17^{+0.02}_{-0.03}$	3120^{+390}_{-360}	$0.036^{+0.005}_{-0.004}$	19^{+3}_{-3}
7746984	1	1	$2.00305^{+0.00002}_{-0.00002}$	$1.49^{+0.02}_{-0.02}$	3130^{+250}_{-230}	$0.036^{+0.003}_{-0.003}$	$5.8^{+0.3}_{-0.3}$
	S	S	$1.35180^{+0.00001}_{-0.00001}$	$1.49^{+0.02}_{-0.02}$	3130^{+250}_{-230}	$0.036^{+0.003}_{-0.003}$	22^{+3}_{-2}
7939065	1	1	$1.728171^{+0.000007}_{-0.000007}$	$1.111^{+0.006}_{-0.006}$	3000^{+40}_{-40}	$0.0347^{+0.0005}_{-0.0005}$	$3.60^{+0.05}_{-0.05}$
8364249	1	1	$1.869376^{+0.000005}_{-0.000005}$	$1.519^{+0.007}_{-0.008}$	3090^{+110}_{-110}	$0.036^{+0.001}_{-0.001}$	$8.7^{+0.2}_{-0.2}$
8375138	1	1	$2.077771^{+0.000007}_{-0.000007}$	$1.64^{+0.01}_{-0.01}$	2930^{+150}_{-150}	$0.034^{+0.002}_{-0.002}$	$7.5^{+0.3}_{-0.3}$
	R	R	$1.407115^{+0.000010}_{-0.000010}$	$1.64^{+0.01}_{-0.01}$	2930^{+150}_{-150}	$0.034^{+0.002}_{-0.002}$	$14.0^{+0.7}_{-0.6}$

KIC	l	m	$f_{\mathrm{dom,inert}}$	f_{rot}	$\mathit{\Delta\Pi}_l$		$\lvert s\rvert$
			[d^{-1}]	[d^{-1}]	[s]	[d]	
8645874	1	1	$1.847014^{+0.000004}_{-0.000004}$	$0.34^{+0.08}_{-0.08}$	3050^{+320}_{-340}	$0.035^{+0.004}_{-0.004}$	$0.510^{+0.003}_{-0.003}$
8836473	1	1	$1.88341^{+0.00001}_{-0.00001}$	$1.13^{+0.01}_{-0.01}$	2900^{+100}_{-100}	$0.034^{+0.001}_{-0.001}$	$2.98^{+0.09}_{-0.09}$
	S	S	$0.52525^{+0.00001}_{-0.00001}$	$1.13^{+0.01}_{-0.01}$	2900^{+100}_{-100}	$0.034^{+0.001}_{-0.001}$	$3.75^{+0.04}_{-0.04}$
9210943	1	1	$2.190853^{+0.000004}_{-0.000004}$	$1.728^{+0.007}_{-0.010}$	3340^{+80}_{-100}	$0.0386^{+0.0010}_{-0.0012}$	$7.5^{+0.2}_{-0.2}$
	R	R	$1.443566^{+0.000009}_{-0.000009}$	$1.728^{+0.007}_{-0.010}$	3340^{+80}_{-100}	$0.0386^{+0.0010}_{-0.0012}$	$12.2^{+0.3}_{-0.3}$
9480469	1	1	$1.994822^{+0.000010}_{-0.000010}$	$1.54^{+0.03}_{-0.03}$	2990^{+410}_{-360}	$0.035^{+0.005}_{-0.004}$	$6.8^{+0.5}_{-0.6}$
	R	R	$1.32598^{+0.00001}_{-0.00001}$	$1.54^{+0.03}_{-0.03}$	2990^{+410}_{-360}	$0.035^{+0.005}_{-0.004}$	14^{+2}_{-2}
9595743	1	1	$1.43459^{+0.00002}_{-0.00002}$	$0.89^{+0.01}_{-0.01}$	3050^{+110}_{-110}	$0.035^{+0.001}_{-0.001}$	$3.3^{+0.1}_{-0.1}$
	1	0	$1.16055^{+0.00002}_{-0.00002}$	$0.89^{+0.01}_{-0.01}$	3050^{+110}_{-110}	$0.035^{+0.001}_{-0.001}$	$1.54^{+0.02}_{-0.02}$
9751996	1	1	$1.35387^{+0.00002}_{-0.00002}$	$0.070^{+0.001}_{-0.001}$	3086^{+12}_{-11}	$0.03572^{+0.00007}_{-0.00007}$	$0.11^{+0.03}_{-0.03}$
	1	0	$1.02805^{+0.00002}_{-0.00002}$	$0.070^{+0.001}_{-0.001}$	3086^{+12}_{-11}	$0.0357^{+0.0001}_{-0.0001}$	$0.14^{+0.03}_{-0.03}$
	1	-1	$1.28331^{+0.00002}_{-0.00002}$	$0.070^{+0.001}_{-0.001}$	3086^{+12}_{-11}	$0.0357^{+0.0001}_{-0.0001}$	$0.11^{+0.03}_{-0.03}$
10256787	1	1	$1.077489^{+0.000008}_{-0.000008}$	$0.59^{+0.04}_{-0.04}$	2730^{+560}_{-490}	$0.032^{+0.006}_{-0.006}$	$2.5^{+0.3}_{-0.4}$
10467146	1	1	$0.954976^{+0.000009}_{-0.000009}$	$0.62^{+0.03}_{-0.04}$	2940^{+600}_{-540}	$0.034^{+0.007}_{-0.006}$	$3.6^{+0.6}_{-0.7}$
11080103	1	1	$1.241393^{+0.000005}_{-0.000005}$	$0.62^{+0.05}_{-0.06}$	3360^{+880}_{-730}	$0.039^{+0.010}_{-0.008}$	$2.0^{+0.3}_{-0.4}$
11099031	1	1	$1.61508^{+0.00001}_{-0.00001}$	$1.025^{+0.009}_{-0.009}$	3560^{+100}_{-110}	$0.041^{+0.001}_{-0.001}$	$3.48^{+0.08}_{-0.08}$
	S	S	$0.916646^{+0.000009}_{-0.000009}$	$1.025^{+0.009}_{-0.009}$	3560^{+100}_{-110}	$0.041^{+0.001}_{-0.001}$	19^{+1}_{-1}
11294808	1	1	$1.16617^{+0.00001}_{-0.00001}$	$0.77^{+0.02}_{-0.02}$	2770^{+350}_{-320}	$0.032^{+0.004}_{-0.004}$	$4.0^{+0.3}_{-0.4}$

KIC	l	m	$f_{\mathrm{dom,inert}}$	f_{rot}	$\mathit{\Delta\Pi}_l$		$\lvert s\rvert$
			$[\mathrm{d}^{-1}]$	$[\mathrm{d}^{-1}]$	[s]	[d]	
	2	2	$2.2247^{+0.0007}_{-0.0007}$	$0.77^{+0.02}_{-0.02}$	1600^{+200}_{--190}	$0.019^{+0.002}_{-0.002}$	$2.3^{+0.2}_{-0.2}$
11456474	1	1	$1.471468^{+0.000006}_{-0.000006}$	$1.05^{+0.02}_{-0.02}$	2810^{+250}_{-240}	$0.033^{+0.003}_{-0.003}$	$5.0^{+0.3}_{-0.3}$
11721304	1	1	$0.92287^{+0.00002}_{-0.00002}$	$0.46^{+0.03}_{-0.03}$	3080^{+430}_{-400}	$0.036^{+0.005}_{-0.005}$	$2.0^{+0.3}_{-0.3}$
11754232	1	1	$1.10338^{+0.00001}_{-0.00001}$	$0.159^{+0.007}_{-0.007}$	3130^{+20}_{-20}	$0.0362^{+0.0002}_{-0.0003}$	$0.34^{+0.02}_{-0.02}$
11826272	1	1	$0.83370^{+0.00001}_{-0.00001}$	$0.36^{+0.02}_{-0.03}$	2950^{+290}_{-280}	$0.034^{+0.003}_{-0.003}$	$1.5^{+0.2}_{-0.2}$
11907454	1	1	$1.77890^{+0.00001}_{-0.00001}$	$1.35^{+0.02}_{-0.02}$	3050^{+290}_{-280}	$0.035^{+0.003}_{-0.003}$	$6.2^{+0.4}_{-0.4}$
	R	R	$1.187153^{+0.000008}_{-0.000008}$	$1.35^{+0.02}_{-0.02}$	3050^{+290}_{-280}	$0.035^{+0.003}_{-0.003}$	17^{+2}_{-2}
11917550	1	1	$1.287680^{+0.000008}_{-0.000008}$	$0.90^{+0.02}_{-0.02}$	2900^{+220}_{-210}	$0.034^{+0.003}_{-0.002}$	$4.6^{+0.3}_{-0.3}$
11920505	1	1	$1.198844^{+0.000009}_{-0.000009}$	$0.75^{+0.02}_{-0.02}$	2980^{+260}_{-250}	$0.035^{+0.003}_{-0.003}$	$3.3^{+0.2}_{-0.3}$
12066947	1	1	$2.72379^{+0.00001}_{-0.00001}$	$2.160^{+0.008}_{-0.008}$	2950^{+70}_{-70}	$0.0342^{+0.0008}_{-0.0008}$	$7.7^{+0.1}_{-0.1}$
	R	R	$1.88748^{+0.00002}_{-0.00002}$	$2.160^{+0.008}_{-0.008}$	2950^{+70}_{-70}	$0.0342^{+0.0008}_{-0.0008}$	$15.8^{+0.4}_{-0.4}$

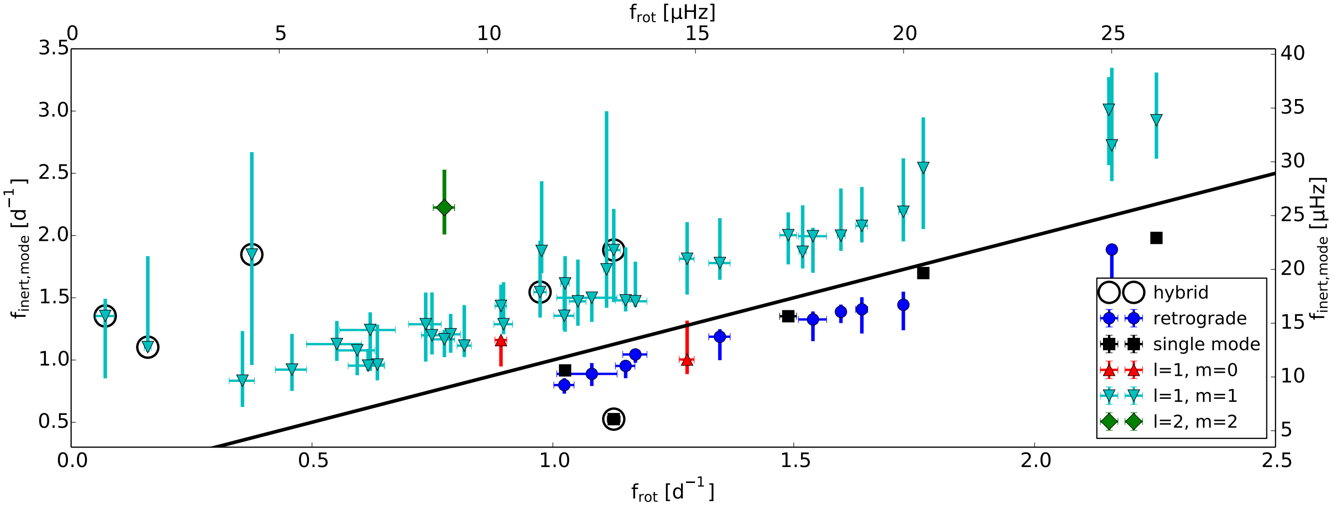

Figure D.1: Dominant pulsation frequency $f_{dom,inert}$ in the inertial frame as a function of the rotation frequency f_{rot} for the identified g-mode pulsations of 40 stars in the sample. The thick vertical lines indicate the full extent of the detected spacing series. The full black line indicates where f_{inert} is equal to f_{rot}.

Bibliography

Aerts, C. 2015, Astronomische Nachrichten, 336, 477

Aerts, C., Christensen-Dalsgaard, J., & Kurtz, D. W. 2010, Asteroseismology, Astronomy and Astrophsyics Library, Springer Berlin Heidelberg

Aerts, C., Molenberghs, G., Kenward, M. G., & Neiner, C. 2014, ApJ, 781, 88

Alvan, L., Brun, A. S., & Mathis, S. 2014, A&A, 565, A42

Arentoft, T., De Ridder, J., Grundahl, F., et al. 2007, A&A, 465, 965

Asplund, M., Grevesse, N., Sauval, A. J., & Scott, P. 2009, ARA&A, 47, 481

Aurière, M., Wade, G. A., Silvester, J., et al. 2007, A&A, 475, 1053

Auvergne, M., Bodin, P., Boisnard, L., et al. 2009, A&A, 506, 411

Badnell, N. R., Bautista, M. A., Butler, K., et al. 2005, MNRAS, 360, 458

Ballot, J., Lignières, F., Prat, V., Reese, D. R., & Rieutord, M. 2012, in Astronomical Society of the Pacific Conference Series, Vol. 462, Progress in Solar/Stellar Physics with Helio- and Asteroseismology, ed. H. Shibahashi, M. Takata, & A. E. Lynas-Gray, 389

Balona, L. A. 2012, MNRAS, 422, 1092

Balona, L. A. 2014, MNRAS, 439, 3453

Balona, L. A., Engelbrecht, C. A., Joshi, Y. C., et al. 2016, MNRAS, 460, 1318

Balona, L. A., Guzik, J. A., Uytterhoeven, K., et al. 2011, MNRAS, 415, 3531

Balona, L. A., Krisciunas, K., & Cousins, A. W. J. 1994, MNRAS, 270, 905

Battino, U., Pignatari, M., Ritter, C., et al. 2016, ApJ, 827, 30

Beck, P. G., Montalban, J., Kallinger, T., et al. 2012, Nat., 481, 55

Bedding, T. R., Murphy, S. J., Colman, I. L., & Kurtz, D. W. 2015, in European Physical Journal Web of Conferences, Vol. 101, European Physical Journal Web of Conferences, 01005

Belkacem, K., Marques, J. P., Goupil, M. J., et al. 2015, A&A, 579, A31

Belkacem, K., Samadi, R., Goupil, M. J., & Kupka, F. 2006a, A&A, 460, 173

Belkacem, K., Samadi, R., Goupil, M. J., Kupka, F., & Baudin, F. 2006b, A&A, 460, 183

Berthomieu, G., Gonczi, G., Graff, P., Provost, J., & Rocca, A. 1978, A&A, 70, 597

Böhm-Vitense, E. 1958, Z. Astrophys., 46, 108

Bouabid, M.-P., Dupret, M.-A., Salmon, S., et al. 2013, MNRAS, 429, 2500

Bouabid, M.-P., Montalbán, J., Miglio, A., et al. 2011, A&A, 531, A145

Bowman, D. M., Kurtz, D. W., Breger, M., Murphy, S. J., & Holdsworth, D. L. 2016, MNRAS, 460, 1970

Bradley, P. A., Guzik, J. A., Miles, L. F., et al. 2015, AJ, 149, 68

Braithwaite, J. & Nordlund, Å. 2006, A&A, 450, 1077

Breger, M. 1990, Delta Scuti Star Newsletter, 2, 13

Breger, M. 2000a, in Astronomical Society of the Pacific Conference Series, Vol. 210, Delta Scuti and Related Stars, ed. M. Breger & M. Montgomery, 3

Breger, M. 2000b, MNRAS, 313, 129

Breger, M., Fossati, L., Balona, L., et al. 2012, ApJ, 759, 62

Breger, M., Stich, J., Garrido, R., et al. 1993, A&A, 271, 482

Brown, T. M., Latham, D. W., Everett, M. E., & Esquerdo, G. A. 2011, AJ, 142, 112

Brunsden, E., Pollard, K. R., Cottrell, P. L., Wright, D. J., & De Cat, P. 2012a, MNRAS, 427, 2512

Brunsden, E., Pollard, K. R., Cottrell, P. L., et al. 2012b, MNRAS, 422, 3535

Canuto, V. M., Goldman, I., & Mazzitelli, I. 1996, ApJ, 473, 550

Canuto, V. M. & Mazzitelli, I. 1991, ApJ, 370, 295

Chadid, M., De Ridder, J., Aerts, C., & Mathias, P. 2001, A&A, 375, 113

Chapellier, E., Mathias, P., Weiss, W. W., Le Contel, D., & Debosscher, J. 2012, A&A, 540, A117

Chaplin, W. J. & Miglio, A. 2013, ARA&A, 51, 353

Charbonneau, P. 1995, ApJS, 101, 309

Cousins, A. W. J. 1992, The Observatory, 112, 53

Cousins, A. W. J., Caldwell, J. A. R., & Menzies, J. W. 1989, Information Bulletin on Variable Stars, 3412

Crowe, R. A. & Mitalas, R. 1982, A&A, 108, 55

Cuypers, J., Aerts, C., De Cat, P., et al. 2009, A&A, 499, 967

Davie, M. W., Pollard, K. R., Cottrell, P. L., et al. 2014, PASA, 31, e025

De Cat, P. & Aerts, C. 2002, A&A, 393, 965

Debosscher, J., Aerts, C., Tkachenko, A., et al. 2013, A&A, 556, A56

Debosscher, J., Blomme, J., Aerts, C., & De Ridder, J. 2011, A&A, 529, A89

Degroote, P., Aerts, C., Baglin, A., et al. 2010, Nat., 464, 259

Degroote, P., Briquet, M., Catala, C., et al. 2009, A&A, 506, 111

Driebe, T., Schoenberner, D., Bloecker, T., & Herwig, F. 1998, A&A, 339, 123

Dupret, M.-A., Grigahcène, A., Garrido, R., Gabriel, M., & Scuflaire, R. 2005, A&A, 435, 927

Dziembowski, W. A. & Goode, P. R. 1992, ApJ, 394, 670

Dziembowski, W. A. & Pamyatnykh, A. A. 1991, A&A, 248, L11

Eckart, G. 1960, Hydrodynamics of oceans and atmospheres, Pergamon Press, Oxford

Foster, H. M., Reed, M. D., Telting, J. H., Østensen, R. H., & Baran, A. S. 2015, ApJ, 805, 94

Fuller, J., Cantiello, M., Lecoanet, D., & Quataert, E. 2015, ApJ, 810, 101

Gallet, F., Charbonnel, C., & Amard, L. 2016, Origins of Life and Evolution of the Biosphere, 46, 395

García Hernández, A., Martín-Ruiz, S., Monteiro, M. J. P. F. G., et al. 2015, ApJL, 811, L29

Gilliland, R. L., Chaplin, W. J., Dunham, E. W., et al. 2011, ApJS, 197, 6

Gizon, L., Sekii, T., Takata, M., et al. 2016, Science Advances, 2

Gössl, S., Zwintz, K., & Kuschnig, R. 2016, Second BRITE-Constellation Science Conference: small satellites - big science, to be published (arXiv1611.04922)

Goupil, M. 2011, in Lecture Notes in Physics, Berlin Springer Verlag, Vol. 832, Lecture Notes in Physics, Berlin Springer Verlag, ed. J.-P. Rozelot & C. Neiner, 223

Gray, D. F. 1992, The observation and analysis of stellar photospheres.

Grec, G., Fossat, E., & Pomerantz, M. A. 1983, Sol. Phys., 82, 55

Guo, Z., Gies, D. R., & Fuller, J. 2017, ApJ, 834, 59

Guzik, J. A., Kaye, A. B., Bradley, P. A., Cox, A. N., & Neuforge, C. 2000, ApJ, 542, L57

Hambleton, K. M., Kurtz, D. W., Prša, A., et al. 2013, MNRAS, 434, 925

Handler, G., Balona, L. A., Shobbrook, R. R., et al. 2002, MNRAS, 333, 262

Hareter, M. 2012, Astronomische Nachrichten, 333, 1048

Heger, A., Langer, N., & Woosley, S. E. 2000, ApJ, 528, 368

Hekker, S. & Christensen-Dalsgaard, J. 2016, The Astronomy and Astrophysics Review, submitted (arXiv1609.07487)

Henry, G. W., Fekel, F. C., & Henry, S. M. 2011, AJ, 142, 39

Henyey, L., Vardya, M. S., & Bodenheimer, P. 1965, ApJ, 142, 841

Herwig, F. 2000, A&A, 360, 952

Herwig, F., Freytag, B., Fuchs, T., et al. 2007, in Astronomical Society of the Pacific Conference Series, Vol. 378, Why Galaxies Care About AGB Stars: Their Importance as Actors and Probes, ed. F. Kerschbaum, C. Charbonnel, & R. F. Wing, 43

Hopkins, P. F., Kereš, D., Oñorbe, J., et al. 2014, MNRAS, 445, 581

Howell, S. B., Sobeck, C., Haas, M., et al. 2014, PASP, 126, 398

Iglesias, C. A. & Rogers, F. J. 1993, ApJ, 412, 752

Iglesias, C. A. & Rogers, F. J. 1996, ApJ, 464, 943

Kahraman Aliçavuş, F., Niemczura, E., De Cat, P., et al. 2016, MNRAS, 458, 2307

Kaye, A. B., Handler, G., Krisciunas, K., Poretti, E., & Zerbi, F. M. 1999, PASP, 111, 840

Keen, M. A., Bedding, T. R., Murphy, S. J., et al. 2015, MNRAS, 454, 1792

Kippenhahn, R., Weigert, A., & Weiss, A. 2012, Stellar Structure and Evolution

Koch, D. G., Borucki, W. J., Basri, G., et al. 2010, ApJ, 713, L79

Krisciunas, K., Aspin, C., Geballe, T. R., et al. 1993, MNRAS, 263, 781

Kupka, F., Piskunov, N., Ryabchikova, T. A., Stempels, H. C., & Weiss, W. W. 1999, A&AS, 138, 119

Kurtz, D. W., Saio, H., Takata, M., et al. 2014, MNRAS, 444, 102

Kurtz, D. W., Shibahashi, H., Murphy, S. J., Bedding, T. R., & Bowman, D. M. 2015, MNRAS, 450, 3015

Ledoux, P. 1951, ApJ, 114, 373

Lee, U. & Saio, H. 1987, MNRAS, 224, 513

Lee, U. & Saio, H. 1993, MNRAS, 261, 415

Lee, U. & Saio, H. 1997, A&A, 491, 839

Lehmann, H., Southworth, J., Tkachenko, A., & Pavlovski, K. 2013, A&A, 557, A79

Longuet-Higgins, M. S. 1968, Philosophical Transactions of the Royal Society of London Series A, 262, 511

Lynden-Bell, D. & Ostriker, J. P. 1967, MNRAS, 136, 293

Maeder, A. 2009, Physics, Formation and Evolution of Rotating Stars

Mathis, S. 2011, in Lecture Notes in Physics, Berlin Springer Verlag, Vol. 832, Lecture Notes in Physics, Berlin Springer Verlag, ed. J.-P. Rozelot & C. Neiner, 275

Mathis, S. & de Brye, N. 2011, A&A, 526, A65

Mathis, S. & de Brye, N. 2012, A&A, 540, A37

Mathis, S., Neiner, C., & Tran Minh, N. 2014, A&A, 565, A47

Matt, S. P. D. O., Brown, B. P., & Brun, A. S. 2011, Astronomische Nachrichten, 332, 897

Metcalfe, T. S. & Charbonneau, P. 2003, Journal of Computational Physics, 185, 176

Miglio, A., Montalbán, J., Noels, A., & Eggenberger, P. 2008, MNRAS, 386, 1487

Miller Bertolami, M. M., Córsico, A. H., Zhang, X., Althaus, L. G., & Jeffery, C. S. 2013, in European Physical Journal Web of Conferences, Vol. 43, European Physical Journal Web of Conferences, 04004

Mitalas, R. 1972, ApJ, 177, 693

Moravveji, E., Aerts, C., Pápics, P. I., Triana, S. A., & Vandoren, B. 2015, A&A, 580, A27

Moravveji, E., Moya, A., & Guinan, E. F. 2012, ApJ, 749, 74

Moravveji, E., Townsend, R. H. D., Aerts, C., & Mathis, S. 2016, ApJ, 823, 130

Morel, T., Butler, K., Aerts, C., Neiner, C., & Briquet, M. 2006, A&A, 457, 651

Mosser, B., Belkacem, K., Pinçon, C., et al. 2017, A&A, 598, A62

Mosser, B., Goupil, M. J., Belkacem, K., et al. 2012, A&A, 548, A10

Mosser, B., Michel, E., Belkacem, K., et al. 2013, A&A, 550, A126

Mowlavi, N., Barblan, F., Saesen, S., & Eyer, L. 2013, A&A, 554, A108

Mowlavi, N., Saesen, S., Semaan, T., et al. 2016, A&A, 595, L1

Murphy, S. J., Bedding, T. R., Shibahashi, H., Kurtz, D. W., & Kjeldsen, H. 2014, MNRAS, 441, 2515

Murphy, S. J., Fossati, L., Bedding, T. R., et al. 2016, MNRAS, 459, 1201

Murphy, S. J., Shibahashi, H., & Kurtz, D. W. 2013, MNRAS, 430, 2986

Neiner, C., Floquet, M., Samadi, R., et al. 2012, A&A, 546, A47

Ouazzani, R.-M., Dupret, M.-A., & Reese, D. R. 2012, A&A, 547, A75

Ouazzani, R.-M., Salmon, S. J. A. J., Antoci, V., et al. 2017, MNRAS, 465, 2294

Pantillon, F. P., Talon, S., & Charbonnel, C. 2007, A&A, 474, 155

Papaloizou, J. & Pringle, J. E. 1978, MNRAS, 182, 423

Pápics, P. I. 2012, Astronomische Nachrichten, 333, 1053

Pápics, P. I., Briquet, M., Baglin, A., et al. 2012, A&A, 542, A55

Pápics, P. I., Moravveji, E., Aerts, C., et al. 2014, A&A, 570, A8

Pápics, P. I., Tkachenko, A., Van Reeth, T., et al. 2017, A&A, 598, A74

Paxton, B., Bildsten, L., Dotter, A., et al. 2011, ApJS, 192, 3

Paxton, B., Cantiello, M., Arras, P., et al. 2013, ApJS, 208, 4

Paxton, B., Marchant, P., Schwab, J., et al. 2015, ApJS, 220, 15

Prat, V., Lignières, F., & Ballot, J. 2016a, A&A, 587, A110

Prat, V., Mathis, S., Lignières, F., Ballot, J., & Culpin, P.-M. 2016b, in European Physical Journal Web of Conferences, Seismology of the Sun and the Distant Stars 2016, to be published (arXiv 1610.08674)

Prat, V., Mathis, S., Lignières, F., Ballot, J., & Culpin, P.-M. 2017, A&A, 598, A105

Raskin, G., van Winckel, H., Hensberge, H., et al. 2011, A&A, 526, A69

Rauer, H., Catala, C., Aerts, C., et al. 2014, Experimental Astronomy, 38, 249

Reed, M. D., Baran, A., Quint, A. C., et al. 2011, MNRAS, 414, 2885

Reed, M. D., Baran, A. S., Østensen, R. H., et al. 2016, MNRAS, 458, 1417

Reese, D. R., Prat, V., Barban, C., van 't Veer-Menneret, C., & MacGregor, K. B. 2013, A&A, 550, A77

Ricker, G. R., Winn, J. N., Vanderspek, R., et al. 2015, Journal of Astronomical Telescopes, Instruments, and Systems, 1, 014003

Rogers, F. J. & Nayfonov, A. 2002, ApJ, 576, 1064

Rogers, F. J., Swenson, F. J., & Iglesias, C. A. 1996, ApJ, 456, 902

Rogers, T. M. 2015, ApJ, 815, L30

Rogers, T. M., Lin, D. N. C., McElwaine, J. N., & Lau, H. H. B. 2013, ApJ, 772, 21

Saio, H. 1982, 256, 717

Saio, H., Kurtz, D. W., Takata, M., et al. 2015, MNRAS, 447, 3264

Salmon, S. J. A. J., Montalbán, J., Reese, D. R., Dupret, M.-A., & Eggenberger, P. 2014, A&A, 569, A18

Samadi, R., Belkacem, K., Goupil, M. J., et al. 2010, Astrophys Space Sci, 328, 253

Savonije, G. J. 2013, A&A, 559, A25

Schaller, G., Schaerer, D., Meynet, G., & Maeder, A. 1992, A&AS, 96, 269

Schmid, V. S. & Aerts, C. 2016, A&A, 592, A116

Schmid, V. S., Tkachenko, A., Aerts, C., et al. 2015, A&A, 584, A35

Schwarzenberg-Czerny, A. 2003, in Astronomical Society of the Pacific Conference Series, Vol. 292, Interplay of Periodic, Cyclic and Stochastic Variability in Selected Areas of the H-R Diagram, ed. C. Sterken, 383

Shibahashi, H. & Kurtz, D. W. 2012, MNRAS, 422, 738

Shulyak, D., Tsymbal, V., Ryabchikova, T., Stütz, C., & Weiss, W. W. 2004, A&A, 428, 993

Silva Aguirre, V., Ballot, J., Serenelli, A. M., & Weiss, A. 2011, A&A, 529, A63

Soszyński, I., Smolec, R., Dziembowski, W. A., et al. 2016, MNRAS, 463, 1332

Soufi, F., Goupil, M. J., & Dziembowski, W. A. 1998, A&A, 334, 911

Spruit, H. C. 2002, A&A, 381, 923

Stello, D., Cantiello, M., Fuller, J., et al. 2016, Nature, 529, 364

Suárez, J. C., García Hernández, A., Moya, A., et al. 2014, A&A, 563, A7

Tassoul, M. 1980, ApJS, 43, 469

Tassoul, M. 1990, ApJ, 358, 313

Tkachenko, A. 2015, A&A, 581, A129

Tkachenko, A., Aerts, C., Yakushechkin, A., et al. 2013a, A&A, 556, A52

Tkachenko, A., Lehmann, H., Smalley, B., & Uytterhoeven, K. 2013b, MNRAS, 431, 3685

Tkachenko, A., Van Reeth, T., Tsymbal, V., et al. 2013c, A&A, 560, A37

Townsend, R. H. D. 2000, MNRAS, 319, 289

Townsend, R. H. D. 2003a, MNRAS, 343, 125

Townsend, R. H. D. 2003b, MNRAS, 340, 1020

Townsend, R. H. D. 2005, MNRAS, 360, 465

Townsend, R. H. D. & Teitler, S. A. 2013, MNRAS, 435, 3406

Trampedach, R., Aarslev, M. J., Houdek, G., et al. 2017, MNRAS, 466, L43

Trampedach, R., Stein, R. F., Christensen-Dalsgaard, J., Nordlund, Å., & Asplund, M. 2014, MNRAS, 445, 4366

Triana, S. A., Moravveji, E., Pápics, P. I., et al. 2015, ApJ, 810, 16

Tsymbal, V. 1996, in Astronomical Society of the Pacific Conference Series, Vol. 108, M.A.S.S., Model Atmospheres and Spectrum Synthesis, ed. S. J. Adelman, F. Kupka, & W. W. Weiss, 198

Unno, W., Osaki, Y., Ando, H., Saio, H., & Shibahashi, H. 1989, Nonradial oscillations of stars

Uytterhoeven, K., Moya, A., Grigahcène, A., et al. 2011, A&A, 534, A125

Vanderburg, A. & Johnson, J. A. 2014, PASP, 126, 948

Walker, G., Matthews, J., Kuschnig, R., et al. 2003, Publications of the Astronomical Society of the Pacific, 115, 1023

Weiss, W. W., Rucinski, S. M., Moffat, A. F. J., et al. 2014, PASP, 126, 573

Welsh, W. F., Orosz, J. A., Aerts, C., et al. 2011, ApJS, 197, 4

Xiong, D. R., Deng, L., Zhang, C., & Wang, K. 2016, MNRAS, 457, 3163

Zahn, J.-P. 1992, A&A, 265, 115

Zahn, J.-P., Talon, S., & Matias, J. 1997, A&A, 322, 320

Curriculum Vitae

Timothy Van Reeth
vanreethtimothy@gmail.com

Timothy Van Reeth was born on the 4th of August 1988 in Herentals, Belgium. His fascination with astronomy began at an early age with the adventures of Tintin in *The Shooting Star*, *Destination Moon* and *Explorers on the Moon*. Over time, his interest in science and astronomy grew, with the support of two very patient parents and two sisters.

In 2006 Timothy attended KU Leuven, and obtained a Bachelor in Physics (with a minor in mathematics) and a Master in Astronomy & Astrophysics, graduating in 2013. Timothy then started a PhD on pulsating γ Doradus stars under the supervision of prof. dr. Conny Aerts and dr. Andrew Tkachenko, finishing in early 2017.

When not at work, Timothy can usually be found reading a book with a cup of tea or coffee, buried in the worlds of sci-fi and fantasy, or with friends.

List of publications

Publications in refereed journals

1. Pápics P. I., Tkachenko A., **Van Reeth T.**, Aerts C., Moravveji E., Van de Sande M., De Smedt K., Bloemen S., Southworth J., Debosscher J., Niemczura E., Gameiro J. F., 2017, "Signatures of internal rotation discovered in the Kepler data of five slowly pulsating B stars", *Astronomy and Astrophysics*, 598, A74

2. **Van Reeth T.**, Tkachenko A., Aerts C., 2016, "Interior rotation of a sample of γ Doradus stars from ensemble modelling of their gravity-mode period spacings", *Astronomy and Astrophysics*, 593, A120

3. Beck P. G., Allende Prieto C., **Van Reeth T.**, Tkachenko A., Raskin G., Van Winckel H., do Nascimento Jr. J.-D., Salabert D., Corsaro E., García R. A., 2016, "The Hermes solar atlas and the spectroscopic analysis of the seismic solar analogue KIC 3241581", *Astronomy and Astrophysics*, 589, A27

4. Escorza A., Zwintz K., Tkachenko A., **Van Reeth T.**, Ryabchikova T., Neiner C., Poretti E., Rainer M., Michel E., Baglin A., Aerts C., 2016, "HD 41641: A classical δ Sct-type pulsator with chemical signatures of an Ap star", *Astronomy and Astrophysics*, 588, A71

5. Schmid V. S., Tkachenko A., Aerts C., Degroote P., Bloemen S., Murphy S. J., **Van Reeth T.**, Pápics P. I., Bedding T. R., Keen M. A., Prsa A., Menu J., Debosscher J., Hrudkova M., De Smedt K., Lombaert R., Nemeth P., 2015, "KIC 10080943: An eccentric binary system containing two pressure- and gravity-mode hybrid pulsators", *Astronomy and Astrophysics*, 584, A35

6. **Van Reeth T.**, Tkachenko A., Aerts C., Pápics. P. I., Triana S. A., Zwintz K., Degroote P., Debosscher J., Bloemen S., Schmid V. S.,

De Smedt K., Frémat Y., Fuentes A. S., Homan W., Hrudkova M., Karjalainen R., Lombaert R., Nemeth P., Østensen R., Van De Steene G., Vos J., Raskin G., Van Winckel H., 2015, “Gravity-mode period spacings as seismic diagnostic for a sample of γ Doradus stars from Kepler space photometry and high-resolution ground-based spectroscopy”, *The Astrophysical Journal Supplement Series*, 218 (2), 27

7. Pápics. P. I., Tkachenko A., Aerts C., **Van Reeth T.**, De Smedt K., Hillen M., Østensen R., Moravveji E., 2015, “Asteroseismic fingerprints of rotation and mixing in the slowly pulsating B8 V star KIC 7760680”, *The Astrophysical Journal Letters*, 803 (2), L25

8. **Van Reeth T.**, Tkachenko A., Aerts C., Pápics P. I., Degroote P., Debosscher J., Zwintz K., Bloemen S., De Smedt K., Hrudkova M., Raskin G., Van Winckel H., 2015, “Detecting non-uniform period spacings in the Kepler photometry of γ Doradus stars: methodology and case studies”, *Astronomy and Astrophysics*, 574, A17

9. Schmid V. S., Themeßl N., Breger M., Degroote P., Aerts C., Beck P. G., Tkachenko A., **Van Reeth T.**, Bloemen S., Debosscher J., Castanheira B. G., McArthur B. E., Pápics P. I., Fritz V., Falcon R. E., 2014, “Discovery of binarity, spectroscopic frequency analysis, and mode identification of the δ Scuti star 4 CVn”, *Astronomy and Astrophysics*, 570, A33

10. Tkachenko A., **Van Reeth T.**, Tsymbal V., Aerts C., Kochukhov O., Debosscher J., 2013, “Denoising spectroscopic data by means of the improved least-squares deconvolution method”, *Astronomy and Astrophysics*, 560, A37

Publications in conference proceedings

1. Beck, P. G., Salabert D., Garcia R. A., do Nascimento Jr. J., Duarte T. S. S., Mathis S., Regulo C., Ballot J., Egeland R., Castro M., Pérez-Herńandez F., Creevey O., Tkachenko A., **Van Reeth T.**, Bigot L., Corsaro E., Metcalfe T., Mathur S., Palle P. L., Allende Prieto C., Montes D., Johnston C., Andersen M. F., Van Winckel H., 2016, “Probing Seismic Solar Analogues Through Observations With The Nasa Kepler Space Telescope And Hermes High-Resolution Spectrograph”, *19th Cambridge Workshop on Cool Stars, Stellar Systems, and the Sun (CS19)*, 42

2. **Van Reeth T.**, 2015, “Stellar evolution in motion: period spacings in γ Doradus stars”, *The Space Photometry Revolution - CoRoT Symposium 3,*

Kepler KASC-7 Joint Meeting, Toulouse, France, Edited by R.A. García; J. Ballot. EPJ Web of Conferences, 101, 06065

3. **Van Reeth T.**, Tkachenko A., Tsymbal V.,2013, “Least-Squares Deconvolution based analysis of stellar spectra”, *Setting a New Standard in the Analysis of Binary Stars, Edited by K. Pavlovski, A. Tkachenko and G. Torres. EAS Publications Series*, 64, 237-244

FACULTY OF SCIENCE
DEPARTMENT OF PHYSICS AND ASTRONOMY
INSTITUTE OF ASTRONOMY
Celestijnenlaan 200D box 2401
B-3001 Leuven
timothy.vanreeth@kuleuven.be
http://ster.kuleuven.be